UNIVERSIDADE DE SÃO PAULO

INSTITUTO DE GEOCIÊNCIAS

# DEFORMATIONAL, CRYSTALLOGRAPHIC AND PETROCHRONOLOGICAL ANALYSES OF THE MYLONITES FROM THE TAXAQUARA SHEAR ZONE IN RIBEIRA BELT (SÃO PAULO)

**BRUNO VIEIRA RIBEIRO**

Dissertação apresentada ao Programa de Pós-Graduação em Geoquímica e Geotectônica do Instituto de Geociências da Universidade de São Paulo como requisito para obtenção do título de Mestre em Ciências

Área de concentração: Geotectônica

Orientador: Prof. Dr. Ginaldo Ademar da Cruz Campanha

SÃO PAULO
2019

Serviço de Biblioteca e Documentação do IGc/USP

Ficha catalográfica gerada automaticamente com dados fornecidos pelo(a) autor(a) via programa desenvolvido pela Seção Técnica de Informática do ICMC/USP

Bibliotecários responsáveis pela estrutura de catalogação da publicação: Sonia Regina Yole Guerra - CRB-8/4208 | Anderson de Santana - CRB-8/6658

Vieira Ribeiro, Bruno
Deformational, crystallographic and thermochronological analyses of mylonites from the Taxaquara Shear Zone in the Ribeira Belt (São Paulo) / Bruno Vieira Ribeiro; orientador Ginaldo Ademar da Cruz Campanha. -- São Paulo, 2019.

76 p.

Dissertação (Mestrado - Programa de Pós-Graduação em Geoquímica e Geotectônica) -- Instituto de Geociências, Universidade de São Paulo, 2019.

1. Faixa Ribeira. 2. Zonas de Cisalhamento. 3. Análises microfísicas. 4. Análises estruturais quantitativas. 5. Petrocronologia I. Ademar da Cruz Campanha, Ginaldo, orient. II. Análises deformacionais, cristalográficas e petrocronológicas dos milonitos da Zona de Cisalhamento de Taxaquara, Faixa Ribeira (São Paulo).

UNIVERSIDADE DE SÃO PAULO
INSTITUTO DE GEOCIÊNCIAS

# DEFORMATIONAL, CRYSTALLOGRAPHIC AND PETROCHRONOLOGICAL ANALYSES OF THE MYLONITES FROM THE TAXAQUARA SHEAR ZONE IN RIBEIRA BELT (SÃO PAULO)

**BRUNO VIEIRA RIBEIRO**

Orientador: Prof. Dr. Ginaldo Ademar da Cruz Campanha

Dissertação de Mestrado

**Nº 840**

COMISSÃO JULGADORA

Dr. Ginaldo Ademar da Cruz Campanha

Dr. Luis Gustavo Ferreira Viegas

Dr. Sérgio Willians de Oliveira Rodrigues

SÃO PAULO
2019

## AGRADECIMENTOS

Essa dissertação de mestrado foi desenvolvida com ajuda e suporte de muitas pessoas excepcionais que fizeram a diferença durante minha jornada. Inicio agradecendo meus orientadores, Prof. Dr. Ginaldo Campanha e Prof. Dr. Frederico Faleiros, por sempre me darem liberdade para que eu pudesse desenvolver meus projetos e por acreditarem nas minhas propostas. Essa liberdade, combinada com conselhos e orientações, foi fundamental para que eu desenvolvesse meu pensamento crítico-científico. Muito obrigado e espero que nossa parceria continue nos projetos futuros. Também agradeço imensamente a todos os professores e funcionários que tanto me ensinaram e auxiliaram durante minha trajetória dentro do IGc USP. Aos Professores Peter Cawood e Roberto Weinberg (Monash University), o meu muito obrigado pela supervisão no exterior.

Com o fim desse mestrado, encerra-se meu período no IGc USP, iniciado em 2012. Durante esses quase 8 anos de USP, fiz amigos e amigas que foram fundamentais para a minha (des)construção e desenvolvimento pessoal e profissional. Agradeço aos amigos e amigas de graduação e pós-graduação por me aguentarem durante todos esses anos, aos amigos e amigas que fiz nos inúmeros BIFEs, aos amigos e amigas dos times de vôlei da USP em especial ao próprio time da Geologia, da FFLCH, Pedagogia e EEFE. Aos amigos do Matemática em Movimento que, mesmo após sairmos da ONG, mantivemos amizades próximas. Muito obrigado por todos esses anos juntos.

Agradeço também minha família que apoiou minhas decisões e tornou possível a conclusão dessa dissertação de mestrado e início das realizações futuras. Aos meus pais, o meu mais sincero obrigado e saibam que grande parte do que sou hoje é fruto do que vocês fizeram e fazem por mim. Se cheguei aonde cheguei foi graças a toda educação e suporte que me foi fornecido durante todos esses anos! *"Ao infinito e além".*

Por último, mas com certeza não menos importante, agradeço imensamente a minha melhor amiga e parceira, Júlia, que acompanhou todo o processo desse mestrado desde minha aprovação no processo de seleção ainda em 2017. Obrigado por me escutar falar sobre zonas de cisalhamento, transpressão, apatita e afins, por elogiar minhas figuras mesmo sem entender nada, sempre me incentivar, me apoiar durante meu estágio no exterior mesmo quando a saudade apertava e por tornar tudo mais fácil ao seu lado. Muito obrigado!

Agradeço ao convênio FAPESP – CAPES pelo apoio financeiro para a realização desse mestrado a partir dos processos FAPESP 2018/00320-9 e 2018/16307-1.

*“Lembre-se de olhar para as estrelas, não para os próprios pés. Tente compreender o que vê e questione o que faz o universo existir. Seja curioso. E por mais que a vida pareça difícil, sempre há algo que você pode e consegue fazer. Nunca desista. Deixe sua imaginação correr solta. Molde o futuro”*

*Breves respostas para grandes questões*
*Stephen Hawking, 2018*

## RESUMO

Ribeiro, B.V, 2019, Análises deformacionais, cristalográficas e petrocronológicas dos milonitos da Zona de Cisalhamento de Taxaquara (Faixa Ribeira, São Paulo) [Dissertação de Mestrado], São Paulo, Instituto de Geociências, Universidade de São Paulo, 76 p.

A Zona de Cisalhamento de Taxaquara (ZCT) corresponde a uma grande estrutura transcorrente da Faixa Ribeira (FR), SE Brasil. Na área de estudo, nos entornos do município de Pilar do Sul no interior de São Paulo, a ZCT apresenta foliação milonítica penetrativa de orientação NE-SW com mergulho preferencial para SE e lineações de estiramento com caimento variado. Dados de vorticidade e *strain* finito indicam que a ZCT foi desenvolvida dentro de um sistema regional transpressivo, com características de *sub-simple shear*, em condições de médio a alto *strain*. A ZCT separa os grupos Votuverava e São Roque e corta as suítes ígneas de Pilar do Sul e Piedade dando origem a milonitos quartzo-feldspáticos com matriz neoformada composta por quartzo + oligoclásio + K-feldspato + biotita + muscovita + rutilo + magnetita. Pseudosseção com isopletas de Si (p.f.u) em muscovita e número molar de sódio ($X_{Na}$) em plagioclásio, acoplada com o geotermômetro muscovita-biotita, restringe as condições de deformação em 513 – 525°C e 3.9 – 4.4kbar. Microestruturas e orientações preferenciais cristalográficas (OPC) indicam que grãos de quartzo de *ribbons* monominerálicos acomodam a deformação através de *dislocation creep* atingindo a transição entre rotação de subgrão e migração de borda de grão, a um *strain rate* médio entre $10^{-13}$ – $10^{-12}$ $s^{-1}$, com fábricas de OPC predominantemente monoclínicas com ativação dos sistemas de deslizamento 'basal-<a>' + 'rhomb-<a>' durante a deformação. No entanto, OPCs de quartzo e feldspato muito finos da matriz polifásica indicam possível mudança no mecanismo de deformação, passando de *dislocation creep* para *diffusion creep*.

Análises petrocronológicas a partir idades de $^{40}Ar/^{39}Ar$ em muscovita e U-Pb (LASS–ICP–MS) de apatita, titanita e zircão indicam que a ZCT esteve ativa, continuamente ou não, entre 544 ± 4.0 Ma e 534 ± 1.5 Ma. Essas idades, casadas com temperaturas de fechamento, indicam *cooling rate* de ~5°C/Ma conforme indicado por estudos regionais. Os dados petrocronológicos da ZCT contrastam com as idades de zonas de cisalhamento próximas, os quais são comumente obtidos por análises de fase minera única e sem demonstrar relação químico-textural com a deformação e metamorfismo. Dessa forma, uma revisão de detalhe das idades de zonas de cisalhamento da FR se faz necessária sob a óptica da petrocronologia

casando idades com textura e química mineral para que o entendimento e o significado dessas estruturas crustais dentro da FR sejam melhores compreendidos.

Palavras-chave: Faixa Ribeira; Zonas de Cisalhamento; Análises microfísicas; Análises estruturais quantitativas; Petrocronologia.

## ABSTRACT

Ribeiro, B.V., 2019, Deformational, crystallographic and petrochronological analyses of mylonites from the Taxaquara Shear Zone in Ribeira Belt (São Paulo) [Master's Thesis], São Paulo, Instituto de Geociências, Universidade de São Paulo, 76 p.

The Taxaquara Shear Zone (TSZ) is a major transcurrent structure in the Ribeira Belt (RB), SE Brazil. In the study area, around Pilar do Sul city in the countryside of São Paulo, the TSZ display a strong NE-SW mylonitic foliation preferentially dipping to W and stretching lineation with variable plunge. It separates the Votuverava and the São Roque Groups and cross-cut granitic rocks from the Pilar do Sul and Piedade Suits giving rise to quartz-feldspathic mylonitic rocks with newformed matrix assemblage composed of quartz + oligoclase + K-feldspar + biotite + muscovite + rutile + magnetite. Pseudosection with Si (p.f.u) in muscovite and sodium molar number in plagioclase ($X_{Na}$) isopleths, couple with muscovite-biotite geothermometer, indicates that the mineral assemblage constrains the deformation condition at 513 – 525°C and 3.9 – 4.4 kbar. Microstructures and crystallographic preferred orientation (CPO) indicate that quartz from monomineralic ribbons accommodates deformation through dislocation creep achieving the transition between subgrain rotation and grain boundary migration, at a mean strain rate of $10^{-12}$ to $10^{-12}$ $s^{-1}$, with monoclinic CPO patterns and activation of 'basal-<a>' + 'rhomb-<a>' slip system during deformation. CPO from fine-grained quartz and feldspar from polyphase matrix, however, indicate a switch in deformation mechanism from dislocation to diffusion creep. Vorticity and three-dimensional finite strain data indicate that the TSZ was developed under moderate to high strain within a transpressional sub-simple shear environment.

Petrochronological analyses using muscovite $^{40}Ar/^{39}Ar$ (step heating) and apatite, titanite and zircon U-Pb ages (LASS – ICP – MS) indicates that the TSZ was active from 544 ± 4.0 Ma to 534 ± 1.5 Ma, continuously or not. These ages, coupled with closure temperature estimates, suggest a cooling rate of ~5°C/Ma as indicated by regional studies. The geochronological data from the TSZ contrast with those from other shear zones in the RB, generally constrained by single mineral dating lacking textural and chemical data between the mineral and deformation. Thus, a detailed revision using multi-mineral method approach is required to improve the understanding the tectonic significance of the shear zones in the RB.



Keywords: Ribeira belt; Shear zones; Microphysical analyses; Quantitative structural analyses; Petrochronology.

# SUMMARY

# 1 CHAPTER 1

## PRESENTATION

### 1.1 Introduction

The Neoproterozoic Ribeira Belt (RB) evolution, SE Brazil, is strongly influenced by a major strike-slip shear zone system developed during late collisional stage in response to the oblique collision between the Paranapanema block, São Francisco, Luís Alves and Congo cratons during late stage of the Southwestern Gondwana assembly (Campanha, 2002; Campanha and Brito Neves, 2004; Egydio-Silva et al., 2018; Vauchez et al., 1994). These shear zones were developed between mid- to upper-crust environment, i.e. between the transition of ductile-brittle behavior for quartz, with preferential dextral shear sense and individual displacement that could reach tens of kilometers (Campanha, 2002). Since shear zones play an important role in the deformation history of the crust unrevealing not only the thermo-tectonic history of the deformation, but often the tectonic evolution of orogenic belts as a whole, it is highly important to proper comprehend this shear zone system in order to broadly understand the Neoproterozoic RB evolution. This shear zone system has been studied throughout the time (Campanha, 2002; Ebert et al., 1996; Ebert and Hasui, 1992; Faleiros, 2003; Faleiros et al., 2010; Passarelli et al., 2011; Ribeiro et al., 2019). Due to its neglected importance in regional tectonic studies, there is still a significant lack of data regarding mechanisms of deformation, well established deformation conditions based on quantitative analyses (e.g., thermodynamic modelling), tectonic system and the timing of development of these shear zones.

The Taxaquara Shear Zone (TSZ) is a regional strike-slip structure being one of the first regional structures recognized (Hennies et al., 1967) with an important tectonic significance within the RB since it seems to separate the Votuverava and the São Roque Group (Campos Neto, 2000; Hasui, 1975, 1973; Hasui and Sadowski, 1976). Hennies et al. (1967) described it as a NE-SW linear vertical structure with sub-horizontal stretching lineation plunging to W. These features drove the authors to classify it as a transcurrent structure, although its kinematic was no clear at that time. Although its claimed tectonic importance, no further detailed study of the TSZ has been done so far. In order to contribute to the understanding of the shear zone system and its role in the Neoproterozoic RB evolution, this Master's dissertation focused on the mechanisms of deformation, deformation condition, tectonic system and the timing of deformation of the TSZ using modern and sophisticated methods. In the end, the performed analyses provided innovative data which are being presented in two manuscripts.

The first manuscript, entitled *"Kinematics, nature of deformation and tectonic setting of the Taxaquara Shear Zone, a major transpressional shear zone of the Ribeira Belt (SE Brazil)"* published on *Tectonophysics* and presented in the Chapter 3 of this dissertation, presents new data regarding mechanisms of deformation of quartz and feldspar from quartz-feldspathic mylonites related to the TSZ through qualitative and quantitative microstructural and crystallographic preferred orientation (CPO) analyses using Fabric Analyzer (Wilson et al., 2007) and EBSD data and deformation conditions based on opening-angle thermometer (Faleiros et al., 2016b), conventional muscovite-biotite geothermometer (Hoisch, 1989) and thermodynamic modelling through pseudosections developed on Perple_X environment (Connolly, 2005). To improve the structural understanding of the TSZ, vorticity methods and finite strain analysis based on the shape preferred orientation (SPO) of feldspar porphyroclasts were performed to quantify the deformation coaxiality (i.e., pure vs. simple shear) and the geometry of the finite strain ellipses.

The second manuscript, entitled *"The missing link in dating mid-crustal shear zones: insights from apatite U-Pb dating and tectonic implications for the Neoproterozoic Ribeira Belt evolution"* submitted to *Tectonics* and presented in the Chapter 4 of this dissertation, presents a groundbreaking and detailed petrochronological study regarding the timing of deformation of the TSZ. Single spot U-Pb and trace elements analyses from apatite, titanite and zircon from granitic mylonite and undeformed granite samples were obtained through laser ablation split stream inductively coupled plasma mass spectrometry (LASS-ICP-MS) at Isotopia Laboratory, School of Earth Atmosphere and Environment, Monash University, Australia. These results, coupled with fish-shaped muscovite $^{40}Ar/^{39}Ar$ ages from granitic mylonite samples and closure temperature estimates for apatite and muscovite based on Pb and Ar diffusion, respectively, improved the understanding of i) how to date shear zones; ii) that apatite U-Pb ages record ductile deformation in mid-crustal shear zones at ~500°C, and iii) a new perspective regarding the tectonic importance of the shear zones in the RB in comparison to the published 'deformational' ages of other shear zones (Faleiros et al., 2011; Machado et al., 2007; Passarelli et al., 2011, 2008, 2007).

In the following dissertation, methods are briefly presented and a more detailed version is presented in the respective manuscripts together with the geological setting of the study area with different focus in each of them. In the end, final conclusions gathering both manuscripts are presented in the Chapter 5.

## 1.2 Research aims

This dissertation is based on the understanding of the processes that gave rise to deformed rocks related with the TSZ in the Ribeira Belt (SE Brazil), regarding its kinematics, nature and condition of deformation, time of motion and tectonic setting. In order to achieve these goals, several analyses were carried out, such as:

i. Recognition of the TSZ kinematics, structures and mechanisms of deformation from field-based and petrographic observations;
ii. Quartz and feldspar qualitative and quantitative microstructural observations, supported by crystallographic preferred orientation (CPO), paleopiezometry and strain rate estimates;
iii. Thermodynamic modelling and geothermometers to constrain the ductile deformation condition regarding pressure and temperature (P-T);
iv. Quantitative structural analysis based on vorticity and finite strain to investigate the tectonic setting; and
v. Geochronology based on $^{40}Ar/^{39}Ar$ (muscovite) and U-Pb (apatite, titanite and zircon) methods to investigate the timing of ductile motion.

Overall, this dissertation aims to contribute to the understanding of the shear zone system developed during the late-stages of Southwestern Gondwana assembly and, in more detail, the continental crust rheology, mechanisms of deformation and regional tectonic setting by comparison with others shear zones. However, the tectonic importance of these structures in the RB is still neglected, imposing difficulties to establish regional correlations based on quantified analyses. Thus, studies like this should be encouraged.

## 1.3 Organization

i. The presentation is based on published/submitted manuscripts to international journals. Hence, each chapter is independent dealing with specific aspects of the TSZ. ‘Chapter 1’ deals with the presentation of the problem here addressed;
ii. ‘Chapter 2’ presents the methods approached by this dissertation;
iii. ‘Chapter 3’ presents a major paper published in Tectonophysics Journal, covering 75% of the research aims;
iv. ‘Chapter 4’ is based on a manuscript regarding the timing of the ductile motion of the TSZ supported by $^{40}Ar/^{39}Ar$ and U-Pb geochronology.
v. ‘Chapter 5’ deals with final considerations and remarks.

# 2 CHAPTER 2

## METHODS OF STUDY

Since the methods approached during the development of this master's dissertation are well detailed in the published and/or submitted papers further presented here, this chapter briefly introduces each of them.

### 2.1 Petrographic and Microstructural Analyses

In order to investigate the mineral assemblage, kinematics, nature of deformation and recrystallization mechanisms, thin sections, cut perpendicular to foliation and parallel to stretching lineation (XZ section) of samples collected along the TSZ were analyzed through optical petrographic microscope. In order to support microstructural analysis, quartz and feldspar domains were chosen and classified through a number of quantitative measures. These domains were manually digitized using ArcGIS® (version 10.0) and analyzed using PolyLX (Lexa, 2003) toolbox (http://petrol.natur.cuni.nz/_ondro/) in MATLAB.

Electron backscattering (BSE) has been used to investigate microstructures in the ultrafine-grained matrix due its capacity to readily distinguish quartz, alkali feldspar and plagioclase. Hence, BSE couple with wavelength-dispersive X-Ray spectroscopy (WDS) were carried out on XZ oriented thin sections of one mylonite (PS-40B) and one ultramylonite sample (PSB-10) using JOEL JXA-8530F microprobe operating at 15kV, current analysis of 20nA and work distance of 11 mm. Both analyses were carried out at the University of São Paulo (Brazil).

### 2.2 Crystallographic Preferred Orientation

There are several methods to obtain quartz crystallographic preferred orientation (CPO) data. The optical petrographic microscope with a universal stage (U-stage), which has been traditionally used (Fedorov, 1982), is progressively being replaced by modern techniques, such as electron backscattering diffraction (EBSD), neutron diffraction (ND) and Fabric Analyzer (FA, Wilson et al., 2007). In this work, analyses were carried out with FA and EBSD.

Quartz [c]-axis measurements were carried out at School of Earth, Atmosphere and Environmental of Monash University (Melbourne, Australia) using a FA (G50). Measurements were collected from quartz-rich aggregates (ribbons). In this study, the CPOs are used to determine slip-system activated during quartz deformation, deformation temperature through opening-angle (OA) thermometer (Faleiros et al., 2016a, 2016b; Kruhl, 1996; Law, 2014) and vorticity studies ($\delta/\beta$ – method; Wallis, 1995, 1992). Data were further processed using MTEX

(https://mtex-toolbox.github.io/) toolbox in MATLAB to quantify OA and the vorticity plane following (Hunter et al., 2018).

In addition to FA analysis, we analyzed one mylonite sample using (EBSD) technique to compare with the FA results to ensure CPO quality and proper quantification of the slip systems activation during deformation based on axis misorientations (Neumann, 2000; Wheeler et al., 2001) and to investigate mechanisms of deformation in the fine-grained quartz-feldspathic matrix. Measurements were made using a 15kV acceleration voltage, 13.7 mm working distance and 70° sample tilt. Data were analyzed using CHANNEL5 producing 'one-pole-per-grain' pole figures of quartz and 'one-pole-per-grain' inverse pole figure.

### 2.3 Paleopiezometry and Strain Rate Estimates

Quartz and feldspar correspond to most abundant phases within the continental crust and its microstructures are useful to understand deformation conditions in the crustal profile (Faleiros et al., 2016a, 2010; Oliot et al., 2014; Prior and Wheeler, 1999; Stipp et al., 2002a, 2002b). The dislocation creep tend to gather into planar walls subdividing grains into subgrains, steady state feature of the substructure (Twiss, 1977), and its size is function of the applied differential stress. The fundamental assumption of this theory is that the formation of new grains through recrystallization processes must be energetically favorable (Twiss, 1997).

Paleopiezometers consist in a calibration related with diameter of new grains originated through recrystallization processes and stress flow (equal to differential stress) being proposed by several authors in the last four decades. In order to estimate the differential stress responsible for the quartz microstructures present in mylonites and ultramylonites samples from the TSZ, we applied Stipp and Tullis (2003) grain size piezometer for quartz, which was calibrated for regimes 2 (subgrain rotation) and 3 (subgrain rotation + grain boundary migration) of Hirth and Tullis (1992).

Since it is known that strain rate, P-T conditions and fluid activity, plays a role in the mechanisms of quartz dynamic recrystallization (Passchier and Trouw, 2005; Platt, 2015; Post and Tullis, 1999; Stipp et al., 2010, 2002b, 2002a; Vauchez, 1987; Viegas et al., 2016), it is fundamental to estimate strain rate to understand if the microstructures and the velocity of deformation is congruent. Therefore, strain rate estimates in this work was carried out using established flow laws (Eq. 01) using differential stress ($\Delta\sigma$) and P-T conditions from paleopiezometry and thermodynamic modelling, respectively. Calculations of water fugacity

were carried out following Pitzer and Sterner (1994) with help from Whiter's fugacity calculator (www.esci.umn.edu/people/researchers/withe012/fugacity.htm).

$$\acute{\varepsilon} = A\Delta\sigma^n f_{H20}^m \cdot exp\left(\frac{-Q}{RT}\right) \quad \text{(Eq. 1)}$$

where A = material constant; $\Delta\sigma$ = differential stress; f = water fugacity; Q = creep activation energy; R = Clapeyron constant; T = temperature; n = stress exponent; m = water fugacity exponent; $\acute{\varepsilon}$ = strain rate ($s^{-1}$). The values of A, n and Q for quartz have been determined by a number of laboratory experiments and here we use the values in Hirth et al. (2001) which has been interpreted as the most reliable for natural deformation.

### 2.4 Thermodynamic Modelling

In order to assess deformation condition, thermodynamic modelling was approached using Perple_X'6.8.3 (Connolly, 2005) based on whole-rock bulk composition to construct a P-T pseudosection, which is a diagram that shows the stability fields of a particular mineral assemblage. Whole-rock bulk composition from ultramylonites samples were analyzed by X-ray fluorescence using fused pellets (PANalytical, Zetium model) at the 'Laboratório de Caracterização Mineral – LCT USP). Phase relationships have been modelled with ten components (NCKFMASHTiO system) using the updated database version of Holland and Powell (2011) and modern activity models (White et al., 2014) taking into consideration melting at high temperature. Chemical compositions of minerals were measured with a Hence JOEL JXA-8530F microprobe operating at 15kV, current analysis 20nA, work distance of 11 mm. Both analyses were carried out at University of São Paulo (Brazil).

### 2.5 Vorticity

Vorticity analysis of naturally deformed rocks displays an important measurement of non-coaxiality of deformation, being essential for kinematic studies of shear zones. The kinematic vorticity number ($W_k$), or mean vorticity number ($W_m$; Passchier, 1988) ranges from 0 for strict pure shear to 1 for strict simple shear and can be quantified by several methods at the mesoscopic and microscopic scale (Passchier, 1988, 1987; Passchier and Urai, 1988; Simpson and De Paor, 1993; Wallis, 1995; Xypolias, 2010).

In this work, the vorticity number was quantified using two methods: rotation of rigid porphyroclasts (Passchier, 1987; Wallis, 1995) and the δ/β (Wallis, 1995). To provide data for the rigid porphyroclast analysis, feldspar porphyroclasts were manually digitized using Adobe Illustrator® with 150-200 grains per sample to ensure a sound statistical representation and

analysed using SPO2003 (Launeau and Robin, 2003a). This freeware calculates shape ratio and the angle between major axis and horizontal (x-direction) for each porphyroclast. The δ/β-method (Wallis, 1995) depends on the relation between the maximum angle (δ) between quartz oblique and main foliations in combination with the angle (β) between the shear plane and principal foliation determined through quartz [c] axis fabric. The measurements of β angles were carried out through a MTEX code developed in MATLAB environmental (Hunter et al., 2018) which estimate the vorticity plane based on the difference the foliation plane (E-W) and the plane perpendicular to the orientation defined by the c-axis maxima. This process enables to estimate the vorticity plane (β) even without data in the centre girdle. The angle δ between oblique and mylonitic foliation, on the other hand, were carried out through petrographic and grain statistical analysis.

### 2.6 Shape Preferred Orientation (SPO)

The current models regarding the shear zones development are based on the relations of strain, geometry and kinematics (e.g., Fossen et al., 1994; Lin et al., 1998; Robin and Cruden, 1994), however very few studies properly quantify tension and the deformation ellipsoid. In order to span the dataset regarding strain ellipsoid and to understand the tectonic setting that gave rise to the TSZ, the shape preferred orientation method (Launeau and Cruden, 1998) was applied.

The SPO method helps to determine the inertia tensor orientation based on the shape ratio and the obliquity between the major axis of each grain (e.g., porphyroclast) and the adopted reference (i.e., horizontal X direction in the TSZ case). Three-dimensional finite strain quantification was performed on four oriented samples of mylonites, two from each sector, on three mutually perpendicular and oriented sections of each sample. Afterwards, we traced the boundaries of feldspar porphyroclasts from samples photographs using Adobe Illustrator™ software and then converted into raster images (bitmap).

The inertia tensor technique (Launeau and Cruden, 1998) was applied to measure the dimensions and orientations of long and short axes (i.e., shape ratio) of individual feldspars grains using the SPO freeware (Launeau and Robin, 2003a), following a similar process of vorticity analysis based on rigid porphyroclasts method. Each two-dimensional section was subdivided into two or four subsections for each sample. Three-dimensional analyses were performed using the ELLIPSOID freeware (Launeau and Robin, 2003b). The parameter $(F)^{1/2}$

(incompatibility index, in %) converge to an ellipsoid for $(F)^{1/2} < 10\%$ and better fits come with lower values of $(F)^{1/2}$ (Launeau and Robin, 2005) being very meaningful to ensure good results.

### 2.7 U-Pb Geochronology and Mineral Trace Element Concentrations

In order to better estimate the time of motion during ductile deformation, we approached the geochronology of the TSZ through $^{40}Ar/^{39}Ar$ and U-Pb methods.

#### 2.7.1 $^{40}Ar/^{39}Ar$

$^{40}Ar/^{39}Ar$ analysis were carried out in the Geochronological Research Center (University of São Paulo, Brazil). The selected grains were irradiated with fast epithermal neutrons flow in the research reactor TRIGA (CLICIT) in the OSU/Oregon (USA), coupled with the international standard Fish Canyon (sanidine, 28.01 ± 0.04 Ma; Phillips and Matchan, 2013), for 15 continuous hours. After irradiation, the samples rested for 20 days until complete cooling and deposited to be analysed through step heating via solid state Nd:YVO4 laser (532nm – Verdi 6W Coherent model) in the Geochronological Research Center of the University of São Paulo (CPGeo/IGc/USP ). The mass of the $^{40}Ar$ and $^{36}Ar$ were simultaneously measured in 5 Faraday collectors (1011 Ω for $^{40}Ar$ mass and 1012 Ω for $^{36}Ar$ mass). During the analysis, the reproducibility was continuously monitored using atmospheric Ar measures (air pippete, $^{40}Ar/^{36}Ar$ weighted mean = 298.5)

After applied the mass discrimination, nucleotides interference and atmospheric contamination corrections, the apparent ages were calculated in each step heating using $J_{factor}$ = 3.308*10-3 ± 4.0*10-6. The plateau ages were defined based on $^{39}Ar_K$ >50% (ideally >70%) and the maximum steps numbers with $^{40}Ar^*/^{39}Ar_K$ coherent with 95% confidence (McDougall and Harrison, 1999). Apparent ages were plotted with 2σ error.

#### 2.7.2 U-Pb

Laser Ablation Split Stream Inductively Coupled Plasma Mass Spectrometry (LASS-ICP-MS) data collection for apatite, titanite and zircon ages and trace elements, as single spot ablations, was performed at Isotopia Laboratory, School of Earth Atmosphere and Environment, Monash University, Australia. Mineral separation was carried out at the University of São Paulo and Monash University. Crushed whole rocks were first sieved and the 125-250 mesh fraction was further processed using isodynamic, gravimetric and magnetic techniques to separate desired phases. Individual grains were mounted and polished in 1-inch² epoxy rounds.

For determining U-Pb ages and trace element concentrations, a LASS-ICP-MS set-up was utilized, whereby the sample is split into two even streams by a Y-piece located between the laser cell and the ICP-MS. A 25 μm diameter laser spot was used, with a laser repetition rate of 10 Hz and 6 mJ laser energy. The experiment consisted of 20 seconds background measurement and 20 seconds of ablation. Trace elements were collected on a Thermo Scientific iCAP Quadruple-ICP-MS, while U-Pb data were acquired with a Thermo Scientific iCAP Triple Quadruple ICP-MS. Acquired data were further reduced in Iolite environment (Paton et al., 2011) using the U-Pb Geochron and Trace Element data reduction schemes.

For the U-Pb experiments in apatite, Madel monazite was used as the primary standard (Payne et al., 2008), while the USGS-44069 monazite (Aleinikoff et al., 2006) and the MAD apatite (Thomson et al., 2012) were employed as secondary standards. For U-Pb experiments in titanite, the OLT titanite (Kennedy et al., 2010) was used as the primary age standard with BRL titanite (Aleinikoff et al., 2007) employed as secondary standard. For zircon experiments, the GJ1 (Jackson et al., 2004) and Plesovice zircon standards (Slama et al., 2008) were undertaken as primary and secondary standards, respectively. All secondary standards were treated as unknows to ensure quality data.

### 2.7.3 Trace elements

A total of 21 elements were measured ($^{31}$P, $^{43}$Ca, $^{88}$Sr, $^{89}$Y, $^{90}$Zr, $^{93}$Nb, $^{139}$La, $^{140}$Ce, $^{141}$Pr, $^{146}$Nd, $^{147}$Sm, $^{151}$Eu, $^{157}$Gd, $^{159}$Tb, $^{163}$Dy, $^{165}$Ho, $^{166}$Er, $^{169}$Tm, $^{172}$Yb, $^{175}$Lu, $^{181}$Ta) through LASS-ICP-MS in the same spot as the U-Pb analyses. The international glass NIST 610 was undertaken as the primary standard for calculation of element concentrations. The NIST 612, BCR2 and ATHO were used as secondary standards.

# 3 CHAPTER 3

## KINEMATICS, NATURE OF DEFORMATION AND TECTONIC SETTING OF THE TAXAQUARA SHEAR ZONE, A MAJOR TRANSPRESSIONAL SHER ZONE OF THE RIBEIRA BELT (SE BRAZIL)


**Abstract**

This chapter is based on the paper published in Tectonophysics. It comprises field-based structural data from the studied area, microstructural analysis, quartz and feldspar CPO, thermodynamic modelling and quantitative structural data from vorticity and shape preferred orientation analysis.

In this paper, a detailed study was made on a 15 km length of the TSZ nearby the cities of Pilar do Sul and Piedade, located at W-SW of São Paulo. The shear zone displays a NE-SW vertical mylonitic foliation dipping NW, with significant sub-horizontal stretching lineation. However, it is possible to observe oblique lineation plunging ~50°. It cross-cuts granitic rocks from Pilar do Sul and Piedade plutons, the Votuverava and São Roque Groups. This work can be subdivided into three main topics: petrographic and microstructural analysis, investigation of the P-T condition of the ductile deformation and tectonic setting.

The results suggest that quartz-ribbons accommodated deformation though dislocation creep achieving the transition between subgrain rotation and grain boundary migration, whereas feldspar porphyroclast presents evidences of simultaneous intracrystalline and brittle deformation. Fine-grained quartz and feldspar present in the granoblastic matrix, instead, present strong evidences of shifting between mechanisms of deformation from dislocation creep to diffusion creep (similar to superplasticity). Deformation is likely to achieved upper-greenschist facies at low pressure (513–525 °C and 3.9–4.4 kbar). Regarding the structural and tectonic setting, the results indicate that the TSZ was developed under a transpressional sub-simple shear environment with moderate to high strain, with predominance of simple over pure shear (i.e., sub-simple shear system). These results together with the compiled finite strain data from the literature strongly indicates a pervasive transpressional system that gave rise to the shear zones in the RB, although local processes can contribute to its development.

Tectonophysics 751 (2019) 83–108

Contents lists available at ScienceDirect

Tectonophysics

journal homepage: www.elsevier.com/locate/tecto

# Kinematics, nature of deformation and tectonic setting of the Taxaquara Shear Zone, a major transpressional zone of the Ribeira Belt (SE Brazil)

B.V. Ribeiro[a,c,*], F.M. Faleiros[a], G.A.C. Campanha[a], L. Lagoeiro[b], R.F. Weinberg[c], N.J.R. Hunter[c]

[a] Instituto de Geociências, Departamento de Mineralogia e Geotectônica, Universidade de São Paulo, Rua do Lago 562, CEP 05508-900 São Paulo, SP, Brazil
[b] Universidade Federal do Paraná, Departamento de Geologia, Rua Francisco Heráclito dos Santos, 100, Bloco VI, CEP 35400000 Curitiba, PR, Brazil
[c] School of Earth, Atmosphere and Environment, Monash University, Clayton, Victoria, 3800, Australia

ARTICLE INFO

*Keywords:*
Ribeira belt
Shear zones
Transpression
Microphysical analyses
Quartz and feldspar CPO
Thermodynamic modelling

ABSTRACT

In this paper we have investigated the Taxaquara Shear Zone (TSZ), a major strike-slip structure within the Ribeira Belt (RB, SE Brazil) in order to assess its kinematics, the nature of deformation of rocks affected by the TSZ and its tectonic setting. The TSZ presents a vertical NE-trending mylonitic foliation and ENE- to WSW stretching lineation with variable plunge. Granitic rocks are intensely deformed giving rise to mylonites with newformed matrix assemblage (quartz + oligoclase + K-feldspar + biotite + muscovite + rutile + magnetite). This assemblage within a pseudosection couple with muscovite-biotite thermometer helps to constrain a metamorphic condition during deformation which spans ~513–525 °C and ~3.9–4.4 kbar with mean peak at ~520 °C and ~4.0 kbar. Quartz accommodates deformation through dislocation creep achieving subgrain rotation with minor contribution of grain boundary migration at a mean strain rate of $10^{-13}$–$10^{-12}$ $s^{-1}$. Feldspar porphyroclasts record brittle deformation (microfaults) and evidences of dislocation creep (e.g., kink twinning). The CPOs for monomineralic quartz ribbons display monoclinic pattern and activation of 'basal- < a > ' + 'rhomb- < a > ' slip systems during deformation. However, the CPOs for quartz and feldspar from fine-grained polyphase matrix show a switch in deformation mechanism from dislocation creep to diffusion creep. The vorticity and three-dimensional finite strain data results suggest that the TSZ was developed under a moderate to high strain conditions and a transpressional sub-simple shear environment, with predominance of simple over pure shear. Regional correlation with other structures from the Ribeira Belt and African Belts based on finite strain quantification support that a major transpressional system was mainly responsible for the shear zones development during late stages of Braziliano-Pan African orogeny.

## 1. Introduction

Quartz and feldspar correspond to the most abundant phases within the continental crust and their microstructures and crystallographic preferred orientation (CPO) are useful to understand deformation mechanisms and conditions and crustal bulk rheology controlling strain localization and shear zone development (Dell'angelo and Tullis, 1989; Dunlap, 1997; Faleiros et al., 2010; Hirth and Tullis, 1992; Stipp et al., 2002b; Stipp et al., 2002a; Platt, 2015). However, these analyses still provide qualitative data requiring some quantification. In this scenario, the mineral equilibria-based geothermobarometry and thermodynamic modelling helps to precisely constrain the P-T conditions in which the rocks were deformed. Quantification of microstructures, supported by petrological analyses, is a useful tool in determining deformation conditions in quartz-feldspathic deformed rocks such as granitic mylonites, particularly when appropriate mineral assemblages that might constrain metamorphic conditions are rare (Faleiros et al., 2010; Cavalcante et al., 2018; Fossen and Cavalcante, 2017; Hunter et al., 2016; Hunter et al., 2018a, 2018b).

The late evolution of the Ribeira belt (RB) in SE Brazil is dominated by a Late Ediacaran to Cambrian strike-slip shear zone system (Fig. 1). This system is composed of brittle-ductile to ductile transcurrent zones and characterized by an anastomosing network of mainly dextral strike-slip shear zones with an outcropping extension of about 1000 km and individual displacements ranging from few to hundreds of kilometers (Campanha, 2002; Campanha and Brito Neves, 2004). This shear zone system is regionally known in reconnaissance scale and few detailed works are available on microstructure regarding deformation conditions and crustal rheology and tectonic evolution (Faleiros et al., 2010; Cavalcante et al., 2018). Field-based and mineral assemblages suggest a

* Corresponding author at: Rua do Lago 562, CEP 05508-900 São Paulo, SP, Brazil.
*E-mail addresses:* bruno.vieira.ribeiro@usp.br (B.V. Ribeiro), ffalei@usp.br (F.M. Faleiros), ginaldo@usp.br (G.A.C. Campanha), roberto.weinberg@monash.edu (R.F. Weinberg), nicholas.hunter@monash.edu (N.J.R. Hunter).

https://doi.org/10.1016/j.tecto.2018.12.025
Received 29 January 2018; Received in revised form 15 December 2018; Accepted 24 December 2018
Available online 28 December 2018
0040-1951/ 

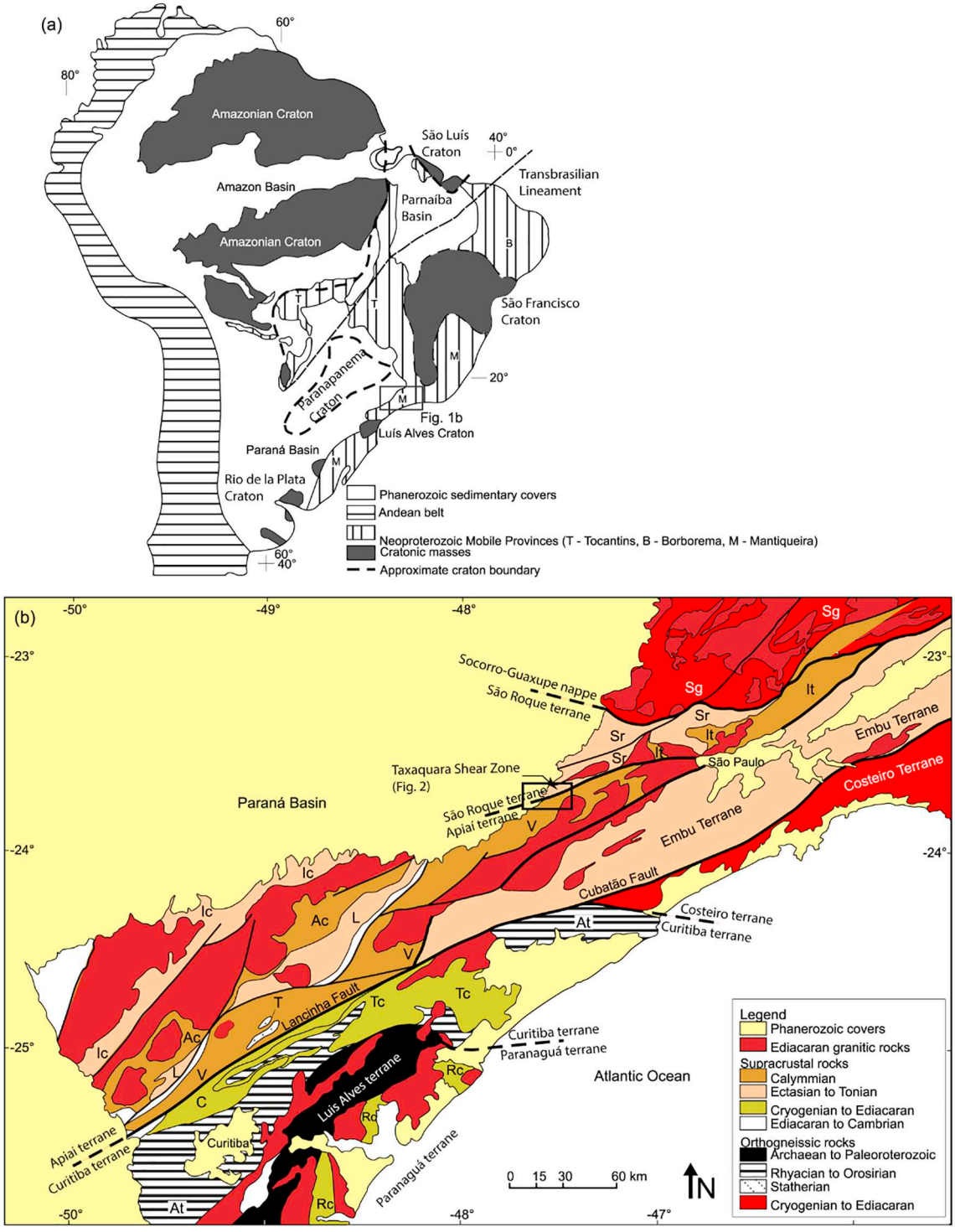


**Fig. 1.** A) Simplified geotectonic map of part of South America. B) Map of southern portion of the Ribeira Belt. Geological units: Itaiacoca Group (Ic), Água Clara Formation (Ac), Lajeado Group (L), Votuverava Group (V), São Roque Group (Sr), Serra do Itaberaba Group (It), Tigre Gneiss (T), Capirú Formation (C), Turvo-Cajati Formation (Tc), Rio das Cobras Formation (Rc), Atuba Complex (At) (adapter from Campanha et al., 2015). The black rectangle delimits the study area (detailed map in Fig. 2).

general trend in which the westernmost portions of the system were developed under lower-grade metamorphic facies and upper crust conditions (e.g., Lancinha lineament) while the easternmost end is characterized by higher metamorphic grade (amphibolite to granulite) (e.g. Além Paraíba Shear Zone), suggestive of deformation under lower crust conditions (Campanha, 2002; Cavalcante et al., 2018).

The Taxaquara Shear Zone (TSZ) is one of the first transcurrent structures of regional importance identified within the RB (Hennies et al., 1967). It cross-cut granitic rocks giving rise to quartz-feldspar mylonites and displays a NE-SW structural trend parallel to the main orientation of RB and places side by side units with distinct structural style, metamorphic grade and temporal evolution. Despite its importance in regional tectonic, it has not yet been studied in detail since its original recognition. The TSZ position in the central portion of the regional shear zone system of the RB makes it a good target area for a detail study of the evolution and crustal conditions based on

quantitative structural, microstructural and thermometric data. In order to investigate the deformation mechanisms and conditions recorded by the TSZ mylonites and to establish regional correlations regarding tectonic setting, this paper presents field-based observations, microphysical analysis (quantitative microstructural, quartz and feldspar CPO), quantitative structural data (vorticity and three-dimensional finite strain) and thermodynamic modelling using samples distributed along the strike of the shear zone since it might record the peak conditions and maximum strain. The results of this paper also add data regarding feldspar CPO that is considerably scarcer than quartz in literature (Prior and Wheeler, 1999).

## 2. Geological setting

### 2.1. Ribeira belt

The RB is a NE-trending accretionary-to-collisional orogen related to the assembly of West Gondwana during the Neoproterozoic (Almeida et al., 1973; Hasui et al., 1975; Campanha and Sadowski, 1999; Campos Neto, 2000; Heilbron et al., 2004; Campanha et al., 2016). It is composed by a set of tectonostratigraphic terranes with ages ranging from Paleoproterozoic to Neoproterozoic and with a voluminous arc-related, late- and post-collision granite magmatism (~630–580 Ma; Leite et al., 2007; Alves et al., 2013). During the late Ediacaran to Cambrian (~600–510 Ma), it underwent a subsequent orogen-parallel, crustal-scale transcurrent shearing related to an oblique collision between the Paranapanema, São Francisco, Luís Alves and Congo cratons, giving rise to the Brazilian Southeastern Shear Zone System (e.g., Vauchez et al., 1994; Campanha, 2002; Campanha and Brito Neves, 2004; Faleiros et al., 2010, 2011; Campanha et al., 2016; Egydio-Silva et al., 2018).

Structural field observations within the RB indicate strain partitioning between coeval, subparallel folds, ductile thrusts and strike-slip shear zones accommodating large-scale orogen-parallel movements and orogeny-perpendicular shortening suggesting a transpressional regime (Ebert and Hasui, 1992; Ebert et al.,1996) in sense of Sanderson and Marchini (1984) and Fossen and Tikoff (1993). Finite strain analysis in the RB indicates dominance of oblate (Ebert et al., 1996) and mixing of prolate and oblate ellipsoids (Campanha and Sadowski, 2002; Faleiros et al., 2016a). Faleiros et al. (2016a) suggest that finite strain variation is caused by deformation superposition while Campanha and Sadowski (2002) suggest strain partitioning due to associated dextral simple shear and shortening components. Despite such differences, a tectonic model with dominant simple shear with a contractional pure shear component (sub-simple shear deformation) is very likely.

The Taxaquara Shear Zone (TSZ) was originally recognized in a segment of ~150 km covered at its tips by the Paleozoic Paraná basin in the west and by the Cenozoic São Paulo basin in the east (Fig. 1B). In the exposed sector, the TSZ separates the São Roque Group to the north from the Votuverava Group and Embu Complex to the south and it cuts across several Ediacaran late- and post-tectonic granites (Janasi et al., 2001; Leite et al., 2007). Its continuity to the east of the São Paulo basin is generally considered to be the Guararema Shear Zone (e.g., Hasui, 1973, 1975; Hasui and Sadowski, 1976; Campos Neto, 2000).

### 2.2. Study area

The studied area is located in the westernmost outcropping region of the exposed TSZ, between the Pilar do Sul town and Bairro dos Leites district (Fig. 2). The São Roque Group, to the north, is composed of low-grade metasedimentary rocks and displays a dominant NE-SW structural trend defined by foliations. Detrital zircons show an important Riacian contribution (ca. 2200 Ma, U—Pb LA-ICP-MS; Campanha et al., 2019; Henrique-Pinto et al., 2015, 2018) and with younger grains at ca. 2000 Ma. The southern region is mainly composed of the Votuverava Group, which is intruded by the Pilar do Sul (ca. 600 Ma, U—Pb TIMS monazite; Leite et al., 2007) and Piedade (ca. 605 Ma, U—Pb TIMS zircon; Janasi et al., 2001) igneous suites. In contrast with the São Roque Group, the Votuverava Group is composed of distal turbidites with significant basic magmatism represented by concordant lenses of metamorphosed mafic rocks (Campanha et al., 2019). It displays a principal NNW-SSE structural trend orthogonal to the TSZ and shows an east to west transition from low-grade to medium-grade metamorphism. Detrital zircon data show Orosirian-Riacian contribution (ca. 1800–2200 Ma, U—Pb LA-ICP-MS; Campanha et al., 2019) with minor Archean ages (ca. 2800–3200 Ma, U—Pb LA-ICP-MS; Campanha et al., 2019) and include zircon with minimum age of ca. 1400 Ma. The metabasites of the Votuverava Group at the Pilar do Sul region show a ca. 1300 Ma crystallization age and a Neoproterozoic metamorphic overprint ca. 600–700 Ma (zircon U—Pb SHRIMP data; Campanha et al., 2019), while metabasites from its southernmost portion display older ages of 1475–1490 Ma (Campanha et al., 2015).

### 2.3. Structural setting

Previous data regarding TSZ structures and tectonics setting are scarce. Hennies et al. (1967) identified the TSZ as a NE-SW linear subvertical structure with a thick mylonitic zone (~1 km), with sub-horizontal stretching lineation plunging to the W. Although kinematic determination was not remained unclear, these characteristics drove them to classify the TSZ as a transcurrent structure. No further detailed studies of the TSZ has been done since.

In the study area, the TSZ is represented by an anastomosed mylonitic zone with thickness varying between hundreds of meters to two kilometers (Fig. 2). The shear zone primarily affected the ~600 Ma granitic rocks of the Pilar do Sul and Piedade suites giving rise to quartz-feldspathic mylonites with feldspar porphyroclasts (Fig. 3A, B). The structure has mean mylonitic foliation/shear plane trending N062E/70SE. It has a sub-horizontal to oblique stretching lineation, mainly marked by elongated quartz grains (Fig. 3C) with an orientation distributed along a girdle parallel to the main mylonitic foliation, with maximum concentrations gently plunging towards the NE (Fig. 2).

Its shear sense from field-based observation is indicated by mesoscopic structures such as C-type shear band cleavage, type-σ and type-δ asymmetric porphyroclasts and internally faulted domino-type feldspar (Fig. 3B). Structures such as shear band cleavage (Fig. 3D) are a common form of strain partitioning accommodating strain due oblique compression and, thus, partition of deformation concentrating a large portion of the simple shear component in transpressional shear zones (Tikoff and Greene, 1997). Tight folds with axial plane parallel to mylonitic foliation can be identified reinforcing the compressive component (Fig. 3E).

## 3. Results

### 3.1. Petrographic and microstructural analysis

Mylonites and ultramylonites samples present polyphase fine-grained matrix which makes it difficult to analyses through optical methods. In order to characterize and distinguish fine-grained feldspars within the recrystallized matrix, we analyzed one mylonite (PS-40B) and one ultramylonite samples (PSB-10) using EBS coupled with WDS chemical analyses.

#### 3.1.1. Mylonites

Since the TSZ cross-cut the Pilar do Sul and Piedade granitic suites, they are the most suitable source to be protoliths of the granitic mylonites analyzed in this paper. The Pilar do Sul suite is composed of a medium- to coarse-grained inequigranular muscovite-biotite monzogranite with igneous foliation in its border and fine-grained muscovite-biotite granite within the core (Leite et al., 2007). The Piedade suit is characterized by a porphyritic muscovite-biotite granodiorite to monzogranite with an igneous foliation of moderate intensity defined by the

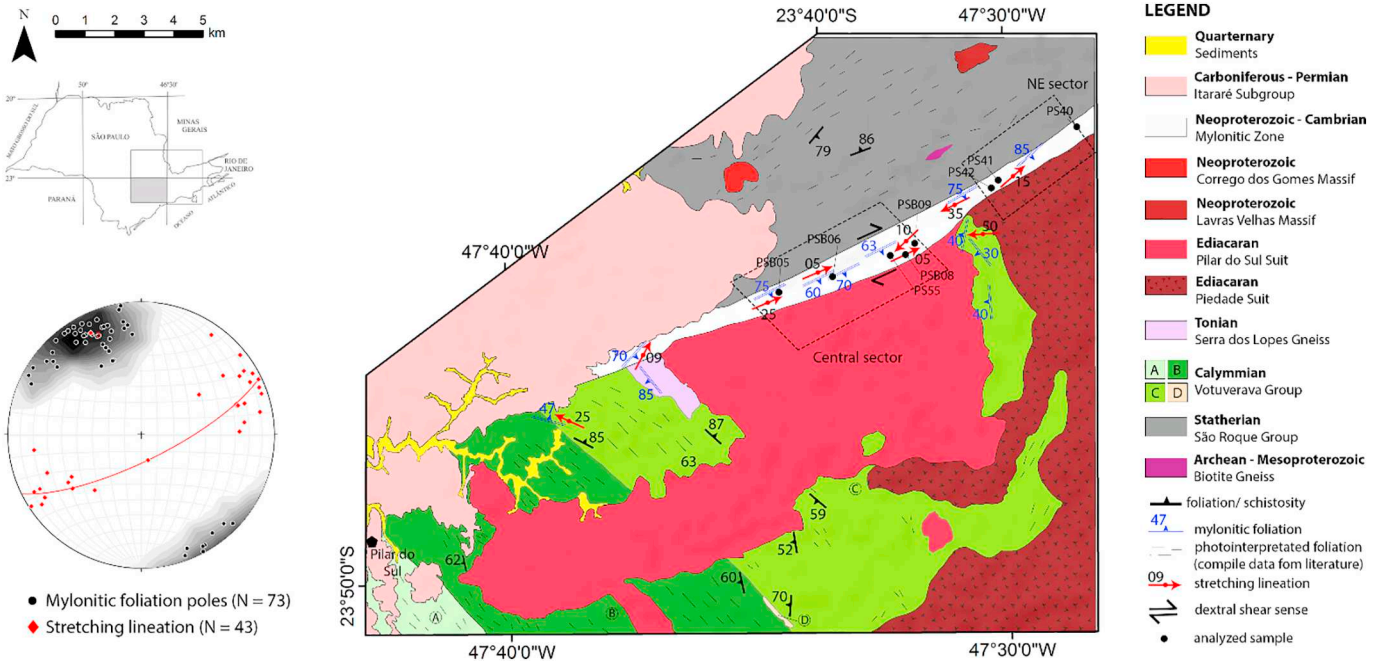


**Fig. 2.** Geological map of the study area with focus on the Taxaquara Shear Zone (compiled and modified from Stein et al., 1983 and Pires et al., 1989). The Votuverava Group is composed of A) sericitic and quartz phyllites; B) quartz-muscovite and muscovite schists; C) mica-quartz and micaschists; D) paragneiss. Stereogram (lower hemisphere, equal area projections) with mylonitic foliation (mean vector 062/70SE; strike/dip) and stretching lineation is presented in the inferior left corner.

alignment of tabular pinkish K-feldspar megacrysts of 1–2 cm (Janasi et al., 2001; Leite et al., 2007). The samples present 50–90% of recrystallized matrix and the remainder is porphyroclasts, and vary from mylonites to ultramylonites as per the classification based on the ratio between recrystallized matrix and porphyroclast (Sibson, 1977; Trouw et al., 2009). The TSZ mylonites generally display lineations defined by elongate quartz, streaks of recrystallized feldspar and micas (biotite and muscovite). Along with vertical foliation, these rocks can be classified as LS tectonites.

The mylonitic granitic rocks form elongated (Fig. 4A) to granular grain aggregates (Fig. 4B). Anastomosed quartz ribbons are common with elongate shape parallel to the foliation and/or wrapping around the feldspar porphyroclasts (Fig. 4A). The recrystallized matrix is primarily composed of quartz + feldspar + biotite + muscovite with

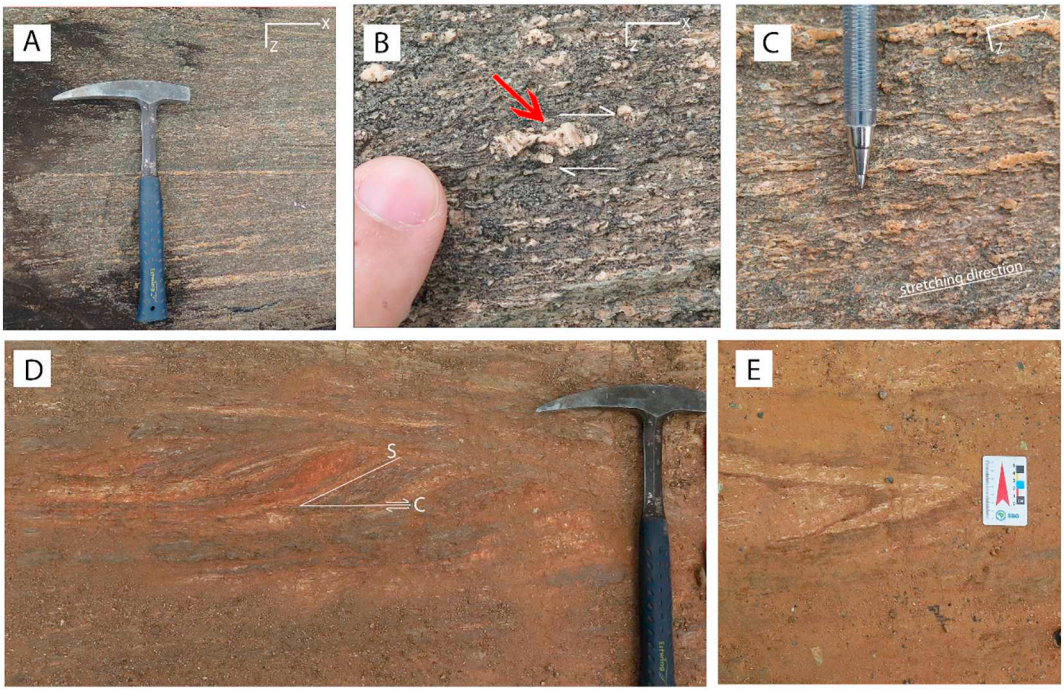


**Fig. 3.** Field structures related with Taxaquara Shear Zone. A) layered mylonitic granite; B) antithetical microfaulting (normal movement) in feldspar porphyroclast; C) streaks of stretched quartz and feldspar parallel to stretching lineation; D) S/C fabric with dextral shear sense; E) tight fold with axial plane parallel to mylonitic foliation.

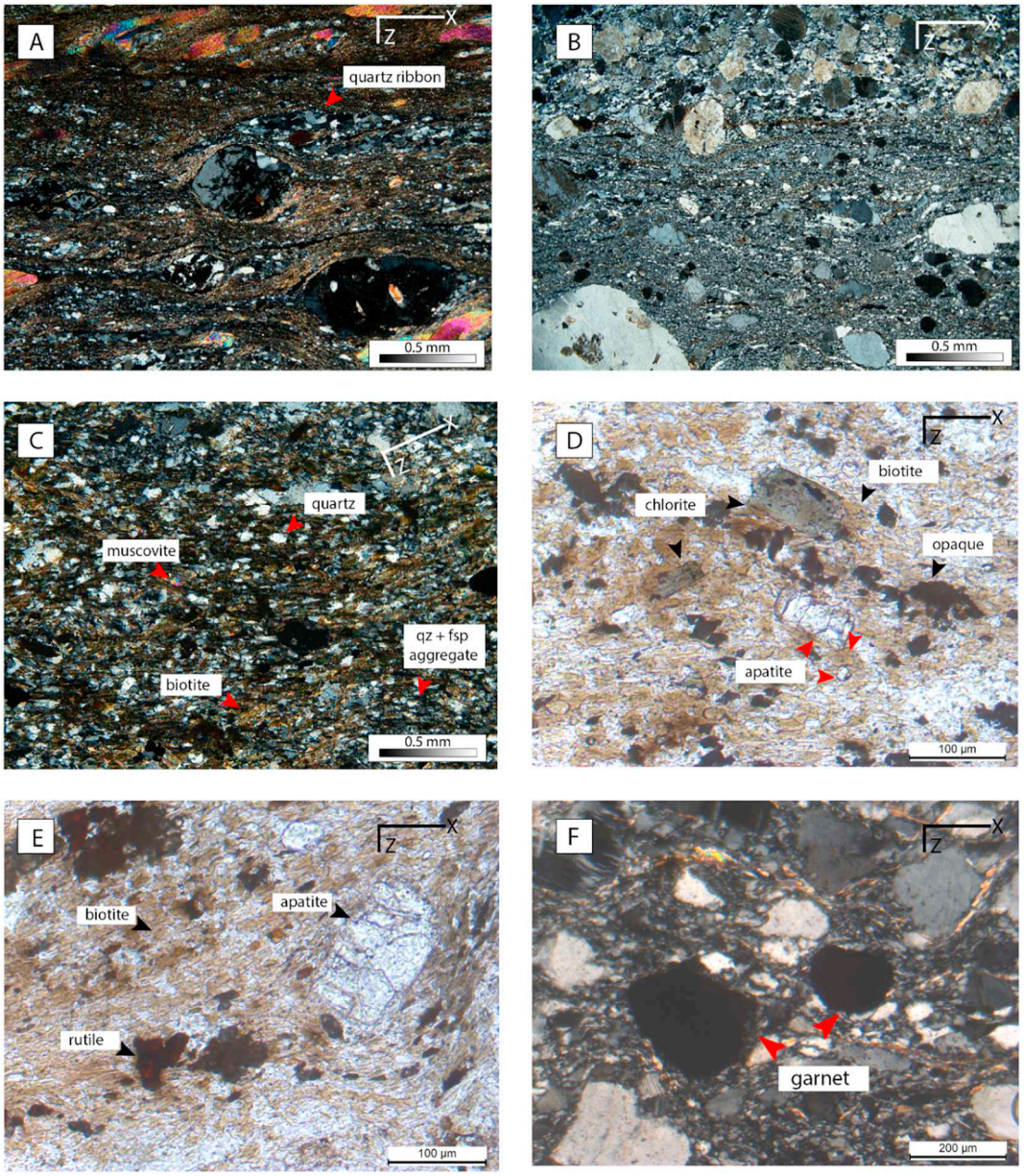


**Fig. 4.** Photomicrographs of TSZ mylonites (XZ section; A–C, F: cross-polarized light). A) lepidoblastic texture with minor component of quartz and feldspar; B) granoblastic texture with two-phase matrix (quartz and feldspar) and feldspar porphyroclasts; C) common mineralogy present in all mylonite samples (quartz + feldspar + biotite + muscovite); D) Chlorite may occur replacing biotite and apatite represent igneous relicts; E) evidence of rutile within the mylonitic matrix; F) garnet crystals within granoblastic mylonitic matrix with no evidence of metamorphic reaction (igneous relicts).

feldspar porphyroclasts (0.1–1.0 cm in thin sections) (Fig. 4C, D). Apatite, magnetite and rutile occur as minor phases (Fig. 4D, E). Garnet (Fig. 4F) is a rare phase occurring only in two mylonite samples (PS40A, PS40D). It is interpreted as an igneous relict preserved as porphyroclasts since there is no growth relationship between garnet and mylonitic matrix that could indicate its metamorphic nature. Calcite, dolomite and tourmaline indicate fluid-rock interaction during shearing.

Results from EDS and WDS analyses show the coexistence of oligoclase (An ~521%) and K-feldspar (Or ~95%) for both mylonitic and ultramylonitic samples (Fig. 5A). BSE images show a predominance of oligoclase over K-feldspar for both samples (Fig. 5B, C). Oligoclase is homogeneously distributed within the matrix, while K-feldspar occurs as individual grains (Fig. 5B) or in granular layers (Fig. 5C).

Feldspar porphyroclasts with pressure shadows and fine-grained mantle are common in mylonites and ultramylonites. BSE image from an oligoclase porphyroclast shows that the strain shadows are composed of K-feldspar, oligoclase, biotite, muscovite and quartz (Fig. 5D). There is also ultrafine-grained oligoclase cross-cutting the porphyroclast with no composition difference (Fig. 5D) possibly indicating fluid-assisted dissolution–precipitation creep.

### 3.1.2. Ultramylonites

The three ultramylonites samples have similar features such as interlayered quartzo-feldspathic granular band and micaceous bands with fine-grained muscovite and biotite characterized by elongate grains (Fig. 6A). Fine-grained biotite and muscovite are important hydrated phase defining the ultramylonitic foliation. Following the mylonites, the ultramylonitic matrix is mainly composed of fine-grained quartz + oligoclase + K-feldspar with granoblastic texture. Oligoclase and K-feldspar porphyroclasts occur in both layers displaying quarter cap structures and antithetic and synthetic microfaults indicating

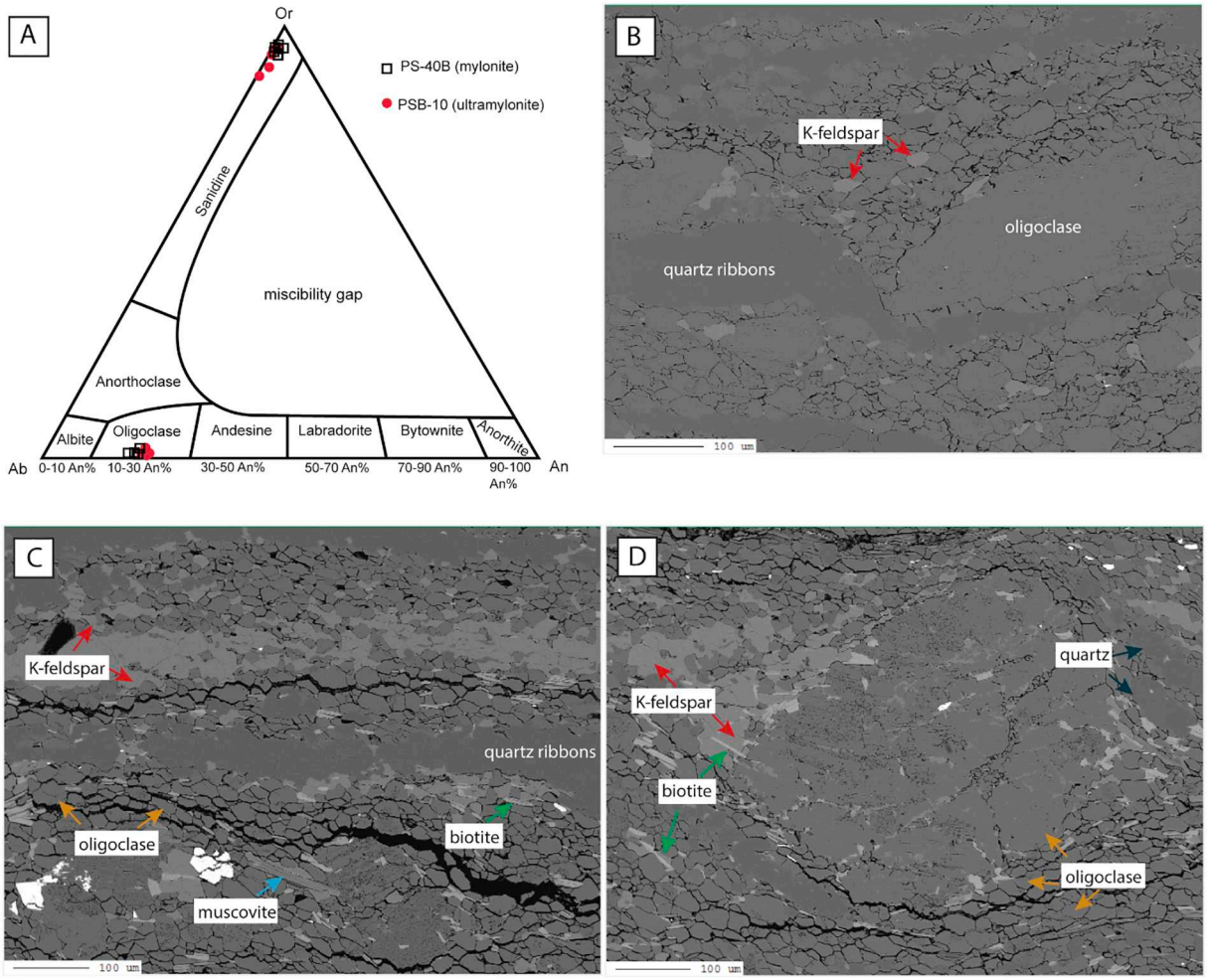


**Fig. 5.** Electron-backscattering (EBS) and chemical analyses (WDS) from feldspars within the fine-grained matrix. A) feldspar ternary diagram showing the feldspars compositions from mylonite and ultramylonite samples.; B–C) mylonite (PS-40B) and ultramylonite (PSB-10) fine-grained matrix, respectively showing the predominance of oligoclase over K-feldspar; D) oligoclase porphyroclast σ-type with K-feldspar, biotite and quartz within the pressure shadows, trails of tiny oligoclase grains cross-cutting the porphyroclast and evidence of K-feldspar/oligoclase replacement within the porphyroclast.

dextral shear sense (Fig. 6B), as well as kinking of plagioclase twinning (albite law) (Fig. 6C) that suggest intracrystalline deformation. Other microstructures related to deformation are observed in K-feldspar which include oriented flame perthites in the shortening direction (Fig. 6D) similar to mylonites samples.

Apatite, magnetite and very fine-grained rutile (Fig. 6E) occur as minor phases homogeneously distributed within the sample. Very-fined grained garnet is present in granular quartzo-feldspathic layers forming narrow bands together with opaque (magnetite). Although with metamorphic signature, it does not seem to be in complete equilibrium with the overall mineral assemblage due to its restricted occurrence and textural relationships, but in local equilibrium due to intrinsic factor such as local composition that allowed its crystallization. Rutile, on the other hand, is an abundant phase in ultramylonite samples as result of the high content of $TiO_2$ (0.29 to 0.52% in Table 3).

### 3.1.3. Microanalysis of kinematic indicators

The main kinematic indicators in thin sections are mica fish, porphyroclasts with asymmetric tails, quartz oblique shape preferred orientation and quarter structures in feldspar porphyroclasts. Coarse-grained muscovite forms fish geometries in a few samples (Fig. 7A). Biotite fish is less common. Feldspars comprise 80% of porphyroclasts and are generally rotated forming mostly σ-clasts (Fig. 7B, C), and less commonly δ-clasts. The asymmetry can be identified by layers of mica and quartz ribbons which wrap around the porphyroclasts, and asymmetric tails of recrystallized feldspar plus quartz. Quartz grains oriented obliquely to foliation is common, observed in 90% of the samples (Fig. 7D). Quarter structures (e.g., caps) are presented in feldspar porphyroclasts from ultramylonites with recrystallization of mica (most sericite and muscovite) induced by dissolution and precipitation (Fig. 6B). Most kinematic indicators display a dextral movement congruent with field-based observations.

### 3.1.4. Quartz recrystallization mechanisms

Mylonites from TSZ are polymineralic, and this affects microstructures of individual minerals since it is known that size and shape can be influenced by second phases such as micas (Urai et al., 1986; Jessell, 1987; Drury and Urai, 1990; Passchier and Trouw, 2005). To avoid or reduce influence of other phases, microstructures were analyzed in predominantly monomineralic quartz ribbons allowing us to relate the microstructures with those described for similar monomineralic rocks (e.g., quartzites) and their deformation conditions (Stipp et al., 2002b; Stipp et al., 2002a; Passchier and Trouw, 2005). In order to identify the quartz mechanism of recrystallization, we documented microstructures, crystallographic data and quantified key topological parameters following Hunter et al. (2018b).

The analyzed quartz domains from eight samples along the length of the TSZ yielded similar results regarding size (Feret diameter) and shape (PARIS factor; Heilbronner and Tullis, 2002). Feret diameter is measurement of an object size along a specified direction (e.g., major

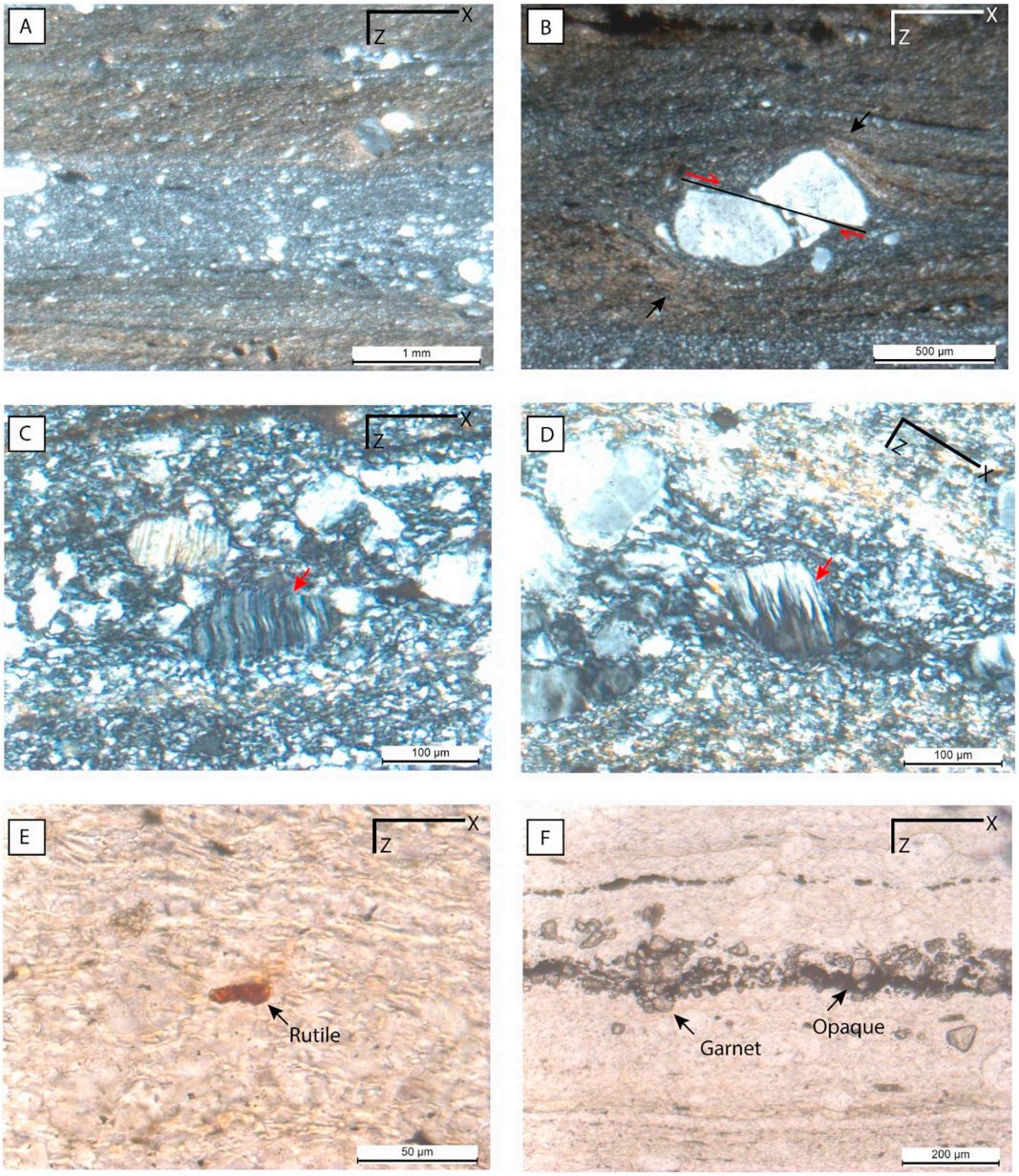


**Fig. 6.** Photomicrographs of TSZ ultramylonites (XZ section; A–D: cross-polarized light). A) interlayering of lepidoblastic and granoblastic layers; B) feldspar porphyroclast with sericite quarter caps (black arrows) and synthetic microfault indicating dextral shear sense; C) plagioclase porphyroclast with twinning kink; D) flames pertites in alkaline feldspar; E) evidence of rutile within ultramylonitic matrix; F) small garnet crystals within granoblastic layer related with opaque phases.

axis), and varies from ~11 μm to ~181 μm with average of ~53 μm (Fig. 8A). Larger grains are outliers and considered to represent igneous relicts. Quartz grains present elongate shape (~1.60 mean aspect ratio) and oblique major axis in relation to the shear plane (X-direction) (Table 2), with a geometry indicative of dextral shear sense.

The relationship between the arithmetic mean of Feret diameter and PARIS factor, with its mean standard deviation ($\sigma_m = \sigma/(n)^{1/2}$, where n is the number of measured grains), result one group of data with similar features plotting within the subgrain mechanism of recrystallization based on grain size (Fig. 8B) (Stipp et al., 2002b). It is also observed in the plot of Feret diameter (D) multiplied by PARIS factor (L) a flat trend showing no or small differences between samples regarding diameter and lobateness (Fig. 8C). According to Hunter et al. (2018b), distinct mechanisms of dynamic recrystallization would result in a positive trend with temperature as grain size and lobateness increase. Our results, however, suggest that there are no significant differences in the dynamic recrystallization of quartz along the strike of the TSZ (Fig. 8C). Taking the grain diameter as an indication of the dominant mechanism of dynamic recrystallization (Stipp et al., 2010), deformation in the TSZ was achieved by subgrain rotation (SGR).

Quartz grains in the polyphase matrix tend to be larger than feldspar, but in minor proportion, with irregular shape. Quartz ribbons are predominant monomineralic with predominant irregular boundaries. Oblique shape in relation to shear direction (Fig. 9A), undulose patchy extinction, deformation bands and subgrains are common features (Fig. 9B, C). Biotite and/or muscovite may occur between quartz boundaries pinning the migration of grain boundaries, indicating that some grain boundary migration occurred as a subsidiary recrystallization mechanism. In addition to recrystallization by SGR and fast grain boundary migration (GBM), bulging (BLG) is also observed locally, not pervasively, at quartz boundary as small (< 0.1 mm) rounded recrystallized grains. The BLG mechanism could be related to the exhumation as it seems locally to overprint the recrystallized grains by SGR or associated to the early stage of the dynamic recrystallization by

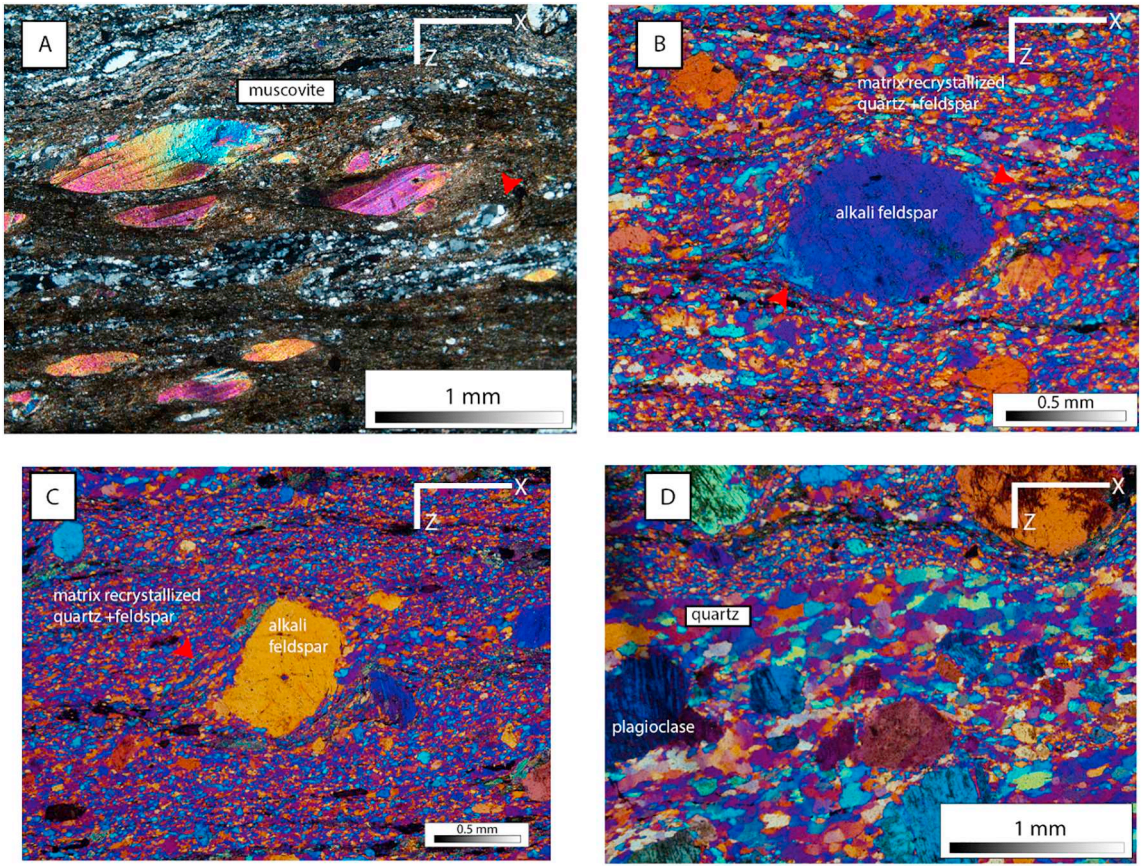


**Fig. 7.** Photomicrographs of TSZ mylonites illustrating main kinematic indicators (XZ section; A: cross-polarized light; B-D: cross-polarized light with gypsum plate). A) muscovite fish and asymmetric fold in quartz ribbons (red arrow); B) σ-K-feldspar porphyroclasts with exsolution (red arrows); C) σ-K-feldspar porphyroclasts within recrystallized matrix with quartz oblique shape in pressure shadows (red arrow); D) Quartz oblique grain shape fabric. All kinematic indicators suggest a dextral shear sense (top to the right). (For interpretation of the references to colour in this figure legend, the reader is referred to the web version of this article.)

grain boundary migration, although preservation in high temperature conditions is very rare.

Quantitative data of topological parameters associated with microstructures strongly suggest that quartz accommodated deformation through SGR mechanism, with minor contribution of GBM indicated by slightly interlobate boundaries (Stipp et al., 2002a, 2010; Platt, 2015).

#### 3.1.5. Feldspar recrystallization mechanisms

Feldspar occurs as minute grains (mean Feret diameter between 11 ± 4.8 to 14.5 ± 4.8 μm) disperse in the matrix with sharp and straight boundaries and with rectangular shape (aspect ratio of 1.8 ± 0.4) and as porphyroclasts (1 to 10 mm).

Both oligoclase and K-feldspar comprise fractured porphyroclasts with microfaults in all samples (Fig. 10A). Mechanical twinning and undulose extinction are evidence for intracrystalline plastic deformation (Fig. 10B, C). Myrmekites and flame pertites induced by deformation occur along the edge of porphyroclasts in minor proportion as quarter structures (Fig. 10B, D). Fine-grained mantle of recrystallization surround porphyroclasts without transitional size grain zone (Fig. 10E) and trails of very fine-grained feldspar grains filling internal microfractures (Fig. 8F) without compositional difference between them and the host grain (Fig. 5D) are common. These features are very similar to those described for feldspar from zone 3 in Pryer (1993) with core-and-mantle structures as the most common feature suggesting that intracrystalline deformation has major importance in comparison with fracturing.

### 3.2. Thermodynamic modelling

The thermodynamic modelling resulted in a *P-T* pseudosection constructed using Perple_X'6.8.3 (Connolly, 2005). Since ductile shear zones commonly work as fluid channels transporting water, we set up a minimum water content to allow melting by water-present reactions. This thermal boundary will be an important limiting factor due the absence of partial melting evidence in the TSZ rocks. The pseudosection has been contoured with isopleths for Si p.f.u in muscovite and albite molar fraction ($X_{Na}$) in plagioclase (Na/Na + K + Ca) to better constrain the *P-T*-deformation condition.

The pseudosection shows twenty-one stability fields with multivariant assemblages (Fig. 11). With minimum water content (1.765% mass amount), partial melting starts to play a role at ~672 °C and 8 kbar increasing temperature following the decrease in pressure. The water content was determined so that the rocks were saturated in water immediately below the solidus (cf., White et al., 2001). The pseudosection also shows that garnet is present in high pressure and low temperature fields supporting the interpretation that the garnet present in the ultramylonites samples is not in complete equilibrium with the peak metamorphic assemblage. Although developed during metamorphism, this garnet may represent a local equilibrium with intrinsic factors that allowed its formation. Since important boundaries between stability fields are represented by Ti-phases such as rutile, titanite and ilmenite, it is important to proper document it based on petrographic descriptions.

The mineral assemblage (quartz + K-feldspar + oligoclase + biotite + muscovite + rutile + magnetite) that represents mylonites and ultramylonites from the TSZ is present within the stability field ranging

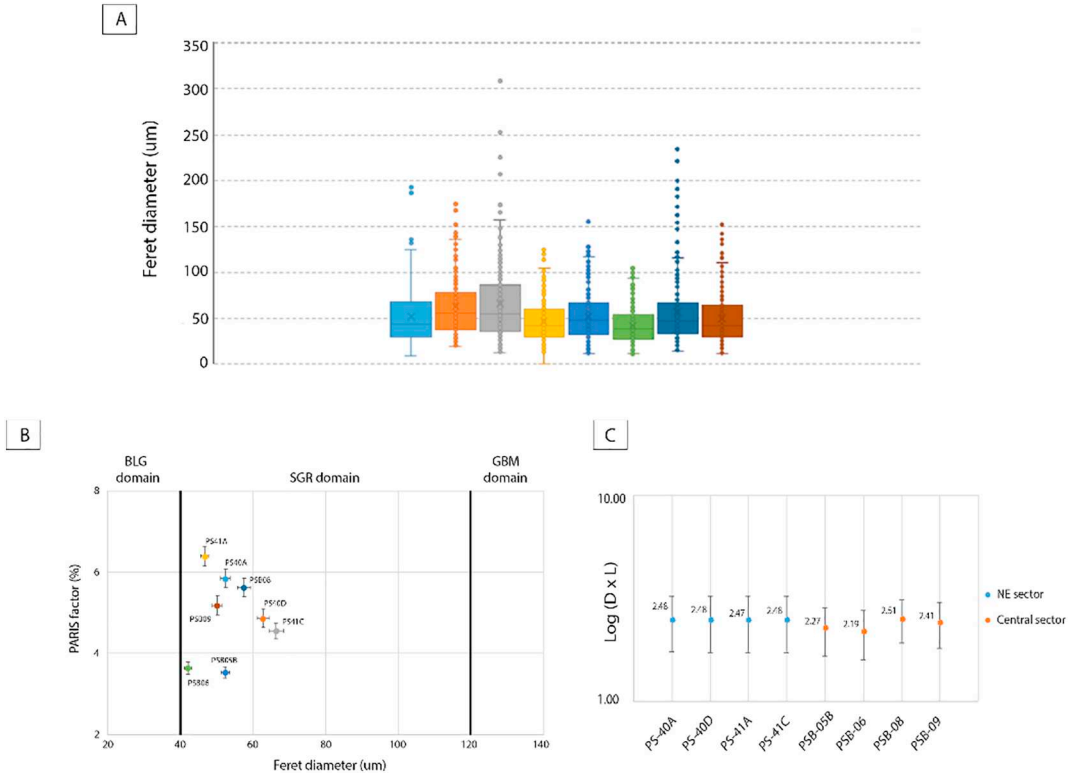


**Fig. 8.** Quartz grain statistics based on digitized grains in ArcGIS (version 10.0) and analyzed using PolyLX toolbox in MATLAB. A) Boxplot diagram with Feret diameter measurements from all analyzed samples. Colour patterns follows the legend in (B) diagram; B) grain lobateness (PARIS FACTOR; Heilbronner and Tullis, 2002) plotted against grain size (Feret diameter) for samples from NE and Central sectors with a strong cluster result considering error bars (standard deviation values). Dark lines represent transitions between mechanisms of dynamic recrystallization between bulging (BLG), subgrain rotation (SGR) and grain boundary migration (GBM) based on diameter of recrystallized grain (Stipp et al., 2010); C) Logarithmic plot of lobateness multiplied by diameter (L × D; Hunter et al., 2018b) for samples from NE and Central sectors with a flat result suggesting no variation between samples along strike of TSZ. (For interpretation of the references to colour in this figure legend, the reader is referred to the web version of this article.)

from ~402–560 °C to ~585–700 °C between 1 kbar and 8 kbar, respectively, where rutile represents the Ti-rich phase (Fig. 11). Due the lack of partial melting evidence, this stability field is truncated by the partial melting boundary at 672 °C in high pressure (6-8 kbar).

The muscovite-biotite geothermometer (Hoisch, 1989) was applied using mineral chemical results from WDS analysis (Table 4) resulting in a field that spans ~458–502 and ~576–620 °C between 1 and 8 kbar. Due to the lack of applicable geobarometer, the mineral isopleths are important to constrain a better deformation interval. The isopleths within the field defined by the muscovite-biotite geothermometer spans 0.77–0.79 and 3.045–3.145 for $X_{Na}$ in plagioclase and Si p.f.u in muscovite, respectively. From mineral chemical analyses, the contents of $X_{Na}$ molar in plagioclase (~0.776–0.779) and the Si p.f.u in muscovite (~3.09–3.10) are very homogeneous. Thus, the intersection between muscovite-biotite geothermometer and isopleths defines a restrict field which spans ~513–525 °C and ~3.9–4.4 kbar with mean peak at ~520 °C and ~4.0 kbar (Fig. 11).

### 3.3. Paleopiezometry and strain rate

Paleopiezometers were applied to quartz and feldspar from monomineralic ribbons and polyphase matrix, respectively. Using the Stipp and Tullis (2003) calibration for regime 2 and 3 for quartz (Hirth and Tullis, 1992), the results consist in a regular differential stress with small data amplitude ranging from 34 ± 4.5 to 24 ± 4.0 MPa with arithmetic mean of 28.5 ± 2.5 MPa. Strain rate estimates for quartz based on peak deformation condition (~520 °C and ~4 kbar) and using the differential stress from quartz paleopiezometry spans the interval from $9.50 * 10^{-13}$ to $1.22 * 10^{-12}\ s^{-1}$ (Table 5).

### 3.4. Crystallographic preferred orientation

#### 3.4.1. Fabric analyzer (FA)

The samples were classified in two groups based on their different CPO patterns of quartz [c]-axis. The first group, located in the northeastern sector of the TSZ (Fig. 2) is characterized by symmetric (Fig. 12; samples PS-40A, PS-40B, PS-41B, PS-42B) to slightly asymmetric CPOs implying a dextral movement (Fig. 12; samples PS-40D, PS-41A, PS-41C) showing maxima subparallel to or at a small angle to the Z direction. Based on general correlations between quartz [c]-axis location and slip systems (Schmid and Casey, 1986), the results suggest activation of 'basal- < a > ' and 'rhomb- < a > ' slip systems during quartz deformation in medium temperature conditions (450–550 °C).

The second group, located in the central sector of the TSZ, has heterogeneous CPO patterns. Samples PS-55 and PSB-05B (Fig. 12) present [c]-axis with two maxima between X and Y directions suggesting an orthorhombic symmetry, which might be a result of a pure shear component for which there is no evidence in NE sector. Samples PSB-06 and PSB-08 display an asymmetric pattern in relation to Z direction, with maxima close to Z and X direction, respectively, and around the Y direction. Sample PSB-09 comprises a symmetric to slightly asymmetric pattern, indicating a possible dextral movement, with maxima close to the Z direction. The [c]-axis location indicates a contribution of 'rhomb- < a > ' slip system (Schmid and Casey, 1986).

Besides the orthorhombic geometries of samples PS-55 and PSB-05B, all CPO are somehow similar to each other. Some show maxima distributed along more than one single concentration and in others maxima distribute along a great circle. One interest aspect to note is that in all of the pole figures there are hokes around the Y direction. This might be the result of the inability of the method to measure

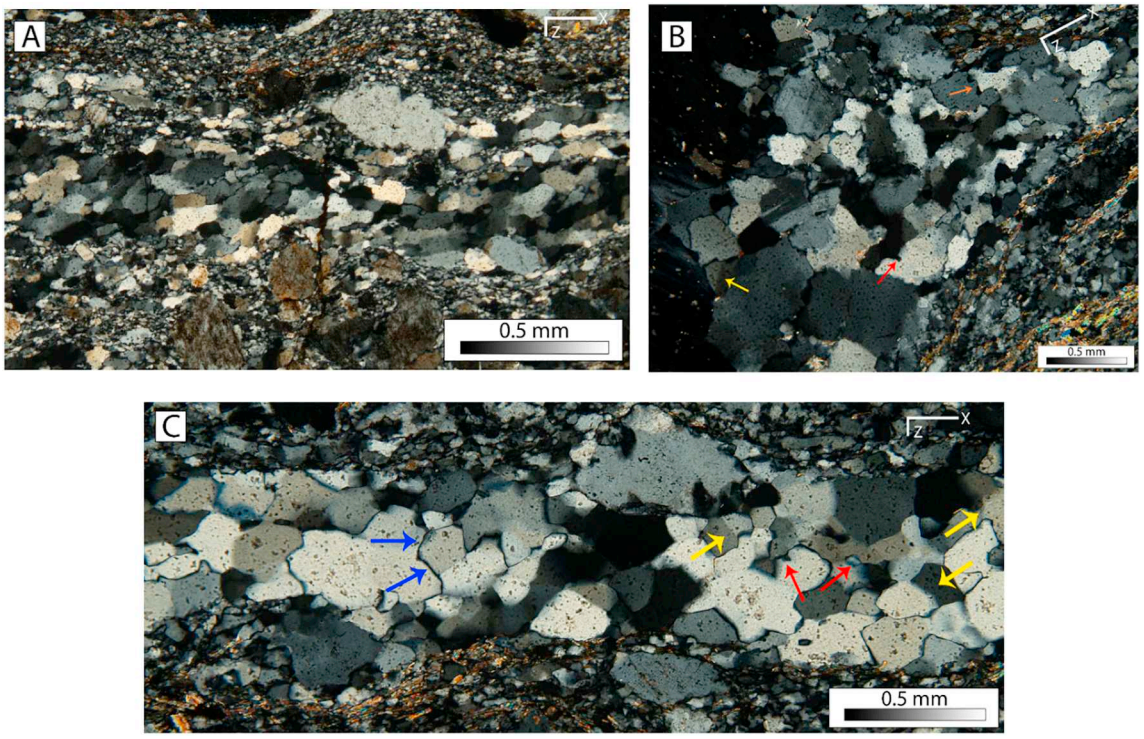


**Fig. 9.** Photomicrographs of TSZ mylonites regarding quartz microstructures (cross-polarized light, XZ section). A) Quartz SGR with oblique grain shape fabric with dextral shear sense; B) Quartz ribbons with BLG (red arrow), SGR (yellow arrow), and GBM (orange arrow) evidence; C) Quartz ribbons parallel to foliation with abundant SGR evidence (yellow arrow), BLG in minor proportion (red arrow) and polygonal boundaries (blue arrows) suggesting contribution of static recrystallization. (For interpretation of the references to colour in this figure legend, the reader is referred to the web version of this article.)

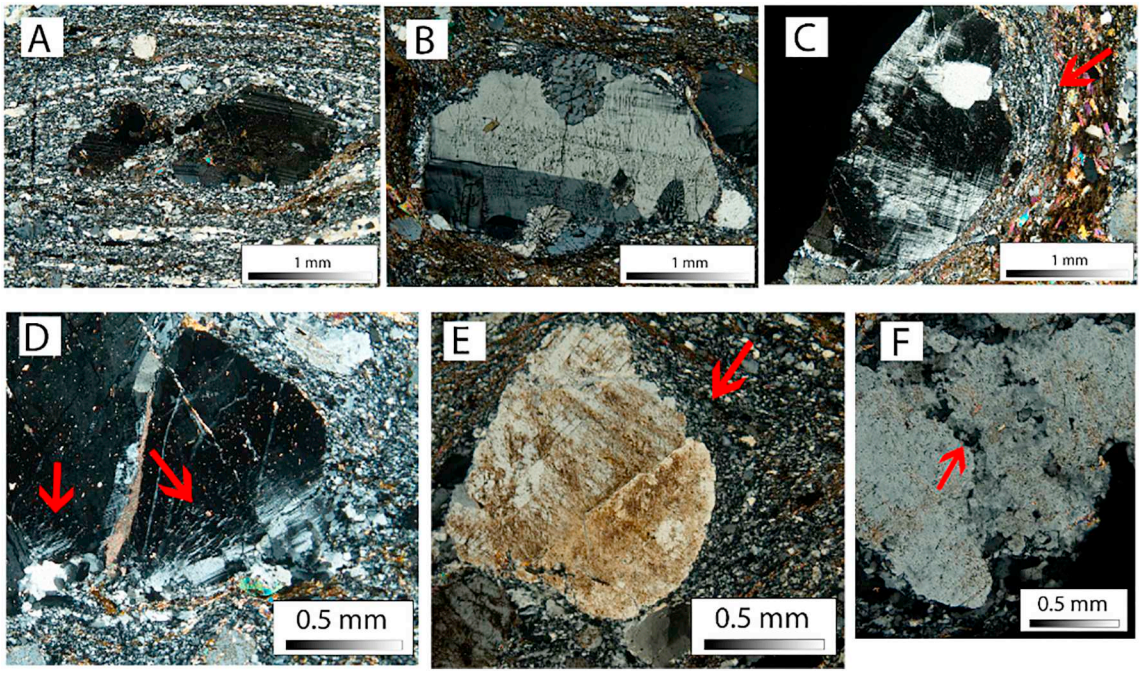


**Fig. 10.** Photomicrographs of TSZ mylonites regarding feldspar deformation (cross-polarized light, XZ section), red arrows indicate microstructures. A) antithetical normal microfault within recrystallized feldspar-bearing matrix (sample PS-55); B) myrmekite induced by deformation along margins of feldspar porphyroclasts (PS-41B); C) mantle of recrystallization (feldspar ± quartz ± sericite) surrounding a feldspar porphyroclasts with undulose extinction and subgrains suggesting SGR mechanism of recrystallization (PS-42B); D) Flame pertites induced by deformation in K-feldspar porphyroclast (PS-42B); E) feldspar porphyroclast with sericite alteration surrounded by mantle of recrystallization (PS-41A); F) tracks of fine-grain feldspar suggesting BLG mechanism of recrystallization individualizing subgrains (PS-42B). (For interpretation of the references to colour in this figure legend, the reader is referred to the web version of this article.)

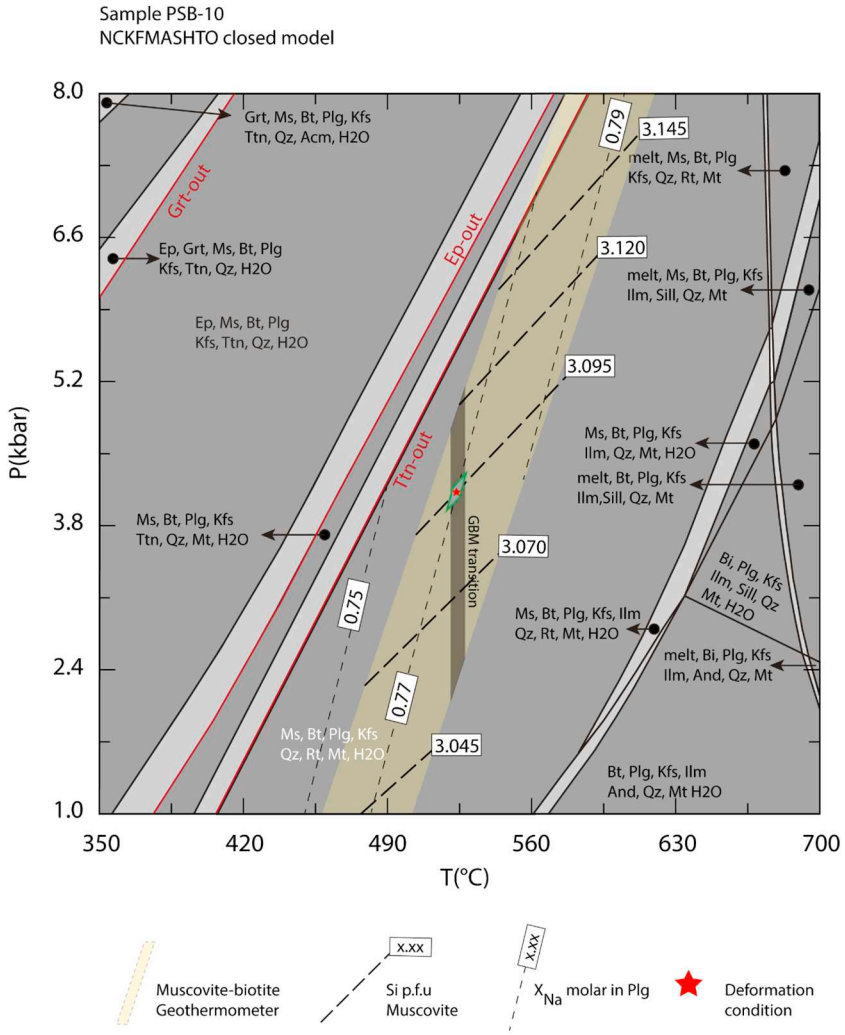


**Fig. 11.** P-T pseudosection calculated using Perple_X (Connolly, 2005) in the NCKFMASHTO system for the ultramylonite composition (sample PSB-10). The red dash-line rectangle correspond to the muscovite-biotite geothermometer with error (Hoisch, 1989) and the gray rectangle represent the transition between subgrain rotation and grain boundary migration mechanisms of recrystallization for quartz (Faleiros et al., 2010; Stipp et al., 2002a). (For interpretation of the references to colour in this figure legend, the reader is referred to the web version of this article.)

vertical optical axes. Due to this lack of data in Y direction, the CPOs are predominant 'point-type', symmetric to slightly asymmetric and suggest activation of 'basal- < a > ' and 'rhomb- < a > ' during quartz deformation at medium temperature conditions. The absence of data in the center girdle makes it difficult to identify geometry (i.e., 'point-type' from 'girdle-type') and whether if the 'prism- < a > ' was activated during deformation. Therefore, EBSD analysis provides important information in order to overcome this deficiency and properly understand this 'point-type' geometry.

### 3.4.2. EBSD analysis

*3.4.2.1. Quartz.* Recrystallized quartz grains from monomineralic ribbons and mylonitic matrix were analyzed using EBSD. As shown in the colour code legend, a predominance of blue, purple and green colour indicates a preferred orientation of the < a > -axes of the quartz grains in the X-direction of the sample (Fig. 13A). The pole figures were constructed using 'one-point-per-grain' to avoid grain size bias on the concentration of poles. There is a spreading of the [c]-axes along a single girdle in the quartz pole figures for monomineralic ribbons (Fig. 13B), although a maximum appears in the half way between Y and Z directions. The < a > -axes of the crystals show discrete concentration at low angles to the X-direction. As shown by the distribution of rotation axes (Fig. 13C), the higher densities occur between the poles to {m} and the rhombohedral plane {π}. On the other hand, the fine-grained quartz from the polyphase matrix presents one high density around Y axis on the [c]-axis pole figure and no preferred shape (Fig. 13D). The misorientation histogram (Fig. 13D) shows high peaks in low (~3–5°) and intermediate angles (~55–60°). These peaks are commonly attribute to the presence of subgrains and Dauphiné twinning, respectively. The good fit between the uncorrelated misorientation angles and the random (theoretical) distribution indicate a random CPO for fine-grained quartz from polyphase matrix even with a maximum concentration probably resulted by early subgrains formation. Since quartz is intensely affected by dynamic recrystallization processes, it is expected a strong and well-shaped CPO, as observed in those fabrics from monomineralic quartz ribbons. Therefore, these differences in CPO indicate a switch between deformation processes.

Although FA and EBSD data for monomineralic quartz ribbons from sample PS-41A present similar results regarding asymmetry and [c]-axes location, EBSD data show a robust pole Fig. with monoclinic geometry (i.e., single girdle), while the result from FA display a 'point-type'-related geometry (Fig. 12). This 'point-type' fabric, present almost in all samples, is masked due to FA limitation with vertical axis measurements. However, EBSD data have shown that this fabric would be a 'single girdle type' if FA was able to measure vertical axis. Hence, it is

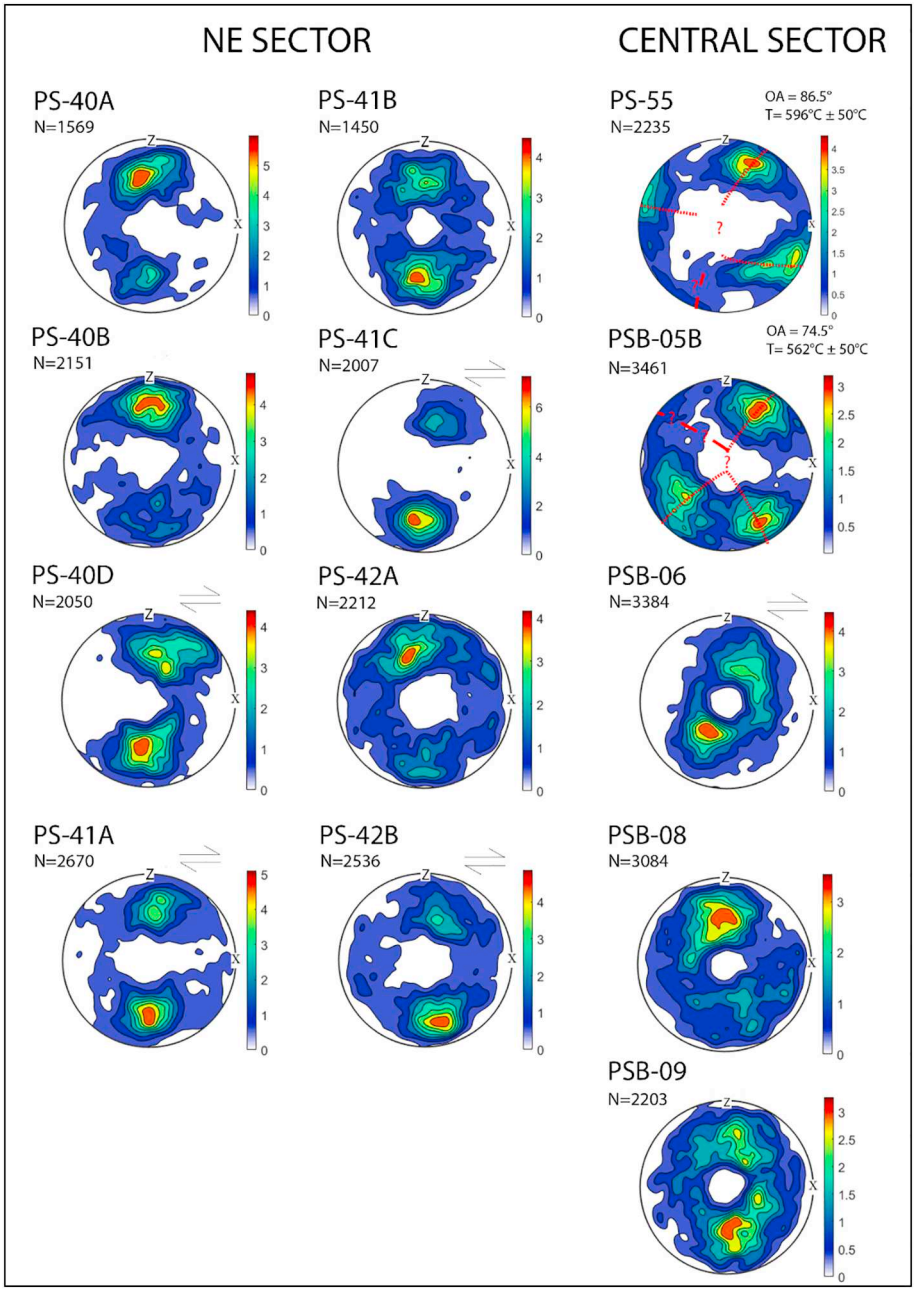


**Fig. 12.** Quartz [c] axis fabric measured using Fabric Analyzer (FA); lower hemisphere equal area projections; foliation oriented left-right and vertical, stretching lineation horizontal. Samples number and the number of analyzed grains (N) are indicated upper left. Opening-angle (OA), values of temperature calculated using Faleiros et al. (2016b) calibration and shear sense are indicated upper right.

possible to extrapolate that our samples with 'point-type' geometry correspond to single girdle fabric since we have homogeneous fabrics between samples. Thus, the predominance of single girdle fabrics implies in strong contribution of simple shear component during deformation.

*3.4.2.2. Feldspar*. The CPO analysis of plagioclase and K-feldspar has been performed on the mylonite sample (PS-41A) and data were collected from fine-grained polyphase mylonitic matrix in order to constrain the mechanisms of recrystallization and deformation since it is possible to determine which slip system was activated during deformation (Tullis and Yund, 1977; Scandale et al., 1983; Menegon et al., 2008).

While the quartz pole figures show a very consistent monoclinic fabric developed during quartz recrystallization, the pole figures for plagioclase and K-feldspar show no preferred orientation for {100}, {010} and {001} directions (Fig. 14A). Besides, the uncorrelated misorientation angles distributions for both phases do not show significant deviations from the random distribution, reinforcing the aleatory fabric present in the pole figures (Fig. 14B). The peak of misorientation around 180° is typically related with twins (e.g., Viegas et al., 2016).

### 3.4.3. Opening-angle thermometer

An opening-angle (OA) corresponds to the angle separating the two girdles that define a cross girdle CPO pattern (orthorhombic symmetry). Kruhl (1996) observed a positive linear correlation between OA and temperature from rocks naturally deformed and proposed it as a deformation-related thermometer. The angle increases with rising temperatures, hydrolytic weakening and with decreasing strain rates (Kruhl, 1996; Morgan and Law, 2004; Law, 2014). Since Kruhl (1996),

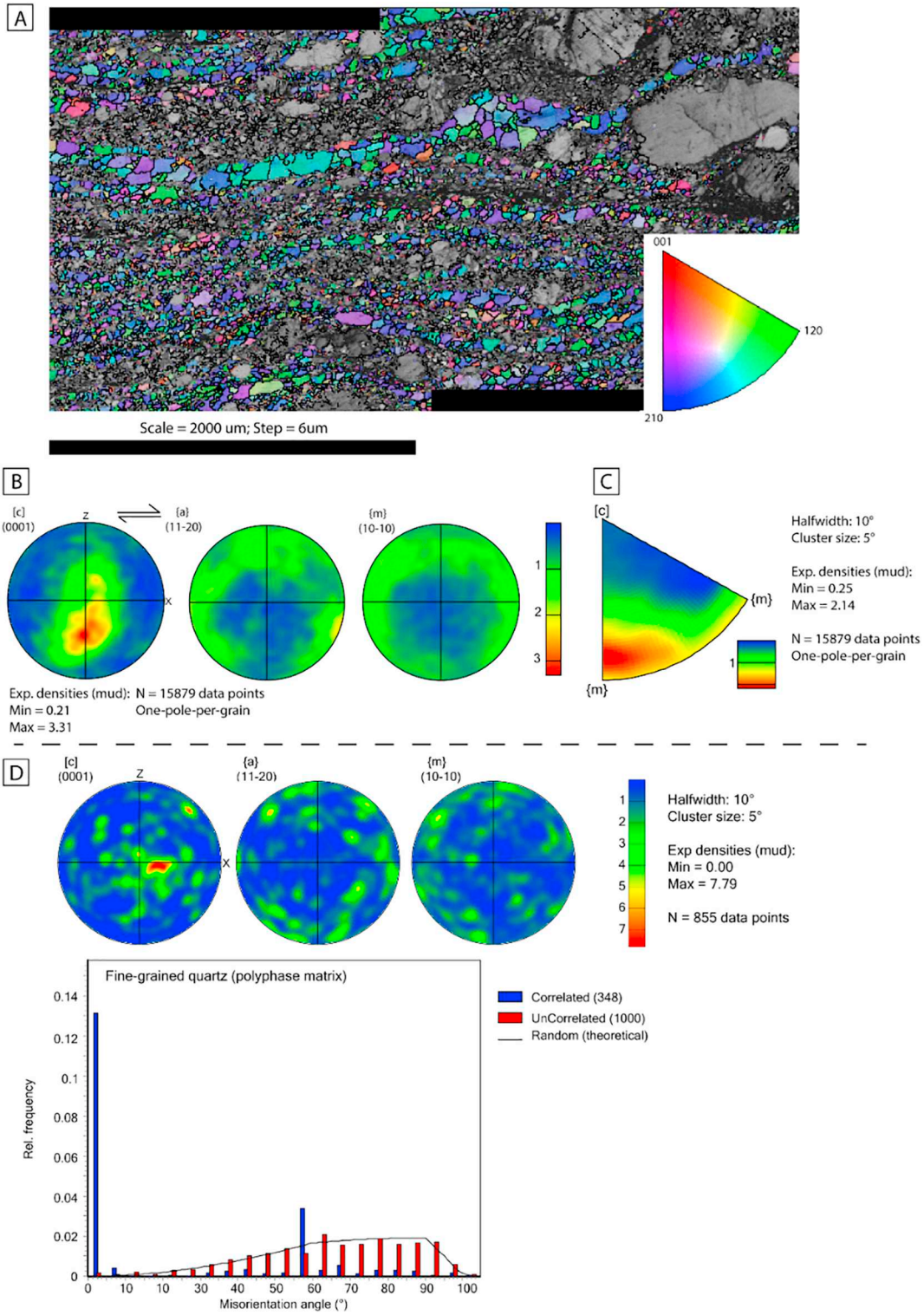


**Fig. 13.** EBSD analysis from mylonite sample PS-41A. A) Inverse pole figure map in X-direction for quartz grains; B) quartz CPO 'one-pole-per-grain' measured using EBSD; lower hemisphere equal area projections; foliation-oriented *E*-W and vertical, stretching lineation horizontal; C) quartz inverse pole figure diagram, 'one-pole-per-grain'; lower hemisphere equal area projection; D) CPO of fine-grained quartz from polyphase matrix (sample PS-41A) measured using EBSD; lower hemisphere equal area projections; foliation-oriented E-W and vertical, stretching lineation horizontal.

the method has undergone minor refinements (Morgan and Law, 2004; Law, 2014) and more recently Faleiros et al. (2016a) compiled and expanded the available data set of OA versus temperature which spans the interval from ~250 to ~1050 °C and ~2.5 to ~15 kbar, and identified a secondary effect of pressure.

Two samples (PSB-55, PSB-05B) display orthorhombic symmetry suggesting a type I asymmetric cross girdle (Lister, 1977) making them suitable for opening-angle thermometer analysis using the Faleiros' et al. (2016b) equations (Eqs. 1, 2). To avoid any visual bias, the OA measurements were carried out through a MTEX routine which determines the location of maxima intensities and the angle between them (Hunter et al., 2018a).

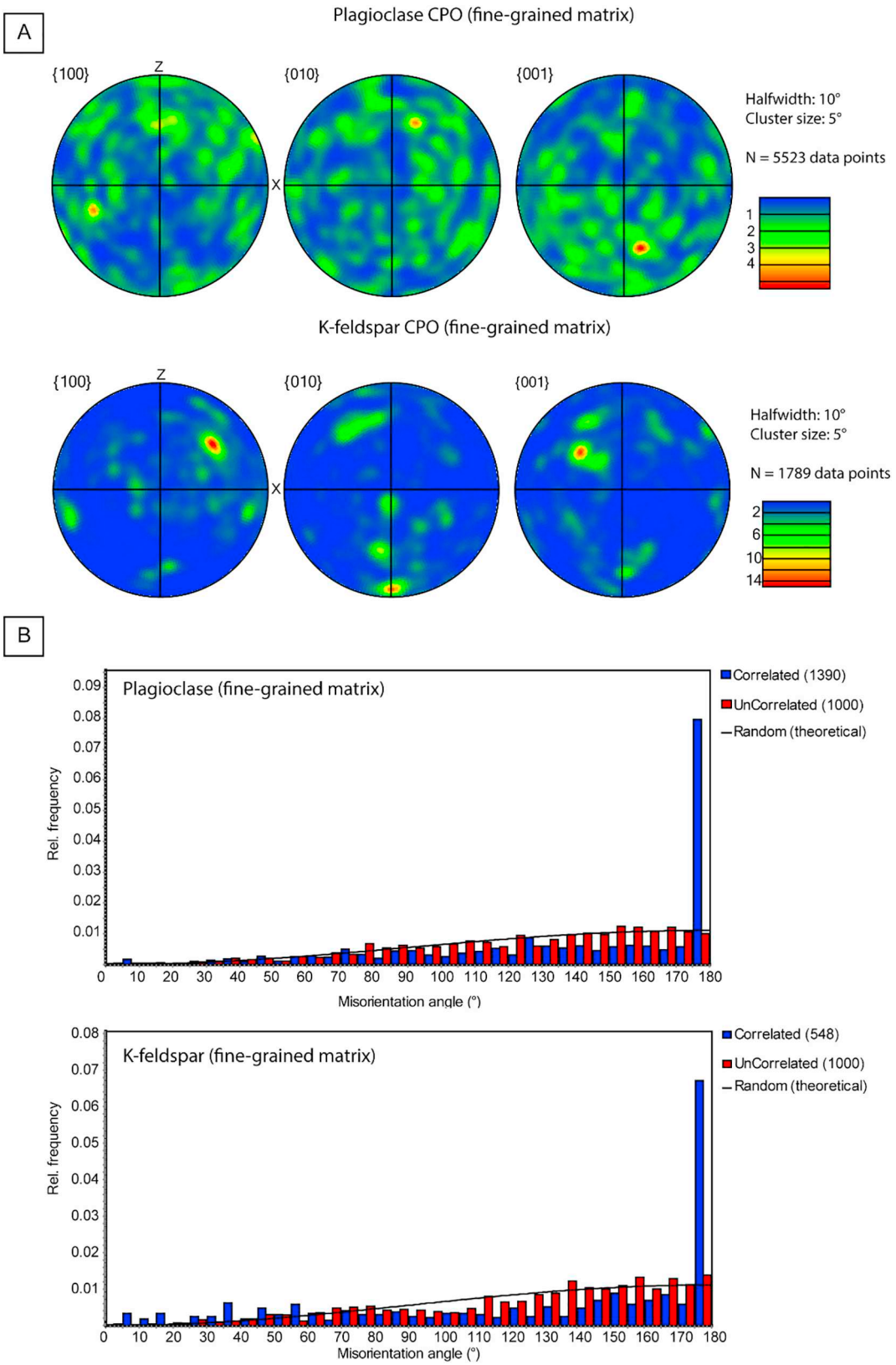


**Fig. 14.** A) Pole figures of plagioclase and K-feldspar from fine-grained polyphase mylonitic matrix; lower hemisphere equal area projections; foliation-oriented E-W and vertical, stretching lineation horizontal. B) Misorientation angle distributions for fine-grained plagioclase and K-feldspar from mylonitic matrix.

$$T(^{\circ}C) = 6.9OA(\text{degree}) + 48 (250^{\circ}C \leq T \leq 650^{\circ}C \wedge OA \leq 87^{\circ}) \quad (1)$$

$$T(^{\circ}C) = 4.6OA(\text{degrees}) + 258 (650^{\circ}C \leq T \leq 1050^{\circ}C \wedge OA \geq 87^{\circ}) \quad (2)$$

The OA measured by the MTEX routine are 86.5° and 74.5° for samples PS-55 and PSB-05B, respectively. From Eq. (1), these opening-angles yield deformation temperatures of ~596 °C ± 50° and ~562 °C ± 50 °C, respectively. According to the calculated

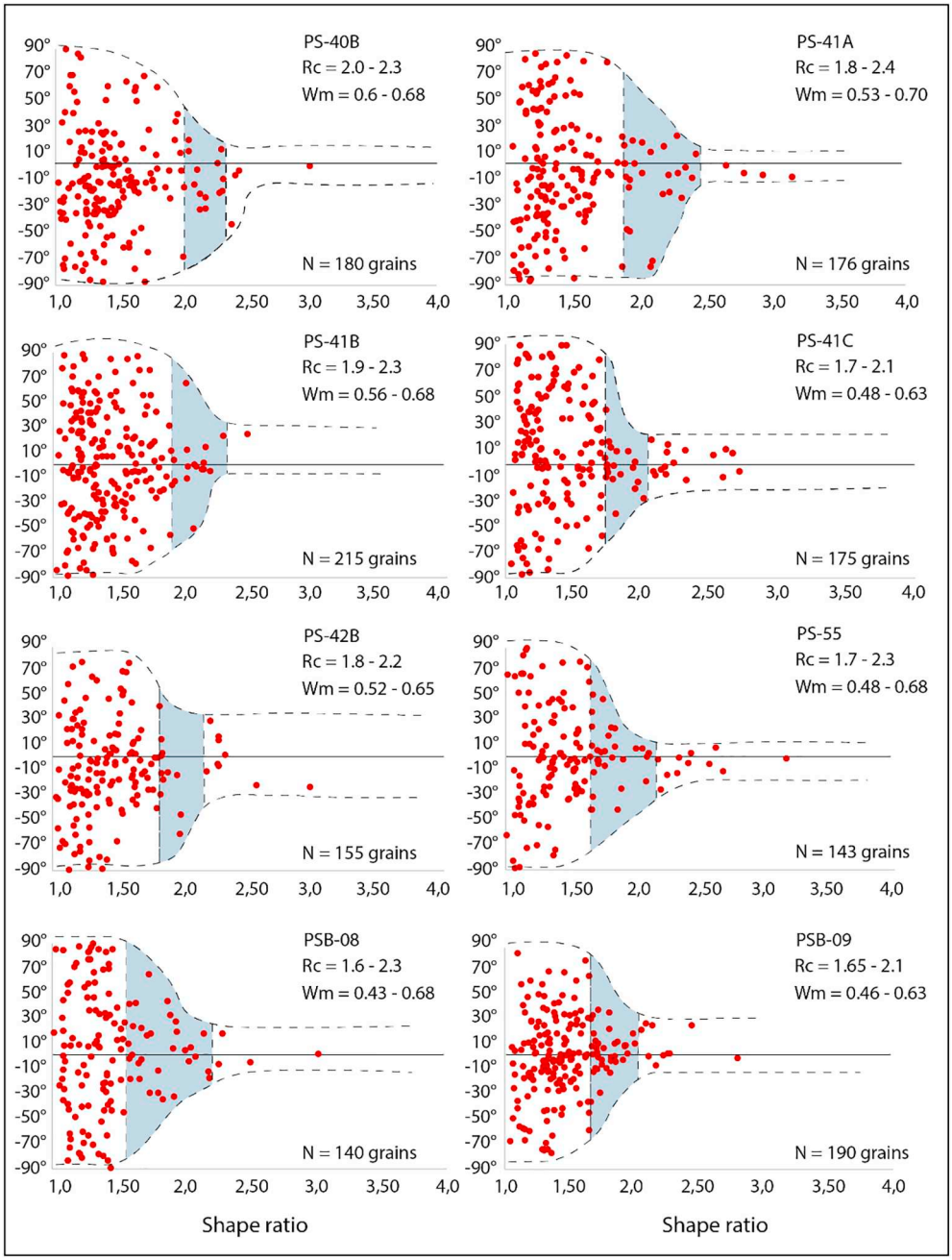


**Fig. 15.** Wallis' plots (Wallis, 1995) of feldspar porphyroclasts: shape ratio versus angle between horizontal foliation and long axis to estimate $R_c$ ranges (blue field) and its corresponding value of vorticity number from rigid porphyroclasts method ($W_m^{RP}$) for each sample. $R_c$, $W_m^{RP}$ and number of grains analyzed are indicated. (For interpretation of the references to colour in this figure legend, the reader is referred to the web version of this article.)

temperature based in OA measurements, GBM should be the main mechanism of recrystallization for quartz in high temperature (amphibolite facies). As shown before in microstructural analysis section, SGR plays the major role in quartz recrystallization with minor contribution of GBM in upper greenschist facies. However, it is well known that OA is sensitive to water activity, strain rate and 3D strain geometry (Faleiros et al., 2016a; Kruhl, 1996; Law, 2014; Lister, 1977; Lister and Hobbs, 1980). Therefore, these results must be carefully interpreted.

### 3.5. Vorticity

The vorticity analysis though RP method result in $W_m^{RP}$ ranging 0.43–0.70 (i.e. 50–70% of pure shear contribution). Results from δ/β method, on the other hand, indicate $W_m^{\delta/\beta}$ range which spans 0.85–0.99 (Table 6), i.e. 65–99% of simple shear contribution, and three samples with $W_m^{\delta/\beta}$ ranging 0.24–0.47 (Table 6, i.e. 68–80% of pure shear, marking the variety in vorticity towards the strike of the shear zone. The RP method presents similar range of values of $W_m^{RP}$ to all samples (Fig. 15) and lower values in relation with $W_m^{\delta/\beta}$. The difference between $W_m$ from both methods will be developed further in discussion *(section 5.3)*.

### 3.6. Finite strain quantification

Strain ellipsoids present low values of $(F)^{1/2}$, between 3.0% and 5.8%, indicating good elliptical adjustments ensuring good data quality, with estimated foliation (strike/dip) and stretching lineation very similar to those measured in the field. Foliations from field-base

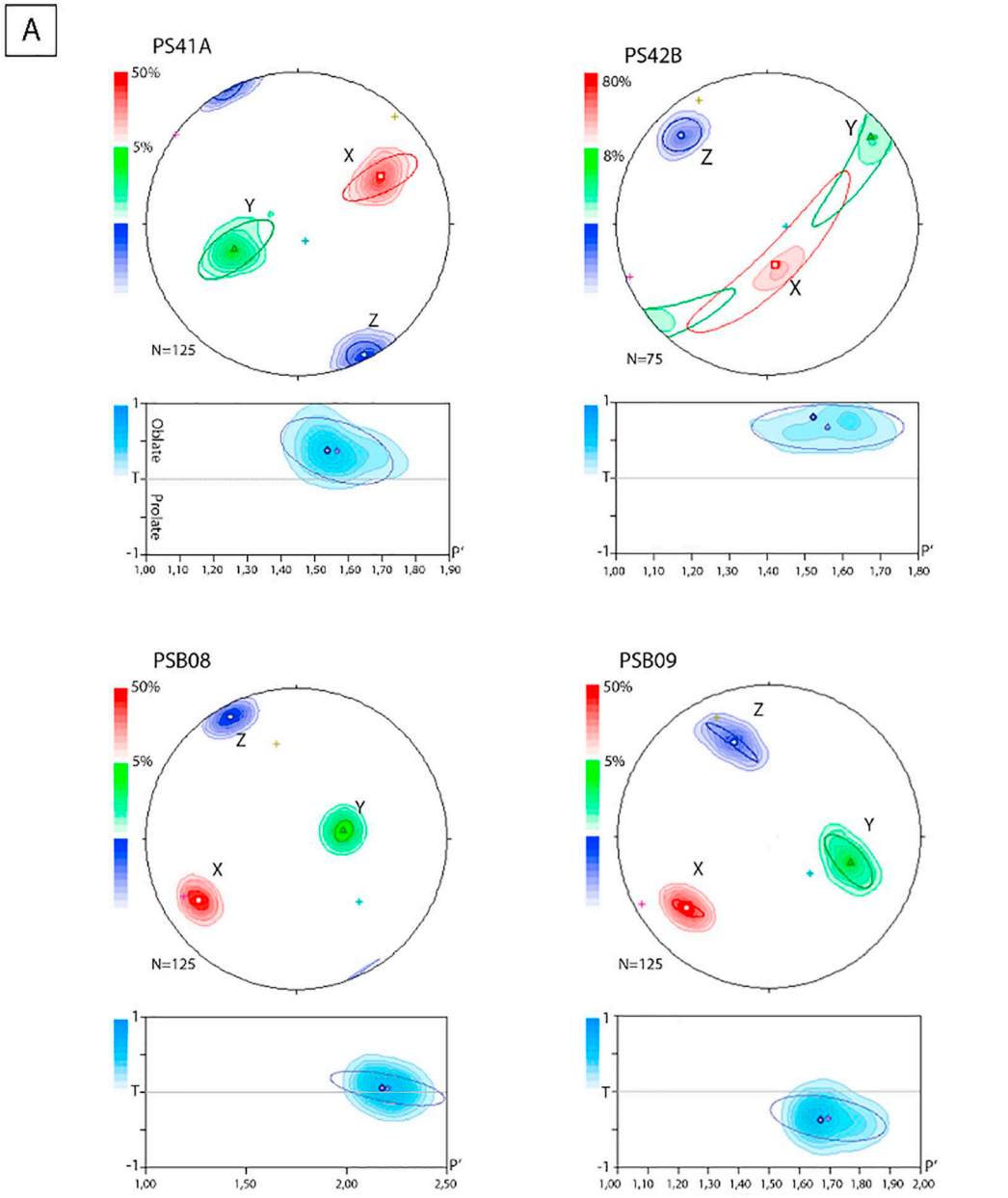


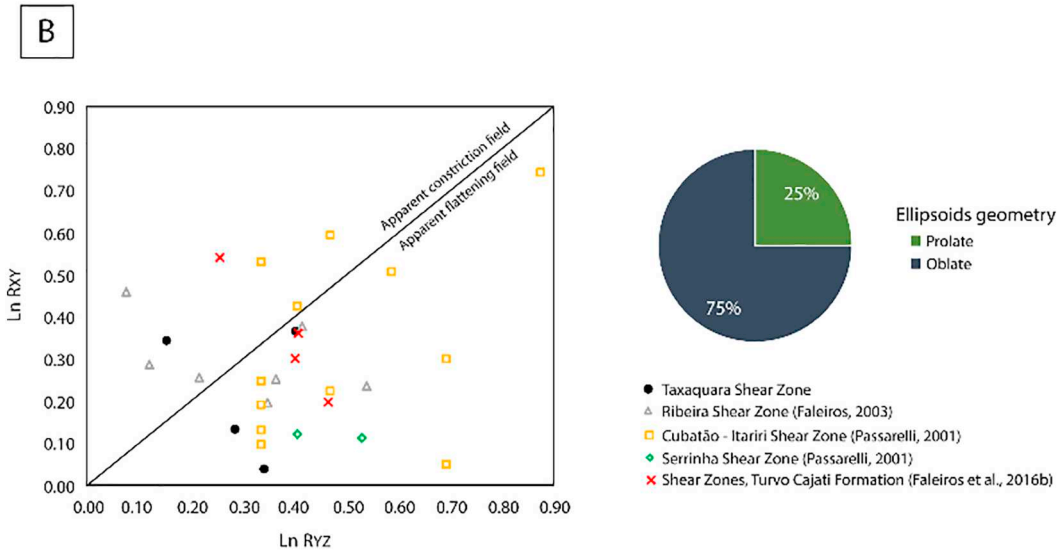


*(caption on next page)*

**Fig. 16.** A) Three dimensional finite strain data from three-dimensional analysis using ELLIPSOID freeware (Launeau and Robin, 2003b, 2005) with anisotropy degree (P′) and shape parameter (T) of Jelinek (1981). Ellipsoids were obtained from combinations of subsections from the analyzed mutually perpendicular sections of each sample; B) Flinn diagram (modified from Ramsay and Huber, 1983) representing the shape of strain ellipsoid based on k-value (Flinn's parameter). The diagram presents new data from Taxaquara Shear Zone and compiled data from RSZ (Faleiros, 2003), CISZ and SSZ (Passarelli, 2001) and minor retrograde shear zones within the Turvo Cajati Formation (Faleiros et al., 2016a). The pie chart presents the percentage of oblate and prolate strain ellipsoid based on Flinn's parameter.

structural analyses and from finite strain quantification strike NE-SW, parallel to the main structural trend of Ribeira belt, with sub-vertical to vertical dip, and stretching lineation with variable plunge between 24 and 67° (Table 7). Based in feldspar porphyroclasts, the samples present low to moderate values of maximum deformation ($1.462 \leq R_{XZ} \leq 2.156$) and anisotropy degree ($1.52 \leq P' \leq 2.17$) suggesting considerably low deformation ratio regarding mylonitic rocks.

Regarding finite strain ellipsoid shape parameter (T; Jelinek, 1981), samples PS41A and PS42B present $T > 0$ classifying them as oblates (Fig. 16A), while samples PSB08 and PSB09 present T values around and lower than zero, respectively, indicating transition between plane strain to prolate ellipsoid (Fig. 16). Strain ellipsoid can also be classified thought Flinn parameter (*k-value*) calculated based on ratio between ellipsoid axis as presented in Eq. (3). Based on Flinn's parameter, strain ellipsoids are classified as plane strain (k = 1), oblate (k < 1) and prolate ($1 < k < \infty$) (Ramsay and Huber, 1983).

$$k = \frac{R_{XY} - 1}{R_{YZ} - 1} \quad (3)$$

Strain ellipsoid classification based on Flinn's parameter reinforce the geometries based on T-parameter (Jelinek, 1981). Samples PS41A, PS42B and PSB08 plotting within the apparent flattening field (oblate shapes) while sample PSB09 within apparent constriction field (prolate shape) (Fig. 16B). Despite small number of analyzed samples, it is possible to observe sub-vertical to vertical foliation, stretching lineation with variable plunge and strain partitioning between flattening and constrictional strain field. These data reinforce the strain partition between pure and simple shear, as also indicated by vorticity analysis.

## 4. Discussion

### 4.1. The Taxaquara Shear Zone

#### 4.1.1. Deformation conditions

Qualitative data from mineral assemblage combined with quantitative data from quartz microstructures, thermodynamic modelling, muscovite-biotite and opening-angle thermometers help to constrain the deformation conditions along the TSZ (Fig. 17). The mineral assemblage composed of quartz + oligoclase + K-feldspar + muscovite + biotite + rutile + magnetite, with *syn*-kinematic biotite and muscovite neocrystallized during mylonitization, suggests deformation under medium-temperature conditions.

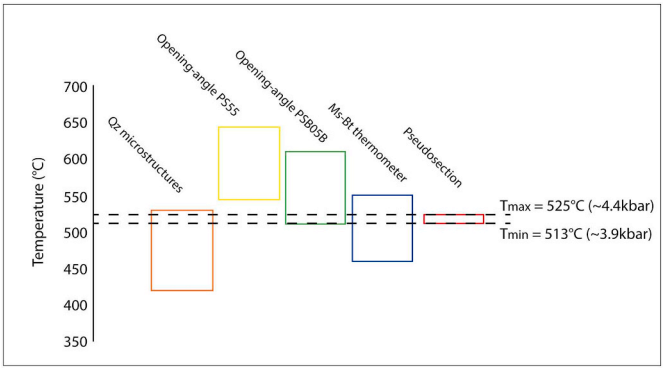


**Fig. 17.** Summary of deformation temperature based on quartz microstructures, opening-angle thermometry based on quartz [c]-axis pole Fig.s, muscovite-biotite thermometer (Hoisch, 1989) and results from pseudosection. Measurements errors for muscovite-biotite ( ± 22 °C) and opening-angle thermometers ( ± 50 °C) are being taken in consideration.

Considering an average strain rate of approximately $10^{-12}\,s^{-1}$, the relationship between quartz microstructures and deformation temperature is well established with BLG being dominant between 280 and 390 °C, SGR in 420–490 °C interval and GBM playing important role above ~530 °C (Faleiros et al., 2010; Stipp et al., 2002a, 2002b). Topological parameters, qualitative descriptions of optical microstructures and strain rate estimates between $10^{-13}$ and $10^{-12}\,s^{-1}$ for quartz indicate that deformation was mainly accommodated by dislocation creep achieving SGR, which prevails at temperatures between 420 and 490 °C for similar strain rates. Thus, it is possible to infer deformation temperature interval between 420 and 530 °C based on quartz microstructures, with the upper temperature limited by the temperature where GBM becomes dominant (Fig. 17). The quartz [c]-axes pole figures from FA (Fig. 12) and EBSD (Fig. 13B) suggest that 'basal- < a > ' and 'rhomb- < a > ' slip systems were activated during quartz deformation (Schmid and Casey, 1986). The inverse pole Fig. from EBSD (Fig. 13C) data indicates higher density between the poles to {m} and the rhombohedral plane {π}, which suggests activation of the 'rhomb- < a > ' slip system as indicated by the location of the [c]-axis.

The opening-angle thermometer ($T_{OA}$) used in two samples yields a temperature interval between 512 and 646 °C, considering error bars, suggesting generally higher temperatures than the other methods (Fig. 17). Factors such as water content and strain rate might influence the $T_{OA}$ results (Law, 2014; Faleiros et al., 2016b) although it is difficult to pinpoint the cause. A possible reason, although speculative, to explain the higher temperatures from $T_{OA}$ may be a result of a higher than average water weakening environment. The most precise deformation condition estimate comes from the thermodynamic modelling which defines a restrict condition which spans ~513–525 °C and ~3.9–4.4 kbar with mean peak at ~520 °C and ~4 kbar indicated by the isopleths' intersection in the pseudosection. This P-T interval intercepts the other temperature estimates based on muscovite-biotite conventional thermometry and dynamic recrystallization mechanisms for quartz and feldspar, reinforcing the data congruency (Fig. 17).

#### 4.1.2. Inferences for continental crust rheology

Assuming a continental crust with regular density ($2.8\,g/cm^3$) and using the limits of the metamorphic conditions during deformation (~513–525 °C, ~3.9–4.4 kbar), it is possible to estimate that the TSZ was developed at ~11–12 km deep with a crustal geothermal gradient of ~46.5–42.5 °C/km. Lower (near normal) geothermal gradients have been inferred for other major structures within the RB such as the Ribeira (~32 °C/km; Faleiros et al., 2010) and the Além Paraíba-Padua Shear Zones (~35 °C/km; Bento dos Santos et al., 2010). Together they suggest that the RB may be affected by any thermal influence (e.g., addition of magma, regional metamorphism or mantle dynamics) promoting a weakening in the lithosphere facilitating the development the shear zones since its known the geothermal gradient controls the maximum strength of the continental crust (Ord and Hobbs, 1989).

Available petrological and thermochronological data indicate that the common domains from the RB undergone metamorphic conditions within granulite facies in low to intermediate pressures (≥750 °C, 5–9 kbar) between 630 and 570 Ma followed by slow cooling rates until 480–470 Ma (Tassinari et al., 2006; Bento dos Santos et al., 2010, 2014; Bento dos Santos et al., 2011; Bento dos Santos et al., 2015). Tassinari

et al. (2006) propose that this thermal setting suggests an important period of high temperatures in the lower to medium continental crust resulting in a long-term elevated geothermal gradient sustained by the upwelling of asthenospheric mantle and magma underplating. Since the geothermal gradient and lithological variation control the distribution of vertical strength within the continental crust, it is possible to infer that this long-term temperature within the RB during the Western Gondwana amalgamation may has influenced the development of ductile shear zones in mid-crustal level.

### 4.2. Microstructures and deformation mechanisms

With the development and advancement of detailed investigative methods, quantitative data, such as grain statistics, EBSD analyses and paleopiezometry, have become important to proper understand mechanisms of recrystallization and deformation (Menegon et al., 2008; Oliot et al., 2014; Platt, 2015; Viegas et al., 2016). Analysis of quartz and feldspar microstructures and textural relationships provide important piece of information regarding deformation mechanisms, conditions and, therefore, crustal rheology. Quartz aggregates from TSZ mylonitic rocks accommodated deformation through dislocation creep, although some tendency of randomness could be accounted to grain boundary sliding as well, followed by SGR mechanism with GBM playing a minor contribution within medium-grade conditions. Besides supported by petrographic descriptions and quantification of topological parameters, this interpretation is also supported by strain rate estimates from flow laws using parameters from Hirth et al. (2001) which indicate a variation between $10^{-13}$ to $10^{-12}$ s-1 for medium grade deformation conditions being in good agreement with SGR mechanism (cf. Stipp et al., 2002b). Regarding quartz CPO, there are fundamental differences between those from monomineralic quartz ribbons and fine-grained quartz from polyphase matrix. The first presents strong asymmetrical CPO with monoclinic fabric indicating that quartz was deformed by dislocation creep also supported by typical microstructures for SGR. The latter, however, display a random distribution indicating a switch from dislocation creep to any other deformation mechanism. Similar switch between deformation mechanisms based on quartz CPOs was described in Kilian et al. (2011) and interpreted as product of diffusion creep.

Plagioclase and K-feldspar porphyroclasts present evidence of intracrystalline deformation such as kink twinning (Fig. 6C), undulose extinction and subgrain development (Fig. 10C). These are found together with microfaults (Fig. 6B) as well as mantles of very fine-grained quartz + feldspar + mica around porphyroclasts (Fig. 10C, E). Trails of very-fine grains filling microfractures in feldspar porphyroclasts with no difference in composition are also very common (Fig. 5D). These microstructures are in good agreement with those from zone 3 in Pryer (1993) in which intracrystalline deformation and recrystallization played a major role in comparison with fracturing in medium-grade conditions at brittle-ductile transition for feldspar (Tullis and Yund, 1985; Pryer, 1993). Matrix feldspars are dominated by oligoclase with minor K-feldspar and have homogeneous diameter (11 to 14 μm), rectangular shape (aspect ratio of 1.8 ± 0.4), well-defined sharp and straight boundaries between grains (Fig. 5C, D) suggestive of a recrystallized fabric. If so, pole figures should indicate strong crystallographic preferred orientation related with recrystallization processes. However, pole figures for plagioclase and K-feldspar from EBSD analyses show diffuse patterns with no preferred orientation (Fig. 14A). These random distributions are supported by the distribution of misorientation angles (Fig. 14B) that shows no substantial peaks outside the random distribution curve. Since feldspar was affected by recrystallization processes, quasi-random crystallographic preferred orientation suggests that the fine grains in the matrix would not be simply produced by dislocation creep and dynamic recrystallization. In addition, the misorientation angle distribution almost completely fit in the random distribution with discrete peaks at low (10–20°) and intermediate angle (30–40°) which might indicate an incipient recrystallization of feldspar by bulging with a minor contribution of subgrain rotation considering the small sizes of the recrystallized grains. These data set the deformation limit in the boundary of brittle-ductile transition for feldspar.

This suggests that instead of dislocation creep, the matrix may have been deformed through diffusion processes such as granular flow fluid assisted dissolution-precipitation creep that would have accommodated diffusive mass transfer through grain boundary sliding (Stünitz and Fitz Gerald, 1993; Prior and Wheeler, 1999; Passchier and Trouw, 2005; Kilian et al., 2011; Oliot et al., 2014). This process allows crystals in fine-grained aggregates slide past each other at the same time that the development of vacancies between grains is prevented by crystal-plastic deformation or solution and precipitation through a grain boundary fluid (Passchier and Trouw, 2005). It is expected to occur at relatively high temperatures (amphibolite facies or upper) and strain, however some authors proposed that the process of diffusion creep may play a role in granitic mylonites at low to moderate temperature (Bas den Brok, 1998; Farver and Yund, 2000). In fact, this process has been described for deformed feldspar (most plagioclase) from shear zones developed under mid-crustal conditions under upper greenschist conditions (Prior and Wheeler, 1999; Oliot et al., 2014).

The difficulty to recognize diffusion creep arises from the fact that it leaves few traces. Indirect evidence for grain boundary sliding are very fine-grained and homogeneous aggregates (e.g. quartzo-feldspathic mylonitic matrix), the lack of lattice-preferred orientation, elongate grains with sharp and straight boundaries, low dislocation density in grains and presence of voids along grain boundaries detected through transmission electron microscope (TEM) analyses (Passchier and Trouw, 2005). Since strain rate seems to control the development of microstructures (Hirth and Tullis, 1992; Post and Tullis, 1999; Oliot et al., 2014; Platt, 2015; Viegas et al., 2016), estimating their values are important to support this interpretation. The strain rate estimates based on the stress and temperatures determined for quartz varies from $10^{-12}$ to $10^{-13}\,s^{-1}$ supporting that quartz accommodate the deformation by dislocation creep, while the feldspar, by diffusion creep (Kilian et al., 2011; Platt, 2015). Therefore, we have shown several indirect evidences and strain rate estimates that support that granular flow acted during feldspar deformation, possibly localizing strain and giving rise to the first nuclei of the TSZ in microscale.

The microstructures described and quantified here from deformed quartz and feldspar support the mechanism for the formation of fine-grained two-phase mixtures proposed in Platt (2015) for mylonitic granitoid. Platt (2015) propose that the grain-size reduction provoked by dislocation creep and dynamic recrystallization causes a switch to grain-boundary diffusion creep that requires grain-boundary sliding. The grain-boundary diffusion creep, therefore, will control the bulk rheology, and the grain size of the resulting mixture is controlled by the finer-grained phase (i.e., mostly oligoclase in the TSZ case).

### 4.3. Tectonic model of the Taxaquara Shear Zone

#### 4.3.1. Sub-simple shear regime

The Taxaquara Shear Zone, parallel to RB structural trend, is characterized by systematic NE-SW mylonitic foliation (mean N062E/70SE) and low to medium dip stretching lineation on average gently plunging NE but scattered along the shear plane (Fig. 2). This scatter may suggest either variety of local transport direction, or that it was developed under a transpressional regime (Sanderson and Marchini, 1984; Fossen and Tikoff, 1993; Fossen et al., 1994; Robin and Cruden, 1994). Syn-kinematic features observed in the field, such as C-type shear band cleavages (Fig. 3C) and tight folds (Fig. 3D) with axial plane parallel to mylonitic foliation reinforce the compressional component.

Vorticity results from rigid porphyroclast method (Fig. 15) indicate similar mean vorticity number to all analyzed samples ranging from 0.43–0.70 (i.e. 50–70% of pure shear contribution). On the other hand,

results from δ/β method indicate partitioning in vorticity with some samples with high contribution of simple or pure shear, with mean vorticity number ranging from 0.85–0.99 (i.e. 65–99% of simple shear contribution) to 0.24–0.47 (i.e. 68–80% of pure shear). Although both methods are related with vorticity measurements, they provided different results as have been observed by others in naturally deformed rocks (Law et al., 2004; Xypolias, 2010; Faleiros et al., 2016a).

Numerical modelling suggests that most general shear flows developed under moderate-high strain tend to produce clasts orientations with similar critical shape ratio ($R_c$) that might point similar contributions of pure and simple shear contributions (Stahr and Law, 2011). Since the results from the rigid porphyroclast method suggest similar contribution of pure and simple shear for most samples, these results suggest a moderate-high strain history whether proper the non-coaxiality of deformation. Hence, we suggest that the mean vorticity number through δ/β method are more reliable for TSZ which show variation between pure and simple shear contribution towards the strike of the shear zone as assumed in recent papers (Faleiros et al., 2016a). Quartz CPO fabrics also suggest the same variation. Monoclinic patters are related with non-coaxial deformation (i.e., simple shear), while orthorhombic fabrics indicate coaxial plane strain (i.e., pure shear) (Hunter et al., 2018a, 2018b; Schmid and Casey, 1986). The dominance of simple shear over pure shear from δ/β vorticity method and quartz [c]-axis monoclinic over orthorhombic fabrics suggest that TSZ developed under a sub-simple shear system (Fossen and Cavalcante, 2017).

#### 4.3.2. Transpressional system

Finite strain analyses show systematic vertical NE-SW foliation with stretching lineation (X axis) plunging towards NE (sample PS41A) and SW (samples PS42B, PSB09 and PSB09) (Fig. 16A) similar to the measured lineations in the field. Regarding the shape of the strain ellipsoid based on the *T-parameter* (Jelinek, 1981) and Flinn's parameter (*K-value*, Ramsay and Huber, 1983), samples from the NE sector display strong oblate shape, while those from central sector show a transitional geometry between weakly oblate/plane strain to prolate geometry (Fig. 16B).

Sanderson and Marchini (1984) proposed a transpression model based on shape and orientation of finite strain ellipsoids in which oblate shapes are dominant due to the shortening across the zone of transpression. For the TSZ, oblate geometries dominate in narrow sectors (e.g., NE sector of TSZ) and prolate in wide sectors (e.g., central sector of TSZ) of the shear zone following the predictions of Sanderson and Marchini (1984). This model implies orthogonal combination of simple and pure shear applied to the same plane producing strain along all three principal strain axes (Fossen and Cavalcante, 2017). Shear zones with higher values of vorticity number may allow change between X and Y axis direction (Sanderson and Marchini, 1984; Fossen and Cavalcante, 2017), which is observed in our finite strain results (Fig. 16A). Vorticity analysis through δ/β method also indicates high values of vorticity number for TSZ.

In short, structural, vorticity and three dimensional finite strain data indicate that the TSZ was developed under a transpressional tectonic model in sense of Sanderson and Marchini (1984) and Robin and Cruden (1994) with sub-simple shear component where the thick zone (i.e. central sector) is dominated by transtension and the thin zone (i.e., NE sector), by transpression which may explain the anastomosed shape in map of the TSZ. To complete the tectonic evolution of the TSZ, we should deal with the associated exhumation processes. However, at this moment we have no capacity to address this problem due to the lack of geochronological/thermochronological data (e.g., $^{40}Ar/^{39}Ar$) to assess the timing of deformation and low-temperature thermochronology (e.g., fission track and U–Th/He) in the existing literature. These data are necessary to support the exhumation rates calculations and we will look after this in further studies.

### 4.4. Regional implications in Ribeira belt and correlations in Western Gondwana

Authors have suggested generic transpression model as the main tectonic setting for this major transcurrent shear zone system developed in the Ribeira Belt during final stages of Southwestern Gondwana assembly. This was based on field-scale observations, emplacement of *syn*-kinematic granitic plutons and a few numerical models (Ebert and Hasui, 1992; Ebert et al., 1996; Hackspacher and Godoy, 1998; Egydio-Silva et al., 2002, 2018; Dehler et al., 2007). However, little has been done in order to quantify finite strain directly, which could support this model or not. In order to address this gap, we compiled finite strain data from six major transcurrent shear zones from the RB (Dayan and Keller, 1990; Passarelli, 2001; Faleiros, 2003; Faleiros et al., 2016a) and merged with our data (Fig. 16B). Together these shear zones comprise a large extension (> 1000 km length) between Paraná and Rio de Janeiro states, covering a representative section of this transcurrent shear zone system. Compiled data are presented in Table S1 (supplementary data). Strain ellipsoid shapes based on T-parameter (Jelinek, 1981) and Flinn's parameter (*k*-value; Ramsay and Huber, 1983) are present in Fig. 16B.

The Flinn's diagram for all shear zones shows that 75% of the analyzed strain ellipsoids plot within the apparent flattening field (pie chart, Fig. 16B). This is suggestive of a transpressional model in the sense of Sanderson and Marchini (1984). The minor amount of samples showing a prolate shape (pie chart; Fig. 16B) can be explained by partition of deformation (Dewey et al., 1998; Ebert and Hasui, 1998; Hackspacher and Godoy, 1998; Egydio-Silva et al., 2005), an important characteristic of transpressional tectonics during oblique collision at high angle of plate boundaries with dominant simple-shear component (Tikoff and Teyssier, 1994). As suggested in the literature, it also can represent episodic localized transtension regime (Dehler et al., 2007) or superposition of thrusts and lateral displacements under a transpressional regime (Faleiros, 2003).

Major transpressional systems developed during late stages of Western Gondwana assembly have been identified in several orogenic belts. In the African continent, the counterpart of South-America eastern margin, the Kaoko belt (Goscombe et al., 2003; Gray et al., 2006; Goscombe and Gray, 2008) and the Pan-African belt in Cameroon (Ngako and Affaton, 2003; Ngako et al., 2008) are two important transpressional belts developed during late stages of Braziliano-Pan African orogeny comprising shear zones with similar features to those of the RB, including partition of deformation into pure shear and simple shear, superposition of deformation with thrusts and transtension with pull-apart basins. Thus, regional correlations support our interpretation that dominated simple-shear transpression played a major role in the RB giving rise to transcurrent shear zones in late orogenic stages due oblique collision and lateral scape tectonics (Campanha and Brito Neves, 2004; Egydio-Silva et al., 2018; Passarelli et al., 2011).

## 5. Conclusions

Our results allow us to infer the deformation conditions and mechanisms based in petrographic, microstructural, crystallographic preferred orientation and thermodynamic modelling data and tectonic setting through based-field observations, vorticity and three-dimensional finite strain quantification prevailing during the deformation of the Taxaquara Shear Zone, Ribeira Belt, Brazil. The remarks conclusions of this paper are:

1. The mylonitization of granitic rocks affected by the TSZ gave rise to mylonites and ultramylonites with neoformed mineral assemblage composed of quartz + oligoclase + K-feldspar + biotite + muscovite + rutile + magnetite under medium temperature condition and relative low pressure (510–530 °C and ~4 kbar) under ordinary velocity for mid-crust (~$10^{-12}$ $s^{-1}$). Pressure estimates indicate that the TSZ was developed under ~11–12 km depth, indicating a

geothermal gradient of ~46.5–42.5 °C/km. This elevated geothermal gradient, also present in other major shear zones within the RB, might be an effect from the upwelling of asthenospheric mantle and magma underplating beneath the crust which may have influenced the development of ductile shear zones in mid-crustal level.
2. Petrographic descriptions, key topological parameters and crystallographic preferred orientation data strongly point out that quartz from monomineralic ribbons was deformed by dislocation creep with strong asymmetrical to symmetrical monoclinic CPO and typical microstructures of subgrain rotation with minor contribution of grain boundary migration mechanism of dynamic recrystallization with mean differential stress of 28.5 ± 2.5 MPa and strain rate between $10^{-12}$ and $10^{-13}$. Fine-grained quartz from polymineralic matrix show a weak to random CPO being interpreted as product of diffusion creep due to a switch in the mechanism of deformation.
3. Feldspars present microstructures suggestive of dislocation creep, however the random CPO for oligoclase and K-feldspar from polymineralic matrix is an evidence that diffusion creep processes (granular flow fluid-assisted dissolution–precipitation creep) was the main mechanism of deformation. This interpretation is supported by microstructural analysis, absence of CPO and strain rate estimates.
4. Vorticity results through rigid porphyroclast method suggest similar mean vorticity number for all analyzed samples indicating medium to high finite strain conditions according to numerical models (Stahr and Law, 2014). Results from δ/β method suggest mean vorticity number with contribution of pure (0.24–0.47) and simple shear (0.85–0.99) with predominance of the latter. The predominance of simple shear over pure shear and the monoclinic over orthorhombic CPO fabrics suggest that the TSZ was developed under a sub-simple shear regime. Three-dimensional finite strain quantification points out that oblate shape predominates in the thin sector of the TSZ while a transition between oblate and prolate shape is present in the thick sector. These data indicate that the TSZ was developed under a sub-simple shear and transpressional regime in sense of Sanderson and Marchini (1984). Regional correlations regarding finite strain ellipsoid shape support the interpretation of a major transpressional system that gave rise to the shear zones within the RB.

Supplementary data to this article can be found online at https://doi.org/10.1016/j.tecto.2018.12.025.

## Acknowledgements

This work was supported by São Paulo Research Foundation (FAPESP) fellowships 2016/22051-4, 2017/08919-4 and 2018/00320-9 to B.V. Ribeiro, 2015/04487-7 and 2018/10012-0 to F.M. Faleiros, CNPq grants 443439/20141, 305074/2015-6 and 302884/2015-7 to G.A.C and 443725/2014-4, 305257/2014-5 to L.E. Lagoeiro. Campanha. FMF thanks the National Council of Technological and Scientific Development (CNPq – Brazil) for the research productivity scholarship grant 302884/2015-7. The authors are grateful for Professor Chris Wilson (Monash University) and PhD student Alice Roberts (Monash University) for all support with Fabric Analyzer and quartz CPO. The technician Bruno Endo Ribeiro from the LATEC Institute is also thanked for the EBSD acquiring data. The authors are thankful for the excellent review and guidance from Whitney Behr, Emilien Oliot and an anonymous reviewer helping to improve this paper substantially. We also thank Philippe Agard for handling editorial process.

## Appendix A

### A.1. Methods

#### A.1.1. Petrography and microstructural analysis

In order to determine kinematics and estimates peak deformation conditions, mechanisms of deformation and tectonic setting, eight mylonites and three ultramylonites samples were collected in the core of TSZ since it may record the peak conditions. Although the TSZ present similar features along the extension of the studied area, samples were divided between those from the northeastern and central sectors (Fig. 2) to allow a comparison of microstructures, quartz CPO and 3D finite strain quantification. In total, we analyzed thirteen thin sections of eleven collected samples, cut perpendicular to foliation and parallel to stretching lineation (XZ section). Microstructures are summarized in Table 1.

**Table 1**
Mineralogical microstructural characterization based on quartz and feldspar deformation to establish a relationship with deformation processes and deformation temperature (Stipp et al., 2002a; Faleiros et al., 2010).

| Sample | Mineral assemblage | | Main deformation mechanisms/Microstructures | |
|---|---|---|---|---|
| | General | Minor amounts | Quartz | Feldspar |
| PS-41B | Qz, Pl, Kfs, Bt | Op, Ap, Rt | SGR, static recovery | Fracturing + Intracrystalline |
| PS-41C | Qz, Pl, Kfs, Bt, Ms | Op, Ap, Rt | SGR | Fracturing + Intracrystalline |
| PS-40D | Qz, Pl, Kfs, Ms | Tur, Grt, Ap, Rt | SGR | Fracturing + Intracrystalline |
| PS-40A | Qz, Pl, Kfs, Bt, Ms | Op, Ap, Rt | SGR | Fracturing + Intracrystalline |
| PS-40B | Qz, Pl, Kfs, Bt, Ms | Op, Ap, Rt, Ep | SGR | Fracturing + Intracrystalline |
| PS-41A | Qz, Pl, Kfs, Bt, Ms | Ap, Op, Hbl | SGR | Fracturing + Intracrystalline |
| PS-42A | Qz, Pl, Kfs, Bt, Ms | Ttn, Ap, Op, Ep, Rt | SGR | Fracturing + Intracrystalline |
| PS-42B | Qz, Pl, Kfs, Bt, Ms., Chl | Op, Ap, Car | SGR | Fracturing + Intracrystalline |
| PS-55 | Qz, Pl, Kfs, Bt, Ms | Op, Ap, Ttn, Rt | SGR, static recovery | Fracturing + Intracrystalline |
| PSB-05B | Qz, Pl, Kfs, Bt, Ms | Op, Ep, Ser, Rt | SGR, static recovery | Fracturing + Intracrystalline |
| PSB-06 | Qz, Pl, Kfs, Bt, Ms | Op, Ser, Rt, Tur | SGR, static recovery | Fracturing + Intracrystalline |
| PSB-07A | Qz, Pl Kfs, Bt, Ms | Op, Ap, Zr, Rt, Grt, Tur | SGR | Intracrystalline |
| PSB-07C | Qz, Pl Kfs, Bt, Ms | Op, Ap, Zr, Rt, Grt | SGR | Fracturing + Intracrystalline |
| PSB-08 | Qz, Pl, Kfs, Bt, Ms | Op, Ser, Rt | SGR | Fracturing + Intracrystalline |
| PSB-09 | Qz, Pl, Kfs, Bt, Ms | Op, Ep, Ser, Rt | SGR | Fracturing + Intracrystalline |
| PSB-10 | Qz, Pl, Kfs, Bt, Ms | Op, Ap, Zr, Rt | SGR | Intracrystalline |

i) Ap: apatite, Bt: biotite; Car: carbonate; Chl: chlorite; Ep: epidote; Grt: garnet; Hbl: hornblend; Kfs: alkali feldspar; Ms.: muscovite; Op: opaque; Qz: quartz; Rt: rutile; Ser: sericite; Ttn: titanite; Tur: tourmalline; Zr: zircon.
ii) SGR: subgrain rotation; GBM: grain boundary migration.

**Table 2**
Grains statistics from monomineralic quartz ribbons using PolyLX *toolbox* (Lexa, 2003) in MATLAB.

| Samples | Number of grains | Area (μm²) | | Roundness (%) | | Long axis orientation (degrees) | | Axial ratio | | Feret Diameter (μm) | | Paris Factor (%) | |
|---|---|---|---|---|---|---|---|---|---|---|---|---|---|
| | | Mean | Sd | Mean | Sd | Mean | Sd | Mean | Sd | Mean | Sd | Mean | Sd |
| PS-40A | 301 | 1530.44 | 2345.29 | 86.38 | 11.25 | 10.00 | 30.28 | 1.63 | 0.35 | 52.46 | 23.16 | 5.84 | 3.90 |
| PS-40D | 244 | 3856.19 | 2855.76 | 50.56 | 11.44 | 18.73 | 23.02 | 1.73 | 0.36 | 62.79 | 24.27 | 4.86 | 3.38 |
| PS-41A | 258 | 2113.41 | 1512.88 | 52.40 | 10.29 | 12.68 | 30.09 | 1.67 | 0.38 | 46.73 | 17.64 | 6.39 | 3.88 |
| PS-41C | 251 | 4947.67 | 4497.72 | 52.34 | 11.34 | 12.93 | 31.42 | 1.69 | 0.35 | 66.40 | 32.20 | 4.55 | 3.10 |
| PSB-05B | 309 | 2664.50 | 1887.42 | 56.91 | 10.83 | 16.00 | 33.18 | 1.54 | 0.28 | 52.35 | 20.00 | 3.53 | 2.44 |
| PSB-06 | 299 | 1703.92 | 1184.86 | 57.15 | 10.98 | 9.66 | 37.44 | 1.52 | 0.28 | 42.12 | 15.73 | 3.64 | 2.71 |
| PSB-08 | 232 | 3727.17 | 3425.63 | 56.63 | 10.12 | 9.63 | 40.13 | 1.51 | 0.27 | 57.54 | 26.31 | 5.62 | 3.49 |
| PSB-09 | 271 | 2594.75 | 2156.00 | 56.02 | 10.41 | 1.00 | 32.63 | 1.53 | 0.27 | 50.17 | 21.85 | 5.18 | 3.90 |

Electron backscattering (EBS) has been used to investigate microstructures in the fine-grained matrix due its capacity to readily differentiate phases with different atomic weight. Hence, EBS couple with wavelength-dispersive X-Ray spectroscopy (WDS) were carried out on XZ oriented thin sections using JOEL JXA-8530F microprobe operating at 15 kV, current analysis of 20 nA and work distance of 11 mm. Both analyses were carried out at the University of São Paulo (Brazil).

In order to support microstructural analysis, quartz and feldspar fabric domains were chosen and classified through a number of quantitative key topological parameters. Quartz and feldspar fabric domains were manually digitized using ArcGIS (*version 10.0)* with 250–300 grains per domain to ensure a sound statistical representation and analyzed using PolyLX (http://petrol.natur.cuni.nz/_ondro/) toolbox in MATLAB (Lexa, 2003; Hunter et al., 2016). Results are summarized in Table 2.

### *A.1.2. Paleopiezometry and strain rate estimates*

Paleopiezometry measures the differential stress using the diameter of new grains originated through certain recrystallization processes (Hirth and Tullis, 1992; Post and Tullis, 1999; Stipp and Tullis, 2003; Stipp et al., 2010)

Descriptive and microphysical analyses are the basis to understand rheology of rocks deformed in the ductile regime as well as strain localization, controls of grain size and development of shear zone (Platt, 2015). In order to assess the nature of deformation in the TSZ and to provide information regarding the rheology of continental crust in the RB during the TSZ development, we applied the paleopiezometers for quartz using Stipp and Tullis (2003) calibration using the Feret diameter (μm) of quartz from monomineralic quartz ribbons.

Since strain rate, together with temperature and fluid activity influences the mechanisms of dynamic recrystallization of quartz and feldspar (Vauchez, 1987; Post and Tullis, 1999; Passchier and Trouw, 2005; Faleiros et al., 2010; Stipp et al., 2010; Stipp et al., 2002b; Stipp et al., 2002a; Platt, 2015; Viegas et al., 2016), strain rate estimates were carried out using established flow laws (Eq. A1) using the stress resulting from paleopiezometry, and maximum and minimum pressure and temperature values estimated from thermodynamic modelling. Calculations of water fugacity were carried following Pitzer and Sterner (1994) with help from Whiter's fugacity calculator (www.esci.umn.edu/people/researchers/withe012/fugacity.htm).

$$\dot{\varepsilon} = A\Delta\sigma^{n} f_{H20}^{m} \bullet \exp\left(\frac{-Q}{RT}\right) \quad \text{(A1)}$$

where A = material constant; $\Delta\sigma$ = differential stress; f = water fugacity; Q = creep activation energy; R = Clapeyron constant; T = temperature; n = stress exponent; m = water fugacity exponent; $\dot{\varepsilon}$ = strain rate ($s^{-1}$). The values of A, n and Q for quartz have been determined by a number of laboratory experiments and here we use the values in Hirth et al. (2001).

### *A.1.3. Quartz crystallographic preferred orientation (CPO)*

Quartz [c]-axis measurements were carried out at School of Earth, Atmosphere and Environmental of Monash University (Melbourne, Australia) using a Fabric Analyzer (FA; model G50) (Wilson et al., 2007). Measurements were collected from monomineralic quartz ribbons sufficiently wide so that included several quartz grains across the strike to minimize the effects of pinning against other minerals at the margin of the ribbon. In this study, the CPOs are used to determine slip-systems activated during quartz deformation, deformation temperature through opening-angle (OA) thermometer (Kruhl, 1996; Law, 2014; Faleiros et al., 2016a) and vorticity (δ/β – method; Wallis, 1992, 1995). Data were further processed using MTEX (https://mtex-toolbox.github.io/) toolbox in MATLAB to quantify OA and the vorticity plane following (Hunter et al., 2018a)

In addition to FA analysis, we analyzed one mylonite sample (PS-41A) using electron backscattering diffraction (EBSD) technique to compare with the FA results to ensure CPO quality and proper quantification of the slip systems activation during deformation based on axis misorientations (Neumann, 2000; Wheeler et al., 2001). Measurements were made using a 15 kV acceleration voltage, 13.7 mm working distance and 70° sample tilt. Data were analyzed using CHANNEL5 producing 'one-pole-per-grain' pole figures of quartz and 'one-pole-per-grain' inverse pole figure.

### *A.1.4. Thermodynamic modelling*

In order to better assess deformation conditions, thermodynamic modelling using Perple_X'6.8.3 (Connolly, 2005) was carried out to calculate pressure (P) and temperature (T) pseudosections. Whole-rock bulk composition from three ultramylonites samples were analyzed by X-ray fluorescence using fused pellets (PANalytical, Zetium model) (Table 3). Phase relationships have been modelled with ten components ($Na_2O$-CaO-$K_2O$-FeO-MgO-$Al_2O_3$-$SiO_2$-$H_2O$-$TiO_2$-$O_2$ system) using the updated database version of Holland and Powell (2011), and its respectively solution models Gt(W), feldspar, Bi(W), Mica(W), Chl(W), St(W), Ep(HPM), Ilm(WPH) and melt(W), and compatible activity models (White et al., 2014) taking into consideration melting at high temperatures. Chemical compositions of minerals (Table 4) were measured with a Hence JOEL JXA-8530F microprobe operating at 15 kV, current analysis 20 nA, work distance of 11 mm. Whole-rock bulk composition and chemical composition analyses were carried out at University of São Paulo (Brazil).

**Table 3**
Bulk rock chemical composition from ultramylonites samples (oxides percentages).

| Bulk rock composition | | | |
|---|---|---|---|
| Wt% oxides | Samples | | |
| | PSB-10 | PSB-07A | PSB-07C |
| $SiO_2$ | 70.60 | 70.80 | 68.00 |
| $TiO_2$ | 0.41 | 0.29 | 0.52 |
| $Al_2O_3$ | 14.00 | 14.80 | 14.50 |
| $Fe_2O_3$ | 3.05 | 2.17 | 3.85 |
| MnO | BDL | BDL | 0.14 |
| MgO | 0.52 | 0.52 | 0.92 |
| CaO | 1.32 | 0.94 | 1.24 |
| $Na_2O$ | 3.24 | 3.67 | 3.60 |
| $K_2O$ | 4.61 | 4.74 | 4.38 |
| $P_2O_5$ | BDL | BDL | BDL |
| Total | 97.75 | 97.93 | 97.15 |

BDL: below detection level.

### *A.1.5. Vorticity analysis*

Vorticity analysis of naturally deformed rocks is an important measurement of non-coaxiality of deformation, essential to kinematic studies of shear zones. The kinematic vorticity number ($W_k$), or mean vorticity number ($W_m$; Passchier, 1988) ranges from 0 for strict pure shear to 1 for strict simple shear and can be quantified by several methods at the mesoscopic and microscopic scale (e.g., Passchier, 1987, 1988; Passchier and Urai, 1988; Simpson and De Paor, 1993; Wallis, 1995).

In this paper, the vorticity numbers were quantified using two methods: rigid porphyroclasts (RP) (Passchier, 1987; Wallis, 1995) and the $\delta/\beta$ methods (Wallis, 1995). For the RP method, feldspar porphyroclasts were manually digitized using *Adobe Illustrator®* with 150–200 grains per sample to ensure a sound statistical representation and analyzed using SPO2003 (Launeau and Robin, 2003a). This freeware calculates shape ratio and the angle between major axis and horizontal (x direction) for each porphyroclast to construct the Wallis' plot (Wallis, 1995). This chart establishes the values of shape ratio ($R_c$) below which the objects rotate continuously. This value is then used to calculate $W_m$ using eq. (A2) (Wallis et al., 1993).

$$W_m^{RP} = \frac{Rc^2 - 1}{Rc^2 + 1} \quad \text{(A2)}$$

The δ/β-method estimates the mean vorticity number (Wallis, 1995) through the relation between the maximum angle (δ) between oblique and main foliation in combination with the angle (β) between the shear plane and principal foliation determined through quartz [c] axis fabric (Xypolias,

**Table 4**
Chemical composition of plagioclase, K-feldspar, biotite and muscovite obtained from microprobe analyses.

| Chemical composition of minerals (oxide wt%) | | | | | | | | | |
|---|---|---|---|---|---|---|---|---|---|
| Sample | Oligoclase | | K-Feldspar | | Sample | Biotite | | Muscovite | |
| | PSB-10 | PS40-B | PSB-10 | PS40-B | | PSB-10 | PS40-B | PSB-10 | PS40-B |
| $SiO_2$ | 62.400 | 63.520 | 63.630 | 64.670 | SiO2 | 38.300 | 35.800 | 44.990 | 45.840 |
| $Al_2O_3$ | 23.490 | 23.100 | 18.780 | 18.720 | Al2O3 | 17.800 | 17.480 | 31.430 | 30.710 |
| FeO | 0.009 | 0.197 | 0.012 | 0.112 | FeO | 16.470 | 21.630 | 4.450 | 4.260 |
| MnO | 0.008 | 0.016 | 0.002 | 0.011 | MnO | 0.266 | 0.254 | 0.006 | 0.023 |
| $K_2O$ | 0.144 | 0.163 | 15.840 | 15.740 | ZnO | 0.168 | 0.084 | 0.038 | 0.014 |
| CaO | 4.420 | 3.870 | 0.001 | 0.004 | Cl | 0.099 | 0.023 | 0.009 | 0.011 |
| SrO | 0.069 | 0.109 | 0.105 | 0.098 | K2O | 9.930 | 9.990 | 11.210 | 11.010 |
| $TiO_2$ | 0.034 | 0.074 | 0.027 | 0.000 | CaO | 0.067 | 0.036 | 0.031 | 0.000 |
| BaO | 0.026 | 0.000 | 0.491 | 0.223 | TiO2 | 1.800 | 2.350 | 0.603 | 0.559 |
| $Na_2O$ | 8.930 | 9.170 | 0.495 | 0.417 | BaO | 0.047 | 0.094 | 0.122 | 0.145 |
| MgO | 0.000 | 0.000 | 0.000 | 0.003 | F | 0.308 | 0.328 | 0.102 | 0.138 |
| Total | 99.532 | 100.241 | 99.384 | 100.011 | Na2O | 0.093 | 0.035 | 0.231 | 0.166 |
| | | | | | MgO | 8.790 | 7.260 | 1.342 | 1.880 |
| | | | | | Total | 94.140 | 95.364 | 94.564 | 94.758 |
| Formula | 8O | 8O | 8O | 8O | Formula | 11O | 11O | 11O | 11O |
| Si | 2.775 | 2.803 | 2.972 | 2.989 | Si | 2.904 | 2.758 | 3.093 | 3.134 |
| Al | 1.231 | 1.201 | 1.034 | 1.020 | Al | 1.562 | 1.587 | 2.547 | 2.475 |
| $Fe^{2+}$ | 0.000 | 0.007 | 0.000 | 0.004 | $Fe^{2+}$ | 1.044 | 1.394 | 0.256 | 0.244 |
| Mn | 0.000 | 0.001 | 0.000 | 0.000 | Mn | 0.017 | 0.017 | 0.000 | 0.001 |
| K | 0.008 | 0.009 | 0.944 | 0.928 | Zn | 0.009 | 0.005 | 0.002 | 0.001 |
| Ca | 0.211 | 0.183 | 0.000 | 0.000 | K | 0.960 | 0.982 | 0.983 | 0.960 |
| Ti | 0.001 | 0.002 | 0.001 | 0.000 | Ca | 0.005 | 0.003 | 0.002 | 0.000 |
| Ba | 0.000 | 0.000 | 0.009 | 0.004 | Ti | 0.103 | 0.136 | 0.031 | 0.029 |
| Na | 0.770 | 0.785 | 0.045 | 0.037 | Ba | 0.001 | 0.003 | 0.003 | 0.004 |
| Mg | 0.000 | 0.000 | 0.000 | 0.000 | Na | 0.014 | 0.005 | 0.031 | 0.022 |
| #K molar | 0.008 | 0.009 | 0.000 | 0.000 | Mg | 0.993 | 0.834 | 0.138 | 0.192 |
| #Na molar | 0.778 | 0.803 | 0.045 | 0.039 | | | | | |
| #Ca molar | 0.213 | 0.187 | 0.955 | 0.961 | | | | | |

**Table 5**
Quartz paleopiezometry and strain rate based on Stipp and Tullis (2003) calibration and parameters from Hirth et al. (2001), respectively.

| Samples | Number of grains | Feret diameter (μm) | Piezometry (Stipp and Tullis, 2003) | Error | Strain rate (Hirth et al., 2001) | | |
|---|---|---|---|---|---|---|---|
| | | Mean | MPa | ± | Main ($s^{-1}$) | Min ($s^{-1}$) | Max ($s^{-1}$) |
| PS-40A | 301 | 52.46 | 28.44 | 4.22 | 8.82E-13 | 4.88E-13 | 1.59E-12 |
| PS-40D | 244 | 62.79 | 25.03 | 4.02 | 5.29E-13 | 9.50E-13 | 2.58E-13 |
| PS-41A | 258 | 46.73 | 31.65 | 4.33 | 1.35E-12 | 7.34E-13 | 2.22E-13 |
| PS-41C | 251 | 66.40 | 23.95 | 3.96 | 4.44E-13 | 8.09E-13 | 2.12E-13 |
| PSB-05B | 309 | 52.35 | 28.49 | 4.23 | 9.44E-13 | 4.92E-13 | 1.60E-12 |
| PSB-06 | 299 | 42.12 | 34.37 | 4.42 | 1.88E-12 | 1.06E-12 | 3.00E-12 |
| PSB-08 | 232 | 57.54 | 26.83 | 4.13 | 7.02E-13 | 3.51E-13 | 1.22E-12 |
| PSB-09 | 271 | 50.17 | 29.91 | 4.27 | 1.08E-12 | 5.71E-13 | 1.81E-12 |

**Table 6**
Vorticity results calculated using rigid porphyroclast ($W_m^{RP}$) and δ/β ($W_m^{\delta/\beta}$) methods.

| Sample | | Rigid porphyroclast method | | | | δ/β method | | |
|---|---|---|---|---|---|---|---|---|
| | | $R_c$ min | $R_c$ max | $W_m^{RP}$ min | $W_m^{RP}$ max | δ(°) | β(°) | $W_m^{\delta/\beta}$ |
| NE sector | PS-40A | – | – | – | – | 20 | 10 | 0.86 |
| | PS-40B | 2.0 | 2.3 | 0.60 | 0.68 | – | 7 | – |
| | PS-40D | – | – | – | – | 19 | 10 | 0.85 |
| | PS-41A | 1.8 | 2.4 | 0.53 | 0.70 | 13 | 1 | 0.40 |
| | PS-41B | 1.9 | 2.3 | 0.56 | 0.68 | – | 11 | – |
| | PS-41C | 1.7 | 2.1 | 0.48 | 0.63 | 13 | 7 | 0.64 |
| | PS-42A | – | – | – | – | – | 5 | – |
| | PS-42B | 1.8 | 2.2 | 0.52 | 0.65 | – | 14 | – |
| Central sector | PS-55 | 1.7 | 2.3 | 0.48 | 0.68 | – | 29 | – |
| | PSB-05B | – | – | – | – | 16 | 28 | 0.99 |
| | PSB-06 | – | – | – | – | 20 | 10 | 0.87 |
| | PSB-08 | 1.6 | 2.3 | 0.43 | 0.68 | 9 | 5 | 0.47 |
| | PSB-09 | 1.65 | 2.1 | 0.46 | 0.63 | 1 | 6 | 0.24 |

**Table 7**
Three-dimensional finite strain quantification based on two-dimensional analyses using the inertia tensor method (Launeau and Cruden, 1998) and three-dimensional analyses using the technique of Launeau and Robin (2005).

| Sample | XY Plane | Axes values | | | Axes Attitudes | | | X/Z | X/Y | Y/Z | k | $(F)^{1/2}$ (%) | Ellipsoid |
|---|---|---|---|---|---|---|---|---|---|---|---|---|---|
| | | X | Y | Z | X | Y | Z | | | | | | |
| PS41A | 243/86 | 0.643 | 0.838 | 1.487 | 061/37 | 248/53 | 153/4 | 1.520 | 1.142 | 1.332 | 0.428 | 4.8 | Oblate |
| PS42B | 046/71 | 0.703 | 0.757 | 1.502 | 169/67 | 050/11 | 316/19 | 1.462 | 1.038 | 1.408 | 0.093 | 3.8 | Oblate |
| PSB08 | 062/81 | 0.375 | 0.778 | 1.742 | 238/24 | 080/64 | 332/09 | 2.156 | 1.44 | 1.497 | 0.885 | 3.0 | Oblate |
| PSB09 | 070/56 | 1.324 | 0.939 | 0.804 | 228/29 | 108/43 | 340/34 | 1.646 | 1.409 | 1.168 | 2.435 | 5.8 | Prolate |

2010) according to the eq. (A3) (Wallis, 1995).

$$W_m^{\delta/\beta} = \sin 2(\delta + \beta) \quad \text{(A3)}$$

The measurements of β angles were carried out using the MTEX code developed in MATLAB environment (Hunter et al., 2018a) which estimate the vorticity plane based on the difference between the foliation plane (*E*-W) and the plane perpendicular to the orientation defined by the c-axis maxima. This process enables estimation of vorticity plane (β) even without data in the centre of the girdle. The angle δ between oblique and main mylonitic foliation, on the other hand, were carried out through petrographic and grain statistical analysis.

*A.1.6. Finite strain quantification*

Three-dimensional finite strain quantification was performed on four oriented samples of mylonites, two from each sector, on three mutually perpendicular and oriented sections of each sample. Afterwards, we traced the boundaries of feldspar porphyroclasts from samples photographs using *Adobe Illustrator*™ software and then converted into raster images (*bitmap*). The inertia tensor technique (Launeau and Cruden, 1998) was applied to measure the dimensions and orientations of long and short axes (i.e., shape ratio) of individual feldspars grains using the SPO freeware (Launeau and Robin, 2003a) following a similar process of vorticity analysis based on rigid porphyroclasts method. Each two-dimensional section was subdivided into two or four subsections for each sample. Three-dimensional analyses were performed using the ELLIPSOID freeware (Launeau and Robin, 2003b, 2005). The parameter $(F)^{1/2}$ (incompatibility index, in %) converge to an ellipsoid for $(F)^{1/2} < 10\%$ and better fits come with lower values of $(F)^{1/2}$ (Launeau and Robin, 2005) being very meaningful to ensure good results.

## References


Almeida, F.F.M., Amaral, G., Cordani, U., Kawashita, K., 1973. The Precambrian evolution of the South American Cratonic Margin, South of Amazon River. In: The Ocean Basin and Margins. Plenum, New York, pp. 411–416.

Alves, A., de A. Janasi, V., da C. Campos Neto, M., Heaman, L., Simonetti, A., 2013. U-Pb geochronology of the granite magmatism in the embu terrane: Implications for the evolution of the central ribeira belt, SE Brazil. Precambrian Res. 230, 1–12. https://doi.org/10.1016/j.precamres.2013.01.018.

Bas den Brok, S.W.J., 1998. Effect of microcracking on pressure-solution strain rate: the Gratz grain-boundary model. Geology 26, 915–918.

Bento dos Santos, T.M., Munhá, J.M., Tassinari, C.C.G., Fonseca, P.E., Dias Neto, C., 2010. Thermochronology of central Ribeira Fold Belt, SE Brazil: Petrological and geochronological evidence for long-term high temperature maintenance during Western Gondwana amalgamation. Precambrian Res. 180, 285–298. https://doi.org/10.1016/j.precamres.2010.05.002.

Bento dos Santos, T.M., Munhá, J.M., Tassinari, C.C.G., Fonseca, P.E., Neto, C.D., 2011. Metamorphic P-T evolution of granulites in the Central Ribeira Fold Belt, SE Brazil. Geosci. J. 15, 27–51. https://doi.org/10.1007/s12303-011-0004-1.

Bento dos Santos, T.M., Tassinari, C.C.G., Fonseca, P.E., 2014. Garnet-biotite diffusion mechanisms in complex high-grade orogenic belts: Understanding and constraining petrological cooling rates in granulites from Ribeira Fold Belt (SE Brazil). J. S. Am. Earth Sci. 56, 128–138. https://doi.org/10.1016/j.jsames.2014.09.003.

Bento dos Santos, T.M., Tassinari, C.C.G., Fonseca, P.E., 2015. Diachronic collision, slab break-off and long-term high thermal flux in the Brasiliano-Pan-African orogeny: Implications for the geodynamic evolution of the Mantiqueira Province. Precambrian Res. 260, 1–22. https://doi.org/10.1016/j.precamres.2014.12.018.

Campanha, G.A.C., 2002. O papel do sistema de zonas de cisalhamento transcorrentes na configuracao da porcao meridional da faixa Ribeira. Institute of Geoscience-University of São Paulohttps://doi.org/10.1073/pnas.0703993104.

Campanha, G.A.C., Brito Neves, B.B., 2004. Frontal and oblique tectonics in the Brazilian Shield. Episodes 27, 255–259. https://doi.org/10.1016/S1342-937X(05)70391-9.

Campanha, G.A.C., Sadowski, G.R., 1999. Tectonics of the southern portion of the Ribeira Belt (Apiaí Domain). Precambrian Res. 98, 31–51. https://doi.org/10.1016/S0301-9268(99)00027-3.

Campanha, G.A.C., Sadowski, G.R., 2002. Determinações da deformação finita em rochas metassedimentares da Faixa Ribeira na região de Iporanga e Apiaí, SP. Revista Brasileira de Geociências 32, 107–118.

Campanha, G.A.C., Faleiros, F.M., Basei, M.A.S., Tassinari, C.C.G., Nutman, A.P., Vasconcelos, P.M., 2015. Geochemistry and age of mafic rocks from the Votuverava Group, southern Ribeira Belt, Brazil: evidence for 1490Ma oceanic back-arc magmatism. Precambrian Res. 266, 530–550. https://doi.org/10.1016/j.precamres.2015.05.026.

Campanha, G.A.C., Basei, M.S., Faleiros, F.M., Nutman, A.P., 2016. The Mesoproterozoic to early Neoproterozoic passive margin Lajeado Group and Apiaí Gabbro, Southeastern Brazil. Geosci. Front. 7, 683–694. https://doi.org/10.1016/j.gsf.2015.08.004.

Campanha, G.A.C., Faleiros, F.M., Cawood, P.A., Cabrita, D.I.G., Ribeiro, B.V., Basei, M.A.S., 2019. The Tonian Embu complex in the Ribeira Belt (Brazil): revision, depositional age and setting in Rodinia and West Gondwana. Precambrian Res. 320, 31–45. https://doi.org/10.1016/j.precamres.2018.10.010.

Campos Neto, M.C., 2000. Orogenic system from southwestern Gondwana: an approach to Brasilian-pan African cycle and orogenic collage in southeastern Brazil. In: Tectonic Evolution of South America, pp. 335–365.

Cavalcante, C., Lagoeiro, L., Fossen, H., Egydio-silva, M., Morales, F.G., Ferreira, F., Conte, T., 2018. Temperature constraints on microfabric patterns in quartzofeldsphatic mylonites, Ribeira belt (SE Brazil). J. Struct. Geol. https://doi.org/10.1016/j.jsg.2018.07.013.

Connolly, J.A., 2005. Computation of phase equilibria by linear programming: a tool for geodynamic modeling and its application to subduction zone decarbonation. Earth Planet. Sci. Lett. 326, 524–541.

Dayan, H., Keller, V.A., 1990. A zona de cisalhamento do rio Paraíba do Sul nas vizinhanças de Três Rios (RJ): uma análise da deformação dada por algumas feições estruturais. Revista Brasileira de Geociências 19, 494–506.

Dehler, N.M., Machado, R., Fassbinder, E., 2007. Shear structures in the Serra do Azeite shear zone, southeastern Brazil: Transtensional deformation during regional transpression in the Central Mantiqueira province (Ribeira belt). J. S. Am. Earth Sci. 23, 176–192. https://doi.org/10.1016/j.jsames.2006.09.017.

Dell'angelo, L.N., Tullis, J., 1989. Fabric development in experimentally sheared quartzites. Tectonophysics 169, 1–21. https://doi.org/10.1016/0040-1951(89)90180-7.

Dewey, J.F., Holdsworth, R.E., Strachan, R.A., 1998. Transpression and transtension zones. In: Holdsworth, R.E., Strachan, R.A., Dewey, J.E. (Eds.), Continental Transpressional and Transtensional Tectonic, pp. 1–14.

Drury, M.R., Urai, J.L., 1990. Deformation-related recrystallization processes. Tectonophysics 112, 235–253.

Dunlap, W.J., 1997. Neocrystallization or cooling? 40Ar/39Ar ages of white micas from low-grade mylonites. Chem. Geol. 143, 181–203. https://doi.org/10.1016/S0009-2541(97)00113-7.

Ebert, H.D., Hasui, Y., 1992. Transpressive evolution of a collisional suture zone in SE-Brazil. In: 29th International Geological Congress.

Ebert, H.D., Hasui, Y., 1998. Transpressional tectonics and strain partitioning during oblique. 1998 In: Holdsworth, R.E., Strachan, R.A., Dewey, J.E. (Eds.), Continental Transpressional and Transtensional Tectonics, pp. 231–252.

Ebert, H.D., Chemale, F., Babinski, M., Van Schmus, W.R., 1996. Tectonic setting and U/Pb zircon dating of the plutonic Socorro Complex in the Transpressive. Tectonics 15, 688–699.

Egydio-Silva, M., Vauchez, A., Bascou, J., Hippertt, J., 2002. High-temperature deformation in the Neoproterozoic transpressional Ribeira belt, Southeast Brazil. Tectonophysics 352, 203–224. https://doi.org/10.1016/S0040-1951(02)00197-X.

Egydio-Silva, M., Vauchez, A., Raposo, M.I.B., Bascou, J., Uhlein, A., 2005. Deformation regime variations in an arcuate transpressional orogen (Ribeira belt, SE Brazil) imaged by anisotropy of magnetic susceptibility in granulites. J. Struct. Geol. 27, 1750–1764. https://doi.org/10.1016/j.jsg.2005.06.001.

Egydio-Silva, M., Vauchez, A., Fossen, H., Gonçalves Cavalcante, G.C., Xavier, B.C., 2018. Connecting the Araçuaí and Ribeira belts (SE – Brazil): progressive transition from contractional to transpressive strain regime during the Brasiliano orogeny. J. S. Am. Earth Sci. 86, 127–139. https://doi.org/10.1016/j.jsames.2018.06.005.

Faleiros, F.M., 2003. Zona de cisalhamento Ribeira: deformação, metamorfismo e termobarometria de veios sin-tectônicos. In: Master's Thesis. University of São Paulo.

Faleiros, F.M., Campanha, G.A.C., Maria, R., Fuzikawa, K., 2010. Quartz recrystallization regimes, c-axis texture transitions and fluid inclusion reequilibration in a prograde greenschist to amphibolite facies mylonite zone (Ribeira Shear Zone, SE Brazil). Tectonophysics 485, 193–214. https://doi.org/10.1016/j.tecto.2009.12.014.

Faleiros, F.M., Campanha, G.A.C., Martins, L., Vlach, S.R.F., Vasconcelos, P.M., 2011. Ediacaran high-pressure collision metamorphism and tectonics of the southern Ribeira Belt (SE Brazil): evidence for terrane accretion and dispersion during Gondwana assembly. Precambrian Res. 189, 263–291.

Faleiros, F.M., Campanha, G.A.C., Pavan, M., Almeida, V.V., Rodrigues, S.W.O., Araújo, B.P., 2016a. Short-lived polyphase deformation during crustal thickening and exhumation of a collisional orogen (Ribeira Belt, Brazil). J. Struct. Geol. 93, 106–130. https://doi.org/10.1016/j.jsg.2016.10.006.

Faleiros, F.M., Moraes, R., Pavan, M., Campanha, G.A.C., 2016b. A new empirical calibration of the quartz c-axis fabric opening-angle deformation thermometer. Tectonophysics 671, 173–182. https://doi.org/10.1016/j.tecto.2016.01.014.

Farver, J., Yund, R.A., 2000. Silicon diffusion in a natural quartz aggregate: constraints on solution-transfer diffusion creep. Tectonophysics 325, 193–205.

Fossen, H., Cavalcante, G.C.G., 2017. Shear zones – a review. Earth Sci. Rev. 171, 434–455. https://doi.org/10.1016/j.earscirev.2017.05.002.

Fossen, H., Tikoff, B., 1993. The deformation matrix for simultaneous pure shear, simple shear, and volume change, and its application to tranpression/transtension tectonics. J. Struct. Geol. 15, 413–425.

Fossen, H., Tikoff, B., Teyssier, C., 1994. Strain modeling of transpressional and transtensional deformation. Nor. Geol. Tidsskr. 74, 134–145.

Goscombe, B.D., Gray, D.R., 2008. Structure and strain variation at mid-crustal levels in a transpressional orogen : a review of Kaoko Belt structure and the character of West Gondwana amalgamation and dispersal. Gondwana Res. 13, 45–85. https://doi.org/10.1016/j.gr.2007.07.002.

Goscombe, B., Hand, M., Gray, D., 2003. Structure of the Kaoko Belt, Namibia : progressive evolution of a classic transpressional orogen. J. Struct. Geol. 25, 1049–1081.

Gray, D.R., Foster, D.A., Goscombe, B., Passchier, C.W., Trouw, R.A.J., 2006. 40Ar/39Ar thermochronology of the Pan-African Damara Orogen, Namibia, with implications for tectonothermal and geodynamic evolution. Precambrian Res. 150, 49–72. https://doi.org/10.1016/j.precamres.2006.07.003.

Hackspacher, P.C., Godoy, A.M., 1998. Vertical displacement during post-collisional escape tectonism (Brasiliano Orogeny) of the Ribeira Belt, Sao Paulo, Brazil. Journal of African Earth Sciences 27, 99–100.

Hasui, Y., 1973. Tectônica da área das folhas de São Roque e Pilar do Sul. In: PhD Thesis-University of São Paulo.

Hasui, Y., 1975. Geologia da folha de são Roque. In: Boletim IG. 6. Instituto de Geociências, USP, pp. 157–183. https://doi.org/10.2307/1134315.

Hasui, Y., Sadowski, G.R., 1976. Evolução geológica do Pré-Cambriano na região sudeste do Estado de São Paulo. Revista Brasileira de Geociências 6, 182–200.

Hasui, Y., Carneiro, C.R., Coimbra, A.M., 1975. The Ribeira folded belt. Revista Brasileira de Geociências 5, 257–266.

Heilbron, M., Pedrosa-Soares, A.C., Campos Neto, M.D.C., Silva, L.D., Trouw, R.A.J., Janasi, V.D.A., 2004. Província Mantiqueira. Geologia Do Continente Sul-Americano: Evolução Da Obra Ed Fernando Flávio Marques de Almeida. pp. 203–235.

Heilbronner, R., Tullis, J., 2002. The effect of static annealing on microstructures and crystallographic preferred orientations of quartzites experimentally deformed in axial compression and shear. Geol. Soc. Lond., Spec. Publ. 200, 191–218. https://doi.org/10.1144/GSL.SP.2001.200.01.12.

Hennies, W.T., Hasui, Y., Penalva, F., 1967. O falhamento transcorrente de Taxaquara. 21 Congresso Brasileiro de Geologia.

Henrique-Pinto, R., Janasi, V., Vasconcellos, A.C.B.C., Sawyer, E.W., Barnes, S.J., Basei, M.A.S., Tassinari, C.C.G., 2015. Zircon provenance in meta-sandstones of the São Roque Domain: Implications for the Proterozoic evolution of the Ribeira Belt, SE Brazil. Precambrian Res. 256, 271–288.

Henrique-Pinto, R., Janasi, V.D.A., da C. Campanha, G.A., 2018. U-Pb dating, Lu-Hf isotope systematics and chemistry of zircon from the Morro do Polvilho meta-trachydacite: constraints on sources of magmatism and on the depositional age of the São Roque Group. Geologia USP. Série Científica 18, 45–56. https://doi.org/10.11606/issn.2316-9095.v18-125793.

Hirth, G., Tullis, J., 1992. Dislocation creep regimes in quartz aggregates. J. Struct. Geol. 14, 145–159. https://doi.org/10.1016/0191-8141(92)90053-Y.

Hirth, G., Teyssier, C., Dunlap, W.J., 2001. An evaluation of quartzite flow laws based on comparisons between experimentally and naturally deformed rocks. Int. J. Earth Sci. 90, 77–87. https://doi.org/10.1007/s005310000152.

Hoisch, T.D., 1989. A muscovite-biotite geothermometer. Am. Mineral. 74, 565–572.

Holland, T.J.B., Powell, R., 2011. An improved and extended internally consistent thermodynamic dataset for phases of petrological interest, involving a new equation of state for solids. J. Metamorph. Geol. 29, 333–383.

Hunter, N.J.R., Hasalová, P., Weinberg, R.F., Wilson, C.J.L., 2016. Fabric controls on strain accommodation in naturally deformed mylonites: the influence of interconnected micaceous layers. J. Struct. Geol. 83, 180–193. https://doi.org/10.1016/j.jsg.2015.12.005.
Hunter, N.J.R., Weinberg, R.F., Wilson, C.J.L., Law, R.D., 2018a. A new technique for quantifying symmetry and opening angles in quartz c-axis pole Fig.S: Implications for interpreting the kinematic and thermal properties of rocks. J. Struct. Geol. 112, 1–6. https://doi.org/10.1016/J.JSG.2018.04.006.
Hunter, N.J.R., Weinberg, R.F., Wilson, C.J.L., Luzin, V., Misra, S., 2018b. Microscopic anatomy of 'hot-on-cold ' shear zones: insights from quartzites of the Main Central Thrust in the Alaknanda region (Garhwal Himalaya). Geological Society of American Bulletin 367.
Janasi, V.A., Leite, R.J., Van Schmus, W.R., 2001. U-Pb chronostratigraphy of the granitic magmatism in the Agudos Grandes Batholith (West of São Paulo, Brazil) - Implications for the evolution of the Ribeira Belt. J. S. Am. Earth Sci. 14, 363–376. https://doi.org/10.1016/S0895-9811(01)00034-7.
Jelinek, V., 1981. Characterization of the magnetic fabric of rocks. Tectonophysics 79, 63–67. https://doi.org/10.1016/0040-1951(81)90110-4.
Jessell, M.W., 1987. Grain-boundary migration microstructures in a naturally deformed quartzite. J. Struct. Geol. 9, 1007–1014.
Kilian, R., Heilbronner, R., Stünitz, H., 2011. Quartz grain size reduction in a granitoid rock and the transition from dislocation to diffusion creep. J. Struct. Geol. 33, 1265–1284. https://doi.org/10.1016/j.jsg.2011.05.004.
Kruhl, J.H., 1996. Prism- and basal-plane parallel subgrain boundaries in quartz: a microstructural geothermobaromether. J. Metamorph. Geol. 14, 581–589. https://doi.org/10.1046/j.1525-1314.1996.00413.x.
Launeau, P., Cruden, A.R., 1998. Magmatic fabric acquisition mechanisms in a syenite: results of a combined anisotropy of magnetic susceptibility and image analysis study. Journal of Geophysical Research: Solid Earth 103, 5067–5089. https://doi.org/10.1029/97JB02670.
Launeau, P., Robin, P.Y.F., 2003a. SPO.
Launeau, P., Robin, P.Y.F., 2003b. Ellipsoid v. 2003.
Launeau, P., Robin, P.Y.F., 2005. Determination of fabric and strain ellipsoids from measured sectional ellipses - Implementation and applications. J. Struct. Geol. 27, 2223–2233. https://doi.org/10.1016/j.jsg.2005.08.003.
Law, R.D., 2014. Deformation thermometry based on quartz c-axis fabrics and recrystallization microstructures: a review. J. Struct. Geol. 66, 129–161. https://doi.org/10.1016/j.jsg.2014.05.023.
Law, R.D., Searle, M.P., Simpson, R.L., 2004. Strain, deformation temperatures and vorticity of flow at the top of the Greater Himalayan Slab, Everest Massif, Tibet. J. Geol. Soc. 161, 305–320. https://doi.org/10.1144/0016-764903-047.
Leite, R.J., Heaman, L.M., de Assis Janasi, V., Martins, L., Creaser, R.A., 2007. The late- to postorogenic transition in the Neoproterozoic Agudos Grandes Granite Batholith (Apiaí Domain, SE Brazil): Constraints from geology, mineralogy, and U-Pb geochronology. J. S. Am. Earth Sci. 23, 193–212. https://doi.org/10.1016/j.jsames.2006.09.022.
Lexa, O., 2003. Numerical Approaches in Structural and Microstructural Analyses. Charles University, Prague.
Lister, G.S., 1977. Discussion: Crossed-girdle c-axis fabrics in quartzites plastically deformed by plane strain and progressive simple shear. Tectonophysics 39, 51–54. https://doi.org/10.1016/0040-1951(77)90087-7.
Lister, G.S., Hobbs, B.E., 1980. The simulation of fabric development during plastic deformation and its application to quartzite: the influence of deformation history. J. Struct. Geol. 2, 355–370. https://doi.org/10.1016/0191-8141(80)90023-1.
Menegon, L., Pennacchioni, G., Spiess, R., 2008. Dissolution-precipitation creep of K-feldspar in mid-crustal granite mylonites. J. Struct. Geol. 30, 565–579. https://doi.org/10.1016/j.jsg.2008.02.001.
Morgan, S.S., Law, R.D., 2004. Unusual transition in quartzite dislocation creep regimes and crystal slip systems in the aureole of the Eureka Valley–Joshua Flat–Beer Creek pluton, California: a case for anhydrous conditions created by decarbonation reactions. Tectonophysics 384, 209–231. https://doi.org/10.1016/j.tecto.2004.03.016.
Neumann, B., 2000. Texture development of recrystallised quartz polycrystals unravelled by orientation and misorientation characteristics. J. Struct. Geol. 22, 1695–1711. https://doi.org/10.1016/S0191-8141(00)00060-2.
Ngako, V., Affaton, P., 2003. Pan-African tectonic evolution in central and southern Cameroon: transpression and transtension during sinistral shear movements. J. Afr. Earth Sci. 36, 207–214. https://doi.org/10.1016/S0899-5362(03)00023-X.
Ngako, V., Affaton, P., Njonfang, E., 2008. Pan-African tectonics in northwestern Cameroon: Implication for the history of western Gondwana. Gondwana Res. 14, 509–522. https://doi.org/10.1016/j.gr.2008.02.002.
Oliot, E., Goncalves, P., Schulmann, K., Marquer, D., Lexa, O., 2014. Mid-crustal shear zone formation in granitic rocks: Constraints from quantitative textural and crystallographic preferred orientations analyses. Tectonophysics 612–613, 63–80. https://doi.org/10.1016/j.tecto.2013.11.032.
Ord, A., Hobbs, B.E., 1989. The strength of the continental crust, detachment zones and the development of plastic instabilities. Tectonophysics 158, 269–289. https://doi.org/10.1016/0040-1951(89)90328-4.
Passarelli, C.R., 2001. Caracterização estrutural e geocronológica dos domínios tectônicos da porção sul-oriental do Estado de São Paulo. In: Ph.D. Thesis. University of São Paulo.
Passarelli, C.R., Basei, M.A.S., Wemmer, K., Siga, O., Oyhantçabal, P., 2011. Major shear zones of southern Brazil and Uruguay: Escape tectonics in the eastern border of Rio de La plata and Paranapanema cratons during the Western Gondwana amalgamation. Int. J. Earth Sci. 100, 391–414. https://doi.org/10.1007/s00531-010-0594-2.
Passchier, C.W., 1987. Stable positions of rigid objects in non-coaxial flow-a study in vorticity analysis. J. Struct. Geol. 9, 679–690. https://doi.org/10.1016/0191-8141(87)90152-0.
Passchier, C.W., 1988. The use of Mohr circles to describe non-coaxial progressive deformation. Tectonophysics 149, 323–338. https://doi.org/10.1016/0040-1951(88)90181-3.
Passchier, C.W., Trouw, R.A.J., 2005. Microtectonics, 2nd ed. Springer, Boston, Mass.
Passchier, C.W., Urai, J.L., 1988. Vorticity and strain analysis using Mohr diagrams. J. Struct. Geol. 10, 755–763. https://doi.org/10.1016/0191-8141(88)90082-X.
Pires, F.A., Fernandes, A.J., Teixeira, A.L, Boggiani, P.C., Massoli, M., Petri, S., 1989. Mapeamento geológico da folha de Salto de Pirapora - SP, escala 1:50.000. Relatório Técnico do Instituto Geológico, São Paulo, pp. 88p.
Pitzer, K., Sterner, S., 1994. Equations of state valid continuously from zero to extreme pressures for $H_2O$ and $CO_2$. J. Chem. Phys. 101, 3111–3116.
Platt, J.P., 2015. Rheology of two-phase systems: a microphysical and observational approach. J. Struct. Geol. 77, 213–227. https://doi.org/10.1016/j.jsg.2015.05.003.
Post, A., Tullis, J., 1999. A recrystallized grain size piezometer for experimentally deformed feldspar aggregates. Tectonophysics 303, 159–173. https://doi.org/10.1016/S0040-1951(98)00260-1.
Prior, D.J., Wheeler, J., 1999. Feldspar fabrics in a greenschist facies albite-rich mylonite from electron backscatter diffraction. Tectonophysics 303, 29–49. https://doi.org/10.1016/S0040-1951(98)00257-1.
Pryer, L.L., 1993. Microstructures in feldspar from a major crustal thrust zone: the Grenville Front, Ontario, Canada. J. Struct. Geol. 15, 21–36.
Ramsay, J.G., Huber, M.I., 1983. The Techniques of Modern Structural Analysis, v. 1: Strain Analysis. Academic Press, London.
Robin, P.Y.F., Cruden, A.R., 1994. Strain and vorticity patterns in ideally ductile transpression zones. J. Struct. Geol. 16, 447–466. https://doi.org/10.1016/0191-8141(94)90090-6.
Sanderson, D.J., Marchini, W.R.D., 1984. Transpression. J. Struct. Geol. 6, 449–458.
Scandale, E., Gandais, M., Willaime, C., 1983. Transmission electron microscopic study of experimentally deformed K-feldspar single crystal. The (010) [001], (001) 1/2[110], (110) 1/2[112] and (111) 1/2[110] slip systems. Phys. Chem. Miner. 9, 182–187.
Schmid, S.M., Casey, M., 1986. Complete fabric analysis of some commonly observed quartz c-axis patterns. In: Mineral and rock deformation: Laboratory studies. 36. pp. 263–286.
Sibson, R.H., 1977. Fault rocks and fault mechanisms. J. Geol. Soc. 133 (3), 191–213. https://doi.org/10.1144/gsjgs.133.3.0191.
Simpson, C., De Paor, D.G., 1993. Strain and kinematic analysis in general shear zones. J. Struct. Geol. 15, 1–20.
Stahr, D.W., Law, R.D., 2011. Effect of finite strain on clast-based vorticity gauges. J. Struct. Geol. 33, 1178–1192. https://doi.org/10.1016/j.jsg.2011.05.002.
Stahr, D.W., Law, R.D., 2014. Strain memory of 2D and 3D rigid inclusion populations in viscous flows — what is clast SPO telling us? J. Struct. Geol. 68, 347–363. https://doi.org/10.1016/j.jsg.2014.05.028.
Stein, D.P., Campanha, G.A.C., Fernandes, L.A., 1989. Mapeamento geológico da folha Pilar do Sul - SP, escala 1:50.000 (Programa de Desenvolvimento de Recursos Minerais. Instituto de Pesquisas Tecnológicas do Estado de São Paulo.
Stipp, M., Tullis, J., 2003. The recrystallized grain size piezometer for quartz. Geophys. Res. Lett. 30, 2088. https://doi.org/10.1002/2017GL073836.
Stipp, M., Stünitz, H., Heilbronner, R., Schmid, S.M., 2002a. The eastern Tonale fault zone: a "natural laboratory" for crystal plastic deformation of quartz over a temperature range from 250 to 700 °C. J. Struct. Geol. 24, 1861–1884. https://doi.org/10.1016/S0191-8141(02)00035-4.
Stipp, M., Stünitz, H., Heilbronner, R., Schmid, S.M., 2002b. Dynamic recrystallization of quartz: correlation between natural and experimental conditions. Geol. Soc. Lond., Spec. Publ. 200, 171–190. https://doi.org/10.1144/GSL.SP.2001.200.01.11.
Stipp, M., Tullis, J., Scherwath, M., Behrmann, J.H., 2010. A new perspective on paleopiezometry: Dynamically recrystallized grain size distributions indicate mechanism changes. Geology 38, 759–762.
Stünitz, H., Fitz Gerald, J.D., 1993. Deformation of granitoids at low metamorphic grades: II. Granular flow in albite rich mylonites. Tectonophysics 221, 299–324.
Tassinari, C.C.G., Munha, J.M.U., Neto, D., Bento dos Santos, T.M., Cordani, U.G., Nutman, A., Fonseca, P.E., 2006. Constrains on the Termochronological Evolution of Ribeira Fold Belt, Se Brasil: evidence for Long-Term Elevated Geothermal Gradient of Neoproterozoic Orogenies. V South American Symposium on Isotope Geology. Punta Del Este. 200–203.
Tikoff, B., Greene, D., 1997. Stretching lineations in transpressional shear zones: an example from the Sierra Nevada Batholith, California. J. Struct. Geol. 19, 29–39. https://doi.org/10.1016/S0191-8141(96)00056-9.
Tikoff, B., Teyssier, C., 1994. Strain modelling of displacement-field partitioning in transpressional orogens. J. Struct. Geol. 16, 1575–1588.
Trouw, R.A., Passchier, C.W., Wiersma, D.J., 2009. Atlas of Mylonites-and related microstructures. Springer Science & Business Media.
Tullis, J., Yund, R.A., 1977. Experimental deformation of dry Westerly granite. J. Geophys. Res. 82, 5705–5718.
Tullis, J., Yund, R.A., 1985. Dynamic recrystallization of feldspar: a mechanism for ductile shear zone formation. Geology 13, 238–241.
Urai, J.L., Means, W.D., Lister, G.S., 1986. Dynamic recrystallization of minerals. Mineral and rock deformation: laboratory studies: The Paterson volume. Mineral and Rock Deformation: Laboratory Studies: The Paterson Volume. pp. 161–199.
Vauchez, A., 1987. The development of discrete shear-zones in a granite: stress, strain and changes in deformation mechanisms. Tectonophysics 133, 137–156. https://doi.org/10.1016/0040-1951(87)90286-1.
Vauchez, A., Tommasi, A., Egydio-Silva, M., 1994. Self-identation of a heterogeneous continental lithosphere. Geology 22, 967–970. https://doi.org/10.1130/0091-7613(1994)022<0967:SIOAHC>2.3.CO;2.
Viegas, G., Menegon, L., Archanjo, C., 2016. Brittle grain-size reduction of feldspar, phase

mixing and strain localization in granitoids at mid-crustal conditions (Pernambuco shear zone, NE Brazil). Solid Earth 7, 375–396. https://doi.org/10.5194/se-7-375-2016.

Wallis, S.R., 1992. Vorticity analysis in a metachert from the Sanbagawa Belt, SW Japan. J. Struct. Geol. 14, 271–280. https://doi.org/10.1016/0191-8141(92)90085-B.

Wallis, S.R., 1995. Vorticity analysis and recognition of ductile extension in the Sanbagawa belt, SW Japan. Journal of Structural Geology 17, 1077–1093.

Wallis, S.R., Platt, J.P., Knott, S.D., 1993. Recognition of syn-convergence extension in accretionary wedges with examples from the Calabrian Arc and the eastern Alps. Am. J. Sci. https://doi.org/10.2475/ajs.293.5.463.

Wheeler, J., Prior, D., Jiang, Z., Spiess, R., Trimby, P., 2001. The petrological significance of misorientations between grains. Contrib. Mineral. Petrol. 141, 109–124. https://doi.org/10.1007/s004100000225.

White, R.W., Powell, R., Holland, T.J.B., 2001. Calculation of partial melting equilibria in the system Na2O-CaO-K2O-FeO-MgO-Al2O3-SiO2-H2O (NCKFMASH). J. Metamorph. Geol. 19, 139–153. https://doi.org/10.1046/j.0263-4929.2000.00303.x.

White, R.W., Powell, R., Johnson, T.E., 2014. The effect of Mn on mineral stability in metapelites revisited: new a–x relations for manganese-bearing minerals. J. Metamorph. Geol. 32, 809–828.

Wilson, C.J.L., Russell-Head, D.S., Kunze, K., Viola, G., 2007. The analysis of quartz c-axis fabrics using a modified optical microscope. J. Microsc. 227, 30–41. https://doi.org/10.1111/j.1365-2818.2007.01784.x.

Xypolias, P., 2010. Vorticity analysis in shear zones: a review of methods and applications. J. Struct. Geol. 32, 2072–2092. https://doi.org/10.1016/j.jsg.2010.08.009.

# 4 CHAPTER 4

## THE MISSING LINK IN DATING MID-CRUSTAL SHEAR ZONES: INSIGHTS FROM APATITE U-Pb DATING AND TECTONIC IMPLICATIONS FOR THE NEOPROTEROZOIC RIBEIRA BELT EVOLUTION


### Abstract

Attempting to constrain the tectono-thermal evolution of the mid-crustal Taxaquara Shear Zone (TSZ), we performed U-Pb LASS-ICP-MS dating of apatite, titanite and zircon from deformed and undeformed granitic rocks within and adjacent to the upper-greenschist facies TSZ, Ribeira Belt (RB), Brazil. Apatite U-Pb ages from deformed granite samples yield a weighted age of 544 ± 4 Ma, interpreted to reflect the timing of shearing and deformation, zircon and titanite U-Pb ages record their presumed granite protolith crystallization age, as does the apatite from the undeformed samples, yielding a weighted age of 606 ± 8 Ma. Fish-shaped muscovite $^{40}Ar/^{39}Ar$ yields a weighted age of 534 ± 1.5 Ma for deformed samples, considerably younger than the apatite U-Pb age. This indicates that apatite U-Pb ages record the timing of motion at higher temperatures (450 – 500°C) than muscovite $^{40}Ar/^{39}Ar$ ages (400 – 450°C), reflecting differences in respective closure temperatures. Apatites present similar REE patterns with no relation with age and similar initial common Pb, indicating the apatite U-Pb isotopic system alone was reset at ~500°C in response to deformation. The multi-mineral phase age data indicates the TSZ was plastically active over a period of 10 Ma with a cooling rate of ~5°C/Ma. These data contrast with those from other shear zones in the RB that are limited to dating a single mineral phase, lacking textural and chemical evidence between the mineral and deformation/metamorphism. It is suggested that the multi-mineral approach performed here yields a more reliable geologic history of shear zones.

## 1. INTRODUCTION

Shear zones play a pivotal role in documenting the deformation history of the crust within the ductile regime and in unravelling not only the thermo-tectonic history of the deformation but often of the tectonic evolution of orogenic belts as a whole. Most mid-crustal shear zones are developed between ~400 – 550°C (Fossen and Cavalcante, 2017) and their timing of motion is commonly constrained through muscovite $^{40}Ar/^{39}Ar$ dating. Although there is a strong relationship between muscovite age and timing of deformation (e.g., Zhu et al., 2005; Oriolo et al., 2016), it could underestimate the timing of motion, because the muscovite closure temperature (350 – 425°C; Oriolo et al., 2018 and references therein) can be considerably lower than the thermal peak of deformation. Apatite represents a promising but underused geochronometer to date middle-crustal shear zones. Unlike to muscovite and hornblende, which are common phases in rocks with felsic and mafic bulk compositions, respectively, apatite is stable in a wide range of rock compositions and pressure-temperature conditions (Engi, 2018 and references therein). Due to its capability to incorporate $^{238}U$ during crystallization, apatite is amenable to U-Pb dating, which has been successfully used to date hydrothermal and magmatic events (e.g., Corfu and Stone, 1998), or thermal overprints in metamorphic terranes (e.g., Bruguier et al., 2002; Flowers et al., 2006; Kirkland et al., 2017, 2018; Hall et al., 2018; Turlin et al., 2018). Recent studies have also demonstrated its potential for sedimentary provenance studies (Chew et al., 2011). Importantly, the closure temperature of Pb diffusion in apatite ranges from ~400 to 550°C (Cherniak et al., 1991), which makes it an ideal tool to investigate the timing of peak temperature deformation in the middle-crustal shear zones.

In this contribution, we investigated apatite U-Pb ages and trace elements via Laser Ablation Split Stream Inductively Coupled Plasma Mass Spectrometry (LASS-ICP-MS) from upper-greenschist facies quartz-feldspar-mylonites from the Taxaquara Shear Zone (TSZ), Ribeira Belt (RB), Brazil, to evaluate whether apatite can faithfully record the timing of ductile deformation at upper greenschist facies conditions and record the time at higher temperatures than muscovite. Thus, we dated apatite from two mylonite samples and two undeformed granite protolith samples from outside the shear zone for comparison. We have also expanded dating to include zircon and titanite grains from mylonite samples to better contextualize apatite results. The results demonstrate the ability of apatite U-Pb dating of mid-crustal shear zones and integration with $^{40}Ar/^{39}Ar$ muscovite dating enables better bracketing the timing of motion and the thermo-tectonic evolution of mid-crustal shear zones.

## 2. GEOLOGICAL SETTING

The NE-trending TSZ is a major strike-slip structure within the Ribeira Belt (RB), an accretionary belt that evolved into a collisional belt during the Neoproterozoic assembly of southwestern Gondwana (Fig. 1A) (Almeida et al., 1973; Campanha and Sadowski, 1999; Campos Neto, 2000; Hasui et al., 1975). The Ribeira Belt is composed of a set of tectonostratigraphic terranes with ages ranging from Paleoproterozoic to Neoproterozoic (Faleiros et al., 2011) and with a voluminous arc-related, late- and post-collision granite magmatism (~630–580 Ma; Alves et al., 2013; Leite et al., 2007; Janasi et al., 2001) (Fig. 1B).

The RB underwent NE-SW dextral transcurrent shearing in response to the late Ediacaran to Cambrian oblique collision between the Paranapanema, São Francisco, Luís Alves and Congo cratons (Almeida et al., 1973; Campanha & Sadowski, 1999; Campanha, 2002; Campos Neto, 2000; Egydio-Silva et al., 2018; Faleiros et al., 2011; Hasui et al., 1975; Heilbron et al., 2004). The shear zone system is continuous over some 500 km of the RB, and merges with NNE-trending strike-slip faults of the Araçuaí Belt (Fig. 1B). Seismic analysis based on S-wave anisotropy parallel to the shear zones in the RB indicates that the vertical foliation cross-cut the continental crust profile, possibly extending to the upper mantle (James and Assumpção, 1996). Thus, the authors suggest that these are lithospheric-scale fractures that boundaries between continental blocks.

The TSZ was first described in Hennies et al. (1967) as a linear subvertical structure traceable over at least 100 km with a mylonitic zone up to ~1 km width. Its strike-slip signature was suggested based on its consistent vertical foliation and sub-horizontal stretching lineation that plunges shallowly to the W. Specific studies regarding the TS was not developed since them. Recently, Ribeiro et al. (2019) documented its kinematics, as well as the nature and conditions of deformation and the tectonic regime responsible for the TSZ development. The authors proposed that the TSZ displays dextral shear sense, and lack evidence for earlier overprinting kinematics in the study area. The TSZ deformed granitic rocks giving rise to mylonites and ultramylonites composed of neoformed quartz + microcline + oligoclase + biotite + muscovite + rutile + magnetite. This assemblage represents the peak of deformation, and thermodynamic modelling couple with muscovite-biotite thermometer constrained the average conditions of ~520 ± 6°C and ~4.1 ± 0.3 kbar. This finding is the basis to interpret the results of geochronology-focused analysis, since the Ar and the Pb systems in muscovite and apatite, respectively, are expected to be reset at these conditions (Oriolo et al., 2018 and references therein).

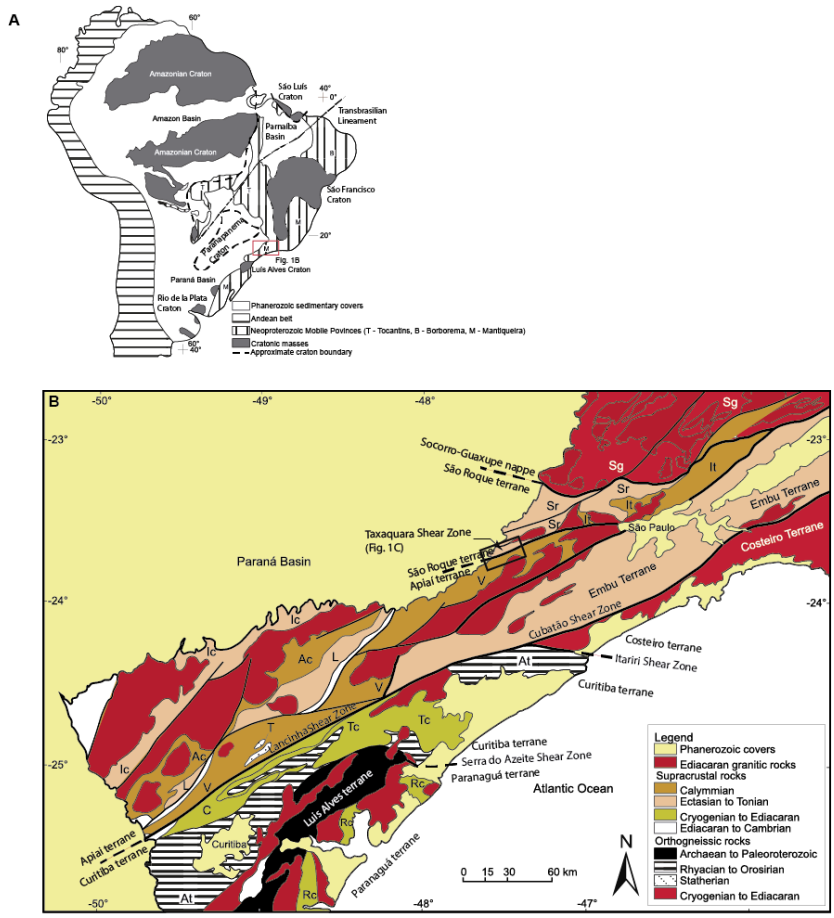


Figure 1. A) Simplified geotectonic map of part of South America. B) Map of central-southern portion of the Ribeira Belt in southeast Brazil. Geological units: Itaiacoca Group (Ic), Água Clara Formation (Ac), Lajeado Group (L), Votuverava Group (V), São Roque Group (Sr), Serra do Itaberaba Group (It), Tigre Gneiss (T), Capirú Formation (C), Turvo-Cajati Formation (Tc), Rio das Cobras Formation (Rc), Atuba Complex (At) (adapter from Campanha et al., 2015). The black rectangle delimits the study area (detailed map in Fig. 2).

### 2.1. Geochronological Background

The TSZ cross-cuts the late orogenic Pilar do Sul and Piedade granites (Fig. 2). The Pilar do Sul granite ranges from medium to coarse-grained inequigranular muscovite-biotite monzogranite at its margins to a fine-grained muscovite biotite monzogranite at the center (Leite et al., 2007). The body yielded a concordant U-Pb TIMS monazite age of 600 ± 4 Ma (Leite et al., 2007).

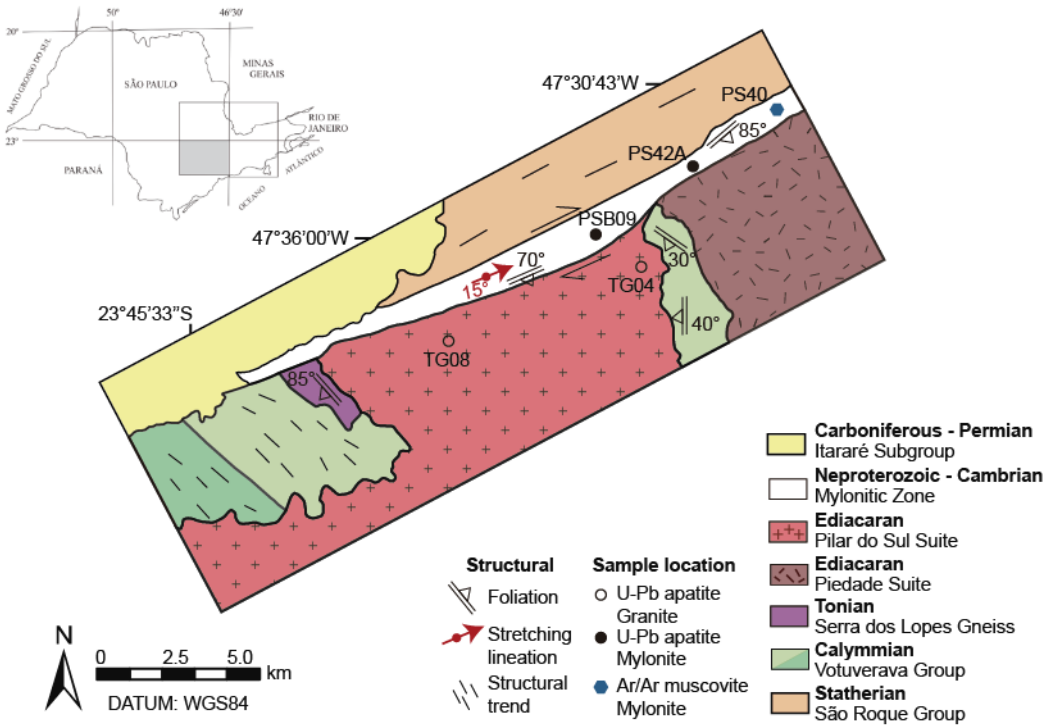


Figure 2. Simplified geological map of the study area focusing the Taxaquara Shear Zone and the site of analysed samples (adapted from Ribeiro et al., 2019). Inset shows the map of the state of Sao Paulo, and shadow area indicates the region of study.

The Piedade granite is an elliptical body composed of porphyritic muscovite-biotite granodiorite to monzogranite, with a magmatic foliation recorded at the margins by the alignment of tabular alkali feldspar. Stretched quartz is locally recognizable, suggesting that deformation started in the magmatic-state and continued in the solid state (Leite et al., 2007). The core of the body is composed of a porphyritic biotite monzogranite with alkali-feldspar megacrysts. Janasi et al. (2001) carried out U-Pb TIMS in igneous monazite with low #mg (0.004 – 0.013) resulting in an age of 601 ± 2 Ma, similar to the TIMS results for the Pilar do Sul body. The authors suggest that it represents the crystallization age, since the regional metamorphism did not reach the monazite closure temperature (~800°C).

Numerous attempts have been made to determine the age of shearing in the RB. The Serra do Azeite Shear Zone was developed in upper-greenschist facies conditions and physically separates two major terranes of distinct evolution histories (Curitiba and Luís Alves Terranes) (Faleiros et al., 2011, 2016). Hornblende $^{40}Ar/^{39}Ar$ from mylonitic orthogneiss yields 594 ± 1 Ma, while muscovite $^{40}Ar/^{39}Ar$ from post-kinematics pegmatite that cross-cut the mylonitic foliation yields 574 ± 1 Ma (Machado et al., 2007). These ages are supported by the U-Pb age

of retrograde monazite (579 ± 8 Ma; Faleiros et al., 2011) with high Y due to garnet consumption during retrograde, lower-greenschist facies shearing.

The Cubatão and Itariri Shear Zones were developed in upper-greenschist facies conditions and represent suture zones by limiting the Mongaguá Domain (Passarelli et al., 2008). The first deformational phase of the Lancinha – Cubatão – Itariri Shear System was dated at 620 – 600 Ma based on metamorphic epidote (598 Ma; Passarelli et al., 2011) extracted from a protomylonite sample from the Juquiá granite and metamorphic monazite (620 Ma; Passarelli et al., 2008) extracted from protomylonite sample from the Sete Barras granite. The Juquiá and Sete Barras granites were dated at 598 ± 8 Ma and 631 ± 23 Ma, respectively, through monazite U-Pb dating (Passarelli et al., 2004). At that time, the authors interpreted it as the crystallization ages. Recently, Passarelli et al. (2019) re-assessed these granites with zircon U-Pb experiments from the Juquiá granite yielding 799 ± 5 Ma and 755 ± 3 Ma, while the zircon and monazite U-Pb analysis from the Sete Barras granite yielded 602 ± 2 Ma and 598 ± 2 Ma, respectively. The second deformation, developed under greenschist facies conditions, was responsible for the wedge formed by the Itariri and Cubatão shear zones at 583 ± 7 Ma defined by concordant U-Pb age of needle-shaped zircons from a mylonite sample of the Cubatão Shear Zone (Passarelli et al., 2008).

According to Passarelli et al. (2008), the Cubatão – Itariri Shear System and the Serrinha Shear Zone, interpreted as an amphibolite shear zone, limit the Registro Domain (Passarelli et al., 2008). The Serrinha Shear zone was dated at 575 ± 5 Ma through U-Pb TIMS of metamorphic monazite extracted from a greenschist facies mylonitic granite from the Jureia Massif. A mylonitic paragneiss from the Jureia massif was dated at 752 ± 4 Ma from U-Pb experiments performed on monazite, being interpreted as the timing of regional metamorphic/thermal event (Passarelli et al., 2004). $^{40}Ar/^{39}Ar$ ages from biotite and muscovite yield 482 – 495 Ma and 501 ± 5 Ma, respectively (Passarelli et al., 2011).

### 2.2. Studied Samples

The mineral assemblage and microstructures from mylonites samples are outlined in Ribeiro et al. (2019) and are briefly described below. Mylonites from the TSZ are composed of neoformed quartz + oligoclase + K-feldspar + biotite + muscovite + rutile + magnetite with evidence of subgrain rotation ± grain boundary migration on quartz and concomitant brittle/ductile deformation recorded on feldspar porphyroclasts. The quartz crystallographic preferred orientation from these samples define a symmetrical to asymmetrical monoclinic

pattern (i.e., single girdle) suggesting activation of 'basal-<a> + 'rhomb-<a>' slip systems. These data suggest that mylonite samples PSB09 and PS42A were deformed at similar conditions close to ~500°C (Ribeiro et al., 2019).

Apatite grains are generally translucent and euhedral with a prismatic shape. In backscattering images, monazite inclusions are detected (Supporting information). Apatite from sample PSB09 presents mean grainsize of 81 ± 16 μm diameter (perpendicular to elongation). In thin section, the mylonitic foliation, marked by lepidoblastic layers, wraps around the apatite grains, suggesting they behaved as rigid porphyroclasts during deformation. Textures indicative of bulging recrystallization are also recognized, like rounded porphyroclast relicts partially mantled by aggregates of very fine-grained neoformed apatite (Fig. 3). Apatite from sample PS42A yields 90 ± 14 μm mean diameter with no evidence of recrystallization, being wrapped by the mylonitic foliation and oriented in the S-direction of the S/C fabric (Fig. 3).

## 3. METHODOLOGY

### 3.1. Closure Temperature Estimate

When dealing with thermochronology, mineral closure temperatures are quoted as well-established values. However, this may not be valid because the temperature is a function of diffusivity, cooling rate and effective radius of the diffusion domain, which can vary from grain to grain (Dodson, 1973). In order to determine the proper closure temperature of muscovite and apatite for the $^{40}Ar/^{39}Ar$ and U-Pb systems, respectively, and better understand the meaning of the ages, we estimated them through the diffusion equation (Eq. 01) proposed in Dodson (1973).

$$\frac{E}{RT_{cn+1}} = \ln \frac{ART_{cn}^2 D}{Ea^2\left(\frac{\delta T}{\delta t}\right)} \quad \text{(Eq. 01)}$$

Where E is the activation energy (J/mol), R is the universal gas constant (8.314 J/mol∗K), A corresponds to a numerical constant related to the geometry of the diffusion system, D is the diffusion coefficient (μm²/Ma), a is the effective diffusion radius (μm). $T_{cn}$ corresponds to the initial estimate for closure temperature, $T_{cn+1}$ is the final estimated closure temperature and $\frac{\delta T}{\delta t}$ is the cooling rate. The activation energy and the diffusion coefficient are intrinsic to each mineral. Therefore, we used the parameters suggested in Harrison et al. (2009) for Ar diffusion in muscovite and Cherniak et al. (1991) for Pb diffusion in apatite. For muscovite, Tc was estimated using plane diffusion geometry and grain size, in μm, and was measured parallel to

the <c>-axis. For the apatite estimates, we used a cylinder diffusion geometry and the grain size, in μm, was measured perpendicular to the <c>-axis.

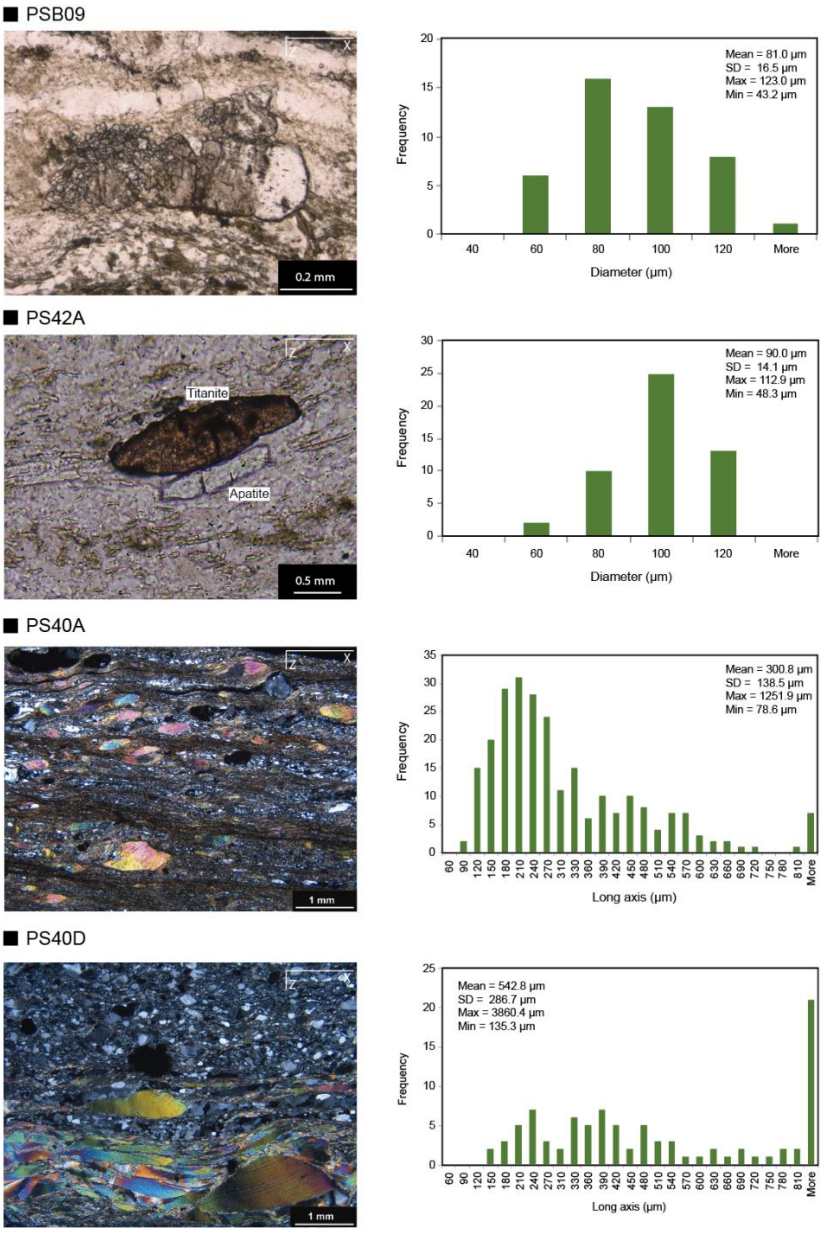


Figure 3. **PSB09:** apatite with evidences of ductile recrystallization, preserving the core and being recrystallized in its borders; **PS42A:** apatite and titanite grains with no evidence of recrystallization oriented parallel to S direction of a S/C structure indicating dextral shear sense; **PS40A:** dextral fish-shaped muscovite with homogeneous grainsize and interference color; **PS40D:** dextral fish-shaped muscovite with heterogeneous grainsize and interference color suggesting a more intense ductile deformation in comparison to the previous sample.

### 3.2. $^{40}Ar/^{39}Ar$ Geochronology

Muscovite was selected from two mylonite samples. $^{40}Ar/^{39}Ar$ analyses were carried out in the Geochronological Research Center (University of São Paulo, Brazil). The selected grains were irradiated with fast epithermal neutrons flow in the research reactor TRIGA (CLICIT) in the OSU/Oregon (USA), coupled with the international standard Fish Canyon (sanidine, 28.01 ± 0.04 Ma; Phillips and Matchan, 2013), for 15 continuous hours. After irradiation, the samples rested for 20 days until complete cooling and deposited to be analyzed through step heating via solid state Nd:$YVO_4$ laser (532nm – Verdi 6W Coherent model) in the Geochronological Research Center of the University of São Paulo (CPGeo/IGc/USP). The mass of the $^{40}Ar$ and $^{36}Ar$ were simultaneously measured in 5 Faraday collectors (1011 Ω for $^{40}Ar$ mass and 1012 Ω for $^{36}Ar$ mass). During the analysis, the reproducibility was continuously monitored using atmospheric Ar measures (air pippete, $^{40}Ar/^{36}Ar$ weighted mean = 298.5).

After applied the mass discrimination, nucleotides interference and atmospheric contamination corrections, the apparent ages were calculated in each step heating using $J_{factor} = 3.308*10^{-3} \pm 4.0*10^{-6}$. The plateau ages were defined based on $^{39}Ar_K > 50$ % (ideally > 70 %) and the maximum steps numbers with $^{40}Ar^*/^{39}Ar_K$ coherent with 95 % confidence (McDougall and Harrison, 1999). Apparent ages were plotted with 2 σ error.

### 3.3. U-Pb Geochronology and Mineral Trace Element Concentrations

Laser Ablation Split Stream Inductively Coupled Plasma Mass Spectrometry (LASS-ICP-MS) data collection for apatite, titanite and zircon ages and trace elements, as single spot ablations, was performed at Isotopia Laboratory, School of Earth Atmosphere and Environment, Monash University, Australia. Mineral separation was carried out at the University of São Paulo and Monash University. Crushed whole rocks were first sieved and the 125-250 mesh fraction was further processed using isodynamic, gravimetric and magnetic techniques to separate desired phases. Individual grains were mounted and polished in 1-inch² epoxy rounds.

For determining U-Pb ages and trace element concentrations, a LASS-ICP-MS set-up was utilized, whereby the sample is split into two even streams by a Y-piece located between the laser cell and the ICP-MS. A 25 μm diameter laser spot was used, with a laser repetition rate of 10 Hz and 6 mJ laser energy. The experiment consisted of 20 seconds background measurement and 20 seconds of ablation. Trace elements were collected on a Thermo Scientific iCAP Quadruple-ICP-MS, while U-Pb data were acquired with a Thermo Scientific iCAP Triple

Quadruple ICP-MS. Acquired data were further reduced in Iolite environment (Paton et al., 2011) using the U-Pb Geochron and Trace Element data reduction schemes.

### 3.3.1. Apatite standard

For the U-Pb experiments in apatite, Madel monazite was used as the primary standard with the following defined ages (Payne et al., 2008): $^{207}Pb/^{238}U$ = 510.4 Ma, $^{206}Pb/^{238}U$ = 514.8 Ma, and $^{207}Pb/^{206}Pb$ = 490.7 Ma. The USGS-44069 monazite (429.9 ± 0.9 Ma; Aleinikoff et al., 2006) and the MAD apatite (485 ± 1.7 Ma; Thomson et al., 2012) were employed as secondary standards and treated as unknowns. The U-Pb ages acquired for the Madel standard yields very similar ages with $^{207}Pb/^{238}U$ = 511.63 ± 0.84 Ma (MSWD = 0.46), $^{206}Pb/^{238}U$ = 516.1 ± 1.2 Ma (MSWD = 2.3), and $^{207}Pb/^{206}Pb$ = 488.8 ± 4.2 Ma (MSWD = 0.58). The USGS-44069 and the MAD standards yielded 420.7 ± 6.1 Ma (MSWD = 0.91) and 478 ± 56 Ma (MSWD = 0.78) ages, respectively.

### 3.3.2. Titanite standard

The OLT titanite (1015 ± 2 Ma, Kennedy et al., 2010) was used as the primary age standard with BRL titanite (1047 ± 0.4 Ma; Aleinikoff et al., 2007) employed as secondary standard and treated as an unknown to verify the data quality. Results from OLT and BRL yield concordia ages of 1008 ± 15 Ma (MSWD = 0.44) and 1046 ± 12 Ma (MSWD = 0.23), respectively, which are within error of the recommended values.

### 3.3.3. Zircon standard

The GJ1 (609 Ma; Jackson et al., 2004) and Plesovice zircon standards (337 Ma; Slama et al., 2008) were undertaken as primary and secondary standards, respectively where the Pleisovice was treated as an unknown to ensure the data quality. The results from GJ1 and Pleisovice yield weighted $^{206}Pb/^{238}U$ ages at 594 ± 3.3 (MSWD = 0.31) and 337 ± 0.9 Ma (MSWD = 0.86), respectively.

### 3.3.4. Trace element concentrations

A total of 21 elements were measured ($^{31}P$, $^{43}Ca$, $^{88}Sr$, $^{89}Y$, $^{90}Zr$, $^{93}Nb$, $^{139}La$, $^{140}Ce$, $^{141}Pr$, $^{146}Nd$, $^{147}Sm$, $^{151}Eu$, $^{157}Gd$, $^{159}Tb$, $^{163}Dy$, $^{165}Ho$, $^{166}Er$, $^{169}Tm$, $^{172}Yb$, $^{175}Lu$, $^{181}Ta$). The international glass NIST 610 was undertaken as the primary standard for calculation of element concentrations. The NIST 612, BCR2 and ATHO were used as secondary trace element standards and treated as unknowns to evaluate the reproducibility of the data within the errors.

## 4. RESULTS

### 4.1. Muscovite and Apatite Closure Temperature Estimates

Closure temperatures were calculated through the diffusion equation of Dodson (1973) diffusion equation using the Ar and Pb diffusion parameters for muscovite and apatite from Harrison et al. (2009) and Cherniak et al. (1991), respectively. Due to the lack of precise cooling rate for the RB, multiple interactions were performed on MATLAB environment with cooling rates between 1 – 5°C/Ma following Tassinari et al. (2006).

The analyzed muscovite grains from samples PS40A and PS40D were extracted from grain-size fraction between 250 – 500 μm and 500 – 707 μm, respectively. The estimates based on the diffusion radius for samples PS40A and PS40D define intervals spanning 400 – 446°C and 420 – 457°C, respectively, both for cooling rates between 1 – 5°C/Ma (Table 1).

| Diffusion ratio (μm) | δt/δT (°C/Ma) | $T_{CA}$ (°C) | Diffusion ratio (μm) | δt/δT (°C/Ma) | $T_{CA}$ (°C) | Diffusion ratio (μm) | δt/δT (°C/Ma) | $T_{CA}$ (°C) |
|---|---|---|---|---|---|---|---|---|
| 125 | 1 | 399.15 | 250 | 1 | 419.21 | 353.5 | 1 | 429.39 |
| | 2 | 410.00 | | 2 | 430.70 | | 2 | 441.33 |
| | 3 | 416.30 | | 3 | 437.40 | | 3 | 448.32 |
| | 4 | 421.10 | | 4 | 442.40 | | 4 | 453.60 |
| | 5 | 424.40 | | 5 | 445.98 | | 5 | 457.28 |
| | 10 | 435.00 | | 10 | 457.30 | | 10 | 468.90 |

Table 1. Closure temperature estimates for muscovite based on Ar diffusion parameters (Harrison et al., 2009).

Apatite grain-size, measured perpendicular to <c>-axis from samples PSB09 and PS42A range from 40 to– 100 μm, defining a closure temperature interval within 435 – 503°C for cooling rates between 1 – 5°C/Ma (Table 2). Taking the mean apatite grain-size (81 ± 16 μm) from sample PSB09, the estimates lie between 453 – 502°C for the same cooling rate interval. For sample PS42A, the estimate yields 460 – 505°C defined by the mean grain-size (90 ± 14 μm). The closure temperature of apatite is overall similar between samples due to similar grain-size.

| Grainsize[a] (μm) | δt/δT (°C/Ma) | $T_{CA}$ (°C) | Grainsize[a] (μm) | δt/δT (°C/Ma) | $T_{CA}$ (°C) |
|---|---|---|---|---|---|
| 40 | 1 | 435.35 | 60 | 1 | 450.31 |
| | 2 | 448.10 | | 2 | 463.60 |
| | 3 | 455.77 | | 3 | 471.60 |
| | 4 | 461.31 | | 4 | 477.39 |
| | 5 | 465.66 | | 5 | 481.94 |
| | 10 | 479.53 | | 10 | 496.43 |

| Grainsize[a] (μm) | δt/δT (°C/Ma) | $T_{CA}$ (°C) | Grainsize[a] (μm) | δt/δT (°C/Ma) | $T_{CA}$ (°C) |
|---|---|---|---|---|---|
| 80 | 1 | 461.31 | 100 | 1 | 470.07 |
| | 2 | 475.01 | | 2 | 484.11 |
| | 3 | 483.27 | | 3 | 492.57 |
| | 4 | 489.23 | | 4 | 498.68 |
| | 5 | 493.93 | | 5 | 503.49 |
| | 10 | 508.89 | | 10 | 518.83 |

Note

[a] Grainsize was measured perpendicular to the apatite <c>-axis

Table 2. Closure temperature estimates for apatite based on Pb diffusion parameters (Cherniak et al., 1991).

## 4.2. Muscovite $^{40}Ar/^{39}Ar$ Dating

### 4.2.1. PS40A

Sample PS40A contains fish-shaped muscovite with dextral shear sense. Most of the muscovite is preserved as single grains and display a homogeneous interference color (yellow, blue and pink). Grain-size distribution, based on the muscovite long axis, is represented by a positive asymmetrical distribution with mean and standard deviation around ~300 μm and ~138 μm, respectively, indicating the dominance of small over large grains (Fig. 3).

Different aliquots from this sample resulted in two plateau ages with spectrum disturbance in high temperature steps, suggesting excess of Ar in the inner grain. The results yield 531 ± 3.0 Ma (MSWD = 0.6) and 535 ± 2.0 (MSWD = 1.09), showing consistent data between aliquots (Fig. 4). The good correlation with total fusion and inverse isochron ages suggests geologically meaning ages (e.g., Zhu et al., 2005). A mean weighted age, incorporating both aliquots, yields an age of ca. 533.5 ± 1.9 Ma (MSWD = 1.4).

### 4.2.2. PS40D

Sample PS40D is muscovite from the granoblastic matrix of the mylonite and contains only a minor amount of fish-shaped muscovite. Muscovite grains have a heterogeneous grain-size distribution, interference color disturbance and evidence of deformation bands, which indicate significant intracrystalline deformation (Fig. 3). These grains were intensely deformed in the stretching direction undergoing ductile grain-size reduction, which gave rise to grains with high aspect ratio. This process is represented in the muscovite long axis histogram, which shows a dominance of large grains (mean ~543 μm), but also with a spread-out distribution represented by the high standard deviation (~287 μm).

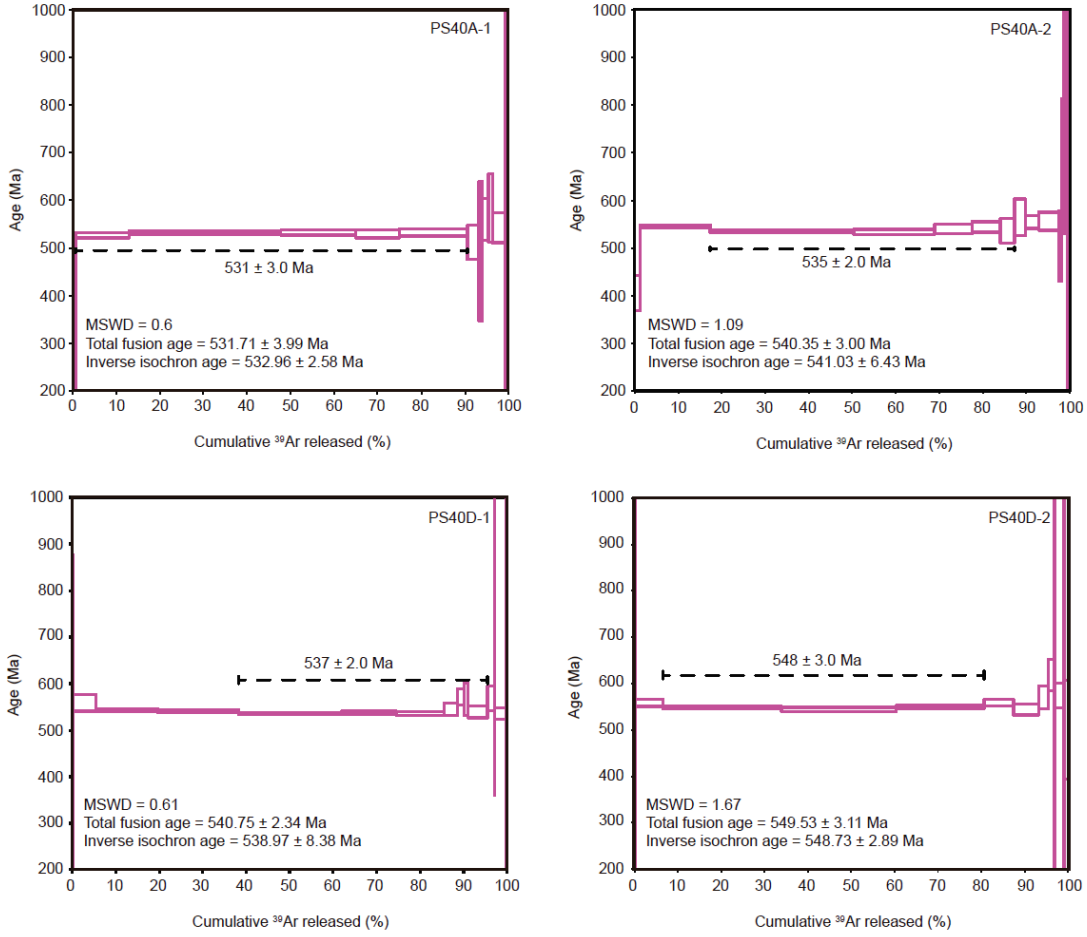


Figure 4. Muscovite $^{40}Ar/^{39}Ar$ plateau ages (>70% $^{39}Ar$ released) from samples PS40A and PS40D with its respective aliquots. The MSWD, total fusion and inverse isochron ages are indicated in the lower-left part of the plots. Steps-width error are 2σ.

The aliquots from sample PS40D display plateau ages with evidence of $^{39}Ar$ excess in the final, high-temperature steps. These plateaus yield ages of 537 ± 2.0 Ma (MSWD = 0.61) and 548 ± 3.0 Ma (MSWD = 1.67). Even though the plateau ages are concordant with total fusion and inverse isochron ages suggesting good quality data, there are significant age differences between aliquots. Due to the evidence of more intense deformation in comparison to muscovite grains from sample PS40A and the age discordance we suspect of a possible Ar excess in the older result. This age could resemble the same event recorded in the apatite ages, but the there is a significant difference in the closure temperatures, which may support the Ar excess due to deformation.

### 4.3. U-Pb Dating and Trace Elements

Apatite and titanite U-Pb ages can be difficult to interpret due to the uncertainties in the composition of common Pb. In order to obtain reliable ages, corrections are usually required (e.g., Chew et al., 2011, 2014; Kirkland et al., 2017). For minerals containing significant amounts of common Pb (e.g., apatite and titanite), data are presented in Tera-Wasserburg inverse concordia diagram (TW) with the uncorrected and corrected regression line with the initial $^{207}Pb/^{206}Pb_i$ calculated through the Stacey & Kramers (1975) approach. The comparison of the common Pb-corrected age from the TW with the weighted corrected apparent age performed on Isoplot (Ludwig, 1991) enables the reliability of the results to be assessed. The common Pb content was determined here through the F207 function (Kirkland et al., 2017). Outlier rejection (discordance > 2σ error) was based on the weighted average of corrected apparent age on Isoplot 4.15 (Ludwig, 1991).

#### 4.3.1. Mylonite samples

##### 4.3.1.1. PSB09

U-Pb analyses were undertaken on zircon and apatite grains from mylonite sample PSB09. Of 62 zircon data points, only 12 present reliable geological information (Fig. 5A, black ellipses), while the remaining have high discordance levels due to high common Pb contents. From those 12, 5 data points represent inherited zircons (> 1000 Ma) and the remaining define a reasonable concordia age at ca. 605 ± 7 Ma (MSWD = 2.1), taken here as the crystallization age (Fig. 5B). The normalized trace elements diagram shows that concordant zircons have positive Ce and negative Eu anomalies and an enrichment trend from LREE to HREE, whereas discordant zircons present a flat trend with no evident anomalies (Fig. 5C).

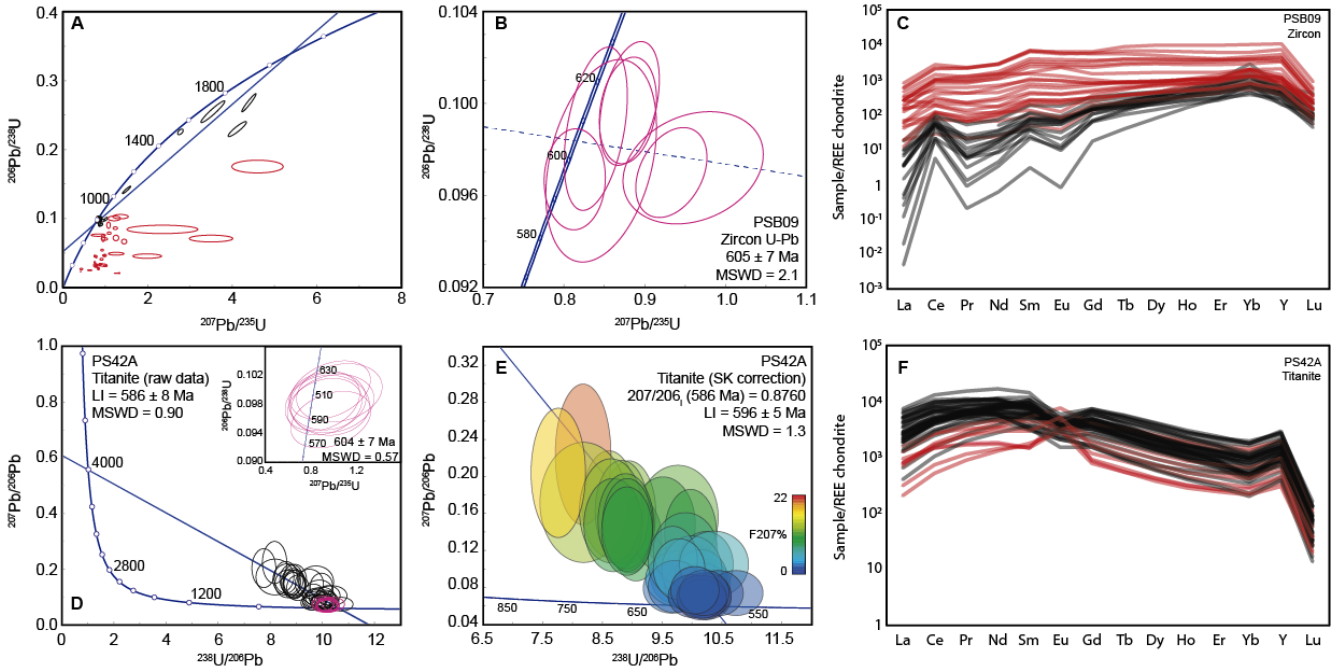


Figure 5. A, B) Zircon U-Pb results from sample PSB09. Red ellipses in (A) correspond to discarded data; D, E) Titanite U-Pb results from sample PS42A; C, F) Chondrite normalized REE + Y (McDonough and Sun, 1995) for zircon and titanite from samples PSB09 and PS42A, respectively. Data-point error ellipses are 2σ.

Eighty-one analyses were undertaken on 42 apatite grains from sample PSB09. Eleven analyses were excluded: 5 with discordant data and 6 with Pb-loss evidence (Fig 6A, red ellipses). Data are distributed along a single inverse isochron with different content of common Pb, with F207 between 15 – 75 % (Fig. 6B). The lower intercept for the natural inverse isochron yields 545 ± 11 Ma (MSWD = 2.7), while anchored isochron using the $^{207}Pb/^{206}Pb_i$ from Stacey & (1975) yields 547 ± 5 Ma (MSWD = 2.7), implying a 0.36% difference between ages. This strong concordance suggests the applicability of the Stacey & Kramers (1975) correction for all data. These ages are also in good agreement with the weighted corrected apparent age (544 ± 5 Ma, MSWD = 2.3). The normalized trace element diagram shows homogeneous geochemical signature with total REE + Sr + Y content of 10, strong negative Sr and Eu anomalies, general positive to flat patterns for LHEE (La to Sm) and HREE (Gd to Yb) with no Y anomaly (Fig. 6C).

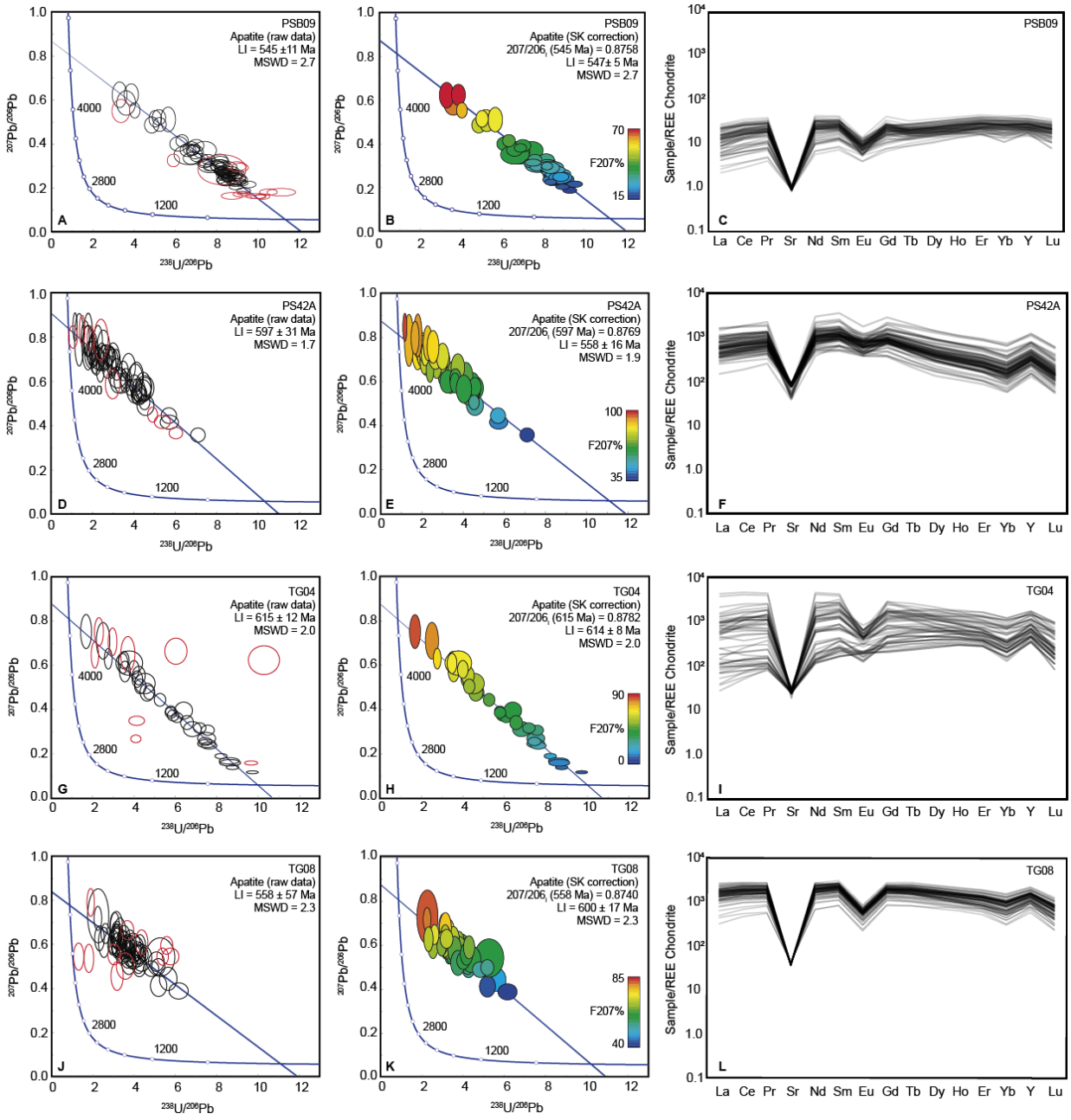


Figure 6. A, D, G, J) Tera-Wasserburg diagrams with natural inverse isochron (raw data) from apatite U-Pb results for samples PSB09, PS42A, TG04 and TG08, respectively. Red ellipses correspond to discarded data; B, E, H, K) Tera-Wasserburg diagrams with anchored inverse isochron from apatite U-Pb results using the initial $^{207}Pb/^{206}Pb_i$ calculated using Stacey & Kramers (1975) approach (values are indicated in the top right of each diagram). The F207 values (colour range) show the variation of common Pb content between analysed data (for more details, see Kirkland,et al., 2018). C, F, I, L) Chondrite normalized REE + Sr + Y (McDonough and Sun, 1995) for apatites from samples PSB09, PS42A, TG04 and TG08, respectively. Note how the values for the mylonite in C is considerably lower compared to the others. Data-point error ellipses are 2σ.

#### 4.3.1.2. PS42A

Titanite and apatite grains were extracted from mylonite sample PS42A and were used for U-Pb analyses. We analyzed 45 titanite grains, resulting in 50 data points. From this, 8 outliers were excluded. The TW diagram with a natural inverse isochron (Fig. 5D) yields a lower intercept at 586 ± 8 Ma (MSWD = 0.90), whereas the anchored inverse isochron using the $^{207}Pb/^{206}Pb_i$ from Stacey & (1975) yields an age of 596 ± 5 Ma (MSWD = 1.3) (Fig. 5E). Very low common Pb data points (F207 < 2%) yield a concordia age at 604 ± 7 Ma (MSWD = 0.57) (Fig. 5D, insert), interpreted as the best estimation for the igneous crystallization of the titanite. The trace elements behavior indicates enrichment and depletion trends in the LREE and HREE, respectively, with a slight negative Eu anomaly (Fig. 5F). However, few grains present positive Eu anomaly, which may suggest fluid interaction during titanite crystallization, since there is no systematic correlation with age.

From 45 apatite grains, we acquired 67 data points. From this, 9 outliers were excluded based on the weighted corrected apparent age (discordance > 2σ) (Fig. 6D, red ellipses). The lower intercept from the natural inverse isochron yields an age of 597 ± 31 Ma (MSWD = 1.7). The apatite grains have high Pb, with F207 between 35 – 100% (Fig. 6E). Therefore, the data are concentrated close to the upper intercept, leading to inaccuracies on the lower intercept and increasing the error. The anchored inverse isochron using the $^{207}Pb/^{206}Pb_i$ from Stacey & Kramers (1975) approach yields a lower intercept at 558 ± 16 Ma (MSWD = 1.9). The weighted corrected apparent age is 557 ± 16 Ma (MSWD = 1.7), reinforcing the reliability of the corrected age from lower intercept (Fig. 6E). The normalized REE + Sr + Y values present homogeneous contents between $10^2$ – $10^3$, general concave shape patterns with positive and negative trends for LREE and HREE, respectively, pronounced negative Sr and Eu anomaly and positive Y anomaly (Fig. 6F).

### 4.3.2. Granites

#### 4.3.2.1. TG04

From 49 apatite grains, 42 data points were acquired from this granite sample. Nine outliers in relation to the natural inverse isochron were excluded (Fig. 6G, red ellipses). The lower intercept from the natural inverse isochron yields 615 ± 12 Ma (MSWD = 2.0). Sample TG04 presents well distributed data along the isochron due to the highly variable common Pb content (Fig. 6H), with F207 between 0 – 90 %. This spread accurately defines the initial $^{207}Pb/^{206}Pb$ composition close to 0.88, requiring very little or no correction due to the similarity with the

calculated $^{207}Pb/^{206}Pb_i$ (0.8782) using Stacey & Kramers (1975). The lower intercept from the anchored inverse isochron using the calculated $^{207}Pb/^{206}Pb_i$ yields 614 ± 8 Ma (MSWD = 2.0), indicating a 0.16% difference between ages. These ages are in good agreement with the weighted corrected apparent age (617 ± 8 Ma, MSWD = 1.8). Normalized REE + Sr + Y contents vary between $10^2 – 10^3$, presenting a general concave shape pattern with positive trend in the LREE (La to Sm), negative Sr and Eu anomalies and positive Y anomaly (Fig. 6I). It also presents enrichment and depletion trends in the LREE and HREE, respectively.

#### 4.3.2.2. TG08

From granite sample TG08, 68 data points were acquired from 53 analyzed apatite grains. Twelve outlier data were excluded (Fig. 6J). The lower intercept of the natural inverse isochron yields 558 ± 57 Ma (MSWD = 2.3). The high error and uncertainties, similar to mylonite sample PS42A, is due to the high common Pb content as shown by the F207 between 40 – 85 % (Fig. 6K). This feature concentrates the data close to the upper intercept, leading uncertainties to the lower intercept. The lower intercept of the anchored inverse isochron using the $^{207}Pb/^{206}Pb_i$ from Stacey & Kramers (1975) yields 600 ± 17 Ma (MSWD = 2.7). The corrected age is in good agreement with the weighted corrected apparent age (599 ± 17 Ma, MSWD = 2.4). Taking errors, the corrected result is similar to the granite sample TG04. Normalized REE + Sr + Y contents are homogeneous around $10^3$ with slightly concave shape distribution patter, well defined negative Sr and Eu anomalies and positive Y anomaly (Fig. 6L). The LREE pattern is similar to the other samples, and the HREE pattern is marked by well-defined depletion trend (from Gd to Yb).

## 5. Discussion

### 5.1. Geochemical Signature of Apatite: Igneous versus Metamorphic type

The apatite chondrite-normalized trace elements data (Figure 6) (McDonough and Sun, 1995) present similar results for samples PS42A, TG04 and TG08 with consistent concave-shape patterns, normalized REE +Sr + Y contents within $10^2 – 10^3$ , negative Sr and Eu anomalies, HREE depletion (from Gd to Yb) and positive Y anomalies, defining the typical normalized profile of igneous apatite (Figure 6F, I, L). While apatite from mylonite sample PS42A is similar to the granites, recording the primary igneous signature, mylonite sample PSB09 has much lower normalized REE +Sr + Y contents (~10), slight enrichment of HREE and absence of positive Y anomaly, possibly indicating different source or re-equilibration

during metamorphism. Depletion in REE and Y has been suggested to be a typical feature of re-equilibrated apatite under upper-greenschist facies conditions (Henrichs et al., 2018).

In the Sr versus $(La/Yb)_N$ diagram (Fig. 7), apatite from the same three samples PS42A, TG04 and TG08 plot above Sr ~180 ppm and present similar ranges of $(La/Yb)_N$. The Sr trend that they define in Fig. 7 may be related to an igneous fractionation pathway (e.g., Chu et al., 2009; Pan et al., 2016). Apatite from mylonite sample PSB09, however, presents very low Sr content (~7 ppm) and a slightly lower $(La/Yb)_N$ ratio than the other samples. Assuming the bulk composition of the continental crust with Sr ~320 ppm (Rudnick and Gao, 2003) and the Sr partition coefficient between apatite and felsic magma (2.1 – 2.4; Watson & Green, 1981), the original magma should have very low Sr content of < 4 ppm to crystallize this apatite, which is very unlikely for granites. This suggest that for sample PSB09, the igneous apatite recrystallized under upper-greenschist facies metamorphism (e.g., Henrichs et al., 2018), which is in agreement with deformation microstructures present in the thin section (Fig. 3A). Similar to sample PSB09, apatite re-equilibrated during metamorphism/deformation described by Nutman (2007) and Henrichs et al. (2018) presents Sr contents below 180 ppm, suggesting a transition between likely igneous to likely metamorphic apatite (Fig. 7).

### 5.2. Geochronology and Time-Temperature Paths of the Mid-crustal Taxaquara Shear Zone

The U-Pb geochronological results can be separated into two groups. The older is represented by the zircon (605 ± 7 Ma, mylonite sample PSB09), titanite (604 ± 7 Ma, mylonite sample PS42A) and the apatite ages (614 ± 8 Ma, TG04; 600 ± 17 Ma, TG08) from undeformed granite samples. These ages overlap within error, and are in good agreement with the more precise monazite U-Pb (TIMS) age of 600 ± 4 Ma for the Pilar do Sul granite (Leite et al., 2007). Therefore, these ages correspond to the igneous crystallization of each sample. The younger group of ages from U-Pb dating of apatite and $^{40}Ar/^{39}Ar$ -dating of muscovite record the cooling times in the mylonitic samples after the peak temperature.

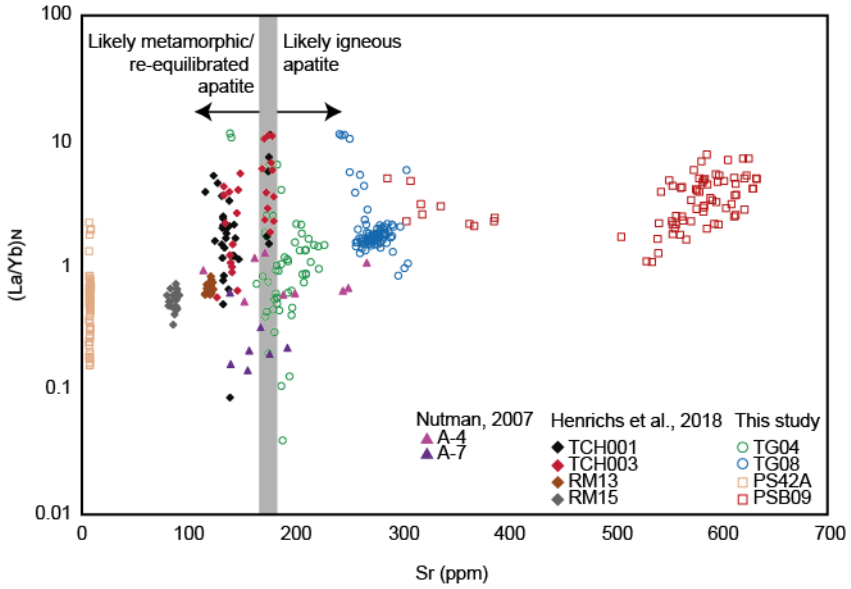


Figure 7. Sr (ppm) vs. normalized La/Yb ratio distinguishing likely igneous apatite from likely metamorphic/re-equilibrated apatite. Hollow symbols correspond to samples from this study. Filled symbols (triangles and diamonds) correspond to metamorphic and/or re-equilibrated apatite during progressive metamorphism from Nutman (2007) and Henrichs et al. (2018), respectively.

The apatite U-Pb results yield ages of 547 ± 5 Ma (sample PSB09) and 558 ± 18 Ma (sample PS42A). The corrected single ages from both samples belong to the same gaussian distribution with a mean age of 544 ± 4 Ma (Fig. 8B). Although the error on the age from sample PS42A is high, due to the high contents of common Pb, the results are, as expected, younger than the zircon and titanite ages from these samples (Fig. 5), and older than the $^{40}Ar/^{39}Ar$ ages. The mean $^{207}Pb/^{206}Pb_i$ for apatite samples calculated from the Stacey & Kramers (1975) approach yields 0.8762 ± 0.0012, which is in agreement with an initial common Pb composition for ~600 – 610 Ma, suggesting that the Pb incorporation into the apatite grains originates from magma crystallization at that time (e.g., Kirkland et al., 2017) with no mixing with later Pb incorporation during metamorphism. The weighted $^{40}Ar/^{39}Ar$ age from muscovite yields 534 ± 1.5 Ma, similar to those from shear zones investigated in Hackspacher et al. (2004), suggested by the author as the typical cooling ages of the RB during transcurrent shearing.

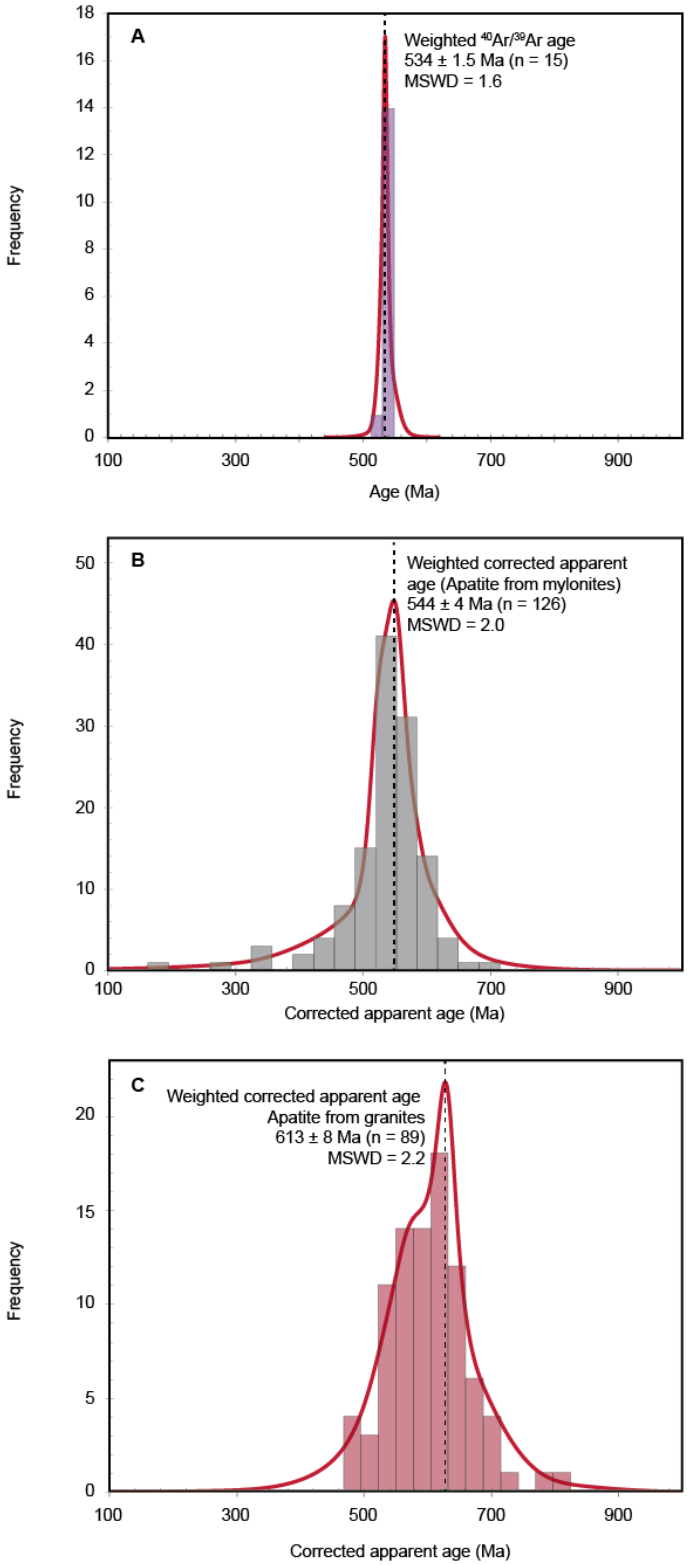


Figure 8. Weighted age using Isoplot (Ludwig, 1991). A) Single distribution of muscovite $^{40}Ar/^{39}Ar$ ages; B) Single distribution of corrected apparent U-Pb ages of apatite from mylonites; C) Single distribution of corrected apparent apatite U-Pb ages of apatite from granites.

Taking individual ages and the mineral respective closure temperature estimates, we can draw the time-temperature path of the TSZ (Fig. 9). The relation between closure temperature and ages suggest an approximate cooling rate of 5°C/Ma. Therefore, we used the estimates for 5°C/Ma to analyze the time-temperature path. Thus, the closure temperature estimates for

muscovite from samples PS40A and PS40D yield 435 ± 11°C and 451 ± 5°C, respectively, with differences related to the variation in the analyzed grain-sizes. The closure temperature estimates for apatite from samples PSB09 and PS42A yield 494 ± 8°C and 498 ± 7°C, respectively. Combining the $^{40}Ar/^{39}Ar$ ages with the closure temperature estimates for Ar in muscovite, we infer that the TSZ was active under greenschist facies conditions between 424 – 456°C at 528 – 539 Ma, taking errors into account. The closure temperature estimate for Pb in apatite is higher than that estimated for Ar in muscovite from our samples, and approaches the equilibrium temperature of the mineral paragenesis in the mylonitic rocks (520 ± 6°C; Ribeiro et al., 2019). This age (544 ± 4 Ma) is inferred to represent an early time of shearing at ~500°C, according to the apatite grain-size, during which apatite may recrystallized (Fig. 3A) and gain its metamorphic composition (Fig. 7C). The time-temperature path suggests a cooling rate of ~5°C/Ma which is in good agreement with published regional estimates for the RB (Tassinari et al., 2006).

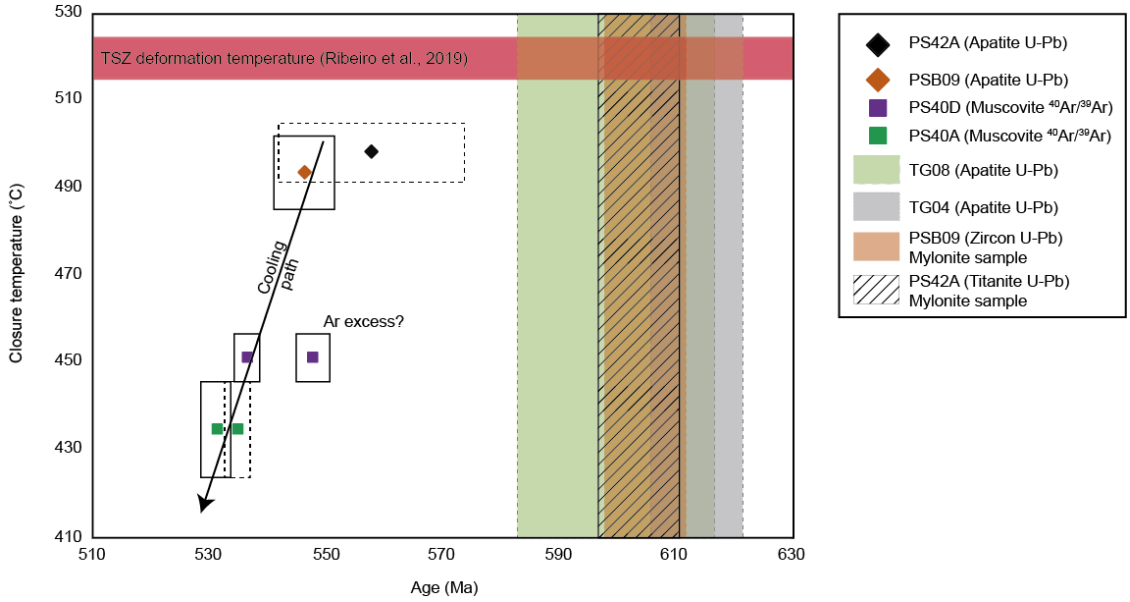


Figure 9. Time-temperature path based on apatite U-Pb and muscovite $^{40}Ar/^{39}Ar$ ages coupled with proper closure temperature estimates (this work). Vertical rectangles on the right indicate the apatite, zircon and titanite U-Pb igneous age with mean age (606 ± 8 Ma) concordant to the monazite U-Pb TIMS age from the Pilar do Sul Granite (600 ± 4 Ma; Leite et al., 2007).

### 5.3. Time of Motion of the Shear Zones System in the Ribeira Belt

In order to contribute to the debate regarding the timing of motion of the shear zones in the RB, here we compared apatite U-Pb ages from granites and mylonites coupled with muscovite $^{40}Ar/^{39}Ar$ ages from mylonites and showed that apatite is susceptible to reset the U-Pb isotopic

system in response to ductile deformation in medium-grade shearing. If we assume that the shear zone was active during both times (544 ± 4 Ma, apatite U-Pb; 534 ± 1.5 Ma, muscovite $^{40}Ar/^{39}Ar$ age), then it must have been plastically active for 10 Ma or so. It is possible that this shear zone was active at higher temperature before cooling through the apatite closure temperature, but the equilibrium syn-kinematic mineral assemblage coupled with active deformation mechanisms in quartz and feldspar aggregates indicate a deformation temperature of 520 ± 6°C (Ribeiro et al., 2019), close to the closure temperature of Pb in apatite. Additionally, there is no relict evidence for higher temperature deformation.

Effort has been made in the last decade to date the ductile motion of the shear zones. However, most ages come from single mineral-method analysis (e.g., monazite U-Pb dating) with no mineral geochemistry and coupled textural evidence to establish the relationship between age and deformation/metamorphism (Passarelli et al., 2011, 2008). Some of the available ages are not clearly related with deformation, being more likely related with the igneous crystallization age instead (Passarelli et al., 2019, 2011, 2008, 2004). The lack of detailed data may lead to overestimated ages and interpretations, suggesting that some of these shear zones correspond to suture zones with ages similar to the regional metamorphism of each tectonic blocks as suggested in the current literature (Passarelli et al., 2011, 2008). The TSZ in particular has a shear history recorded at greenschist facies, condition in which many commonly datable minerals are closed for resetting or require special conditions to reset (e.g. monazite, zircon, titanite U-Pb). We have shown that zircon and titanite record the igneous age even from grains extracted from strongly deformed (mylonite to ultramylonite) samples, while the two methods that constrain lower temperature (i.e., $^{40}Ar/^{39}Ar$ in muscovite and U-Pb in apatite) cooling times have yielded younger ages that are interpreted as constraining the duration of ductile shearing. It suggests that geochronological analysis by a single mineral phase is not sufficient to accurately date shear zones (e.g., Van Der Pluijm et al., 1994; Schärer et al., 1994).

Therefore, it is possible that the RB shear zones have nucleated at earlier times, implying in a different tectonic role. The results presented for the TSZ indicate a ~60 Ma interval between the protolith crystallization age (ca. 606 ± 8 Ma) obtained through U-Pb ages from zircon, titanite and apatite from deformed and undeformed samples and the timing of deformation obtained through apatite U-Pb ages from mylonite samples (ca. 544 ± 4 Ma at ~500°C). As discussed before, the data from the TSZ suggest a minimum interval of ductile deformation of ~10 Ma with a cooling rate of ~5°C/Ma, which is in good agreement with a more regional study presented in Tassinari et al. (2006). Since some of the previously published ages cannot be

directly correlated with the shear zone kinematics, we suggest a detailed geochronological revision through multiple analysis in view of the petrochronology tools (Engi, 2018) by using different mineral phases and methods with their respective closure temperature estimates, textural relationships, geochemical signature (e.g., Engi, 2018; Van Der Pluijm et al., 1994; Schärer et al., 1994). Proper pressure-temperature estimates from the shear zones is, however, required to indicate which minerals are more susceptible to record the timing of the ductile deformation (e.g., Oliot et al., 2010; Ribeiro et al., 2019; Schärer et al., 1994). In case younger ages than the previously published were found, the tectonic model of the shear zone in the RB need to be reviewed, since it is possible that some of these shear zones could correspond to crustal structures related to scape tectonics assisting in the terranes dispersion during collisional late stages instead of sutures zones.

## 6. CONCLUSIONS

The investigation of the ages of multiple time markers allowed us to better constrain shearing and deformation on the upper-greenschist facies Taxaquara Shear Zone, a major transpressive dextral-shear zone in the Ribeira Belt (Brazil) (Ribeiro et al., 2019). From this, our main conclusions are:

i. Apatite grains from medium-grade granitic mylonite underwent recrystallization and chemical re-equilibration modifying both its original REE + Sr + Y as well as resetting its age when compared with similar results from igneous apatite in the undeformed protolith. Due to the lack of detailed studies regarding apatite mechanisms of recrystallization, investigations evolving electron backscattering diffraction (EBSD) coupled with electron microprobe chemical analyses are required to understand the driving factors behind this mechanism;

ii. U-Pb dating on apatite from medium-grade mylonites can faithfully record the timing of motion of a mid-crustal shear zone in response to ductile deformation. Textural relations, P-T conditions and closure temperature estimates established the link between age and deformation condition. As shown in this study, the apatite age can be independent of its chemistry, suggesting that apatite with igneous or metamorphic geochemical signature are susceptible to have the U-Pb system reset in response to deformation;

iii. The apatite U-Pb ages from middle-crustal shear zones can significantly expand the geochronological data set in comparison to commonly applied muscovite $^{40}Ar/^{39}Ar$ ages determinations due to the significant distinguished closure temperature. While

the muscovite analysed in this paper yields a closure temperature interval between 424 – 457 °C for 5°C/Ma of cooling rate, the apatite yields 466 – 503°C allowing it to record a deformation at higher grade and close to the peak of temperature of the TSZ. In this case, there is a 10 Ma duration of ductile deformation (continuous or not) that was not resolvable before. Since most mid-crustal shear zones are investigated through muscovite $^{40}Ar/^{39}Ar$ dating, this finding suggests that many of them may have an underestimated timing of motion.

iv. The comparison between our results with the published data regarding the timing of motion of the shear zones in the RB suggests a significant discrepancy. While our results indicate an interval of motion of ~10 Ma and a cooling rate of ~5°C/Ma, the data for other shear zones, interpreted as suture zones, indicate an interval of motion of 90 – 100 Ma with highly variable cooling rates. We suggest that a detailed characterization of the dated minerals is necessary to interpret the significance of age results and basing interpretations on whether the age dates magma crystallization or metamorphism/deformation. Our approach using multiple geochronological analysis of different mineral phases with different closure temperature, supported by textural relationships, mineral geochemical and P-T estimates for the deformation, is necessary to support age interpretation and can be used as a template for other shear zones. In case it results in younger ages such as the TSZ, it is possible that these shear zones do not correspond to suture zones with ages similar to regional metamorphism, but to crustal structures related to scape tectonics in late collisional stages, which may play a major role in the terranes dispersion.

## 5 ACKNOWLEDGEMENTS

Financial support was provided by FAPESP (São Paulo Research Foundation – Brazil) via postgraduate scholarships 2018/00320-9 and 2018/16307-1 to BVR, and research grants 2018/10012-0 to FMF and 2015/03737-0 to MAS Basei, CNPq grants 443439/2014-1 and 305074/2015-6 to GACC and by the Australian Research Council through grant FL160100168 to PAC. The authors thank the undergraduate student Erilio Soares for helping with the mineral separation. Dr. Ashley Wainwright and Dr. Massimo Raveggi are thanked for the assistance with U-Pb and trace elements data acquisition. Jinwei Guo, PhD candidate at China University of Geosciences (Wuhan), is thanked for the rich discussions during development of the manuscript.

# 5 CHAPTER 5

## CONCLUSIONS

### 5.1 Conditions and mechanisms of deformation of the TSZ

The TSZ cross-cut schists from the Votuverava and São Roque Groups, but they are not preserved due to the intense tropical weathering. It also affects igneous rocks from the Piedade and Pilar do Sul Suits giving rise to quartz-feldspathic mylonites and ultramylonites, recording deformation in macro to micro scale. Since its recognition in Hennies et al. (1967), its deformation and mechanisms of deformation have never been properly descripted and quantified.

The granitic mylonites and ultramylonites present a neoformed assemblage composed of quartz + oligoclase + K-feldspar + biotite + muscovite + rutile + magnetite. Monomineralic quartz ribbons and feldspar porphyroclasts (mostly σ-type) are common features in all samples. The pseudosection with Si (p.f.u) from muscovite and sodium molar number from plagioclase ($X_{Na}$) performed on Perple_X'6.8.3 (Connolly, 2005), couple with muscovite – biotite geothermometer (Hoisch, 1989), constrain the deformation condition at 513 – 525°C and 3.9 – 4.4kbar. These data indicate that the TSZ correspond to a mid-crustal structure developed at ~11 – 12 km depth and a geothermal gradient of ~46.5 – 42.5°C/km. The temperature interval indicates ductile behavior for quartz and transitional brittle-ductile behavior for feldspar, as recorded in the microstructures.

Evidences from petrographic descriptions, topological parameters (e.g., grain-size) and CPOs from monomineralic quartz ribbons indicate that quartz accommodated deformation via dislocation creep achieving the transition between regimes 2 and 3 of Hirth and Tullis (1992), at a mean strain rate of $10^{-13}$ – $10^{-12}$ $s^{-1}$, with asymmetrical to symmetrical monoclinic CPO and activation of 'basal-<a>' + 'rhomb-<a>' slip systems. Fine-grained quartz from polymineralic matrix, however, presents random to weak CPO, which may indicate the shift between dislocation creep to diffusion creep (Kilian et al., 2011; Platt, 2015). Feldspar is present as porphyroclasts and in the fine-grained polyphase matrix. The feldspar porphyroclasts display evidences of dislocation creep (e.g., mechanical twinning) concomitant with brittle microstructures (e.g., microfaults). In the matrix, it presents textural evidence of recrystallization but with random CPO for both oligoclase and K-feldspar, which may suggest that diffusion creep processes via granular flow fluid-assisted dissolution-precipitation creep played a role (e.g., Oliot et al., 2014; Platt, 2015).

## 5.2 Kinematics, vorticity and strain patterns of the TSZ

The Taxaquara Shear Zone (TSZ) was firstly described as a structure with vertical NE-SW foliation with sub-horizontal stretching lineation plunging to W (Hennies et al., 1967). At that time, the TSZ was classified as a transcurrent structure, but its kinematics was unclear. On this Master's dissertation, the kinematics and structural setting was detailed characterized.

The TSZ display a penetrative mylonitic foliation trending N062/70SE with stretching lineation mainly marked by elongated quartz grains and variable plunging (~0 – 40°) to NE. The dextral kinematics was characterized through field-based observation such as C-type shear band cleavage, type-σ and type-δ tail feldspar porphyroclasts and internally faulted domino-type feldspar. Fish-shaped muscovite, feldspar porphyroclasts with asymmetrical tails, quartz oblique shape preferred orientation and quarter structures in feldspar also demonstrate the dextral kinematics in thin sections from mylonite and ultramylonite samples. Superposed deformation and/or sinistral kinematics was nor observed.

Vorticity data from the rigid porphyroclast method range from 50 – 70% of pure shear contribution, while the results from the δ/β method indicate partitioning of deformation varying between 65 – 99% of simple shear contribution and 68-80% of pure shear contribution recorded in different samples. The similar vorticity number for all samples from the rigid porphyroclast method represents the medium to high strain rather than simple vs. pure shear contribution (Stahr and Law, 2014, 2011). Therefore, the TSZ was developed under a sub-simple shear environment with partitioning between pure and simple shear with predominance of the last. The geometries of the strain ellipsoids obtained through SPO analyses indicate a transition from oblate to prolate as indicated in Sanderson and Marchini (1984) and the compilation of strain data from other transcurrent shear zones in the RB indicates the predominance of oblate geometry (75%), strongly pointing that these structures were developed under a regional transpressive system.

## 5.3 Petrochronology of the TSZ: dating the timing of deformation of mid-crustal shear zones

Muscovite $^{40}Ar/^{39}Ar$ and apatite, titanite and zircon U-Pb analyses were carried out in order to constrain the timing of deformation of the TSZ. Fish-shaped muscovite from granitic mylonite samples yields an average $^{40}Ar/^{39}Ar$ age of 534 ± 1.5 Ma at ~435 ± 11°C, according to the closure temperature estimates based on Ar diffusion in muscovite. However, it is proved that the apatite U-Pb ages from granitic mylonite samples are reliable to record ductile at higher

condition than the muscovite as shown by the age difference between the granitic mylonite samples (544 ± 4 Ma) and the undeformed granite samples (613 ± 8 Ma), suggesting the reset of the U-Pb system in response to deformation. Thus, due to the proximity between the apatite closure temperature estimates based on Pb diffusion (495 ± 7°C) and the deformation temperature (519 ± 6°C; Ribeiro et al., 2019) and to the absence of evidences of previous deformation at higher temperature condition, it is likely that ductile deformation in the TSZ started around 544 ± 4 Ma. Taking the muscovite $^{40}Ar/^{39}Ar$ and apatite U-Pb ages from granitic mylonite samples with its respective closure temperatures, a cooling rate of ~5ºC/Ma can be estimated which resemble that regionally proposed in Tassinari et al. (2006).

The comparison between the geochronological results from the TSZ with the published ages from other shear zones geographically close to it suggests a significant difference. While the results from the TSZ indicate an interval of motion of ~10 Ma with a cooling rate of 5°C/Ma, the published data for other shear zones indicate an interval of motion of 90 – 100 Ma with variable cooling rates (Passarelli et al., 2008). While the approach for the TSZ was based on petrochronology, i.e. linking the ages with textures, mineral geochemistry and proper closure temperature estimates in comparison to the TSZ deformation condition, theses published ages from greenschist-amphibolite facies shear zones were obtained through zircon, monazite and allanite U-Pb ages with no textural and/or chemical evidence of metamorphic signature and isotopic system resetting (Passarelli et al., 2008). Due to the significant discrepancy, a detailed revision of these ages is required under the petrochronology approach to improve the understanding of the role of these shear zones in the RB. In case this revision results in younger ages such as the TSZ, a new tectonic model is required. It is now suggested that many of these shear zones in the RB correspond to suture zones with ages similar to the ‘regional metamorphism’ (Passarelli et al., 2011, 2008), however secondary model based on detailed petrochronology could show that they correspond to crustal structure related to scape tectonics in late collision stages, which may play a role in the terranes dispersion.

# 6 CHAPTER 6

## REFERENCES


Aleinikoff, J.N., Schenck, W.S., Plank, M.O., Srogi, L., Fanning, C.M., Kamo, S.L., Bosbyshell, H., 2006. Deciphering igneous and metamorphic events in high-grade rocks of the Wilmington Complex, Delaware: Morphology, cathodoluminescence and backscattered electron zoning, and SHRIMP U-Pb geochronology of zircon and monazite. Geol. Soc. Am. Bull. 118, 39–64.

Aleinikoff, J.N., Wintsch, R.P., Tollo, R.P., Unruh, D.M., Fanning, C.M., Schmitz, M.D., 2007. Ages and origins of rocks of the Killingworth dome, south-central Connecticut: Implications for the tectonic evolution of southern New England. Am. J. Sci. 307, 63–118.

Almeida, F.F.M., Amaral, G., Cordani, U., Kawashita, K., 1973. The Precambrian evolution of the South American Cratonic Margin, South of Amazon River, in: The Ocean Basin and Margins. New York Plenum, pp. 411–416.

Alves, A., Janasi, V. de A., Campos Neto, M. da C., Heaman, L., Simonetti, A., 2013. U-Pb geochronology of the granite magmatism in the embu terrane: Implications for the evolution of the central ribeira belt, SE Brazil. Precambrian Res. 230, 1–12. https://doi.org/10.1016/j.precamres.2013.01.018

Bruguier, O., Byrne, D.I., Harris, L.B., Pidgeon, R.T., Bosch, D., 2002. U-Pb chronology of the Northampton Complex, Western Australia - evidence for Grenvillian sedimentation, metamorphism and deformation and geodynamic implications. Contrib. to Mineral. Petrol. 136, 258–272. https://doi.org/10.1007/s004100050537

Campanha, G.A.C., 2002. O papel do sistema de zonas de cisalhamento transcorrentes na configuracao da porcao meridional da faixa Ribeira. Inst. Geosci. - Univ. São Paulo. https://doi.org/10.1073/pnas.0703993104

Campanha, G.A.C., Brito Neves, B.B., 2004. Frontal and oblique tectonics in the Brazilian shield. Episodes 27, 255–259.

Campanha, G.A.C., Faleiros, F.M., Basei, M.A.S., Tassinari, C.C.G., Nutman, A.P., Vasconcelos, P.M., 2015. Geochemistry and age of mafic rocks from the Votuverava

Group, southern Ribeira Belt, Brazil: Evidence for 1490Ma oceanic back-arc magmatism. Precambrian Res. 266, 530–550. https://doi.org/10.1016/j.precamres.2015.05.026

Campanha, G.A.C., Sadowski, G.R., 1999. Tectonics of the southern portion of the Ribeira Belt (Apiaí Domain). Precambrian Res. 98, 31–51. https://doi.org/10.1016/S0301-9268(99)00027-3

Campos Neto, M.C., 2000. Orogenic system from southwestern Gondwana: an approach to brasilian-pan afrian cycle and orogenic collage in southeastern Brazil, in: Tectonic Evolution of South America. pp. 335–365.

Cherniak, D.J., Lanford, W.A., Ryerson, F.J., 1991. Lead diffusion in apatite and zircon using ion implantation and Rutherford Backscattering techniques. Geochim. Cosmochim. Acta 55, 1663–1673.

Chew, D.M., Petrus, J.A., Kamber, B.S., 2014. U-Pb LA-ICPMS dating using accessory mineral standards with variable common Pb. Chem. Geol. 363, 185–199. https://doi.org/10.1016/j.chemgeo.2013.11.006

Chew, D.M., Sylvester, P.J., Tubrett, M.N., 2011. U-Pb and Th-Pb dating of apatite by LA-ICPMS. Chem. Geol. 280, 200–216. https://doi.org/10.1016/j.chemgeo.2010.11.010

Chu, M., Wang, K., Griffin, W.L., Chung, S., Reilly, S.Y.O., Pearson, N.J., Iizuka, Y., 2009. Apatite Composition: Tracing Petrogenetic Processes inTranshimalayan Granitoids. J. Petrol. 50, 1829–1855. https://doi.org/10.1093/petrology/egp054

Connolly, J.A.., 2005. Computation of phase equilibria by linear programming: A tool for geodynamic modeling and its application to subduction zone decarbonation. Earth Planet. Sci. Lett. 326, 524–541.

Corfu, F., Stone, D., 1998. The significance of titanite and apatite U-Pb ages: Constraints for the post-magmatic thermal-hydrothermal evolution of a batholithic complex, Berens River area, northwestern Superior Province, Canada. Geochim. Cosmochim. Acta 62, 2979–2995. https://doi.org/10.1016/S0016-7037(98)00225-7

Dodson, M.H., 1973. Closure temperature in cooling geochronological and petrological systems. Contrib. to Mineral. Petrol. 40, 259–274.

Ebert, H.D., Chemale, F., Babinski, M., Schmus, W.R. Van, 1996. Tectonic setting and U/Pb

zircon dating of the plutonic Socorro Complex in the Transpressive. Tectonics 15, 688–699.

Ebert, H.D., Hasui, Y., 1992. Transpressive evolution of a collisional suture zone in SE-Brazil. 29th Int. Geol. Congr.

Egydio-Silva, M., Vauchez, A., Fossen, H., Gonçalves Cavalcante, G.C., Xavier, B.C., 2018. Connecting the Araçuaí and Ribeira belts (SE – Brazil): Progressive transition from contractional to transpressive strain regime during the Brasiliano orogeny. J. South Am. Earth Sci. 86, 127–139. https://doi.org/10.1016/j.jsames.2018.06.005

Engi, M., 2018. Petrochronology Based on REE-Minerals: Monazite, Allanite, Xenotime, Apatite. Rev. Mineral. Geochemistry 83, 365–418. https://doi.org/10.2138/rmg.2017.83.12

Faleiros, F.M., 2003. Zona de cisalhamento Ribeira: deformação, metamorfismo e termobarometria de veios sin-tectônicos. University of São Paulo.

Faleiros, F.M., Campanha, G.A.C., Maria, R., Fuzikawa, K., 2010. Quartz recrystallization regimes , c -axis texture transitions and fl uid inclusion reequilibration in a prograde greenschist to amphibolite facies mylonite zone ( Ribeira Shear Zone , SE Brazil ). Tectonophysics 485, 193–214. https://doi.org/10.1016/j.tecto.2009.12.014

Faleiros, F.M., Campanha, G.A.C., Martins, L., Vlach, S.R.F., Vasconcelos, P.M., 2011. Ediacaran high-pressure collision metamorphism and tectonics of the southern Ribeira Belt (SE Brazil): evidence for terrane accretion and dispersion during Gondwana assembly. Precambrian Res. 189, 263–291.

Faleiros, F.M., Campanha, G.A.C., Pavan, M., Almeida, V. V., Rodrigues, S.W.O., Araújo, B.P., 2016a. Short-lived polyphase deformation during crustal thickening and exhumation of a collisional orogen (Ribeira Belt, Brazil). J. Struct. Geol. 93, 106–130. https://doi.org/10.1016/j.jsg.2016.10.006

Faleiros, F.M., Moraes, R., Pavan, M., Campanha, G.A.C., 2016b. A new empirical calibration of the quartz c-axis fabric opening-angle deformation thermometer. Tectonophysics 671, 173–182. https://doi.org/10.1016/j.tecto.2016.01.014

Fedorov, E.S., 1982. Eine neue Methode der optischen Untersuchung von Krystallplatten in parallelem Lichte. Tschermak's Mineral. und Petrogr. Mitth. 12, 505–509.

Flowers, R.M., Bowring, S.A., Reiners, P.W., 2006. Low long-term erosion rates and extreme continental stability documented by ancient (U-Th)/He dates. Geology 34, 925–928.

Fossen, H., Cavalcante, G.C.G., 2017. Shear zones – A review. Earth-Science Rev. 171, 434–455. https://doi.org/10.1016/j.earscirev.2017.05.002

Fossen, H., Tikoff, B., Teyssier, C., 1994. Strain modeling of transpressional and transtensional deformation. Nor. Geol. Tidsskr. 74, 134–145.

Hackspacher, P.C., Fetter, A.H., Teixeira, W., Dantas, E.L., Ebert, H.D., Trouw, R.A.J., Vasconcelos, P., 2004. Final stages of the Brasiliano Orogenesis in SE Brazil: U-Pb and40Ar/39Ar evidence for overprinting of the Brasília Belt by the Ribeira Belt Tectonics. J. Virtual Explor. 17, 1–18.

Hall, J.W., Glorie, S., Reid, A.J., Boone, S.C., Collins, A.S., Gleadow, A., 2018. An apatite U–Pb thermal history map for the northern Gawler Craton, South Australia. Geosci. Front. 9, 1293–1308. https://doi.org/10.1016/j.gsf.2017.12.010

Harrison, T.M., Célérier, J., Aikman, A.B., Hermann, J., Heizler, M.T., 2009. Diffusion of40Ar in muscovite. Geochim. Cosmochim. Acta 73, 1039–1051. https://doi.org/10.1016/j.gca.2008.09.038

Hasui, Y., 1975. Geologia da folha de são Roque. Bol. IG, Inst. Geociências, USP 6, 157–183. https://doi.org/10.2307/1134315

Hasui, Y., 1973. Tectônica da área das folhas de São Roque e Pilar do Sul. University of São Paulo.

Hasui, Y., Carneiro, C.R., Coimbra, A.M., 1975. The Ribeira folded belt. Rev. Bras. Geociências 5, 257–266.

Hasui, Y., Sadowski, G.R., 1976. Evolução geológica do Pré-Cambriano na região sudeste do Estado de São Paulo. Rev. Bras. Geociências 6, 182–200.

Heilbron, M., Pedrosa-Soares, A.C., Campos Neto, M.D.C., Silva, L.D., Trouw, R.A.J., Janasi, V.D.A., 2004. Província Mantiqueira, in: Geologia Do Continente Sul-Americano: Evolução Da Obra Ed Fernando Flávio Marques de Almeida. pp. 203–235.

Hennies, W.T., Hasui, Y., Penalva, F., 1967. O falhamento transcorrente de Taxaquara. Congr. Bras. Geol. 21.

Henrichs, I.A., O'Sullivan, G., Chew, D.M., Mark, C., Babechuk, M.G., McKenna, C., Emo, R., 2018. The trace element and U-Pb systematics of metamorphic apatite. Chem. Geol. 483, 218–238. https://doi.org/10.1016/j.chemgeo.2017.12.031

Hirth, G., Teyssier, C., Dunlap, W.J., 2001. An evaluation of quartzite flow laws based on comparisons between experimentally and naturally deformed rocks. Int. J. Earth Sci. 90, 77–87. https://doi.org/10.1007/s005310000152

Hirth, G., Tullis, J., 1992. Dislocation creep regimes in quartz aggregates. J. Struct. Geol. 14, 145–159. https://doi.org/10.1016/0191-8141(92)90053-Y

Hoisch, T.D., 1989. A muscovite-biotite geothermometer. Am. Mineral. 74, 565–572.

Holland, T.J.B., Powell, R., 2011. An improved and extended internally consistent thermodynamic dataset for phases of petrological interest, involving a new equation of state for solids. J. Metamorph. Geol. 29, 333–383.

Hunter, N.J.R., Weinberg, R.F., Wilson, C.J.L., Law, R.D., 2018. A new technique for quantifying symmetry and opening angles in quartz c-axis pole figures: Implications for interpreting the kinematic and thermal properties of rocks. J. Struct. Geol. 112, 1–6. https://doi.org/10.1016/J.JSG.2018.04.006

Jackson, S.E., Pearson, N.J., Griffin, W.L., Belousova, E.A., 2004. The application of laser ablation-inductively coupled plasma-mass spectrometry to in situ U–Pb zircon geochronology. Chem. Geol. 211, 47–69.

James, D.E., Assumpção, M., 1996. Tectonic implications of S-wave anisotropy beneath SE Brazil. Geophys. J. Int. 126, 1–10. https://doi.org/10.1111/j.1365-246X.1996.tb05263.x

Janasi, V.A., Leite, R.J., Van Schmus, W.R., 2001. U-Pb chronostratigraphy of the granitic magmatism in the Agudos Grandes Batholith (West of São Paulo, Brazil) - Implications for the evolution of the Ribeira Belt. J. South Am. Earth Sci. 14, 363–376. https://doi.org/10.1016/S0895-9811(01)00034-7

Kennedy, A.K., Kamo, S.L., Nasdala, L., Timms, N.E., 2010. Grenville Skarn Titanite: Potential Reference Material for Sims U-Th–Pb Analysis. Can. Mineral. 48, 1423–1443.

Kilian, R., Heilbronner, R., Stünitz, H., 2011. Quartz grain size reduction in a granitoid rock and the transition from dislocation to diffusion creep. J. Struct. Geol. 33, 1265–1284. https://doi.org/10.1016/j.jsg.2011.05.004

Kirkland, C.L., Fougerouse, D., Reddy, S.M., Hollis, J., Saxey, D.W., 2018a. Assessing the mechanisms of common Pb incorporation into titanite. Chem. Geol. 483, 558–566. https://doi.org/10.1016/j.chemgeo.2018.03.026

Kirkland, C.L., Hollis, J., Danišík, M., Petersen, J., Evans, N.J., McDonald, B.J., 2017. Apatite and titanite from the Karrat Group, Greenland; implications for charting the thermal evolution of crust from the U-Pb geochronology of common Pb bearing phases. Precambrian Res. 300, 107–120. https://doi.org/10.1016/j.precamres.2017.07.033

Kirkland, C.L., Yakymchuk, C., Szilas, K., Evans, N., Hollis, J., McDonald, B., Gardiner, N.J., 2018b. Apatite: a U-Pb thermochronometer or geochronometer? Lithos 318–319, 143–157. https://doi.org/10.1016/j.lithos.2018.08.007

Kruhl, J.H., 1996. Prism- and basal-plane parallel subgrain boundaries in quartz: a microstructural geothermobaromether. J. Metamorph. Geol. 14, 581–589. https://doi.org/10.1046/j.1525-1314.1996.00413.x

Launeau, P., Cruden, A.R., 1998. Magmatic fabric acquisition mechanisms in a syenite: Results of a combined anisotropy of magnetic susceptibility and image analysis study. J. Geophys. Res. Solid Earth 103, 5067–5089. https://doi.org/10.1029/97JB02670

Launeau, P., Robin, P.Y.F., 2005. Determination of fabric and strain ellipsoids from measured sectional ellipses - Implementation and applications. J. Struct. Geol. 27, 2223–2233. https://doi.org/10.1016/j.jsg.2005.08.003

Launeau, P., Robin, P.Y.F., 2003a. SPO.

Launeau, P., Robin, P.Y.F., 2003b. Ellipsoid v. 2003.

Law, R.D., 2014. Deformation thermometry based on quartz c-axis fabrics and recrystallization microstructures: A review. J. Struct. Geol. 66, 129–161. https://doi.org/10.1016/j.jsg.2014.05.023

Leite, R.J., Heaman, L.M., de Assis Janasi, V., Martins, L., Creaser, R.A., 2007. The late- to postorogenic transition in the Neoproterozoic Agudos Grandes Granite Batholith (Apiaí Domain, SE Brazil): Constraints from geology, mineralogy, and U-Pb geochronology. J. South Am. Earth Sci. 23, 193–212. https://doi.org/10.1016/j.jsames.2006.09.022

Lexa, O., 2003. Numerical Approaches in Structural and Microstructural Analyses. Charles University, Prague.

Lin, S., Jiang, D., Williams, P.F., 1998. Transpression (or transtension) zones of triclinic symmetry: natural example and theoretical modelling. Geol. Soc. London, Spec. Publ. 135, 41–57. https://doi.org/10.1144/GSL.SP.1998.135.01.04

Ludwig, K.R., 1991. Isoplot–a plotting and regression program for radiogenic isotope data. USGS Open-file Rep. 91–445.

Machado, R., Dehler, N.M., Vasconcelos, P., 2007. 40Ar/39Ar ages (600-570 Ma) of the Serra do Azeite transtensional shear zone: Evidence for syncontractional extension in the Cajati area, southern Ribeira belt. An. Acad. Bras. Cienc. 79, 713–723. https://doi.org/10.1182/blood-2006-09-046128

McDonough, W.F., Sun, S. -s., 1995. The composition of the Earth. Chem. Geol. 2541, 223–253.

McDougall, I., Harrison, T.M., 1999. Geochronology and Thermocronology by the 40Ar/39Ar Method, Second edi. ed. Oxford University Press, New York.

Nutman, A.P., 2007. Apatite recrystallisation during prograde metamorphism, Cooma, southeast Australia: Implications for using an apatite-graphite association as a biotracer in ancient metasedimentary rocks. Aust. J. Earth Sci. 54, 1023–1032. https://doi.org/10.1080/08120090701488321

Oliot, E., Goncalves, P., Marquer, D., 2010. Role of plagioclase and reaction softening in a metagranite shear zone at mid-crustal conditions (Gotthard Massif, Swiss Central Alps). J. Metamorph. Geol. 28, 849–871. https://doi.org/10.1111/j.1525-1314.2010.00897.x

Oliot, E., Goncalves, P., Schulmann, K., Marquer, D., Lexa, O., 2014. Mid-crustal shear zone formation in granitic rocks: Constraints from quantitative textural and crystallographic preferred orientations analyses. Tectonophysics 612–613, 63–80. https://doi.org/10.1016/j.tecto.2013.11.032

Oriolo, S., Oyhantçabal, P., Wemmer, K., Basei, M.A.S., Benowitz, J., Pfänder, J., Hannich, F., Siegesmund, S., 2016. Timing of deformation in the Sarandí del Yí Shear Zone, Uruguay: Implications for the amalgamation of western Gondwana during the Neoproterozoic Brasiliano-Pan-African Orogeny. Tectonics 35, 754–771. https://doi.org/10.1002/2015TC004052

Oriolo, S., Wemmer, K., Oyhantçabal, P., Fossen, H., Schulz, B., Siegesmund, S., 2018.

Geochronology of shear zones – A review. Earth-Science Rev. 185, 665–683. https://doi.org/10.1016/j.earscirev.2018.07.007

Pan, L.C., Hu, R.Z., Wang, X.S., Bi, X.W., Zhu, J.J., Li, C., 2016. Apatite trace element and halogen compositions as petrogenetic-metallogenic indicators: Examples from four granite plutons in the Sanjiang region, SW China. Lithos 254–255, 118–130. https://doi.org/10.1016/j.lithos.2016.03.010

Passarelli, C.R., Basei, M.A.S., Campos Neto, M.C., Siga Jr., O., Prazeres Filho, H.J., 2004. Geocronologia e Geologia Isotópica dos Terrenos Pré -Cambrianos da Porção Sul-Oriental do Estado de São Paulo. Geol. USP - Ser. Cient. 4, 55–74. https://doi.org/10.5327/S1519-874X2004000100004

Passarelli, C.R., Basei, M.A.S., Prazeres-Filho, H.J., Siga, O., Szabó, G.A.J., Marco-Neto, J., 2007. Structural and geochronological constraints on the evolution of the Juréia Massif, Registro Domain, State of São Paulo, Brazil. An. Acad. Bras. Cienc. 79, 441–455.

Passarelli, C.R., Basei, M.A.S., Wemmer, K., Siga, O., Oyhantçabal, P., 2011. Major shear zones of southern Brazil and Uruguay: Escape tectonics in the eastern border of Rio de La plata and Paranapanema cratons during the Western Gondwana amalgamation. Int. J. Earth Sci. 100, 391–414. https://doi.org/10.1007/s00531-010-0594-2

Passarelli, C.R., Verma, S.K., McReath, I., Basei, M.A.S., Siga, O., 2019. Tracing the history from Rodinia break-up to the Gondwana amalgamation in the Embu Terrane, southern Ribeira Belt, Brazil. Lithos 342–343, 1–17. https://doi.org/10.1016/j.lithos.2019.05.024

Passarelli, C.R., Wemmer, K., Basei, M.A.S., Siga Jr., O., 2008. Tectono-thermal evolution of the SE São Paulo State Precambrian terranes, in: VI South American Symposium on Isotope Geology. p. 6.

Passchier, C.W., 1988. The use of Mohr circles to describe non-coaxial progressive deformation. Tectonophysics 149, 323–338. https://doi.org/10.1016/0040-1951(88)90181-3

Passchier, C.W., 1987. Stable positions of rigid objects in non-coaxial flow-a study in vorticity analysis. J. Struct. Geol. 9, 679–690. https://doi.org/10.1016/0191-8141(87)90152-0

Passchier, C.W., Trouw, R.A.J., 2005. Microtectonics, 2nd ed. ed. Springer, Boston, Mass.

Passchier, C.W., Urai, J.L., 1988. Vorticity and strain analysis using Mohr diagrams. J. Struct. Geol. 10, 755–763. https://doi.org/10.1016/0191-8141(88)90082-X

Paton, C., Hellstrom, J., Paul, B., Woodhead, J., Hergt, J., 2011. Iolite: Freeware for the visualisation and processing of mass spectrometric data. J. Anal. At. Spectrom. 26, 2508–2518.

Payne, J.L., Hand, M., Barovich, K.M., Wade, B.P., 2008. Temporal constraints on the timing of high-grade metamorphism in the northern Gawler Craton: implications for assembly of the Australian Proterozoic. Aust. J. Earth Sci. 55, 623–640.

Phillips, D., Matchan, E.L., 2013. Ultra-high precision40Ar/39Ar ages for Fish Canyon Tuff and Alder Creek Rhyolite sanidine: New dating standards required? Geochim. Cosmochim. Acta 121, 229–239. https://doi.org/10.1016/j.gca.2013.07.003

Pitzer, K., Sterner, S., 1994. Equations of state valid continuously from zero to extreme pressures for H20 and CO2. J. Chem. Phys. 101, 3111–3116.

Platt, J.P., 2015. Rheology of two-phase systems: A microphysical and observational approach. J. Struct. Geol. 77, 213–227. https://doi.org/10.1016/j.jsg.2015.05.003

Post, A., Tullis, J., 1999. A recrystallized grain size piezometer for experimentally deformed feldspar aggregates. Tectonophysics 303, 159–173. https://doi.org/10.1016/S0040-1951(98)00260-1

Prior, D.J., Wheeler, J., 1999. Feldspar fabrics in a greenschist facies albite-rich mylonite from electron backscatter diffraction. Tectonophysics 303, 29–49. https://doi.org/10.1016/S0040-1951(98)00257-1

Ribeiro, B.V., Campanha, G.A.C., Faleiros, F.M., Weinberg, R.F., Hunter, N.J.R., Lagoeiro, L., 2019. Kinematics, deformational conditions and tectonic setting of the Taxaquara Shear Zone, a major transpressional zone of the Ribeira Belt (SE Brazil). Tectonophysics 751, 83–108. https://doi.org/10.1016/j.tecto.2018.12.025

Robin, P.Y.F., Cruden, A.R., 1994. Strain and vorticity patterns in ideally ductile transpression zones. J. Struct. Geol. 16, 447–466. https://doi.org/10.1016/0191-8141(94)90090-6

Sanderson, D.J., Marchini, W.R.D., 1984. Transpression. J. Struct. Geol. 6, 449–458.

Schärer, U., Lian-Sheng Zhang, Tapponnier, P., 1994. Duration of strike-slip movements in large shear zones: The Red River belt, China. Earth Planet. Sci. Lett. 126, 379–397. https://doi.org/10.1016/0012-821X(94)90119-8

Simpson, C., De Paor, D.G., 1993. Strain and kinematic analysis in general shear zones. J. Struct. Geol. 15, 1–20. https://doi.org/10.1016/0191-8141(93)90075-L

Slama, J., Kosler, J., Condon, D.J., Crowley, J.L., Gerdes, A., Hanchar, J. M. Horstwood, M. S. A. Morris, G.A., Nasdala, L., Norberg, N., Schaltegger, U. Schoene, N., Tubrett, M. N. Whitehouse, M.J., 2008. Plesovice zircon - a new natural reference material for U-Pb and Hf isotopic microanalysis. Chem. Geol. 249, 1–35.

Stacey, J.S., Kramers, J.D., 1975. Approximation of terrestrial lead isotope evolution by a two-stage model. Earth Planet. Sci. Lett. 26, 207–221. https://doi.org/10.1016/0012-821X(75)90088-6

Stahr, D.W., Law, R.D., 2014. Strain memory of 2D and 3D rigid inclusion populations in viscous flows - What is clast SPO telling us? J. Struct. Geol. 68, 347–363. https://doi.org/10.1016/j.jsg.2014.05.028

Stahr, D.W., Law, R.D., 2011. Effect of finite strain on clast-based vorticity gauges. J. Struct. Geol. 33, 1178–1192. https://doi.org/10.1016/j.jsg.2011.05.002

Stipp, M., Stünitz, H., Heilbronner, R., Schmid, S.M., 2002a. The eastern Tonale fault zone: A “natural laboratory” for crystal plastic deformation of quartz over a temperature range from 250 to 700 °C. J. Struct. Geol. 24, 1861–1884. https://doi.org/10.1016/S0191-8141(02)00035-4

Stipp, M., Stünitz, H., Heilbronner, R., Schmid, S.M., 2002b. Dynamic recrystallization of quartz: correlation between natural and experimental conditions. Geol. Soc. London, Spec. Publ. 200, 171–190. https://doi.org/10.1144/GSL.SP.2001.200.01.11

Stipp, M., Tullis, J., 2003. The recrystallized grain size piezometer for quartz, Geophysical Research Letters. https://doi.org/10.1029/2003GL018444

Stipp, M., Tullis, J., Scherwath, M., Behrmann, J.H., 2010. A new perspective on paleopiezometry: Dynamically recrystallized grain size distributions indicate mechanism changes. Geology 38, 759–762.

Tassinari, C.C.G., Munha, J.M.U., Neto, D., Bento dos Santos, T.M., Cordani, U.G., Nutman,

A., Fonseca, P.E., 2006. Constrains on the Termochronological Evolution of Ribeira Fold Belt , Se Brasil : Evidence for Long-Term Elevated Geothermal Gradient of Neoproterozoic Orogenies. V South Am. Symp. Isot. Geol. Punta del Este., pp. 200–203 200–203.

Thomson, S.N., Gehrels, G.E., Ruiz, J., Buchwaldt, R., 2012. Routine low-damage apatite U-Pb dating using laser ablation–multicollector–ICPMS. Geochemistry, Geophys. Geosystems 13.

Turlin, F., Deruy, C., Eglinger, A., Vanderhaeghe, O., André-Mayer, A.S., Poujol, M., Moukhsil, A., Solgadi, F., 2018. A 70 Ma record of suprasolidus conditions in the large, hot, long-duration Grenville Orogen. Terra Nov. 30, 233–243. https://doi.org/10.1111/ter.12330

Twiss, R.J., 1977. Theory and applicability of a recrystallized grain size paleopiezometer, in: Stress in the Earth. pp. 227–244.

Van Der Pluijm, B.A., Mezger, K., Cosca, M.A., Essene, E.J., 1994. Determining the significance of high-grade shear zones by using temperature-time paths, with examples from the Grenville orogen. Geology 22, 743–746. https://doi.org/10.1130/0091-7613(1994)022<0743:DTSOHG>2.3.CO;2

Vauchez, A., 1987. The development of discrete shear-zones in a granite: stress, strain and changes in deformation mechanisms. Tectonophysics 133, 137–156. https://doi.org/10.1016/0040-1951(87)90286-1

Vauchez, A., Tommasi, A., Egydio-Silva, M., 1994. Self-identation of a heterogeneous continental lithosphere. Geology 22, 967–970. https://doi.org/10.1130/0091-7613(1994)022<0967:SIOAHC>2.3.CO;2

Viegas, G., Menegon, L., Archanjo, C., 2016. Brittle grain-size reduction of feldspar, phase mixing and strain localization in granitoids at mid-crustal conditions (Pernambuco shear zone, NE Brazil). Solid Earth 7, 375–396. https://doi.org/10.5194/se-7-375-2016

Wallis, S.R., 1995. Vorticity analysis and recognition of ductile extension in the Sanbagawa belt, SW Japan. J. Struct. Geol. 17, 1077–1093.

Wallis, S.R., 1992. Vorticity analysis in a metachert from the Sanbagawa Belt, SW Japan. J. Struct. Geol. 14, 271–280. https://doi.org/10.1016/0191-8141(92)90085-B

Watson, E.B., Green, T.H., 1981. Apatite/liquid partition coefficients for the rare earth elements and strontium. Earth Planet. Sci. Lett. 56, 405–421. https://doi.org/10.1016/0012-821X(81)90144-8

White, R.W., Powell, R., Johnson, T.E., 2014. The effect of Mn on mineral stability in metapelites revisited: new a–x relations for manganese-bearing minerals. J. Metamorph. Geol. 32, 809–828.

Wilson, C.J.L., Russell-Head, D.S., Kunze, K., Viola, G., 2007. The analysis of quartz c-axis fabrics using a modified optical microscope. J. Microsc. 227, 30–41. https://doi.org/10.1111/j.1365-2818.2007.01784.x

Xypolias, P., 2010. Vorticity analysis in shear zones: A review of methods and applications. J. Struct. Geol. 32, 2072–2092. https://doi.org/10.1016/j.jsg.2010.08.009

Zhu, G., Wang, Y., Liu, G., Niu, M., Xie, C., Li, C., 2005. 40Ar/39Ar dating of strike-slip motion on the Tan-Lu fault zone, East China. J. Struct. Geol. 27, 1379–1398. https://doi.org/10.1016/j.jsg.2005.04.007

# APÊNDICE A. Tabelas com resultados das análises geocronológicas

Sample PSB09 Apatite

| Spot | Isotopic ratios | | | | | Ages | | F207 | |
|---|---|---|---|---|---|---|---|---|---|
| | $^{206}Pb/^{238}U$ | $^{238}U/^{206}Pb$ | $^{238}U/^{206}Pb$ (2σ) | $^{207}Pb/^{206}Pb$ | $^{207}Pb/^{206}Pb$ (2σ) | $^{207}Pb/^{206}Pb$ Corrected ages | 2σ | % | |
| AP_PSB09B | 0.1203 | 8.313 | 0.256 | 0.256 | 0.011 | 563 | 19 | 24.137 | |
| AP_PSB09E | 0.1074 | 9.311 | 0.277 | 0.189 | 0.011 | 557 | 18 | 15.971 | |
| AP_PSB09_1 | 0.1125 | 8.889 | 0.284 | 0.251 | 0.013 | 531 | 19 | 23.681 | |
| AP_PSB09_2B | 0.1167 | 8.569 | 0.294 | 0.253 | 0.019 | 549 | 34 | 23.826 | |
| AP-PSB09-2E | 0.1179 | 8.482 | 0.367 | 0.236 | 0.017 | 569 | 28 | 21.731 | |
| AP_PSB09_3E | 0.277 | 3.610 | 0.378 | 0.587 | 0.045 | 602 | 110 | 64.663 | |
| AP_PSB09_4 | 0.1396 | 7.163 | 0.349 | 0.338 | 0.016 | 567 | 31 | 34.140 | |
| AP_PSB09_5 | 0.1102 | 9.074 | 0.305 | 0.229 | 0.012 | 539 | 20 | 20.864 | |
| AP_PSB09_7 | 0.1134 | 8.818 | 0.241 | 0.268 | 0.012 | 521 | 17 | 25.771 | |
| AP_PSB09_9 | 0.1923 | 5.200 | 0.270 | 0.522 | 0.029 | 514 | 48 | 56.839 | |
| AP_PSB09_10 | 0.206 | 4.854 | 0.283 | 0.487 | 0.030 | 603 | 58 | 52.401 | |
| AP_PSB09_11 | 0.1165 | 8.584 | 0.280 | 0.247 | 0.012 | 553 | 20 | 23.115 | |
| AP_PSB09_12 | 0.1293 | 7.734 | 0.502 | 0.302 | 0.026 | 560 | 42 | 29.811 | |
| AP_PSB09_13 | 0.1187 | 8.425 | 0.334 | 0.276 | 0.022 | 538 | 28 | 26.673 | |
| AP_PSB09_16 | 0.118 | 8.475 | 0.208 | 0.219 | 0.007 | 548 | 15 | 24.808 | |
| AP_PSB09_17 | 0.1127 | 8.873 | 0.283 | 0.223 | 0.011 | 556 | 19 | 20.073 | |
| AP_PSB09_18 | 0.146 | 6.849 | 0.258 | 0.374 | 0.019 | 553 | 28 | 38.650 | |
| AP_PSB09_19 | 0.1214 | 8.237 | 0.299 | 0.279 | 0.013 | 547 | 22 | 27.053 | |
| AP_PSB09_20 | 0.1102 | 9.074 | 0.371 | 0.223 | 0.011 | 544 | 22 | 20.099 | |
| AP_PSB09_21 | 0.1223 | 8.177 | 0.341 | 0.320 | 0.020 | 514 | 27 | 32.135 | |
| AP_PSB09_22 | 0.1346 | 7.429 | 0.469 | 0.372 | 0.033 | 513 | 45 | 38.461 | |
| AP_PSB09_23 | 0.1171 | 8.540 | 0.350 | 0.268 | 0.018 | 538 | 26 | 25.671 | |
| AP_PSB09_24 | 0.304 | 3.289 | 0.292 | 0.624 | 0.048 | 576 | 120 | 69.255 | |
| AP_PSB09_25 | 0.259 | 3.861 | 0.283 | 0.625 | 0.040 | 491 | 83 | 69.443 | |
| AP_PSB09_26 | 0.1177 | 8.496 | 0.383 | 0.265 | 0.016 | 543 | 27 | 25.334 | |
| AP_PSB09_27B | 0.1624 | 6.158 | 0.345 | 0.401 | 0.027 | 581 | 44 | 41.925 | |
| AP_PSB09_27E | 0.1158 | 8.636 | 0.365 | 0.263 | 0.018 | 536 | 26 | 25.128 | |
| AP_PSB09_28 | 0.1185 | 8.439 | 0.299 | 0.249 | 0.012 | 561 | 22 | 23.271 | |
| AP_PSB09_29 | 0.1438 | 6.954 | 0.329 | 0.364 | 0.025 | 556 | 36 | 37.359 | |
| AP_PSB09_30 | 0.1475 | 6.780 | 0.322 | 0.380 | 0.026 | 552 | 37 | 39.388 | |
| AP_PSB09_31 | 0.1143 | 8.749 | 0.283 | 0.273 | 0.012 | 521 | 19 | 26.355 | |
| AP_PSB09_32 | 0.1231 | 8.123 | 0.356 | 0.302 | 0.023 | 534 | 30 | 29.842 | |
| AP_PSB09_33 | 0.1117 | 8.953 | 0.273 | 0.205 | 0.010 | 556 | 18 | 19.357 | |
| AP_PSB09_34 | 0.1463 | 6.835 | 0.364 | 0.336 | 0.023 | 595 | 39 | 33.908 | |
| AP_PSB09_35 | 0.126 | 7.937 | 0.460 | 0.301 | 0.018 | 547 | 34 | 29.716 | |
| AP_PSB09_36 | 0.1181 | 8.467 | 0.387 | 0.237 | 0.018 | 569 | 29 | 21.864 | |
| AP_PSB09_37 | 0.151 | 6.623 | 0.570 | 0.352 | 0.036 | 569 | 63 | 38.888 | |
| AP_PSB09_38 | 0.1103 | 9.066 | 0.362 | 0.240 | 0.018 | 530 | 25 | 22.311 | |
| AP_PSB09_39 | 0.1119 | 8.937 | 0.280 | 0.261 | 0.014 | 520 | 19 | 24.926 | |
| AP_PSB09_40 | 0.1118 | 8.945 | 0.336 | 0.264 | 0.017 | 517 | 23 | 25.310 | |
| AP_PSB09_41 | 0.1219 | 8.203 | 0.236 | 0.275 | 0.014 | 553 | 20 | 26.521 | |
| AP_PSB09_42 | 0.1211 | 8.258 | 0.286 | 0.281 | 0.014 | 544 | 22 | 27.291 | |
| AP_PSB09_43 | 0.1195 | 8.368 | 0.294 | 0.272 | 0.017 | 545 | 23 | 26.176 | |
| AP_PSB09_44 | 0.1227 | 8.150 | 0.325 | 0.328 | 0.022 | 509 | 28 | 33.040 | |
| AP_PSB09_46 | 0.248 | 4.032 | 0.211 | 0.554 | 0.029 | 601 | 60 | 60.599 | |
| AP_PSB09_47 | 0.1349 | 7.413 | 0.286 | 0.313 | 0.017 | 573 | 27 | 31.092 | |
| AP_PSB09_50 | 0.1906 | 5.247 | 0.259 | 0.489 | 0.026 | 556 | 44 | 52.740 | |
| AP_PSB09_51 | 0.1427 | 7.008 | 0.314 | 0.393 | 0.023 | 521 | 33 | 41.012 | |
| AP_PSB09_52 | 0.1106 | 9.042 | 0.302 | 0.243 | 0.012 | 529 | 19 | 22.674 | |
| AP_PSB09_53 | 0.1208 | 8.278 | 0.274 | 0.270 | 0.012 | 553 | 20 | 25.852 | |
| AP_PSB09_55 | 0.1767 | 5.659 | 0.291 | 0.512 | 0.046 | 487 | 64 | 55.590 | |
| AP_PSB09_56 | 0.1216 | 8.224 | 0.338 | 0.307 | 0.018 | 523 | 26 | 30.500 | |
| AP_PSB09_57 | 0.1178 | 8.489 | 0.303 | 0.261 | 0.014 | 547 | 22 | 24.824 | |
| AP_PSB09_58B | 0.1129 | 8.857 | 0.463 | 0.246 | 0.022 | 537 | 32 | 23.056 | |
| AP_PSB09_61 | 0.1196 | 8.361 | 0.517 | 0.296 | 0.022 | 524 | 36 | 29.197 | |
| AP_PSB09_62 | 0.1513 | 6.609 | 0.315 | 0.373 | 0.024 | 574 | 37 | 38.449 | |
| AP_PSB09_63 | 0.1195 | 8.368 | 0.238 | 0.226 | 0.011 | 586 | 19 | 20.366 | |
| AP_PSB09_64 | 0.1152 | 8.681 | 0.324 | 0.282 | 0.013 | 517 | 21 | 27.514 | |
| AP_PSB09_65 | 0.1316 | 7.599 | 0.277 | 0.330 | 0.019 | 543 | 26 | 33.220 | |
| AP_PSB09_66 | 0.1048 | 9.542 | 0.310 | 0.217 | 0.012 | 522 | 19 | 19.519 | |
| AP_PSB09_67 | 0.1128 | 8.865 | 0.322 | 0.250 | 0.016 | 534 | 23 | 23.436 | |
| AP_PSB09_68 | 0.158 | 6.329 | 0.248 | 0.415 | 0.023 | 550 | 33 | 43.630 | |
| AP_PSB09_69 | 0.1301 | 7.686 | 0.254 | 0.294 | 0.014 | 571 | 22 | 28.810 | |
| AP_PSB09_70 | 0.1992 | 5.020 | 0.247 | 0.515 | 0.031 | 543 | 51 | 55.882 | |
| AP_PSB09_71B | 0.1196 | 8.361 | 0.364 | 0.292 | 0.021 | 528 | 29 | 28.634 | |
| AP_PSB09_71E | 0.122 | 8.197 | 0.222 | 0.299 | 0.014 | 532 | 19 | 29.486 | |
| AP_PSB09_72 | 0.145 | 6.897 | 0.247 | 0.382 | 0.016 | 541 | 25 | 39.624 | |
| AP_PSB09_74 | 0.1331 | 7.513 | 0.316 | 0.315 | 0.013 | 563 | 26 | 31.433 | |
| AP_PSB09_6 | 0.0977 | 10.235 | 0.283 | 0.162 | 0.010 | 527 | 16 | 12.809 | |
| AP_PSB09_8 | 0.1692 | 5.910 | 0.251 | 0.326 | 0.023 | 698 | 40 | 32.413 | |
| AP_PSB09_14E | 0.1084 | 9.225092 | 0.3404093 | 0.173 | 0.011 | 575 | 22 | 13.934 | |
| AP_PSB09_15 | 0.0998 | 10.02004 | 0.3112437 | 0.161 | 0.0072 | 539 | 17 | 12.618 | |
| AP_PSB09_45 | 0.1077 | 9.285051 | 0.2155304 | 0.1755 | 0.0057 | 569 | 13 | 14.319 | |
| AP_PSB09_48 | 0.121 | 8.264463 | 0.9562188 | 0.284 | 0.055 | 541 | 77 | 27.649 | |
| AP_PSB09_49 | 0.1143 | 8.748906 | 0.4209885 | 0.165 | 0.012 | 612 | 30 | 12.870 | Over discordat |
| AP_PSB09_54 | 0.0897 | 11.14827 | 0.5717063 | 0.182 | 0.014 | 472 | 25 | 15.311 | |
| AP_PSB09_58E | 0.1009 | 9.910803 | 0.4027184 | 0.1647 | 0.0095 | 542 | 22 | 13.069 | |
| AP_PSB09_59 | 0.095 | 10.52632 | 0.3545706 | 0.182 | 0.011 | 499 | 18 | 15.282 | |
| AP_PSB09_60B | 0.1113 | 8.984726 | 0.3794089 | 0.299 | 0.017 | 486 | 24 | 29.645 | |
| AP_PSB09_60E | 0.298 | 3.355705 | 0.3490834 | 0.55 | 0.043 | 727 | 120 | 59.939 | |
| AP_PSB09_73 | 0.1096 | 9.124088 | 0.3413208 | 0.293 | 0.016 | 484 | 22 | 28.859 | |

Sample PS42A Apatite

| Spot | Isotopic ratios | | | | | Ages | | F207 | |
|---|---|---|---|---|---|---|---|---|---|
| | $^{206}Pb/^{238}U$ | $^{238}U/^{206}Pb$ | $^{238}U/^{206}Pb$ (2σ) | $^{207}Pb/^{206}Pb$ | $^{207}Pb/^{206}Pb$ (2σ) | $^{207}Pb/^{206}Pb^{b}$ Corrected ages | 2σ | % | |
| un_PS42A_2 | 0.357 | 2.801 | 0.220 | 0.717 | 0.039 | 438 | 110 | 80.306 | |
| un_PS42A_4 | 0.510 | 1.961 | 0.261 | 0.721 | 0.051 | 605 | 210 | 80.707 | |
| un_PS42A_5 | 0.315 | 3.175 | 0.212 | 0.655 | 0.040 | 532 | 100 | 72.690 | |
| un_PS42A_6 | 0.295 | 3.390 | 0.276 | 0.602 | 0.046 | 613 | 110 | 66.183 | |
| un_PS42A_7 | 0.232 | 4.310 | 0.242 | 0.543 | 0.034 | 586 | 68 | 58.981 | |
| un_PS42A_9 | 0.342 | 2.924 | 0.180 | 0.686 | 0.058 | 498 | 150 | 76.516 | |
| un_PS42A_10 | 0.141 | 7.097 | 0.287 | 0.358 | 0.026 | 552 | 35 | 36.549 | |
| un_PS42A_11 | 0.219 | 4.566 | 0.334 | 0.492 | 0.037 | 635 | 75 | 52.731 | |
| un_PS42A_12 | 0.175 | 5.714 | 0.359 | 0.416 | 0.026 | 608 | 50 | 43.482 | |
| un_PS42A_14 | 0.235 | 4.255 | 0.254 | 0.543 | 0.028 | 593 | 61 | 58.999 | |
| un_PS42A_16 | 0.730 | 1.370 | 0.188 | 0.788 | 0.097 | 501 | 530 | 88.929 | |
| un_PS42A_17 | 0.554 | 1.805 | 0.166 | 0.810 | 0.080 | 291 | 340 | 91.665 | |
| un_PS42A_19 | 0.318 | 3.145 | 0.168 | 0.694 | 0.042 | 445 | 110 | 77.525 | |
| un_PS42A_20 | 0.401 | 2.494 | 0.162 | 0.693 | 0.034 | 561 | 110 | 77.326 | |
| un_PS42A_22 | 0.340 | 2.941 | 0.182 | 0.671 | 0.036 | 533 | 110 | 74.648 | |
| un_PS42A_23 | 0.241 | 4.149 | 0.189 | 0.534 | 0.029 | 624 | 60 | 57.827 | |
| un_PS42A_24 | 0.352 | 2.841 | 0.178 | 0.717 | 0.034 | 432 | 100 | 80.310 | |
| un_PS42A_25 | 0.439 | 2.278 | 0.244 | 0.704 | 0.041 | 578 | 150 | 78.632 | |
| un_PS42A_26 | 0.557 | 1.795 | 0.235 | 0.753 | 0.082 | 529 | 340 | 84.646 | |
| un_PS42A_27 | 0.392 | 2.551 | 0.228 | 0.706 | 0.048 | 511 | 150 | 78.955 | |
| un_PS42A_28 | 0.333 | 3.003 | 0.243 | 0.714 | 0.049 | 416 | 130 | 79.982 | |
| un_PS42A_29 | 0.311 | 3.215 | 0.352 | 0.619 | 0.039 | 607 | 110 | 68.252 | |
| un_PS42A_30 | 0.220 | 4.545 | 0.351 | 0.571 | 0.045 | 511 | 83 | 62.502 | |
| un_PS42A_32 | 0.236 | 4.237 | 0.251 | 0.562 | 0.041 | 563 | 79 | 61.329 | |
| un_PS42A_33 | 0.335 | 2.985 | 0.214 | 0.694 | 0.044 | 468 | 120 | 77.523 | |
| un_PS42A_34 | 0.263 | 3.810 | 0.160 | 0.574 | 0.030 | 601 | 66 | 62.775 | |
| un_PS42A_35 | 0.225 | 4.444 | 0.316 | 0.558 | 0.041 | 544 | 79 | 60.866 | |
| un_PS42A_36 | 0.224 | 4.464 | 0.299 | 0.577 | 0.053 | 510 | 94 | 63.247 | |
| un_PS42A_38 | 0.421 | 2.375 | 0.175 | 0.694 | 0.038 | 585 | 130 | 77.436 | |
| un_PS42A_39 | 0.244 | 4.098 | 0.235 | 0.574 | 0.030 | 560 | 65 | 62.805 | |
| un_PS42A_40 | 0.286 | 3.497 | 0.196 | 0.648 | 0.036 | 498 | 84 | 71.918 | |
| un_PS42A_42 | 0.439 | 2.278 | 0.176 | 0.775 | 0.064 | 347 | 220 | 87.402 | |
| un_PS42A_43 | 0.235 | 4.255 | 0.308 | 0.542 | 0.039 | 595 | 80 | 58.854 | |
| un_PS42A_44 | 0.308 | 3.247 | 0.306 | 0.601 | 0.043 | 642 | 110 | 66.001 | |
| un_PS42A_47 | 0.487 | 2.053 | 0.169 | 0.742 | 0.064 | 503 | 240 | 83.336 | |
| un_PS42A_49 | 0.246 | 4.065 | 0.297 | 0.615 | 0.052 | 490 | 100 | 67.896 | |
| un_PS42A_50 | 0.456 | 2.193 | 0.188 | 0.684 | 0.045 | 666 | 160 | 76.132 | |
| un_PS42A_52 | 0.510 | 1.961 | 0.188 | 0.728 | 0.041 | 579 | 170 | 81.574 | |
| un_PS42A_53 | 0.511 | 1.957 | 0.153 | 0.733 | 0.052 | 561 | 200 | 82.207 | |
| un_PS42A_54 | 0.405 | 2.469 | 0.165 | 0.721 | 0.044 | 483 | 140 | 80.789 | |
| un_PS42A_55 | 0.472 | 2.119 | 0.175 | 0.695 | 0.049 | 651 | 180 | 77.487 | |
| un_PS42A_56 | 0.369 | 2.710 | 0.191 | 0.669 | 0.045 | 582 | 130 | 74.395 | |
| un_PS42A_57 | 0.564 | 1.773 | 0.173 | 0.782 | 0.057 | 414 | 250 | 88.240 | |
| un_PS42A_59 | 0.377 | 2.653 | 0.267 | 0.711 | 0.045 | 478 | 140 | 79.584 | |
| un_PS42A_60 | 0.242 | 4.132 | 0.273 | 0.622 | 0.054 | 470 | 100 | 68.747 | |
| un_PS42A_61 | 0.267 | 3.745 | 0.267 | 0.665 | 0.051 | 432 | 110 | 74.041 | |
| un_PS42A_64 | 0.219 | 4.566 | 0.250 | 0.577 | 0.034 | 499 | 63 | 63.250 | |
| un_PS42A_66 | 0.176 | 5.688 | 0.301 | 0.446 | 0.029 | 572 | 48 | 47.220 | |
| un_PS42A_67 | 0.221 | 4.521 | 0.204 | 0.506 | 0.027 | 619 | 53 | 54.438 | |
| un_PS42A_69 | 0.940 | 1.064 | 0.181 | 0.801 | 0.042 | 552 | 320 | 90.489 | |
| un_PS42A_71 | 0.276 | 3.623 | 0.223 | 0.614 | 0.037 | 550 | 85 | 67.730 | |
| un_PS42A_72 | 0.394 | 2.538 | 0.238 | 0.758 | 0.061 | 362 | 190 | 85.340 | |
| un_PS42A_73 | 0.278 | 3.597 | 0.194 | 0.595 | 0.037 | 593 | 84 | 65.341 | |
| un_PS42A_74 | 0.494 | 2.024 | 0.135 | 0.751 | 0.049 | 478 | 190 | 84.419 | |
| un_PS42A_75 | 0.601 | 1.664 | 0.161 | 0.799 | 0.061 | 365 | 280 | 90.307 | |
| un_PS42A_76 | 0.248 | 4.032 | 0.309 | 0.566 | 0.052 | 583 | 100 | 61.833 | |
| un_PS42A_77 | 0.464 | 2.155 | 0.153 | 0.727 | 0.045 | 531 | 160 | 81.496 | |
| un_PS42A_78 | 0.855 | 1.170 | 0.078 | 0.847 | 0.052 | 209 | 350 | 96.146 | |
| un_PS42A_62 | 0.0462 | 21.64502 | 1.030715 | 0.705 | 0.04 | 62 | 15 | 79.082 | |
| un_PS42A_15 | 0.663 | 1.508296 | 0.1114728 | 0.833 | 0.053 | 233 | 280 | 94.449 | |
| un_PS42A_51 | 0.522 | 1.915709 | 0.1357878 | 0.797 | 0.044 | 326 | 180 | 90.063 | |
| un_PS42A_37 | 0.413 | 2.421308 | 0.281411 | 0.788 | 0.076 | 287 | 240 | 88.977 | |
| un_PS42A_13 | 0.186 | 5.376344 | 0.3179558 | 0.418 | 0.025 | 643 | 51 | 43.608 | Over discordant |
| un_PS42A_8 | 0.2037 | 4.90918 | 0.2000304 | 0.45 | 0.028 | 655 | 50 | 47.497 | |
| un_PS42A_65 | 0.1658 | 6.031363 | 0.2619169 | 0.367 | 0.021 | 636 | 37 | 37.461 | |
| un_PS42A_58 | 0.419 | 2.386635 | 0.1480967 | 0.651 | 0.044 | 714 | 140 | 72.046 | |
| un_PS42A_45 | 0.335 | 2.985075 | 0.2851415 | 0.587 | 0.053 | 730 | 150 | 64.208 | |

Sample TG04 Apatite

| Spot | Isotopic ratios | | | | | Ages | | F207 | |
|---|---|---|---|---|---|---|---|---|---|
| | $^{206}Pb/^{238}U$ | $^{238}U/^{206}Pb$ | $^{238}U/^{206}Pb$ (2σ) | $^{207}Pb/^{206}Pb$ | $^{207}Pb/^{206}Pb$ (2σ) | $^{207}Pb/^{206}Pb^{b}$ Corrected ages | 2σ | % | |
| unk_TG04_4 | 0.190 | 5.260 | 0.227 | 0.445 | 0.024 | 618 | 41 | 47.074 | |
| unk_TG04_5 | 0.133 | 7.502 | 0.355 | 0.271 | 0.022 | 608 | 35 | 25.801 | |
| unk_TG04_6 | 0.122 | 8.210 | 0.243 | 0.191 | 0.010 | 628 | 20 | 15.992 | |
| unk_TG04_10 | 0.399 | 2.506 | 0.264 | 0.712 | 0.068 | 498 | 200 | 79.871 | |
| unk_TG04_12 | 0.362 | 2.762 | 0.153 | 0.631 | 0.038 | 668 | 100 | 69.839 | |
| unk_TG04_13 | 0.211 | 4.733 | 0.224 | 0.479 | 0.026 | 632 | 49 | 51.251 | |
| unk_TG04_15 | 0.170 | 5.896 | 0.226 | 0.375 | 0.021 | 640 | 35 | 38.458 | |
| unk_TG04_16 | 0.216 | 4.630 | 0.279 | 0.480 | 0.033 | 644 | 33 | 51.361 | |
| unk_TG04_18 | 0.116 | 8.606 | 0.400 | 0.169 | 0.012 | 619 | 29 | 13.267 | |
| unk_TG04_19 | 0.114 | 8.757 | 0.245 | 0.141 | 0.008 | 632 | 18 | 9.802 | |
| unk_TG04_20 | 0.147 | 6.817 | 0.353 | 0.313 | 0.028 | 622 | 43 | 30.950 | |
| unk_TG04_21 | 0.132 | 7.564 | 0.263 | 0.308 | 0.019 | 567 | 26 | 30.454 | |
| unk_TG04_22 | 0.133 | 7.508 | 0.349 | 0.247 | 0.015 | 631 | 31 | 22.797 | |
| unk_TG04_25 | 0.165 | 6.079 | 0.225 | 0.365 | 0.018 | 633 | 31 | 37.278 | |
| unk_TG04_27 | 0.281 | 3.559 | 0.215 | 0.573 | 0.038 | 642 | 85 | 62.734 | |
| unk_TG04_28 | 0.173 | 5.777 | 0.207 | 0.395 | 0.019 | 627 | 32 | 40.988 | |
| unk_TG04_29 | 0.131 | 7.634 | 0.303 | 0.238 | 0.013 | 629 | 27 | 21.761 | |
| unk_TG04_30 | 0.285 | 3.509 | 0.209 | 0.624 | 0.032 | 544 | 73 | 69.105 | |
| unk_TG04_31 | 0.240 | 4.167 | 0.208 | 0.539 | 0.031 | 610 | 61 | 58.647 | |
| unk_TG04_34 | 0.221 | 4.525 | 0.409 | 0.519 | 0.038 | 596 | 79 | 56.170 | |
| unk_TG04_35 | 0.236 | 4.237 | 0.251 | 0.555 | 0.034 | 573 | 66 | 60.612 | |
| unk_TG04_36 | 0.265 | 3.774 | 0.527 | 0.611 | 0.045 | 532 | 110 | 67.537 | |
| unk_TG04_38 | 0.103 | 9.718 | 0.236 | 0.118 | 0.005 | 588 | 44 | 7.189 | |
| unk_TG04_41 | 0.156 | 6.398 | 0.348 | 0.397 | 0.031 | 566 | 46 | 41.286 | |
| unk_TG04_44 | 0.232 | 4.310 | 0.223 | 0.506 | 0.027 | 647 | 55 | 54.493 | |
| unk_TG04_45 | 0.288 | 3.472 | 0.193 | 0.609 | 0.037 | 582 | 83 | 67.193 | |
| unk_TG04_46 | 0.134 | 7.440 | 0.260 | 0.257 | 0.015 | 627 | 25 | 23.995 | |
| unk_TG04_47 | 0.116 | 8.643 | 0.418 | 0.161 | 0.012 | 623 | 30 | 12.302 | |
| unk_TG04_49 | 0.591 | 1.692 | 0.218 | 0.753 | 0.063 | 553 | 280 | 84.844 | |
| unk_TG04_53 | 0.250 | 4.000 | 0.208 | 0.582 | 0.033 | 556 | 66 | 63.969 | |
| unk_TG04_58 | 0.140 | 7.168 | 0.247 | 0.318 | 0.019 | 587 | 27 | 31.661 | |
| unk_TG04_59 | 0.173 | 5.787 | 0.228 | 0.387 | 0.020 | 636 | 34 | 39.994 | |
| unk_TG04_61 | 0.152 | 6.562 | 0.250 | 0.343 | 0.026 | 612 | 36 | 34.653 | |
| | | | | | | | | | |
| unk_TG04_1 | 0.242 | 4.132231 | 0.3073561 | 0.35 | 0.017 | 947 | 73 | 34.611 | |
| unk_TG04_2 | 0.244 | 4.098361 | 0.2015587 | 0.269 | 0.014 | 1095 | 96 | 24.122 | |
| unk_TG04_32 | 0.337 | 2.967359 | 0.1672992 | 0.707 | 0.051 | 435 | 130 | 79.285 | |
| unk_TG04_50 | 0.0973 | 10.27749 | 0.6126357 | 0.624 | 0.053 | 189 | 40 | 69.422 | |
| unk_TG04_56 | 0.166 | 6.024096 | 0.4354768 | 0.665 | 0.048 | 169 | 62 | 83.998 | Over discordant |
| unk_TG04_3 | 0.473 | 2.114165 | 0.1430302 | 0.648 | 0.049 | 808 | 170 | 71.769 | |
| unk_TG04_7 | 0.1035 | 9.661836 | 0.261383 | 0.1597 | 0.0074 | 560 | 15 | 12.314 | |
| unk_TG04_26 | 0.27 | 3.703704 | 0.2743484 | 0.652 | 0.065 | 460 | 130 | 72.606 | |
| unk_TG04_33 | 0.432 | 2.314815 | 0.1768261 | 0.752 | 0.052 | 410 | 170 | 84.799 | |

Sample TG08 Apatite

| Spot | Isotopic ratios | | | | | Ages | | F207 | |
|---|---|---|---|---|---|---|---|---|---|
| | $^{206}Pb/^{238}U$ | $^{238}U/^{206}Pb$ | $^{238}U/^{206}Pb$ (2σ) | $^{207}Pb/^{206}Pb$ | $^{207}Pb/^{206}Pb$ (2σ) | $^{207}Pb/^{206}Pb^{b}$ Corrected ages | 2σ | % | |
| unk_TG08_1 | 0.442 | 2.262 | 0.415 | 0.730 | 0.100 | 483 | 330 | 82.397 | |
| unk_TG08_2 | 0.318 | 3.145 | 0.208 | 0.636 | 0.043 | 576 | 110 | 70.608 | |
| unk_TG08_3 | 0.283 | 3.534 | 0.250 | 0.604 | 0.045 | 581 | 100 | 66.674 | |
| unk_TG08_4 | 0.253 | 3.953 | 0.312 | 0.583 | 0.056 | 560 | 110 | 64.129 | |
| unk_TG08_5 | 0.263 | 3.802 | 0.231 | 0.603 | 0.051 | 543 | 100 | 66.585 | |
| unk_TG08_6 | 0.302 | 3.311 | 0.241 | 0.648 | 0.060 | 521 | 140 | 72.127 | |
| unk_TG08_7 | 0.235 | 4.255 | 0.272 | 0.504 | 0.041 | 657 | 80 | 54.344 | |
| unk_TG08_11 | 0.242 | 4.132 | 0.273 | 0.581 | 0.043 | 540 | 83 | 63.894 | |
| unk_TG08_12 | 0.270 | 3.704 | 0.247 | 0.531 | 0.031 | 699 | 74 | 57.582 | |
| unk_TG08_13 | 0.197 | 5.076 | 0.309 | 0.523 | 0.036 | 526 | 60 | 56.844 | |
| unk_TG08_14 | 0.269 | 3.717 | 0.221 | 0.592 | 0.044 | 576 | 91 | 65.254 | |
| unk_TG08_17 | 0.177 | 5.650 | 0.351 | 0.444 | 0.043 | 577 | 65 | 47.099 | |
| unk_TG08_18 | 0.193 | 5.181 | 0.322 | 0.414 | 0.040 | 670 | 68 | 43.250 | |
| unk_TG08_19 | 0.162 | 6.161 | 0.380 | 0.389 | 0.030 | 596 | 50 | 40.318 | |
| unk_TG08_20 | 0.256 | 3.906 | 0.244 | 0.536 | 0.039 | 654 | 81 | 58.290 | |
| unk_TG08_21 | 0.321 | 3.115 | 0.175 | 0.632 | 0.041 | 591 | 100 | 70.089 | |
| unk_TG08_22 | 0.444 | 2.252 | 0.152 | 0.718 | 0.045 | 530 | 150 | 80.700 | |
| unk_TG08_27 | 0.190 | 5.263 | 0.582 | 0.543 | 0.071 | 480 | 110 | 59.315 | |
| unk_TG08_29 | 0.265 | 3.774 | 0.199 | 0.533 | 0.027 | 683 | 62 | 57.824 | |
| unk_TG08_30 | 0.260 | 3.846 | 0.192 | 0.590 | 0.031 | 561 | 64 | 65.029 | |
| unk_TG08_31 | 0.245 | 4.082 | 0.183 | 0.558 | 0.029 | 588 | 57 | 61.019 | |
| unk_TG08_32 | 0.263 | 3.802 | 0.159 | 0.573 | 0.034 | 601 | 69 | 62.846 | |
| unk_TG08_33 | 0.316 | 3.165 | 0.200 | 0.652 | 0.043 | 535 | 100 | 72.616 | |
| unk_TG08_34 | 0.291 | 3.436 | 0.177 | 0.624 | 0.034 | 554 | 77 | 69.161 | |
| unk_TG08_35 | 0.309 | 3.236 | 0.230 | 0.627 | 0.045 | 580 | 110 | 69.533 | |
| unk_TG08_36 | 0.301 | 3.322 | 0.166 | 0.552 | 0.030 | 731 | 73 | 60.108 | |
| unk_TG08_37 | 0.224 | 4.456 | 0.181 | 0.554 | 0.028 | 546 | 50 | 60.611 | |
| unk_TG08_40 | 0.237 | 4.219 | 0.214 | 0.505 | 0.030 | 661 | 60 | 54.439 | |
| unk_TG08_41 | 0.259 | 3.861 | 0.209 | 0.596 | 0.036 | 548 | 73 | 65.743 | |
| unk_TG08_44 | 0.283 | 3.534 | 0.225 | 0.625 | 0.050 | 537 | 110 | 69.304 | |
| unk_TG08_45 | 0.327 | 3.058 | 0.187 | 0.686 | 0.049 | 471 | 120 | 76.820 | |
| unk_TG08_46 | 0.233 | 4.292 | 0.221 | 0.559 | 0.039 | 558 | 71 | 61.195 | |
| unk_TG08_47 | 0.279 | 3.584 | 0.231 | 0.585 | 0.036 | 612 | 81 | 64.305 | |
| unk_TG08_48 | 0.242 | 4.132 | 0.205 | 0.565 | 0.030 | 568 | 59 | 61.938 | |
| unk_TG08_49 | 0.240 | 4.167 | 0.313 | 0.546 | 0.039 | 597 | 80 | 59.569 | |
| unk_TG08_50 | 0.288 | 3.472 | 0.265 | 0.584 | 0.041 | 633 | 96 | 64.175 | |
| unk_TG08_51 | 0.296 | 3.378 | 0.183 | 0.595 | 0.041 | 626 | 93 | 65.547 | |
| unk_TG08_52 | 0.315 | 3.175 | 0.202 | 0.578 | 0.033 | 704 | 86 | 63.367 | |
| unk_TG08_53 | 0.394 | 2.538 | 0.219 | 0.609 | 0.056 | 787 | 170 | 67.044 | |
| unk_TG08_54 | 0.229 | 4.367 | 0.400 | 0.539 | 0.050 | 582 | 97 | 58.741 | |
| unk_TG08_57 | 0.207 | 4.831 | 0.303 | 0.491 | 0.029 | 601 | 56 | 52.795 | |
| unk_TG08_58 | 0.288 | 3.472 | 0.241 | 0.559 | 0.037 | 686 | 89 | 61.012 | |
| unk_TG08_60 | 0.310 | 3.226 | 0.239 | 0.598 | 0.046 | 648 | 110 | 65.888 | |
| unk_TG08_62 | 0.318 | 3.145 | 0.237 | 0.682 | 0.055 | 468 | 130 | 76.321 | |
| unk_TG08_63 | 0.319 | 3.135 | 0.216 | 0.621 | 0.060 | 613 | 140 | 68.727 | |
| unk_TG08_64 | 0.333 | 3.003 | 0.207 | 0.611 | 0.044 | 663 | 110 | 67.471 | |
| unk_TG08_66 | 0.339 | 2.950 | 0.183 | 0.596 | 0.036 | 712 | 97 | 65.552 | |
| unk_TG08_72 | 0.278 | 3.597 | 0.272 | 0.580 | 0.050 | 620 | 110 | 63.685 | |
| unk_TG08_73 | 0.267 | 3.745 | 0.281 | 0.521 | 0.047 | 711 | 110 | 56.327 | |
| unk_TG08_74 | 0.313 | 3.195 | 0.255 | 0.630 | 0.035 | 581 | 91 | 69.868 | |
| unk_TG08_75 | 0.250 | 4.000 | 0.256 | 0.531 | 0.033 | 649 | 71 | 57.633 | |
| unk_TG08_77 | 0.193 | 5.173 | 0.262 | 0.500 | 0.030 | 549 | 50 | 54.012 | |
| unk_TG08_78 | 0.382 | 2.618 | 0.171 | 0.650 | 0.037 | 649 | 110 | 72.273 | |
| unk_TG08_79 | 0.240 | 4.167 | 0.243 | 0.561 | 0.042 | 571 | 79 | 61.409 | |
| unk_TG08_80 | 0.431 | 2.320 | 0.188 | 0.628 | 0.046 | 799 | 150 | 69.384 | |
| unk_TG08_85 | 0.233 | 4.292 | 0.221 | 0.592 | 0.043 | 501 | 77 | 65.314 | |
| unk_TG08_81 | 0.179 | 5.577 | 0.240 | 0.596 | 0.033 | 382 | 46 | 65.952 | |
| unk_TG08_8 | 0.229 | 4.367 | 0.248 | 0.610 | 0.046 | 462 | 81 | 67.555 | |
| unk_TG08_9 | 0.553 | 1.808 | 0.190 | 0.537 | 0.052 | 1375 | 240 | 57.007 | |
| unk_TG08_25 | 0.527 | 1.898 | 0.140 | 0.790 | 0.052 | 346 | 200 | 89.537 | |
| unk_TG08_15 | 0.280 | 3.571 | 0.344 | 0.502 | 0.049 | 783 | 120 | 53.876 | |
| unk_TG08_10 | 0.071 | 14.184 | 0.865 | 0.522 | 0.046 | 192 | 27 | 57.118 | Over discordant |
| unk_TG08_38 | 0.760 | 1.316 | 0.208 | 0.545 | 0.051 | 1835 | 400 | 56.671 | |
| unk_TG08_59 | 0.315 | 3.175 | 0.242 | 0.457 | 0.053 | 980 | 140 | 47.877 | |
| unk_TG08_61 | 0.272 | 3.676 | 0.257 | 0.665 | 0.035 | 436 | 75 | 74.274 | |
| unk_TG08_67 | 0.173 | 5.770 | 0.330 | 0.546 | 0.031 | 434 | 46 | 59.814 | |
| unk_TG08_70 | 0.186 | 5.373 | 0.228 | 0.545 | 0.032 | 467 | 47 | 59.628 | |
| unk_TG08_76 | 0.329 | 3.040 | 0.249 | 0.554 | 0.038 | 792 | 110 | 60.266 | |

Sample PS42A Titanite

| Spot | Isotopic ratios | | | | | Ages | | F207 | |
|---|---|---|---|---|---|---|---|---|---|
| | $^{206}Pb/^{238}U$ | $^{238}U/^{206}Pb$ | $^{238}U/^{206}Pb$ (2σ) | $^{207}Pb/^{206}Pb$ | $^{207}Pb/^{206}Pb$ (2σ) | $^{207}Pb/^{206}Pb^{b}$ Corrected ages | 2σ | % | |
| unk_sph_PS42_1 | 0.100 | 10.030 | 0.352 | 0.085 | 0.023 | 595 | 26 | 3.016 | |
| unk_sph_PS42_2 | 0.098 | 10.225 | 0.335 | 0.083 | 0.023 | 585 | 24 | 2.870 | |
| unk_sph_PS42_3 | 0.103 | 9.756 | 0.552 | 0.156 | 0.046 | 557 | 45 | 11.954 | |
| unk_sph_PS42_4 | 0.112 | 8.937 | 0.367 | 0.162 | 0.045 | 602 | 43 | 12.525 | |
| unk_sph_PS42_5 | 0.116 | 8.598 | 0.370 | 0.171 | 0.047 | 618 | 47 | 13.488 | |
| unk_sph_PS42_9 | 0.110 | 9.058 | 0.353 | 0.133 | 0.037 | 618 | 37 | 8.865 | |
| unk_sph_PS42_12 | 0.103 | 9.718 | 0.349 | 0.094 | 0.026 | 606 | 28 | 4.212 | |
| unk_sph_PS42_13 | 0.100 | 9.960 | 0.337 | 0.081 | 0.022 | 602 | 25 | 2.505 | |
| unk_sph_PS42_14 | 0.112 | 8.945 | 0.344 | 0.146 | 0.041 | 615 | 40 | 10.464 | |
| unk_sph_PS42_15 | 0.105 | 9.506 | 0.443 | 0.148 | 0.042 | 578 | 41 | 10.832 | |
| unk_sph_PS42_16 | 0.122 | 8.170 | 0.380 | 0.224 | 0.062 | 601 | 61 | 20.168 | |
| unk_sph_PS42_17 | 0.122 | 8.177 | 0.595 | 0.172 | 0.053 | 648 | 65 | 13.535 | |
| unk_sph_PS42_18 | 0.113 | 8.818 | 0.365 | 0.162 | 0.045 | 610 | 44 | 12.480 | |
| unk_sph_PS42_19 | 0.116 | 8.636 | 0.433 | 0.163 | 0.046 | 622 | 48 | 12.525 | |
| unk_sph_PS42_20 | 0.104 | 9.653 | 0.391 | 0.080 | 0.022 | 621 | 29 | 2.389 | |
| unk_sph_PS42_21 | 0.099 | 10.081 | 0.366 | 0.093 | 0.026 | 586 | 28 | 4.070 | |
| unk_sph_PS42_22 | 0.100 | 9.960 | 0.347 | 0.081 | 0.022 | 601 | 26 | 2.675 | |
| unk_sph_PS42_24 | 0.115 | 8.673 | 0.399 | 0.148 | 0.041 | 632 | 44 | 10.663 | |
| unk_sph_PS42_30 | 0.113 | 8.881 | 0.379 | 0.152 | 0.042 | 614 | 42 | 11.252 | |
| unk_sph_PS42_31 | 0.100 | 9.970 | 0.358 | 0.139 | 0.039 | 559 | 34 | 9.685 | |
| unk_sph_PS42_32 | 0.102 | 9.804 | 0.481 | 0.090 | 0.025 | 604 | 34 | 3.701 | |
| unk_sph_PS42_33 | 0.101 | 9.881 | 0.439 | 0.121 | 0.033 | 577 | 34 | 7.475 | |
| unk_sph_PS42_34 | 0.098 | 10.225 | 0.376 | 0.105 | 0.029 | 569 | 29 | 5.645 | |
| unk_sph_PS42_35 | 0.098 | 10.173 | 0.352 | 0.080 | 0.022 | 590 | 25 | 2.500 | |
| unk_sph_PS42_36 | 0.129 | 7.752 | 0.373 | 0.204 | 0.057 | 652 | 61 | 17.494 | |
| unk_sph_PS42_38 | 0.099 | 10.142 | 0.360 | 0.090 | 0.025 | 584 | 27 | 3.830 | |
| unk_sph_PS42_40 | 0.100 | 9.990 | 0.409 | 0.099 | 0.030 | 587 | 32 | 4.762 | |
| unk_sph_PS42_41 | 0.112 | 8.913 | 0.342 | 0.148 | 0.041 | 615 | 40 | 10.784 | |
| unk_sph_PS42_43 | 0.103 | 9.671 | 0.337 | 0.109 | 0.030 | 597 | 30 | 6.157 | |
| unk_sph_PS42_44 | 0.103 | 9.709 | 0.368 | 0.081 | 0.023 | 617 | 28 | 2.483 | |
| unk_sph_PS42_46 | 0.097 | 10.363 | 0.472 | 0.106 | 0.029 | 561 | 32 | 5.778 | |
| unk_sph_PS42_47 | 0.112 | 8.905 | 0.349 | 0.141 | 0.039 | 621 | 39 | 9.951 | |
| unk_sph_PS42_48 | 0.093 | 10.730 | 0.368 | 0.074 | 0.020 | 564 | 23 | 1.897 | |
| unk_sph_PS42_50 | 0.102 | 9.775 | 0.354 | 0.100 | 0.027 | 599 | 29 | 4.815 | |
| unk_sph_PS42_7 | 0.100 | 10.000 | 0.330 | 0.071 | 0.019 | 607 | 23 | 1.264 | Concordia data |
| unk_sph_PS42_8 | 0.098 | 10.235 | 0.335 | 0.069 | 0.019 | 594 | 23 | 1.205 | |
| unk_sph_PS42_11 | 0.096 | 10.428 | 0.348 | 0.074 | 0.020 | 580 | 23 | 1.831 | |
| unk_sph_PS42_23 | 0.098 | 10.215 | 0.355 | 0.072 | 0.020 | 594 | 24 | 1.407 | |
| unk_sph_PS42_26 | 0.098 | 10.163 | 0.341 | 0.067 | 0.018 | 600 | 23 | 0.870 | |
| unk_sph_PS42_27 | 0.099 | 10.152 | 0.340 | 0.070 | 0.019 | 598 | 23 | 1.316 | |
| unk_sph_PS42_28 | 0.098 | 10.194 | 0.343 | 0.074 | 0.020 | 593 | 24 | 1.781 | |
| unk_sph_PS42_45 | 0.100 | 10.040 | 0.333 | 0.077 | 0.021 | 600 | 24 | 2.064 | |
| unk_sph_PS42_6 | 0.093 | 10.799 | 0.828 | 0.112 | 0.031 | 535 | 44 | 6.552 | Discordant data |
| unk_sph_PS42_10 | 0.095 | 10.526 | 0.465 | 0.148 | 0.042 | 523 | 36 | 11.040 | |
| unk_sph_PS42_25 | 0.130 | 7.675 | 0.542 | 0.165 | 0.046 | 695 | 63 | 12.634 | |
| unk_sph_PS42_37 | 0.118 | 8.467 | 0.358 | 0.132 | 0.036 | 661 | 40 | 8.570 | |
| unk_sph_PS42_29 | 0.095 | 10.526 | 0.410 | 0.099 | 0.027 | 558 | 28 | 4.825 | |
| unk_sph_PS42_42 | 0.109 | 9.217 | 0.323 | 0.091 | 0.025 | 641 | 29 | 3.643 | |
| unk_sph_PS42_49 | 0.122 | 8.183 | 0.395 | 0.162 | 0.046 | 656 | 50 | 12.340 | |
| unk_sph_PS42_39 | 0.133 | 7.496 | 0.517 | 0.346 | 0.096 | 534 | 99 | 35.259 | |

Sample PSB09 Zircon

| Spot | Isotopic ratios | | | | | Ages | | | | |
|---|---|---|---|---|---|---|---|---|---|---|
| | $^{207}Pb/^{235}U$ | Error (2σ) | $^{206}Pb/^{238}U$ | Error (2σ) | Error correlation | $^{207}Pb/^{235}U$ | 2σ | $^{206}Pb/^{238}U$ | 2σ | Concord. |
| PSB09_31 | 0.960 | 0.071 | 0.097 | 0.002 | 0.238 | 679 | 37 | 598 | 12 | 93.657 |
| PSB09_14 | 0.933 | 0.036 | 0.097 | 0.002 | 0.341 | 667 | 19 | 597 | 10 | 94.462 |
| PSB09_16 | 0.881 | 0.030 | 0.100 | 0.002 | 0.387 | 640 | 16 | 615 | 13 | 98.008 |
| PSB09_56 | 0.879 | 0.029 | 0.100 | 0.002 | 0.209 | 638 | 16 | 613 | 11 | 97.969 |
| PSB09_25 | 0.846 | 0.056 | 0.098 | 0.004 | 0.336 | 617 | 30 | 599 | 21 | 98.520 |
| PSB09_31 | 0.839 | 0.032 | 0.099 | 0.003 | 0.406 | 618 | 18 | 608 | 17 | 99.184 |
| PSB09_9 | 0.813 | 0.031 | 0.097 | 0.002 | 0.034 | 602 | 17 | 595 | 11 | 99.424 |
| PSB09_2 | 1.498 | 0.080 | 0.141 | 0.005 | 0.945 | 923 | 31 | 852 | 25 | 96.000 |
| PSB09_3 | 0.827 | 0.015 | 0.027 | 0.001 | -0.167 | 612 | 8 | 171 | 4 | 43.775 |
| PSB09_6 | 0.907 | 0.029 | 0.041 | 0.001 | 0.421 | 655 | 15 | 257 | 7 | 56.297 |
| PSB09_8 | 1.321 | 0.015 | 0.021 | 0.001 | 0.658 | 855 | 7 | 133 | 4 | 26.858 |
| PSB09_10 | 0.763 | 0.035 | 0.032 | 0.002 | -0.630 | 572 | 20 | 203 | 14 | 52.387 |
| PSB09_13 | 0.948 | 0.030 | 0.072 | 0.005 | 0.178 | 679 | 14 | 448 | 27 | 79.503 |
| PSB09_15 | 4.600 | 0.500 | 0.176 | 0.008 | 0.902 | 1694 | 80 | 1040 | 41 | 76.079 |
| PSB09_17 | 0.962 | 0.025 | 0.046 | 0.001 | 0.888 | 683 | 13 | 292 | 7 | 59.854 |
| PSB09_18 | 0.768 | 0.026 | 0.030 | 0.001 | -0.423 | 578 | 15 | 193 | 6 | 50.143 |
| PSB09_19 | 2.350 | 0.690 | 0.084 | 0.005 | 0.948 | 1110 | 150 | 528 | 32 | 64.469 |
| PSB09_20 | 0.429 | 0.027 | 0.026 | 0.001 | -0.277 | 360 | 19 | 168 | 6 | 63.636 |
| PSB09_21 | 3.500 | 0.420 | 0.071 | 0.004 | 0.925 | 1476 | 92 | 440 | 24 | 45.929 |
| PSB09_23 | 1.270 | 0.050 | 0.020 | 0.000 | 0.351 | 827 | 22 | 129 | 2 | 27.042 |
| PSB09_28 | 0.411 | 0.008 | 0.023 | 0.000 | 0.518 | 349 | 6 | 145 | 2 | 58.686 |
| PSB09_30 | 1.246 | 0.054 | 0.072 | 0.003 | 0.545 | 817 | 25 | 446 | 20 | 70.625 |
| PSB09_33 | 4.120 | 0.180 | 0.230 | 0.009 | 0.916 | 1651 | 35 | 1332 | 47 | 89.306 |
| PSB09_34 | 0.869 | 0.017 | 0.033 | 0.001 | 0.602 | 635 | 9 | 208 | 5 | 49.430 |
| PSB09_35 | 1.210 | 0.120 | 0.100 | 0.003 | 0.644 | 793 | 52 | 614 | 18 | 87.278 |
| PSB09_36 | 1.990 | 0.280 | 0.045 | 0.003 | 0.955 | 1043 | 93 | 286 | 16 | 43.040 |
| PSB09_37 | 0.919 | 0.025 | 0.054 | 0.001 | 0.456 | 661 | 13 | 340 | 7 | 67.879 |
| PSB09_38 | 1.360 | 0.150 | 0.103 | 0.003 | 0.779 | 842 | 60 | 630 | 15 | 85.598 |
| PSB09_39 | 0.834 | 0.013 | 0.026 | 0.001 | 0.319 | 615 | 7 | 165 | 3 | 42.211 |
| PSB09_40 | 0.821 | 0.024 | 0.029 | 0.001 | 0.760 | 607 | 13 | 182 | 5 | 46.095 |
| PSB09_41 | 0.788 | 0.033 | 0.032 | 0.001 | -0.086 | 588 | 19 | 205 | 5 | 51.721 |
| PSB09_42 | 0.780 | 0.015 | 0.044 | 0.001 | -0.221 | 585 | 9 | 280 | 9 | 64.716 |
| PSB09_43 | 1.072 | 0.036 | 0.090 | 0.004 | 0.550 | 737 | 17 | 556 | 21 | 86.002 |
| PSB09_44 | 0.882 | 0.032 | 0.034 | 0.001 | 0.564 | 639 | 17 | 214 | 4 | 50.229 |
| PSB09_45 | 0.938 | 0.073 | 0.032 | 0.001 | 0.607 | 661 | 33 | 205 | 8 | 47.379 |
| PSB09_46 | 0.973 | 0.059 | 0.070 | 0.002 | 0.250 | 685 | 28 | 437 | 9 | 77.842 |
| PSB09_47 | 0.628 | 0.040 | 0.025 | 0.001 | -0.291 | 491 | 24 | 157 | 3 | 48.527 |
| PSB09_48 | 0.830 | 0.140 | 0.076 | 0.001 | 0.960 | 595 | 49 | 469 | 8 | 88.189 |
| PSB09_49 | 0.744 | 0.017 | 0.045 | 0.001 | 0.538 | 564 | 10 | 287 | 6 | 67.356 |
| PSB09_50 | 1.230 | 0.042 | 0.086 | 0.002 | 0.413 | 812 | 19 | 530 | 11 | 79.023 |
| PSB09_51 | 1.090 | 0.038 | 0.079 | 0.001 | 0.253 | 745 | 19 | 487 | 8 | 79.078 |
| PSB09_52 | 1.444 | 0.050 | 0.066 | 0.003 | -0.369 | 904 | 20 | 413 | 17 | 62.718 |
| PSB09_53 | 0.997 | 0.036 | 0.031 | 0.001 | 0.878 | 700 | 19 | 197 | 6 | 43.872 |
| PSB09_54 | 1.250 | 0.150 | 0.049 | 0.002 | 0.914 | 810 | 61 | 307 | 11 | 54.969 |
| PSB09_55 | 0.985 | 0.031 | 0.046 | 0.001 | 0.551 | 694 | 16 | 291 | 8 | 59.029 |
| PSB09_57 | 0.746 | 0.016 | 0.036 | 0.001 | 0.178 | 565 | 9 | 231 | 7 | 57.936 |
| PSB09_1 | 6.488 | 0.052 | 0.348 | 0.004 | 0.315 | 2044 | 7 | 1925 | 20 | 97.004 |
| PSB09_4 | 2.772 | 0.052 | 0.226 | 0.003 | 0.539 | 1346 | 14 | 1312 | 17 | 98.721 |
| PSB09_5 | 1.337 | 0.060 | 0.138 | 0.004 | 0.915 | 864 | 27 | 834 | 24 | 98.233 |
| PSB09_5 | 2.801 | 0.082 | 0.235 | 0.005 | 0.761 | 1354 | 22 | 1360 | 26 | 99.779 |
| PSB09_7 | 6.480 | 0.260 | 0.343 | 0.009 | 0.931 | 2036 | 32 | 1910 | 46 | 96.807 |
| PSB09_11 | 3.540 | 0.230 | 0.255 | 0.013 | 0.952 | 1517 | 59 | 1459 | 66 | 98.051 |
| PSB09_24 | 4.390 | 0.140 | 0.268 | 0.011 | 0.960 | 1703 | 29 | 1528 | 59 | 94.584 |
| PSB09_32 | 1.008 | 0.032 | 0.099 | 0.002 | 0.656 | 706 | 16 | 609 | 12 | 92.624 |
| PSB09_26 | 0.806 | 0.033 | 0.098 | 0.002 | -0.058 | 597 | 19 | 603 | 10 | 99.541 |
| PSB09_27 | 0.865 | 0.024 | 0.092 | 0.003 | 0.256 | 632 | 13 | 569 | 17 | 94.754 |
| PSB09_22 | 0.892 | 0.035 | 0.091 | 0.002 | 0.296 | 644 | 19 | 563 | 10 | 93.289 |
| PSB09_12 | 0.831 | 0.041 | 0.101 | 0.002 | 0.028 | 611 | 23 | 621 | 13 | 99.188 |

Concordia age

| Sample | Mineral | Run-ID | Laser (W) | $^{36}Ar/^{39}Ar$ | 1σ | $^{37}Ar/^{39}Ar$ | 1σ | $^{40}Ar/^{39}Ar$ | 1σ | $^{40}Ar^*/^{39}Ar$ | 2σ | $^{39}Ar_k$ (%) | $^{40}Ar^*$ (%) | Age (Ma) | ± (2σ) |
|---|---|---|---|---|---|---|---|---|---|---|---|---|---|---|---|
| PS40A.1 J = 0.003308 ± 0.000004 | Muscovite | PS40A-1A | 0.100 | 0.055 | 0.048 | -0.195 | 0.132 | 77.669 | 0.192 | 61.303 | 28.374 | 0.633 | 78.939 | 333.9 | 141.1 |
| | | **PS40A-1B** | **0.200** | **0.011** | **0.002** | **-0.005** | **0.006** | **105.723** | **0.215** | **102.298** | **1.359** | **12.289** | **96.761** | **527.1** | **6.1** |
| | | **PS40A-1C** | **0.300** | **0.003** | **0.001** | **0.018** | **0.001** | **104.269** | **0.130** | **103.425** | **0.775** | **34.799** | **99.189** | **532.1** | **3.5** |
| | | **PS40A-1D** | **0.400** | **0.002** | **0.002** | **-0.005** | **0.004** | **103.969** | **0.157** | **103.453** | **1.111** | **17.243** | **99.504** | **532.2** | **5.0** |
| | | **PS40A-1E** | **0.500** | **0.003** | **0.003** | **0.106** | **0.005** | **103.893** | **0.317** | **103.038** | **1.895** | **10.056** | **99.169** | **530.4** | **8.5** |
| | | **PS40A-1F** | **0.600** | **0.000** | **0.003** | **0.048** | **0.000** | **103.447** | **0.117** | **103.416** | **1.629** | **15.532** | **99.966** | **532.1** | **7.3** |
| | | PS40A-1G | 0.700 | -0.005 | 0.013 | 0.047 | 0.046 | 97.321 | 0.497 | 98.894 | 7.967 | 2.635 | 101.613 | 511.8 | 35.9 |
| | | PS40A-1H | 0.800 | 0.028 | 0.053 | 0.931 | 0.025 | 102.981 | 2.187 | 94.776 | 32.087 | 0.885 | 91.973 | 493.1 | 146.1 |
| | | PS40A-1I | 0.900 | -0.013 | 0.016 | 0.562 | 0.008 | 105.701 | 1.371 | 109.630 | 9.863 | 1.281 | 103.677 | 559.6 | 43.3 |
| | | PS40A-1J | 1.000 | -0.033 | 0.023 | 0.127 | 0.108 | 105.327 | 4.326 | 115.283 | 16.510 | 1.011 | 109.443 | 584.2 | 71.5 |
| | | PS40A-1K | 1.200 | -0.001 | 0.012 | 0.103 | 0.041 | 105.385 | 0.442 | 105.812 | 7.198 | 2.755 | 100.398 | 542.7 | 31.9 |
| | | PS40A-1L | 1.400 | -0.173 | 0.265 | 2.821 | 1.746 | 180.147 | 76.413 | 232.384 | 249.358 | 0.099 | 128.744 | 1031.2 | 843.3 |
| | | PS40A-1M | 1.600 | -0.210 | 0.275 | 2.401 | 1.492 | 106.455 | 33.243 | 169.501 | 191.916 | 0.090 | 158.958 | 805.0 | 735.6 |
| | | PS40A-1N | 1.800 | -0.015 | 0.031 | 0.120 | 0.126 | 124.343 | 2.945 | 128.797 | 19.326 | 0.670 | 103.573 | 641.8 | 81.1 |
| | | PS40A-1O | 2.000 | 3.111 | 7.766 | 1.819 | 6.482 | 258.728 | 624.487 | -670.658 | 3451.048 | 0.017 | -258.886 | 0.0 | 16941.3 |
| | | PS40A-1P | 2.200 | 4.334 | 19.714 | 23.680 | 105.143 | 656.327 | 2850.465 | -645.009 | 6715.329 | 0.006 | -96.658 | 0.0 | 35433.0 |
| | | PS40A-1Q | 2.400 | 0.368 | 1.622 | 1.927 | 4.933 | 184.163 | 261.301 | 74.881 | 942.234 | 0.020 | 40.606 | 400.2 | 4517.4 |
| | | PS40A-1R | 2.600 | 0.750 | 2.373 | 0.869 | 5.368 | -198.313 | 439.586 | -422.331 | 2129.164 | -0.021 | 212.834 | 0.0 | 32075.2 |

| Sample | Mineral | Run-ID | Laser (W) | $^{36}Ar/^{39}Ar$ | 1σ | $^{37}Ar/^{39}Ar$ | 1σ | $^{40}Ar/^{39}Ar$ | 1σ | $^{40}Ar^*/^{39}Ar$ | 2σ | $^{39}Ar_k$ (%) | $^{40}Ar^*$ (%) | Age (Ma) | ± (2σ) |
|---|---|---|---|---|---|---|---|---|---|---|---|---|---|---|---|
| PS40A.2 J = 0.003308 ± 0.000004 | Muscovite | PS40A-2A | 0.1 | 0.020 | 0.013 | -0.084 | 0.086 | 81.996 | 0.368 | 75.977 | 7.778 | 1.202 | 92.664 | 405.4 | 37.2 |
| | | PS40A-2B | 0.2 | 0.001 | 0.001 | 0.003 | 0.007 | 106.644 | 0.082 | 106.325 | 0.630 | 16.140 | 99.701 | 545.0 | 2.8 |
| | | **PS40A-2C** | **0.3** | **0.002** | **0.001** | **0.000** | **0.003** | **104.549** | **0.101** | **103.958** | **0.441** | **32.950** | **99.435** | **534.5** | **2.0** |
| | | **PS40A-2D** | **0.4** | **0.002** | **0.002** | **-0.003** | **0.005** | **104.422** | **0.289** | **103.767** | **1.155** | **18.676** | **99.373** | **533.6** | **5.1** |
| | | **PS40A-2E** | **0.5** | **-0.002** | **0.004** | **0.005** | **0.011** | **104.622** | **0.319** | **105.246** | **2.319** | **8.512** | **100.597** | **540.2** | **10.3** |
| | | **PS40A-2F** | **0.6** | **-0.001** | **0.004** | **0.099** | **0.003** | **105.810** | **0.465** | **106.110** | **2.421** | **6.480** | **100.276** | **544.0** | **10.7** |
| | | **PS40A-2G** | **0.7** | **0.005** | **0.009** | **-0.007** | **0.023** | **105.578** | **0.949** | **104.201** | **5.813** | **3.237** | **98.696** | **535.6** | **25.9** |
| | | PS40A-2H | 0.8 | -0.001 | 0.014 | 0.007 | 0.046 | 110.260 | 0.799 | 110.685 | 8.658 | 2.564 | 100.385 | 564.2 | 37.9 |
| | | PS40A-2I | 0.9 | -0.002 | 0.005 | -0.015 | 0.027 | 107.922 | 0.340 | 108.529 | 3.131 | 3.004 | 100.563 | 554.7 | 13.8 |
| | | PS40A-2J | 1 | 0.001 | 0.007 | -0.001 | 0.013 | 108.989 | 0.148 | 108.697 | 4.341 | 4.601 | 99.732 | 555.5 | 19.1 |
| | | PS40A-2K | 1.2 | 0.027 | 0.027 | 0.110 | 0.154 | 105.339 | 1.794 | 97.204 | 16.257 | 0.768 | 92.270 | 504.2 | 73.6 |
| | | PS40A-2L | 1.4 | 0.010 | 0.056 | -0.022 | 0.171 | 138.678 | 4.391 | 135.793 | 34.374 | 0.537 | 97.921 | 670.9 | 141.9 |
| | | PS40A-2M | 1.6 | -0.662 | 0.518 | 1.893 | 2.529 | 280.013 | 126.817 | 478.526 | 502.003 | 0.045 | 170.670 | 1716.0 | 1162.6 |
| | | PS40A-2N | 1.8 | -0.054 | 0.022 | 0.936 | 0.024 | 114.666 | 0.665 | 130.876 | 13.453 | 0.772 | 114.063 | 650.5 | 56.2 |
| | | PS40A-2O | 2 | -0.067 | 0.715 | 7.468 | 7.837 | 378.938 | 349.468 | 401.725 | 858.902 | 0.027 | 105.463 | 1528.7 | 2206.1 |
| | | PS40A-2P | 2.2 | 0.010 | 0.046 | 0.328 | 0.148 | 96.597 | 2.341 | 93.614 | 28.102 | 0.487 | 96.889 | 487.8 | 128.4 |

| Sample | Mineral | Run-ID | Laser (W) | $^{36}Ar/^{39}Ar$ | 1σ | $^{37}Ar/^{39}Ar$ | 1σ | $^{40}Ar/^{39}Ar$ | 1σ | $^{40}Ar^*/^{39}Ar$ | 2σ | $^{39}Ar_k$ (%) | $^{40}Ar^*$ (%) | Age (Ma) | ± (2σ) |
|---|---|---|---|---|---|---|---|---|---|---|---|---|---|---|---|
| PS40D.1 J = 0.003308 ± 0.000004 | Muscovite | PS40D-1A | 0.1 | 0.100 | 0.130 | -0.111 | 0.435 | 123.162 | 24.704 | 93.366 | 85.127 | 0.136 | 75.813 | 486.7 | 389.1 |
| | | PS40D-1B | 0.2 | 0.011 | 0.007 | 0.002 | 0.010 | 112.943 | 0.220 | 109.562 | 4.121 | 5.298 | 97.007 | 559.3 | 18.1 |
| | | PS40D-1C | 0.3 | 0.002 | 0.001 | -0.006 | 0.003 | 106.245 | 0.168 | 105.786 | 0.747 | 14.298 | 99.569 | 542.6 | 3.3 |
| | | PS40D-1D | 0.4 | 0.001 | 0.001 | -0.002 | 0.001 | 105.487 | 0.110 | 105.281 | 0.644 | 18.595 | 99.804 | 540.4 | 2.9 |
| | | **PS40D-1E** | **0.5** | **-0.001** | **0.001** | **0.003** | **0.004** | **104.101** | **0.187** | **104.260** | **0.634** | **23.642** | **100.153** | **535.8** | **2.8** |
| | | **PS40D-1F** | **0.6** | **-0.001** | **0.001** | **-0.003** | **0.005** | **104.406** | **0.193** | **104.702** | **0.858** | **12.553** | **100.283** | **537.8** | **3.8** |
| | | **PS40D-1G** | **0.7** | **-0.002** | **0.001** | **0.009** | **0.003** | **103.720** | **0.214** | **104.282** | **0.833** | **11.056** | **100.541** | **535.9** | **3.7** |
| | | **PS40D-1H** | **0.8** | **0.002** | **0.004** | **0.028** | **0.017** | **106.665** | **0.668** | **106.206** | **2.997** | **3.005** | **99.567** | **544.5** | **13.3** |
| | | PS40D-1I | 0.9 | -0.009 | 0.006 | -0.012 | 0.018 | 109.731 | 0.611 | 112.342 | 3.992 | 1.593 | 102.381 | 571.4 | 17.4 |
| | | PS40D-1J | 1 | -0.020 | 0.013 | -0.037 | 0.050 | 105.186 | 0.952 | 111.213 | 7.868 | 0.884 | 105.733 | 566.5 | 34.4 |
| | | **PS40D-1K** | **1.2** | **-0.003** | **0.005** | **-0.011** | **0.018** | **104.341** | **0.542** | **105.106** | **2.944** | **4.449** | **100.734** | **539.6** | **13.1** |
| | | PS40D-1L | 1.4 | -0.009 | 0.010 | 0.203 | 0.015 | 109.076 | 1.064 | 111.758 | 6.141 | 1.598 | 102.445 | 568.9 | 26.8 |
| | | PS40D-1M | 1.6 | 0.078 | 0.075 | 2.362 | 0.862 | 214.799 | 77.341 | 191.952 | 144.597 | 0.124 | 89.217 | 889.0 | 529.0 |
| | | PS40D-1N | 1.8 | 0.008 | 0.004 | 0.002 | 0.024 | 106.730 | 0.909 | 104.258 | 2.758 | 2.535 | 97.683 | 535.8 | 12.3 |
| | | PS40D-1O | 2 | 0.490 | 0.706 | -1.964 | 3.226 | 393.431 | 313.648 | 246.594 | 526.367 | 0.024 | 62.764 | 1078.6 | 1734.1 |
| | | PS40D-1P | 2.2 | 0.040 | 0.092 | 0.019 | 0.279 | 33.285 | 0.811 | 21.301 | 54.732 | 0.209 | 63.993 | 123.1 | 305.9 |

| Sample | Mineral | Run-ID | Laser (W) | $^{36}Ar/^{39}Ar$ | 1σ | $^{37}Ar/^{39}Ar$ | 1σ | $^{40}Ar/^{39}Ar$ | 1σ | $^{40}Ar^*/^{39}Ar$ | 2σ | $^{39}Ar_k$ (%) | $^{40}Ar^*$ (%) | Age (Ma) | ± (2σ) |
|---|---|---|---|---|---|---|---|---|---|---|---|---|---|---|---|
| PS40D.2 J = 0.003308 ± 0.000004 | Muscovite | PS40D-2A | 0.1 | 0.399 | 0.332 | -0.232 | 0.592 | 232.973 | 125.180 | 113.960 | 194.459 | 0.080 | 48.923 | 578.5 | 844.8 |
| | | PS40D-2B | 0.2 | 0.011 | 0.002 | 0.018 | 0.013 | 112.676 | 0.401 | 109.309 | 1.670 | 6.542 | 97.011 | 558.1 | 7.3 |
| | | **PS40D-2C** | **0.3** | **0.001** | **0.001** | **0.001** | **0.004** | **107.547** | **0.116** | **107.103** | **0.649** | **27.319** | **99.587** | **548.4** | **2.9** |
| | | **PS40D-2D** | **0.4** | **0.004** | **0.002** | **0.000** | **0.003** | **107.229** | **0.211** | **106.139** | **1.026** | **26.510** | **98.984** | **544.2** | **4.5** |
| | | **PS40D-2E** | **0.5** | **0.000** | **0.001** | **0.007** | **0.004** | **107.132** | **0.122** | **107.269** | **0.799** | **20.226** | **100.128** | **549.2** | **3.5** |
| | | PS40D-2F | 0.6 | -0.006 | 0.002 | 0.025 | 0.010 | 107.645 | 0.205 | 109.407 | 1.525 | 6.743 | 101.635 | 558.6 | 6.7 |
| | | PS40D-2G | 0.7 | 0.000 | 0.004 | -0.012 | 0.007 | 106.007 | 0.255 | 106.107 | 2.623 | 5.893 | 100.096 | 544.0 | 11.6 |
| | | PS40D-2H | 0.8 | -0.012 | 0.009 | 0.017 | 0.022 | 108.588 | 0.517 | 112.098 | 5.753 | 2.135 | 103.231 | 570.4 | 25.1 |
| | | PS40D-2I | 0.9 | -0.009 | 0.013 | 0.000 | 0.070 | 120.730 | 1.211 | 123.339 | 8.042 | 1.211 | 102.161 | 618.8 | 34.2 |
| | | PS40D-2J | 1 | 0.256 | 0.223 | 0.554 | 0.556 | 210.024 | 54.963 | 133.647 | 144.869 | 0.168 | 63.610 | 662.0 | 600.9 |
| | | PS40D-2K | 1.2 | 0.404 | 0.223 | -0.445 | 1.151 | 238.141 | 84.590 | 117.635 | 132.056 | 0.101 | 49.413 | 594.4 | 568.7 |
| | | PS40D-2L | 1.4 | -0.002 | 0.010 | 0.027 | 0.030 | 112.397 | 0.400 | 112.877 | 6.189 | 2.117 | 100.425 | 573.8 | 27.0 |
| | | PS40D-2M | 1.6 | 0.317 | 0.178 | -1.052 | 0.987 | 237.464 | 93.430 | 142.636 | 135.251 | 0.136 | 60.110 | 698.9 | 549.7 |
| | | PS40D-2N | 1.8 | 0.844 | 0.544 | -2.207 | 2.195 | 305.949 | 159.019 | 53.821 | 199.847 | 0.055 | 17.619 | 296.3 | 1014.8 |
| | | PS40D-2O | 2 | 0.101 | 0.039 | -0.207 | 0.098 | 126.628 | 0.206 | 96.367 | 23.444 | 0.759 | 76.113 | 500.4 | 106.3 |
| | | PS40D-2P | 2.2 | 16.183 | 65.354 | -1.556 | 21.360 | 1085.832 | 4359.366 | -3740.769 | 30298.077 | 0.005 | -344.880 | 0.0 | 15933.9 |

# APÊNDICE B. Tabelas com resultados das análises de elementos traços (LASS-ICP-MS)

| Spot | Sample PSB09 - Apatite REE elements (ppm) - Quad ICP-MS | | | | | | | | | | | | | | | | | | | |
|---|---|---|---|---|---|---|---|---|---|---|---|---|---|---|---|---|---|---|---|---|
| | P | Ca | Sr | Y | Zr | Nb | La | Ce | Pr | Nd | Sm | Eu | Gd | Tb | Dy | Ho | Er | Tm | Yb | Lu |
| AP_PSB09_1 | 4394.00 | 10760.00 | 7.27 | 49.00 | 0.00 | 0.00 | 3.83 | 13.10 | 2.21 | 12.02 | 4.09 | 0.61 | 5.66 | 0.84 | 6.46 | 1.63 | 5.35 | 0.81 | 5.10 | 0.63 |
| AP_PSB09_2 | 4313.00 | 10650.00 | 6.46 | 43.40 | 0.00 | 0.00 | 3.02 | 10.32 | 1.80 | 10.10 | 3.48 | 0.49 | 5.12 | 0.76 | 5.82 | 1.42 | 4.62 | 0.70 | 4.27 | 0.52 |
| AP_PSB09_3 | 4316.00 | 10680.00 | 7.65 | 27.35 | 0.01 | 0.00 | 5.00 | 16.30 | 2.71 | 14.20 | 4.30 | 0.41 | 5.31 | 0.71 | 4.73 | 0.99 | 2.69 | 0.34 | 1.78 | 0.19 |
| AP_PSB09_4 | 4399.00 | 10910.00 | 7.97 | 28.10 | 0.00 | 0.00 | 5.10 | 16.60 | 2.75 | 14.70 | 4.60 | 0.42 | 5.53 | 0.74 | 4.85 | 1.02 | 2.80 | 0.34 | 1.79 | 0.20 |
| AP_PSB09_5 | 4347.00 | 10910.00 | 6.86 | 45.40 | 0.00 | BDL | 2.12 | 8.52 | 1.61 | 9.80 | 3.82 | 0.52 | 5.69 | 0.81 | 5.95 | 1.49 | 4.93 | 0.73 | 4.46 | 0.56 |
| AP_PSB09_6 | 4364.00 | 10880.00 | 6.84 | 53.80 | 0.01 | 0.00 | 2.53 | 10.55 | 2.04 | 12.47 | 4.68 | 0.65 | 6.95 | 0.97 | 7.38 | 1.84 | 6.01 | 0.90 | 5.51 | 0.68 |
| AP_PSB09_7 | 4435.00 | 10790.00 | 6.65 | 36.44 | 0.01 | BDL | 2.56 | 10.11 | 1.90 | 11.75 | 4.01 | 0.60 | 5.55 | 0.63 | 4.31 | 1.08 | 3.86 | 0.67 | 4.41 | 0.57 |
| AP_PSB09_8 | 4397.00 | 10770.00 | 6.53 | 34.71 | 0.01 | BDL | 1.23 | 5.02 | 1.06 | 7.44 | 2.93 | 0.47 | 4.52 | 0.54 | 3.94 | 1.03 | 3.82 | 0.64 | 4.16 | 0.54 |
| AP_PSB09_9 | 4382.00 | 10700.00 | 7.00 | 36.05 | 0.00 | 0.00 | 2.17 | 7.64 | 1.37 | 8.01 | 2.97 | 0.41 | 4.52 | 0.65 | 4.90 | 1.17 | 3.74 | 0.52 | 2.97 | 0.36 |
| AP_PSB09_10 | 4316.00 | 10650.00 | 6.64 | 31.41 | BDL | BDL | 1.14 | 4.15 | 0.78 | 4.99 | 1.97 | 0.31 | 3.32 | 0.48 | 3.85 | 0.98 | 3.26 | 0.47 | 2.81 | 0.35 |
| AP_PSB09_11 | 4373.00 | 10640.00 | 6.86 | 45.30 | 0.00 | BDL | 3.24 | 11.08 | 1.83 | 10.28 | 3.64 | 0.55 | 5.39 | 0.80 | 5.90 | 1.45 | 4.79 | 0.73 | 4.41 | 0.56 |
| AP_PSB09_12 | 4349.00 | 10710.00 | 6.72 | 29.71 | 75.00 | 0.00 | 3.21 | 13.11 | 2.46 | 14.75 | 4.93 | 0.48 | 6.31 | 0.66 | 4.16 | 0.91 | 2.97 | 0.52 | 3.50 | 0.45 |
| AP_PSB09_13 | 4333.00 | 10700.00 | 6.45 | 26.60 | 0.00 | 0.00 | 5.50 | 16.20 | 2.59 | 14.60 | 4.35 | 0.30 | 5.44 | 0.57 | 3.51 | 0.82 | 2.72 | 0.45 | 2.90 | 0.37 |
| AP_PSB09_14 | 4461.00 | 10860.00 | 7.29 | 68.50 | 0.01 | 0.00 | 6.66 | 22.40 | 3.67 | 19.81 | 6.35 | 0.78 | 8.43 | 1.19 | 9.11 | 2.24 | 7.29 | 1.15 | 6.95 | 0.89 |
| AP_PSB09_15 | 4335.00 | 10800.00 | 6.88 | 59.40 | 0.01 | BDL | 3.68 | 13.78 | 2.51 | 14.95 | 5.12 | 0.63 | 4.99 | 1.03 | 7.85 | 2.01 | 6.69 | 1.02 | 6.31 | 0.80 |
| AP_PSB09_16 | 4334.00 | 10670.00 | 7.72 | 54.55 | 0.00 | BDL | 5.79 | 18.83 | 3.03 | 15.72 | 5.20 | 0.68 | 4.61 | 0.99 | 7.42 | 1.80 | 5.90 | 0.92 | 5.65 | 0.73 |
| AP_PSB09_17 | 4342.00 | 10740.00 | 7.64 | 51.22 | 0.00 | BDL | 5.41 | 17.25 | 2.79 | 15.08 | 4.91 | 0.66 | 4.33 | 0.93 | 6.93 | 1.72 | 5.54 | 0.85 | 5.34 | 0.69 |
| AP_PSB09_18 | 4303.00 | 10880.00 | 6.66 | 28.52 | 0.00 | 0.00 | 0.74 | 2.34 | 0.46 | 3.17 | 1.29 | 0.31 | 1.54 | 0.37 | 3.06 | 0.87 | 3.20 | 0.51 | 3.19 | 0.41 |
| AP_PSB09_19 | 4357.00 | 10750.00 | 6.63 | 39.47 | 0.00 | 0.00 | 1.24 | 4.02 | 0.76 | 4.65 | 1.87 | 0.43 | 2.13 | 0.51 | 4.35 | 1.24 | 4.41 | 0.73 | 4.72 | 0.59 |
| AP_PSB09_20 | 4390.00 | 10800.00 | 7.28 | 45.93 | 0.00 | BDL | 3.38 | 11.90 | 2.03 | 11.28 | 3.95 | 0.59 | 3.54 | 0.79 | 5.99 | 1.52 | 5.04 | 0.79 | 4.84 | 0.62 |
| AP_PSB09_21 | 4353.00 | 10610.00 | 6.80 | 33.40 | 0.00 | 0.00 | 1.44 | 4.82 | 0.90 | 5.46 | 2.07 | 0.40 | 2.12 | 0.47 | 3.82 | 1.03 | 3.65 | 0.58 | 3.67 | 0.46 |
| AP_PSB09_22 | 4409.00 | 10780.00 | 7.03 | 33.20 | 0.00 | BDL | 2.53 | 8.35 | 1.39 | 7.86 | 2.68 | 0.44 | 2.44 | 0.54 | 4.18 | 1.07 | 3.55 | 0.55 | 3.46 | 0.43 |
| AP_PSB09_23 | 4434.00 | 10790.00 | 7.14 | 40.70 | 0.00 | BDL | 1.97 | 7.79 | 1.42 | 8.58 | 3.02 | 0.51 | 2.77 | 0.64 | 5.02 | 1.29 | 4.47 | 0.69 | 4.32 | 0.54 |
| AP_PSB09_24 | 4316.00 | 10790.00 | 6.57 | 23.93 | BDL | BDL | 0.52 | 1.76 | 0.37 | 2.59 | 1.08 | 0.22 | 1.34 | 0.33 | 2.72 | 0.76 | 2.50 | 0.37 | 2.14 | 0.26 |
| AP_PSB09_25 | 4381.00 | 10730.00 | 6.90 | 29.19 | 0.00 | BDL | 1.55 | 5.45 | 1.00 | 6.05 | 2.18 | 0.33 | 2.15 | 0.49 | 3.80 | 0.95 | 3.02 | 0.41 | 2.42 | 0.29 |
| AP_PSB09_26 | 4407.00 | 10780.00 | 7.25 | 44.60 | 0.00 | BDL | 2.91 | 10.16 | 1.74 | 9.79 | 3.44 | 0.50 | 3.08 | 0.74 | 5.59 | 1.43 | 4.81 | 0.72 | 4.38 | 0.57 |
| AP_PSB09_27 | 4369.00 | 10730.00 | 7.52 | 41.80 | 0.00 | BDL | 3.23 | 10.75 | 1.78 | 10.12 | 3.47 | 0.55 | 3.08 | 0.71 | 5.39 | 1.36 | 4.57 | 0.69 | 4.24 | 0.54 |
| AP_PSB09_28 | 4355.00 | 10820.00 | 7.26 | 48.21 | 0.00 | BDL | 3.53 | 12.20 | 2.10 | 11.55 | 4.08 | 0.64 | 3.63 | 0.83 | 6.23 | 1.59 | 5.31 | 0.80 | 5.03 | 0.64 |
| AP_PSB09_29 | 4351.00 | 10740.00 | 6.81 | 33.40 | 0.00 | BDL | 1.29 | 4.06 | 0.71 | 4.49 | 1.80 | 0.34 | 1.92 | 0.46 | 3.71 | 1.00 | 3.54 | 0.55 | 3.39 | 0.43 |
| AP_PSB09_30 | 4444.00 | 10770.00 | 6.53 | 33.03 | BDL | BDL | 1.01 | 3.47 | 0.66 | 4.31 | 1.75 | 0.34 | 2.49 | 0.47 | 3.85 | 1.04 | 3.63 | 0.58 | 3.52 | 0.43 |
| AP_PSB09_31 | 4380.00 | 10770.00 | 6.74 | 41.24 | 0.00 | 0.00 | 2.12 | 8.06 | 1.52 | 9.27 | 3.13 | 0.38 | 3.89 | 0.66 | 5.18 | 1.36 | 4.58 | 0.68 | 4.23 | 0.53 |
| AP_PSB09_32 | 4460.00 | 10830.00 | 6.95 | 52.80 | 0.00 | BDL | 4.61 | 16.41 | 2.79 | 15.49 | 4.72 | 0.51 | 5.31 | 0.91 | 7.03 | 1.78 | 5.76 | 0.89 | 5.47 | 0.69 |
| AP_PSB09_33 | 4405.00 | 10660.00 | 7.13 | 58.80 | 0.01 | 0.00 | 4.88 | 16.05 | 2.60 | 13.70 | 4.77 | 0.74 | 5.63 | 0.98 | 7.79 | 1.95 | 6.48 | 1.00 | 6.13 | 0.75 |
| AP_PSB09_34 | 4422.00 | 10760.00 | 6.45 | 26.34 | 0.00 | BDL | 2.60 | 9.50 | 1.72 | 10.03 | 3.30 | 0.31 | 4.02 | 0.61 | 4.08 | 0.92 | 2.62 | 0.37 | 2.17 | 0.26 |
| AP_PSB09_35 | 4383.00 | 10730.00 | 6.47 | 35.31 | 0.00 | 0.00 | 0.99 | 3.46 | 0.72 | 4.77 | 1.95 | 0.39 | 3.07 | 0.52 | 4.21 | 1.11 | 3.86 | 0.61 | 3.82 | 0.47 |
| AP_PSB09_36 | 4368.00 | 10720.00 | 6.53 | 36.81 | 0.00 | BDL | 1.36 | 5.03 | 0.98 | 6.14 | 2.42 | 0.42 | 3.54 | 0.59 | 4.57 | 1.19 | 4.03 | 0.63 | 3.84 | 0.48 |
| AP_PSB09_37 | 4411.00 | 10910.00 | 7.28 | 39.60 | 0.00 | BDL | 3.32 | 11.20 | 1.94 | 11.20 | 3.54 | 0.45 | 4.53 | 0.67 | 5.08 | 1.31 | 4.37 | 0.66 | 4.18 | 0.52 |
| AP_PSB09_38 | 4379.00 | 10740.00 | 6.96 | 35.53 | 0.00 | BDL | 5.10 | 18.27 | 3.15 | 17.54 | 5.25 | 0.53 | 5.39 | 0.65 | 4.28 | 1.04 | 3.91 | 0.69 | 4.46 | 0.57 |
| AP_PSB09_39 | 4418.00 | 10690.00 | 6.96 | 31.43 | 0.00 | BDL | 4.62 | 16.22 | 2.78 | 15.51 | 4.43 | 0.48 | 4.81 | 0.56 | 3.75 | 0.95 | 3.45 | 0.61 | 4.03 | 0.52 |
| AP_PSB09_40 | 4384.00 | 10660.00 | 6.72 | 43.20 | 0.00 | BDL | 1.81 | 6.20 | 1.11 | 6.87 | 2.69 | 0.48 | 4.09 | 0.64 | 5.15 | 1.35 | 4.65 | 0.73 | 4.51 | 0.57 |
| AP_PSB09_41 | 4360.00 | 10890.00 | 6.95 | 42.90 | 0.00 | BDL | 3.72 | 12.15 | 2.04 | 11.11 | 3.74 | 0.55 | 4.88 | 0.75 | 5.67 | 1.44 | 4.61 | 0.69 | 4.29 | 0.52 |
| AP_PSB09_42 | 4468.00 | 10820.00 | 6.89 | 43.18 | 0.00 | BDL | 3.18 | 10.90 | 1.83 | 10.33 | 3.55 | 0.54 | 4.72 | 0.75 | 5.66 | 1.40 | 4.58 | 0.70 | 4.20 | 0.52 |
| AP_PSB09_43 | 4373.00 | 10660.00 | 6.87 | 42.80 | 0.00 | BDL | 3.86 | 12.23 | 2.02 | 10.88 | 3.71 | 0.56 | 4.92 | 0.77 | 5.80 | 1.43 | 4.51 | 0.69 | 4.27 | 0.53 |
| AP_PSB09_44 | 4392.00 | 10670.00 | 7.17 | 38.10 | 0.00 | 0.00 | 3.00 | 10.00 | 1.71 | 9.45 | 3.23 | 0.50 | 4.24 | 0.63 | 4.88 | 1.23 | 4.04 | 0.63 | 3.92 | 0.49 |
| AP_PSB09_45 | 4384.00 | 10800.00 | 7.17 | 57.70 | 0.00 | BDL | 5.47 | 17.60 | 2.88 | 15.40 | 5.01 | 0.74 | 5.24 | 1.02 | 7.84 | 1.96 | 6.45 | 1.00 | 6.42 | 0.79 |
| AP_PSB09_46 | 4386.00 | 10850.00 | 7.28 | 33.46 | 0.00 | BDL | 3.70 | 11.48 | 1.91 | 10.14 | 3.16 | 0.48 | 3.28 | 0.61 | 4.47 | 1.12 | 3.56 | 0.53 | 3.34 | 0.41 |
| AP_PSB09_47 | 4428.00 | 10780.00 | 7.45 | 46.80 | 0.00 | BDL | 4.32 | 14.20 | 2.31 | 12.52 | 4.23 | 0.62 | 4.18 | 0.85 | 6.29 | 1.56 | 5.14 | 0.78 | 4.80 | 0.60 |
| AP_PSB09_48 | 4358.00 | 10870.00 | 6.51 | 31.85 | 0.00 | BDL | 6.20 | 20.10 | 3.39 | 18.50 | 5.90 | 0.34 | 4.93 | 0.85 | 5.59 | 1.19 | 3.28 | 0.44 | 2.42 | 0.26 |
| AP_PSB09_49 | 4384.00 | 10880.00 | 6.28 | 51.00 | 0.01 | 0.00 | 14.60 | 41.00 | 5.90 | 28.70 | 8.00 | 0.50 | 6.53 | 1.22 | 8.04 | 1.79 | 5.39 | 0.76 | 4.50 | 0.55 |
| AP_PSB09_50 | 4444.00 | 10760.00 | 7.34 | 32.53 | 0.00 | 0.00 | 3.02 | 10.26 | 1.76 | 9.93 | 3.32 | 0.43 | 3.16 | 0.61 | 4.41 | 1.08 | 3.39 | 0.51 | 2.91 | 0.36 |
| AP_PSB09_51 | 4473.00 | 10700.00 | 7.20 | 33.38 | 0.00 | BDL | 2.76 | 10.01 | 1.75 | 10.00 | 3.38 | 0.43 | 3.20 | 0.62 | 4.55 | 1.11 | 3.51 | 0.52 | 3.01 | 0.36 |
| AP_PSB09_52 | 4451.00 | 10840.00 | 7.22 | 45.00 | 0.00 | BDL | 3.09 | 10.21 | 1.76 | 9.73 | 3.44 | 0.56 | 3.45 | 0.72 | 5.52 | 1.43 | 5.04 | 0.79 | 4.89 | 0.63 |
| AP_PSB09_53 | 4411.00 | 10740.00 | 7.03 | 44.30 | 0.00 | BDL | 3.85 | 13.34 | 2.28 | 12.69 | 4.10 | 0.54 | 3.90 | 0.75 | 5.72 | 1.46 | 4.83 | 0.75 | 4.71 | 0.60 |
| AP_PSB09_54 | 4348.00 | 10710.00 | 6.58 | 45.90 | 0.00 | 0.00 | 2.37 | 8.98 | 1.69 | 10.30 | 3.54 | 0.52 | 3.63 | 0.73 | 5.65 | 1.52 | 5.23 | 0.82 | 5.24 | 0.66 |
| AP_PSB09_55 | 4329.00 | 10730.00 | 6.56 | 24.26 | 0.00 | 0.01 | 0.63 | 2.30 | 0.45 | 3.11 | 1.23 | 0.23 | 1.56 | 0.32 | 2.62 | 0.74 | 2.63 | 0.42 | 2.64 | 0.33 |
| AP_PSB09_56 | 4441.00 | 10910.00 | 6.59 | 35.11 | 0.00 | BDL | 3.03 | 11.14 | 2.00 | 11.45 | 3.71 | 0.41 | 3.52 | 0.67 | 4.85 | 1.17 | 3.62 | 0.54 | 3.37 | 0.41 |
| AP_PSB09_57 | 4434.00 | 10750.00 | 6.64 | 38.25 | 0.00 | BDL | 3.38 | 12.63 | 2.20 | 12.68 | 4.10 | 0.46 | 3.83 | 0.74 | 5.31 | 1.26 | 3.99 | 0.59 | 3.60 | 0.44 |
| AP_PSB09_58 | 4418.00 | 10910.00 | 6.89 | 50.70 | 0.00 | 0.00 | 3.88 | 13.09 | 2.24 | 12.20 | 4.18 | 0.63 | 4.18 | 0.86 | 6.56 | 1.69 | 5.46 | 0.84 | 5.32 | 0.65 |
| AP_PSB09_59 | 4388.00 | 10850.00 | 7.15 | 58.50 | 0.01 | BDL | 5.64 | 18.50 | 3.01 | 16.00 | 5.34 | 0.74 | 5.06 | 1.04 | 7.81 | 1.98 | 6.34 | 0.98 | 6.04 | 0.75 |
| AP_PSB09_60 | 4348.00 | 10600.00 | 6.30 | 36.75 | 0.03 | 0.00 | 2.84 | 10.87 | 2.08 | 12.57 | 4.41 | 0.30 | 4.57 | 0.77 | 5.30 | 1.23 | 3.90 | 0.58 | 3.38 | 0.40 |
| AP_PSB09_61 | 4397.00 | 10790.00 | 6.64 | 33.50 | 0.00 | BDL | 2.12 | 9.71 | 1.93 | 11.37 | 4.09 | 0.39 | 4.19 | 0.72 | 5.06 | 1.16 | 3.45 | 0.49 | 2.68 | 0.32 |
| AP_PSB09_62 | 4404.00 | 10780.00 | 6.39 | 29.47 | 0.00 | BDL | 1.73 | 8.43 | 1.75 | 10.71 | 3.75 | 0.32 | 4.08 | 0.67 | 4.60 | 1.05 | 3.04 | 0.42 | 2.39 | 0.27 |
| AP_PSB09_63 | 4408.00 | 10810.00 | 7.74 | 51.40 | 0.00 | BDL | 5.43 | 17.00 | 2.78 | 15.03 | 4.92 | 0.69 | 5.42 | 0.91 | 6.89 | 1.75 | 5.68 | 0.87 | 5.48 | 0.69 |
| AP_PSB09_64 | 4401.00 | 10840.00 | 7.06 | 42.91 | 0.00 | BDL | 3.62 | 11.97 | 2.04 | 11.14 | 3.78 | 0.57 | 4.54 | 0.76 | 5.65 | 1.42 | 4.51 | 0.70 | 4.38 | 0.54 |
| AP_PSB09_65 | 4442.00 | 10750.00 | 6.91 | 36.47 | 0.00 | BDL | 2.47 | 8.51 | 1.49 | 8.66 | 3.01 | 0.48 | 3.83 | 0.61 | 4.73 | 1.19 | 3.87 | 0.58 | 3.61 | 0.44 |
| AP_PSB09_66 | 4496.00 | 10700.00 | 5.90 | 39.10 | 0.01 | 0.00 | 3.70 | 13.70 | 2.41 | 14.00 | 4.57 | 0.46 | 4.97 | 0.75 | 5.34 | 1.28 | 4.12 | 0.64 | 3.84 | 0.45 |
| AP_PSB09_67 | 4386.00 | 10780.00 | 6.06 | 39.90 | 0.00 | 0.00 | 2.13 | 8.86 | 1.75 | 11.18 | 3.96 | 0.39 | 4.56 | 0.72 | 5.20 | 1.29 | 4.27 | 0.67 | 3.97 | 0.48 |
| AP_PSB09_68 | 4500.00 | 10680.00 | 6.88 | 38.88 | 0.00 | BDL | 4.06 | 13.01 | 2.12 | 11.36 | 3.60 | 0.49 | 4.10 | 0.69 | 5.14 | 1.26 | 4.03 | 0.62 | 3.70 | 0.45 |
| AP_PSB09_69 | 4420.00 | 10690.00 | 7.12 | 45.50 | 0.00 | BDL | 4.44 | 14.41 | 2.38 | 12.75 | 4.10 | 0.53 | 4.65 | 0.81 | 5.83 | 1.48 | 4.84 | 0.73 | 4.42 | 0.56 |
| AP_PSB09_70 | 4448.00 | 10580.00 | 6.72 | 29.07 | 0.00 | BDL | 1.85 | 5.81 | 0.96 | 5.48 | 1.96 | 0.35 | 2.63 | 0.45 | 3.50 | 0.91 | 2.93 | 0.46 | 2.74 | 0.33 |
| AP_PSB09_71 | 4409.00 | 10670.00 | 6.06 | 49.80 | 0.00 | 0.00 | 1.48 | 6.19 | 1.28 | 8.21 | 3.05 | 0.49 | 4.19 | 0.73 | 5.91 | 1.61 | 5.39 | 0.87 | 5.43 | 0.66 |
| AP_PSB09_72 | 4402.00 | 10860.00 | 6.26 | 39.50 | 0.00 | 0.00 | 1.49 | 5.56 | 1.06 | 6.72 | 2.44 | 0.38 | 3.31 | 0.57 | 4.53 | 1.23 | 4.27 | 0.67 | 4.16 | 0.52 |
| AP_PSB09_73 | 4479.00 | 10820.00 | 6.21 | 36.80 | 0.00 | 0.00 | 1.27 | 4.11 | 0.74 | 4.56 | 1.92 | 0.38 | 2.86 | 0.54 | 4.35 | 1.14 | 3.90 | 0.62 | 3.80 | 0.48 |
| AP_PSB09_74 | 4421.00 | 10650.00 | 6.91 | 46.08 | 0.00 | BDL | 5.23 | 16.19 | 2.59 | 13.16 | 4.21 | 0.62 | 4.76 | 0.83 | 6.32 | 1.52 | 4.72 | 0.71 | 4.31 | 0.51 |

Sample PS42A - Apatite REE elements (ppm) - Quad ICP-MS

| Spot | P | Ca | Sr | Y | Zr | Nb | La | Ce | Pr | Nd | Sm | Eu | Gd | Tb | Dy | Ho | Er | Tm | Yb | Lu |
|---|---|---|---|---|---|---|---|---|---|---|---|---|---|---|---|---|---|---|---|---|
| AP_PS42A | 170400.00 | 435500.00 | 595.00 | 420.00 | 0.95 | BDL | 140.60 | 453.00 | 78.20 | 468.00 | 158.60 | 44.20 | 159.20 | 17.41 | 79.70 | 13.34 | 30.60 | 3.48 | 20.58 | 2.98 |
| AP_PS42A_1 | 175700.00 | 437900.00 | 578.00 | 466.00 | 1.01 | 0.01 | 134.20 | 437.00 | 75.20 | 477.00 | 165.90 | 47.70 | 167.90 | 19.18 | 85.40 | 14.84 | 32.90 | 3.89 | 23.50 | 3.31 |
| AP_PS42A_2 | 173000.00 | 434700.00 | 562.00 | 365.00 | BDL | BDL | 115.00 | 352.00 | 61.00 | 382.00 | 140.00 | 32.30 | 142.00 | 16.90 | 74.00 | 12.60 | 28.10 | 3.08 | 18.40 | 2.55 |
| AP_PS42A_3 | 175100.00 | 432400.00 | 553.00 | 479.00 | 0.09 | 0.01 | 152.00 | 462.00 | 78.70 | 499.00 | 181.00 | 38.90 | 192.00 | 22.10 | 101.00 | 16.30 | 36.50 | 4.15 | 23.80 | 3.36 |
| AP_PS42A_4 | 174600.00 | 437000.00 | 552.80 | 667.00 | 0.47 | 0.08 | 103.70 | 331.00 | 60.20 | 385.00 | 163.00 | 49.60 | 201.00 | 24.90 | 123.90 | 22.00 | 49.30 | 5.66 | 33.40 | 4.72 |
| AP_PS42A_5 | 174000.00 | 435700.00 | 552.30 | 624.00 | 0.05 | BDL | 102.20 | 326.00 | 58.40 | 377.00 | 152.10 | 47.30 | 179.80 | 22.47 | 109.00 | 19.73 | 45.50 | 5.30 | 31.00 | 4.56 |
| AP_PS42A_6 | 175700.00 | 435900.00 | 307.60 | 736.00 | 0.07 | 0.04 | 272.80 | 762.00 | 119.70 | 643.00 | 222.30 | 33.30 | 233.30 | 29.88 | 147.50 | 25.61 | 58.10 | 6.89 | 39.30 | 4.83 |
| AP_PS42A_7 | 172400.00 | 437000.00 | 285.40 | 573.00 | 0.03 | BDL | 221.70 | 603.00 | 91.70 | 507.00 | 171.60 | 26.80 | 176.90 | 22.76 | 113.00 | 19.25 | 44.60 | 5.58 | 30.20 | 3.81 |
| AP_PS42A_8 | 174100.00 | 434600.00 | 585.00 | 280.00 | 0.51 | BDL | 157.00 | 506.00 | 88.00 | 518.00 | 147.00 | 34.60 | 129.00 | 13.00 | 55.70 | 9.10 | 20.50 | 2.39 | 13.80 | 2.11 |
| AP_PS42A_9 | 176100.00 | 440100.00 | 385.70 | 1780.00 | 4.50 | BDL | 389.00 | 1119.00 | 181.00 | 1035.00 | 383.00 | 54.50 | 437.00 | 63.90 | 340.00 | 60.40 | 149.00 | 19.30 | 116.80 | 14.70 |
| AP_PS42A_10 | 174900.00 | 440400.00 | 386.30 | 1640.00 | 0.24 | BDL | 378.00 | 1072.00 | 169.00 | 948.00 | 354.00 | 47.60 | 403.00 | 58.40 | 312.00 | 55.60 | 136.00 | 18.10 | 107.00 | 13.60 |
| AP_PS42A_11 | 176400.00 | 443900.00 | 367.20 | 1205.00 | 0.11 | BDL | 244.00 | 731.00 | 119.30 | 704.00 | 263.00 | 38.70 | 300.00 | 42.00 | 223.00 | 39.90 | 98.40 | 12.96 | 80.20 | 10.26 |
| AP_PS42A_12 | 173800.00 | 436100.00 | 362.50 | 1155.00 | 0.12 | BDL | 239.00 | 720.00 | 119.10 | 691.00 | 249.00 | 36.40 | 291.00 | 41.20 | 216.00 | 38.40 | 93.50 | 12.87 | 75.90 | 9.50 |
| AP_PS42A_13 | 177600.00 | 436300.00 | 631.00 | 536.00 | 0.09 | 0.04 | 216.90 | 630.00 | 105.40 | 636.00 | 209.70 | 45.30 | 202.70 | 23.92 | 107.80 | 18.62 | 42.00 | 5.04 | 29.80 | 3.85 |
| AP_PS42A_14 | 175300.00 | 435600.00 | 620.00 | 471.00 | 0.10 | 0.02 | 182.00 | 528.00 | 86.70 | 534.00 | 179.30 | 40.50 | 179.20 | 21.30 | 96.10 | 15.96 | 36.30 | 4.45 | 25.00 | 3.36 |
| AP_PS42A_15 | 178600.00 | 450400.00 | 631.70 | 361.00 | 0.02 | BDL | 143.00 | 414.00 | 66.90 | 404.00 | 137.00 | 32.30 | 138.00 | 16.20 | 73.90 | 11.81 | 27.90 | 3.23 | 19.90 | 2.62 |
| AP_PS42A_16 | 174000.00 | 430700.00 | 622.00 | 440.00 | 0.10 | BDL | 183.90 | 533.00 | 89.50 | 549.00 | 177.00 | 32.80 | 171.00 | 19.96 | 91.60 | 14.98 | 34.40 | 4.09 | 23.90 | 3.11 |
| AP_PS42A_17 | 171500.00 | 437000.00 | 624.00 | 458.00 | 0.05 | 0.03 | 239.60 | 713.00 | 120.10 | 682.00 | 199.60 | 46.20 | 183.00 | 20.06 | 87.30 | 15.00 | 34.00 | 3.96 | 22.70 | 3.38 |
| AP_PS42A_18 | 177400.00 | 441200.00 | 619.00 | 487.00 | 0.07 | 0.03 | 259.60 | 773.00 | 128.30 | 747.00 | 218.40 | 42.00 | 190.90 | 21.32 | 93.60 | 15.79 | 36.30 | 4.34 | 24.70 | 3.56 |
| AP_PS42A_19 | 164400.00 | 433800.00 | 539.00 | 268.80 | 0.10 | 0.03 | 32.30 | 99.90 | 16.60 | 101.20 | 41.80 | 18.49 | 60.70 | 8.60 | 43.50 | 8.39 | 19.10 | 2.38 | 13.61 | 1.88 |
| AP_PS42A_20 | 176600.00 | 431700.00 | 566.00 | 697.00 | 0.02 | BDL | 87.00 | 268.70 | 46.60 | 312.90 | 130.30 | 44.50 | 180.50 | 24.80 | 127.70 | 23.27 | 54.40 | 6.48 | 37.10 | 5.04 |
| AP_PS42A_21 | 178000.00 | 433500.00 | 555.00 | 1057.00 | 0.03 | BDL | 174.00 | 497.00 | 86.30 | 567.00 | 240.20 | 47.30 | 301.60 | 40.79 | 204.40 | 35.60 | 83.20 | 10.17 | 60.10 | 8.21 |
| AP_PS42A_22 | 175000.00 | 438000.00 | 580.00 | 376.60 | 0.04 | BDL | 182.00 | 579.00 | 99.20 | 585.00 | 173.70 | 36.10 | 152.80 | 16.12 | 69.60 | 11.65 | 26.49 | 3.14 | 18.10 | 2.63 |
| AP_PS42A_23 | 180200.00 | 442000.00 | 605.00 | 387.50 | 0.04 | 0.03 | 192.90 | 605.00 | 104.20 | 604.00 | 177.70 | 34.90 | 155.60 | 16.62 | 72.30 | 12.00 | 25.89 | 2.98 | 18.84 | 2.66 |
| AP_PS42A_24 | 178300.00 | 439900.00 | 572.80 | 225.00 | 0.04 | BDL | 79.10 | 242.00 | 41.80 | 256.00 | 91.00 | 21.50 | 96.60 | 10.50 | 46.50 | 7.55 | 16.60 | 1.85 | 9.30 | 1.30 |
| AP_PS42A_25 | 174300.00 | 436500.00 | 581.10 | 340.00 | 0.01 | BDL | 99.80 | 314.00 | 59.80 | 371.00 | 138.60 | 23.31 | 149.80 | 16.40 | 72.50 | 11.80 | 26.50 | 2.74 | 14.80 | 2.10 |
| AP_PS42A_26 | 177000.00 | 442000.00 | 586.00 | 346.80 | 0.04 | BDL | 100.00 | 315.40 | 57.80 | 382.00 | 140.10 | 23.83 | 151.80 | 16.79 | 74.70 | 12.10 | 25.46 | 2.84 | 15.27 | 1.93 |
| AP_PS42A_27 | 175500.00 | 431000.00 | 578.00 | 447.00 | 0.08 | BDL | 147.40 | 445.00 | 75.70 | 484.00 | 177.80 | 36.10 | 186.80 | 21.28 | 96.10 | 16.01 | 33.60 | 3.69 | 20.20 | 2.87 |
| AP_PS42A_28 | 175800.00 | 440400.00 | 560.00 | 961.00 | 0.06 | BDL | 137.00 | 403.00 | 69.00 | 440.00 | 193.00 | 45.10 | 253.00 | 35.00 | 179.00 | 31.60 | 74.80 | 9.03 | 53.10 | 7.29 |
| AP_PS42A_29 | 175200.00 | 430100.00 | 505.00 | 235.00 | BDL | BDL | 27.50 | 77.40 | 12.59 | 77.60 | 31.10 | 14.39 | 43.20 | 6.39 | 33.00 | 6.31 | 15.30 | 1.99 | 11.10 | 1.70 |
| AP_PS42A_30 | 178300.00 | 436800.00 | 628.00 | 451.00 | 0.02 | BDL | 139.00 | 417.00 | 72.50 | 452.00 | 165.00 | 35.20 | 177.00 | 20.80 | 95.30 | 16.00 | 35.10 | 4.12 | 23.00 | 3.24 |
| AP_PS42A_31 | 177000.00 | 434000.00 | 582.00 | 623.00 | 0.08 | BDL | 136.60 | 427.00 | 76.30 | 484.00 | 193.40 | 38.30 | 212.70 | 26.36 | 124.80 | 21.59 | 48.40 | 5.76 | 32.20 | 4.51 |
| AP_PS42A_32 | 183200.00 | 438000.00 | 594.00 | 698.00 | 0.04 | BDL | 177.10 | 550.00 | 97.90 | 622.00 | 235.90 | 38.90 | 245.80 | 30.16 | 142.50 | 24.20 | 53.30 | 6.47 | 37.40 | 4.94 |
| AP_PS42A_33 | 177600.00 | 433000.00 | 553.30 | 816.00 | BDL | 0.00 | 116.00 | 357.00 | 63.80 | 413.00 | 182.00 | 45.80 | 231.00 | 30.40 | 154.00 | 27.30 | 64.00 | 8.06 | 44.70 | 6.25 |
| AP_PS42A_34 | 177600.00 | 440500.00 | 335.70 | 665.00 | 0.11 | BDL | 163.00 | 477.00 | 79.70 | 480.00 | 169.80 | 26.70 | 189.20 | 25.65 | 129.40 | 22.92 | 54.30 | 6.79 | 37.10 | 4.49 |
| AP_PS42A_35 | 179000.00 | 442700.00 | 596.00 | 547.00 | 0.07 | BDL | 86.00 | 284.00 | 50.80 | 340.00 | 139.00 | 27.70 | 172.00 | 22.90 | 113.00 | 19.70 | 45.30 | 4.99 | 27.50 | 3.51 |
| AP_PS42A_36 | 178900.00 | 434700.00 | 611.90 | 464.20 | 0.01 | 0.06 | 78.60 | 257.60 | 46.50 | 313.60 | 129.00 | 24.40 | 155.50 | 20.08 | 95.40 | 16.17 | 36.86 | 4.21 | 21.10 | 2.83 |
| AP_PS42A_37 | 174900.00 | 435900.00 | 590.00 | 545.00 | 11.00 | 0.06 | 146.10 | 454.00 | 76.30 | 440.00 | 157.30 | 53.90 | 167.30 | 20.50 | 100.10 | 17.24 | 41.30 | 4.95 | 29.80 | 4.21 |
| AP_PS42A_38 | 176200.00 | 433400.00 | 588.00 | 673.00 | 0.80 | 0.03 | 190.20 | 583.00 | 97.60 | 576.00 | 197.60 | 56.20 | 211.60 | 26.40 | 126.70 | 21.67 | 51.80 | 6.30 | 37.40 | 5.32 |
| AP_PS42A_39 | 174400.00 | 429900.00 | 562.10 | 580.00 | 0.49 | 0.02 | 107.00 | 358.00 | 65.90 | 416.00 | 155.00 | 41.40 | 172.00 | 20.50 | 100.00 | 18.30 | 43.70 | 5.15 | 29.70 | 4.06 |
| AP_PS42A_40 | 177200.00 | 432000.00 | 570.00 | 554.00 | 225.00 | 0.04 | 145.90 | 466.00 | 83.40 | 508.00 | 169.80 | 42.70 | 172.90 | 21.01 | 98.60 | 17.32 | 41.00 | 4.98 | 29.90 | 4.01 |
| AP_PS42A_41 | 178300.00 | 432700.00 | 576.00 | 462.00 | 0.06 | BDL | 132.20 | 417.00 | 71.40 | 429.00 | 149.00 | 49.70 | 160.00 | 18.90 | 87.20 | 14.60 | 34.00 | 4.26 | 22.70 | 3.30 |
| AP_PS42A_42 | 175500.00 | 432300.00 | 317.30 | 526.00 | 0.02 | 0.02 | 129.50 | 363.00 | 60.50 | 359.00 | 127.40 | 23.30 | 147.10 | 19.90 | 100.40 | 17.80 | 41.30 | 5.07 | 28.50 | 3.66 |
| AP_PS42A_43 | 179000.00 | 439400.00 | 318.40 | 606.00 | 0.02 | BDL | 126.80 | 366.00 | 61.60 | 377.00 | 139.50 | 27.90 | 168.00 | 22.30 | 114.30 | 20.30 | 47.40 | 5.99 | 33.80 | 4.19 |
| AP_PS42A_44 | 179000.00 | 442400.00 | 583.00 | 227.00 | 0.00 | BDL | 83.60 | 240.00 | 39.80 | 229.00 | 76.00 | 25.60 | 76.40 | 9.17 | 41.70 | 7.11 | 16.40 | 1.90 | 11.61 | 1.66 |
| AP_PS42A_45 | 174700.00 | 438000.00 | 593.10 | 259.00 | BDL | BDL | 106.00 | 307.00 | 48.50 | 283.00 | 95.00 | 28.10 | 95.00 | 10.60 | 48.40 | 8.50 | 19.50 | 2.40 | 13.50 | 1.88 |
| AP_PS42A_46 | 177700.00 | 434500.00 | 582.20 | 323.00 | BDL | BDL | 71.00 | 222.00 | 39.40 | 251.00 | 98.00 | 25.10 | 114.00 | 14.10 | 67.00 | 11.30 | 25.30 | 2.92 | 16.10 | 2.18 |
| AP_PS42A_47 | 178600.00 | 440000.00 | 608.00 | 428.00 | BDL | BDL | 99.00 | 298.00 | 52.20 | 336.00 | 129.00 | 31.30 | 150.00 | 19.00 | 87.00 | 15.10 | 33.70 | 3.80 | 21.70 | 2.93 |
| AP_PS42A_48 | 174500.00 | 433600.00 | 575.30 | 473.20 | 0.72 | BDL | 89.10 | 296.00 | 53.40 | 383.00 | 159.60 | 32.70 | 180.10 | 21.86 | 100.40 | 16.94 | 36.10 | 3.83 | 21.40 | 2.95 |
| AP_PS42A_49 | 175500.00 | 432000.00 | 611.00 | 494.00 | 0.21 | 0.04 | 84.70 | 291.00 | 54.70 | 392.00 | 169.80 | 33.00 | 192.80 | 24.01 | 106.40 | 17.93 | 38.90 | 4.12 | 23.50 | 3.04 |
| AP_PS42A_50 | 175700.00 | 432400.00 | 582.00 | 374.60 | 0.07 | BDL | 121.40 | 384.30 | 68.80 | 445.00 | 157.20 | 34.80 | 157.70 | 17.60 | 75.50 | 12.21 | 26.94 | 3.01 | 17.20 | 2.34 |
| AP_PS42A_51 | 177100.00 | 435000.00 | 612.30 | 443.00 | BDL | BDL | 113.10 | 337.00 | 57.60 | 346.00 | 137.80 | 35.20 | 151.20 | 18.52 | 90.40 | 14.92 | 33.50 | 3.92 | 21.00 | 2.78 |
| AP_PS42A_52 | 178400.00 | 437300.00 | 611.20 | 528.00 | 0.10 | BDL | 133.80 | 406.00 | 68.70 | 421.00 | 164.60 | 39.90 | 186.00 | 23.10 | 106.80 | 17.80 | 40.10 | 4.46 | 25.20 | 3.42 |
| AP_PS42A_53 | 180000.00 | 443400.00 | 585.00 | 829.00 | 0.69 | BDL | 128.20 | 408.00 | 72.20 | 465.00 | 197.40 | 48.20 | 241.70 | 32.08 | 160.60 | 27.84 | 64.20 | 7.76 | 44.40 | 5.74 |
| AP_PS42A_54 | 176100.00 | 437000.00 | 592.00 | 772.00 | 0.42 | 0.03 | 133.30 | 416.00 | 73.70 | 474.00 | 197.10 | 45.80 | 233.30 | 31.90 | 156.00 | 26.30 | 61.10 | 7.26 | 42.40 | 5.68 |
| AP_PS42A_55 | 177800.00 | 437500.00 | 596.60 | 525.00 | 0.41 | BDL | 221.00 | 668.00 | 112.90 | 637.00 | 204.60 | 44.40 | 190.70 | 21.13 | 98.10 | 16.98 | 39.90 | 5.03 | 28.70 | 3.88 |
| AP_PS42A_56 | 176700.00 | 438200.00 | 611.00 | 621.00 | 0.97 | BDL | 210.00 | 650.00 | 110.00 | 690.00 | 252.00 | 62.00 | 249.00 | 28.80 | 127.00 | 20.70 | 46.10 | 5.21 | 28.20 | 4.18 |
| AP_PS42A_57 | 176100.00 | 437800.00 | 601.20 | 590.00 | 1.10 | BDL | 192.00 | 600.00 | 101.00 | 620.00 | 224.00 | 64.00 | 232.00 | 26.70 | 119.00 | 18.80 | 42.20 | 4.94 | 27.60 | 3.83 |
| AP_PS42A_58 | 176100.00 | 437100.00 | 628.70 | 535.00 | 0.31 | BDL | 158.00 | 489.00 | 84.40 | 531.00 | 197.00 | 37.50 | 205.00 | 24.30 | 113.70 | 18.30 | 40.40 | 4.86 | 26.00 | 3.62 |
| AP_PS42A_59 | 178800.00 | 437000.00 | 603.00 | 515.00 | 0.39 | BDL | 107.00 | 345.00 | 59.40 | 368.00 | 143.00 | 44.90 | 164.00 | 20.40 | 98.00 | 16.70 | 37.50 | 4.59 | 25.40 | 3.58 |
| AP_PS42A_60 | 177500.00 | 432000.00 | 612.00 | 405.00 | BDL | BDL | 132.00 | 402.00 | 71.00 | 421.00 | 155.00 | 35.60 | 159.00 | 18.60 | 85.30 | 13.70 | 30.70 | 3.31 | 20.00 | 2.71 |
| AP_PS42A_61 | 180700.00 | 439000.00 | 533.70 | 1134.00 | 0.15 | BDL | 92.20 | 310.00 | 60.00 | 419.00 | 225.20 | 52.30 | 319.00 | 43.80 | 223.00 | 39.60 | 90.10 | 10.56 | 59.00 | 7.89 |
| AP_PS42A_62 | 180400.00 | 436400.00 | 539.80 | 1109.00 | 0.06 | BDL | 104.90 | 351.00 | 66.80 | 470.00 | 240.90 | 49.70 | 324.10 | 43.70 | 220.10 | 37.80 | 87.80 | 10.22 | 57.10 | 7.56 |
| AP_PS42A_63 | 176700.00 | 441200.00 | 562.30 | 1861.00 | 2.02 | 0.08 | 345.00 | 1140.00 | 210.10 | 1366.00 | 534.00 | 100.00 | 568.00 | 71.90 | 346.00 | 59.20 | 141.00 | 17.08 | 102.70 | 14.79 |
| AP_PS42A_64 | 177700.00 | 434200.00 | 556.20 | 1170.00 | 0.89 | 0.06 | 194.00 | 670.00 | 124.00 | 830.00 | 338.00 | 65.80 | 377.00 | 46.80 | 224.00 | 38.50 | 90.00 | 10.50 | 62.30 | 9.10 |
| AP_PS42A_65 | 176200.00 | 433100.00 | 303.70 | 758.00 | 0.11 | BDL | 137.90 | 420.00 | 71.50 | 453.00 | 174.10 | 33.10 | 205.40 | 28.10 | 147.00 | 26.06 | 62.50 | 7.45 | 41.70 | 5.20 |
| AP_PS42A_66 | 176700.00 | 435700.00 | 556.00 | 374.00 | BDL | BDL | 69.00 | 211.00 | 36.30 | 232.00 | 96.00 | 25.70 | 117.00 | 14.00 | 68.50 | 12.10 | 26.80 | 3.00 | 18.80 | 2.45 |
| AP_PS42A_67 | 179000.00 | 438500.00 | 528.90 | 975.00 | 0.10 | BDL | 84.00 | 263.00 | 45.90 | 309.00 | 157.00 | 38.10 | 235.00 | 34.10 | 181.00 | 33.10 | 81.00 | 9.58 | 53.10 | 7.09 |
| AP_PS42A_68 | 174500.00 | 426900.00 | 542.30 | 228.00 | 0.13 | BDL | 59.30 | 176.00 | 30.30 | 206.00 | 72.60 | 20.80 | 76.10 | 8.57 | 40.90 | 7.05 | 16.30 | 1.75 | 10.43 | 1.43 |
| AP_PS42A_69 | 178200.00 | 430700.00 | 575.00 | 489.00 | BDL | 0.02 | 151.60 | 471.00 | 82.90 | 503.00 | 170.80 | 42.50 | 168.60 | 19.70 | 90.00 | 14.92 | 35.10 | 4.21 | 25.50 | 3.63 |
| AP_PS42A_70 | 175600.00 | 435000.00 | 582.10 | 463.00 | BDL | BDL | 95.30 | 301.00 | 52.40 | 326.00 | 127.00 | 34.60 | 148.00 | 18.00 | 84.80 | 14.70 | 33.70 | 4.14 | 24.10 | 3.42 |
| AP_PS42A_71 | 177500.00 | 435900.00 | 560.70 | 770.00 | 0.27 | 0.02 | 241.00 | 756.00 | 128.00 | 759.00 | 264.00 | 69.00 | 276.00 | 31.60 | 144.80 | 24.60 | 55.10 | 6.67 | 39.10 | 5.50 |
| AP_PS42A_72 | 179300.00 | 436800.00 | 277.50 | 695.00 | BDL | BDL | 35.10 | 113.40 | 23.60 | 175.00 | 94.70 | 22.11 | 141.00 | 21.68 | 117.50 | 22.19 | 53.20 | 6.63 | 35.40 | 4.55 |
| AP_PS42A_73 | 175200.00 | 427000.00 | 550.00 | 194.00 | 4.50 | 0.04 | 64.10 | 211.00 | 39.30 | 238.00 | 76.90 | 21.90 | 72.50 | 7.67 | 32.80 | 5.89 | 13.80 | 1.66 | 9.07 | 1.41 |
| AP_PS42A_74 | 176400.00 | 429000.00 | 540.00 | 566.00 | 0.03 | 0.02 | 94.00 | 293.00 | 53.90 | 355.00 | 152.00 | 32.60 | 184.00 | 23.40 | 112.00 | 19.20 | 43.60 | 5.10 | 29.40 | 4.03 |
| AP_PS42A_75 | 176100.00 | 435400.00 | 570.00 | 519.00 | 0.16 | BDL | 88.10 | 268.00 | 44.70 | 288.00 | 117.30 | 31.30 | 145.50 | 19.69 | 99.00 | 17.60 | 41.90 | 4.98 | 26.60 | 3.53 |
| AP_PS42A_76 | 176500.00 | 433800.00 | 620.00 | 671.00 | 0.20 | 0.02 | 142.10 | 454.00 | 80.20 | 517.00 | 207.10 | 38.30 | 233.60 | 29.73 | 142.70 | 23.65 | 52.70 | 6.22 | 34.80 | 4.51 |

Sample TG04 - Apatite REE elements (ppm) - Quad ICP-MS

| Spot | P | Ca | Sr | Y | Zr | Nb | La | Ce | Pr | Nd | Sm | Eu | Gd | Tb | Dy | Ho | Er | Tm | Yb | Lu |
|---|---|---|---|---|---|---|---|---|---|---|---|---|---|---|---|---|---|---|---|---|
| AP_TG04 | 179000.00 | 435600.00 | 209.10 | 2167.00 | 3.60 | BDL | 220.70 | 667.00 | 101.90 | 521.00 | 191.50 | 24.59 | 234.50 | 47.20 | 329.50 | 71.60 | 203.40 | 28.90 | 175.30 | 22.32 |
| AP_TG04_1 | 177000.00 | 429000.00 | 209.40 | 2168.00 | BDL | BDL | 221.40 | 663.00 | 102.00 | 528.00 | 189.90 | 26.81 | 236.70 | 47.90 | 331.20 | 73.40 | 204.60 | 28.73 | 177.70 | 22.89 |
| AP_TG04_2 | 179600.00 | 442100.00 | 182.20 | 629.00 | BDL | BDL | 26.00 | 69.50 | 10.64 | 62.50 | 31.40 | 12.35 | 54.10 | 11.38 | 85.10 | 20.00 | 54.70 | 6.48 | 32.40 | 3.54 |
| AP_TG04_3 | 180600.00 | 435000.00 | 213.60 | 1602.00 | 0.08 | BDL | 138.50 | 468.00 | 79.40 | 440.00 | 179.40 | 24.10 | 209.40 | 39.30 | 272.00 | 56.10 | 142.60 | 16.80 | 88.70 | 10.11 |
| AP_TG04_4 | 181500.00 | 442000.00 | 181.60 | 2039.00 | 0.27 | 0.06 | 185.00 | 642.00 | 107.20 | 588.00 | 245.00 | 31.10 | 297.00 | 56.00 | 355.00 | 69.60 | 179.10 | 22.90 | 126.40 | 14.20 |
| AP_TG04_5 | 180700.00 | 439000.00 | 186.30 | 2400.00 | 0.21 | 0.03 | 233.00 | 783.00 | 128.10 | 683.00 | 273.60 | 35.40 | 335.00 | 64.40 | 406.00 | 81.60 | 212.60 | 27.83 | 155.40 | 17.72 |
| AP_TG04_6 | 178300.00 | 446700.00 | 189.50 | 1355.00 | 1.60 | 0.04 | 138.00 | 650.00 | 138.80 | 910.00 | 360.00 | 34.80 | 374.00 | 50.80 | 265.00 | 48.20 | 116.50 | 14.50 | 81.60 | 9.71 |
| AP_TG04_7 | 177200.00 | 437000.00 | 196.20 | 519.80 | 5.40 | BDL | 23.20 | 60.00 | 9.14 | 55.50 | 24.30 | 11.44 | 42.30 | 8.22 | 64.70 | 16.36 | 44.50 | 5.41 | 25.30 | 2.74 |
| AP_TG04_8 | 179500.00 | 433000.00 | 192.50 | 508.00 | 0.00 | 0.01 | 22.40 | 61.30 | 9.33 | 55.70 | 25.00 | 11.14 | 39.70 | 8.29 | 64.40 | 15.94 | 43.80 | 5.07 | 25.40 | 2.74 |
| AP_TG04_9 | 181200.00 | 440300.00 | 184.20 | 522.40 | BDL | 0.04 | 16.00 | 48.10 | 8.32 | 52.80 | 23.90 | 11.00 | 41.70 | 8.78 | 67.90 | 16.38 | 45.30 | 5.15 | 25.20 | 2.73 |
| AP_TG04_10 | 179100.00 | 429700.00 | 173.10 | 548.00 | BDL | 0.07 | 16.80 | 48.90 | 8.46 | 51.90 | 24.80 | 10.55 | 44.30 | 9.03 | 71.40 | 16.60 | 46.30 | 5.58 | 26.90 | 2.81 |
| AP_TG04_11 | 178700.00 | 441000.00 | 199.10 | 1052.00 | 2.60 | BDL | 132.40 | 379.40 | 57.80 | 290.00 | 110.50 | 24.70 | 138.80 | 27.80 | 179.10 | 36.00 | 89.30 | 10.78 | 58.80 | 7.25 |
| AP_TG04_12 | 182300.00 | 438000.00 | 209.00 | 1266.00 | 0.06 | BDL | 154.40 | 442.00 | 66.50 | 329.00 | 126.70 | 25.70 | 159.20 | 31.50 | 209.90 | 43.50 | 114.10 | 14.74 | 80.40 | 9.77 |
| AP_TG04_13 | 1230.00 | 423000.00 | 7000.00 | 1.24 | BDL | BDL | 20.60 | 35.60 | 3.00 | BDL | BDL | 7.50 | BDL | BDL | BDL | 0.07 | BDL | 0.23 | BDL | BDL |
| AP_TG04_14 | 180300.00 | 433000.00 | 178.70 | 1020.00 | 0.25 | 0.04 | 182.00 | 869.00 | 172.30 | 1007.00 | 363.60 | 35.30 | 347.80 | 46.30 | 226.60 | 37.36 | 82.00 | 9.38 | 49.50 | 5.93 |
| AP_TG04_15 | 179300.00 | 428000.00 | 172.10 | 832.00 | 0.15 | 0.04 | 144.40 | 687.00 | 135.30 | 810.00 | 294.70 | 28.70 | 285.10 | 37.70 | 181.70 | 31.40 | 67.00 | 7.53 | 39.40 | 4.67 |
| AP_TG04_16 | 178500.00 | 436000.00 | 169.00 | 670.00 | 0.04 | BDL | 26.30 | 84.90 | 14.00 | 86.40 | 38.30 | 7.18 | 64.80 | 13.12 | 93.40 | 21.18 | 53.80 | 5.39 | 22.00 | 2.03 |
| AP_TG04_19 | 180900.00 | 437000.00 | 170.80 | 2089.00 | 0.35 | 0.03 | 301.80 | 977.00 | 165.70 | 915.00 | 406.00 | 30.30 | 475.00 | 80.10 | 447.00 | 75.50 | 171.00 | 20.60 | 113.30 | 12.42 |
| AP_TG04_20 | 185700.00 | 433000.00 | 173.10 | 2480.00 | 0.59 | BDL | 342.00 | 1124.00 | 191.00 | 1055.00 | 465.00 | 35.30 | 552.00 | 93.40 | 526.00 | 90.30 | 206.00 | 25.30 | 137.70 | 15.40 |
| AP_TG04_21 | 176200.00 | 430200.00 | 171.40 | 1065.00 | 0.32 | 0.12 | 26.20 | 86.00 | 15.67 | 105.50 | 53.20 | 11.27 | 93.40 | 19.28 | 148.00 | 35.10 | 92.40 | 10.26 | 46.20 | 4.56 |
| AP_TG04_22 | 182700.00 | 436000.00 | 212.20 | 1068.00 | 0.20 | 0.05 | 209.70 | 737.00 | 131.70 | 772.00 | 279.70 | 36.50 | 283.40 | 42.00 | 220.10 | 39.50 | 98.10 | 13.64 | 88.30 | 11.18 |
| AP_TG04_25 | 183300.00 | 438000.00 | 217.20 | 1448.00 | 0.03 | BDL | 226.00 | 669.00 | 102.30 | 504.00 | 173.70 | 25.50 | 193.70 | 38.42 | 255.10 | 50.10 | 132.80 | 17.64 | 106.10 | 12.51 |
| AP_TG04_26 | 181400.00 | 441000.00 | 139.60 | 1268.00 | 0.20 | 0.01 | 886.00 | 2468.00 | 364.20 | 1877.00 | 567.00 | 21.60 | 521.00 | 65.60 | 302.00 | 47.40 | 102.00 | 10.84 | 56.60 | 6.22 |
| AP_TG04_27 | 185900.00 | 436000.00 | 137.90 | 1371.00 | 0.11 | BDL | 1011.00 | 2789.00 | 406.30 | 2040.00 | 619.00 | 23.01 | 568.00 | 70.90 | 324.30 | 52.50 | 108.50 | 11.45 | 60.30 | 6.60 |
| AP_TG04_28 | 182900.00 | 430600.00 | 221.80 | 1743.00 | 0.05 | BDL | 164.60 | 529.00 | 83.60 | 443.00 | 179.30 | 24.65 | 226.30 | 45.28 | 297.60 | 59.30 | 156.00 | 20.59 | 120.50 | 14.24 |
| AP_TG04_29 | 187500.00 | 454000.00 | 175.10 | 778.00 | 1.90 | 0.04 | 370.00 | 1342.00 | 227.90 | 1236.00 | 389.00 | 36.90 | 347.00 | 40.80 | 185.30 | 29.00 | 62.50 | 7.14 | 39.30 | 4.88 |
| AP_TG04_30 | 183700.00 | 434300.00 | 186.30 | 1277.00 | 0.09 | BDL | 311.00 | 1017.00 | 167.40 | 918.00 | 335.50 | 23.08 | 350.00 | 52.50 | 264.80 | 47.00 | 103.20 | 10.91 | 52.60 | 5.63 |
| AP_TG04_31 | 183400.00 | 435300.00 | 182.70 | 1304.00 | 0.10 | BDL | 502.00 | 1521.00 | 234.20 | 1205.00 | 397.00 | 24.24 | 393.90 | 56.10 | 283.80 | 47.50 | 104.40 | 11.14 | 53.50 | 6.04 |
| AP_TG04_32 | 182700.00 | 440000.00 | 184.00 | 709.00 | BDL | BDL | 43.00 | 127.60 | 22.10 | 139.60 | 62.00 | 9.29 | 90.40 | 17.12 | 114.90 | 24.13 | 60.00 | 6.38 | 32.70 | 3.74 |
| AP_TG04_33 | 182000.00 | 440700.00 | 181.10 | 685.00 | 0.01 | BDL | 42.80 | 124.20 | 21.54 | 139.00 | 60.80 | 8.88 | 86.20 | 17.40 | 112.80 | 24.12 | 57.70 | 6.40 | 32.10 | 3.65 |
| AP_TG04_34 | 185900.00 | 430000.00 | 207.30 | 1740.00 | 0.09 | BDL | 119.00 | 502.00 | 98.90 | 600.00 | 272.00 | 28.20 | 320.00 | 56.10 | 329.00 | 59.20 | 145.00 | 18.90 | 111.20 | 12.90 |
| AP_TG04_37 | 182200.00 | 439300.00 | 209.30 | 998.00 | 1.70 | 0.15 | 108.70 | 229.00 | 41.40 | 296.00 | 129.00 | 19.20 | 158.00 | 24.60 | 155.00 | 33.60 | 88.10 | 10.85 | 55.90 | 6.22 |
| AP_TG04_38 | 181100.00 | 443000.00 | 181.50 | 674.00 | BDL | BDL | 28.50 | 83.00 | 13.94 | 81.20 | 39.20 | 11.58 | 66.30 | 12.89 | 97.00 | 21.95 | 59.70 | 7.01 | 35.00 | 3.92 |
| AP_TG04_39 | 164700.00 | 438000.00 | 192.80 | 713.00 | 310.00 | 0.33 | 58.80 | 178.00 | 27.90 | 157.00 | 65.00 | 15.10 | 88.10 | 16.90 | 110.00 | 23.70 | 61.30 | 7.03 | 37.30 | 4.44 |
| AP_TG04_40 | 184000.00 | 437700.00 | 187.80 | 1200.00 | 0.05 | 0.05 | 6.60 | 31.20 | 7.98 | 62.10 | 43.90 | 7.49 | 89.00 | 22.10 | 177.00 | 41.00 | 120.00 | 17.40 | 115.00 | 14.90 |
| AP_TG04_42 | 186000.00 | 442000.00 | 206.30 | 2590.00 | 0.60 | 0.13 | 237.00 | 740.00 | 119.20 | 610.00 | 246.00 | 47.00 | 313.00 | 62.60 | 436.00 | 92.20 | 256.00 | 33.90 | 192.00 | 23.60 |
| AP_TG04_43 | 180600.00 | 434300.00 | 179.60 | 870.00 | BDL | BDL | 16.90 | 58.30 | 10.82 | 73.40 | 36.90 | 10.63 | 68.70 | 14.85 | 116.40 | 28.10 | 74.20 | 8.57 | 39.70 | 4.38 |
| AP_TG04_44 | 182800.00 | 439600.00 | 174.30 | 932.00 | BDL | 0.03 | 12.48 | 42.30 | 8.16 | 57.40 | 32.10 | 10.66 | 66.60 | 14.63 | 119.30 | 29.88 | 80.60 | 8.90 | 43.40 | 4.56 |
| AP_TG04_45 | 184300.00 | 434800.00 | 174.30 | 1024.00 | BDL | 0.06 | 59.40 | 108.10 | 15.11 | 86.70 | 52.50 | 17.60 | 94.80 | 20.27 | 146.30 | 34.03 | 92.60 | 10.87 | 54.90 | 5.67 |
| AP_TG04_46 | 185200.00 | 437000.00 | 192.30 | 553.00 | 0.15 | 0.03 | 33.60 | 77.80 | 11.40 | 64.50 | 28.60 | 12.06 | 50.50 | 9.86 | 76.40 | 17.88 | 46.50 | 4.78 | 20.40 | 2.08 |
| AP_TG04_47 | 3289.00 | 7800.00 | 3.03 | 9.01 | BDL | BDL | 0.56 | 1.51 | 0.22 | 1.22 | 0.49 | 0.15 | 0.77 | 0.15 | 1.17 | 0.28 | 0.80 | 0.10 | 0.52 | 0.06 |
| AP_TG04_48 | 188500.00 | 434600.00 | 200.60 | 876.00 | 0.03 | BDL | 168.20 | 411.20 | 56.70 | 275.40 | 94.40 | 23.57 | 105.10 | 22.28 | 147.90 | 30.10 | 75.20 | 9.83 | 53.70 | 6.46 |
| AP_TG04_49 | 184600.00 | 439000.00 | 204.60 | 947.00 | 0.00 | BDL | 195.40 | 458.00 | 62.90 | 296.00 | 101.30 | 26.20 | 114.30 | 23.70 | 160.40 | 32.60 | 84.70 | 10.86 | 63.20 | 7.77 |
| AP_TG04_50 | 190300.00 | 429000.00 | 182.60 | 2259.00 | 0.08 | BDL | 122.30 | 488.00 | 85.20 | 473.00 | 200.30 | 22.15 | 256.80 | 52.10 | 371.60 | 80.00 | 222.40 | 29.19 | 169.70 | 21.01 |
| AP_TG04_51 | 188500.00 | 432000.00 | 196.30 | 2610.00 | 0.65 | BDL | 129.40 | 559.00 | 102.10 | 573.00 | 256.10 | 31.69 | 326.00 | 67.50 | 463.00 | 98.20 | 260.00 | 33.70 | 192.00 | 23.40 |
| AP_TG04_52 | 183200.00 | 431000.00 | 193.80 | 710.70 | 0.04 | 0.06 | 8.80 | 34.40 | 7.40 | 56.50 | 38.10 | 6.85 | 72.00 | 16.01 | 115.20 | 24.58 | 63.90 | 8.32 | 46.70 | 5.32 |
| AP_TG04_53 | 183900.00 | 430000.00 | 181.30 | 738.00 | 0.08 | 0.17 | 35.00 | 156.40 | 34.80 | 257.00 | 129.80 | 17.01 | 167.50 | 26.00 | 142.40 | 27.40 | 66.90 | 7.68 | 40.00 | 4.40 |
| AP_TG04_54 | 186700.00 | 438000.00 | 196.10 | 563.00 | 285.00 | 0.18 | 19.40 | 61.90 | 10.71 | 65.30 | 32.60 | 17.72 | 52.70 | 11.19 | 80.40 | 18.25 | 49.50 | 5.99 | 33.24 | 3.90 |
| AP_TG04_56 | 189100.00 | 447800.00 | 178.40 | 680.00 | BDL | BDL | 21.30 | 65.40 | 10.33 | 64.40 | 35.10 | 7.51 | 63.00 | 12.97 | 98.00 | 22.48 | 58.90 | 6.68 | 33.10 | 3.51 |
| AP_TG04_57 | 188400.00 | 437400.00 | 203.40 | 1070.00 | BDL | BDL | 91.70 | 300.20 | 48.70 | 265.60 | 106.60 | 21.30 | 142.90 | 28.40 | 190.20 | 38.17 | 90.00 | 9.65 | 47.60 | 5.45 |
| AP_TG04_58 | 185600.00 | 434000.00 | 179.90 | 689.00 | BDL | 0.05 | 26.10 | 84.90 | 13.80 | 89.00 | 40.20 | 8.82 | 61.80 | 12.58 | 96.20 | 21.94 | 59.30 | 6.94 | 33.50 | 3.48 |
| AP_TG04_59 | 188600.00 | 445400.00 | 186.00 | 861.00 | BDL | BDL | 9.30 | 44.10 | 10.11 | 79.70 | 55.50 | 11.03 | 93.60 | 20.93 | 148.40 | 29.77 | 76.70 | 10.04 | 59.00 | 6.51 |
| AP_TG04_60 | 188600.00 | 434000.00 | 205.60 | 904.00 | 285.00 | 0.15 | 101.80 | 317.30 | 50.70 | 261.90 | 102.70 | 22.19 | 132.30 | 25.27 | 168.70 | 32.74 | 74.40 | 8.17 | 38.50 | 4.47 |
| AP_TG04_61 | 1250.00 | 421000.00 | 7120.00 | 6.10 | BDL | 0.81 | 121.00 | 175.00 | 17.20 | 34.00 | 8.60 | 14.10 | 4.10 | BDL | BDL | BDL | 0.78 | BDL | BDL | 0.07 |
| AP_TG04_62 | 3337.00 | 7830.00 | 3.44 | 24.94 | BDL | BDL | 1.87 | 5.94 | 1.04 | 5.97 | 2.74 | 0.47 | 3.72 | 0.70 | 4.39 | 0.92 | 2.40 | 0.31 | 1.68 | 0.20 |
| AP_TG04_63 | 192300.00 | 441000.00 | 226.70 | 1643.00 | BDL | BDL | 272.30 | 776.00 | 113.00 | 554.00 | 195.30 | 27.07 | 217.60 | 42.30 | 282.90 | 57.50 | 152.00 | 20.42 | 127.30 | 15.55 |
| AP_TG04_64 | 185300.00 | 435500.00 | 163.10 | 355.10 | 0.46 | BDL | 18.90 | 49.60 | 7.39 | 35.90 | 15.74 | 7.74 | 26.40 | 5.57 | 44.70 | 11.42 | 31.90 | 3.86 | 18.20 | 1.96 |
| AP_TG04_65 | 191000.00 | 451000.00 | 221.00 | 1741.00 | BDL | BDL | 239.00 | 756.00 | 117.30 | 610.00 | 222.00 | 29.80 | 258.00 | 50.60 | 332.00 | 64.00 | 162.80 | 20.60 | 115.00 | 13.29 |

| Spot | Sample TG08 Apatite - REE elements (ppm) - Quad ICP-MS | | | | | | | | | | | | | | | | | | | |
|---|---|---|---|---|---|---|---|---|---|---|---|---|---|---|---|---|---|---|---|---|
| | P | Ca | Sr | Y | Zr | Nb | La | Ce | Pr | Nd | Sm | Eu | Gd | Tb | Dy | Ho | Er | Tm | Yb | Lu |
| AP_TG08 | 151100.00 | 426000.00 | 279.00 | 1020.00 | 0.15 | 0.04 | 149.00 | 468.00 | 79.50 | 451.00 | 166.00 | 16.85 | 217.50 | 36.24 | 210.80 | 39.21 | 96.00 | 10.49 | 51.80 | 6.05 |
| AP_TG08_1 | 177100.00 | 431800.00 | 276.00 | 1172.00 | 0.04 | BDL | 181.00 | 582.00 | 94.00 | 522.00 | 196.40 | 20.80 | 247.70 | 41.90 | 243.70 | 45.80 | 109.90 | 12.75 | 62.90 | 7.27 |
| AP_TG08_2 | 177600.00 | 434800.00 | 278.40 | 1461.00 | BDL | BDL | 280.00 | 826.00 | 126.30 | 654.00 | 225.00 | 23.90 | 279.00 | 48.20 | 288.00 | 55.10 | 135.80 | 16.60 | 91.40 | 10.96 |
| AP_TG08_3 | 173700.00 | 447000.00 | 286.70 | 1451.00 | 0.23 | 0.01 | 251.00 | 739.00 | 114.00 | 585.00 | 209.00 | 22.70 | 275.00 | 45.20 | 273.00 | 53.10 | 133.00 | 16.60 | 94.00 | 11.36 |
| AP_TG08_4 | 178900.00 | 440900.00 | 281.40 | 1622.00 | 0.11 | BDL | 308.30 | 916.00 | 137.90 | 723.00 | 251.10 | 25.90 | 307.10 | 53.50 | 314.50 | 60.50 | 150.50 | 18.95 | 103.90 | 12.64 |
| AP_TG08_5 | 180400.00 | 437000.00 | 266.40 | 1659.00 | 2.10 | 0.16 | 268.00 | 795.00 | 120.10 | 656.00 | 250.10 | 29.30 | 314.00 | 54.60 | 319.00 | 59.20 | 143.10 | 18.16 | 99.60 | 11.63 |
| AP_TG08_6 | 181500.00 | 436400.00 | 266.90 | 2547.00 | 0.10 | BDL | 414.00 | 1226.00 | 187.20 | 962.00 | 356.50 | 36.10 | 434.00 | 76.90 | 465.00 | 88.50 | 229.60 | 30.30 | 181.00 | 22.08 |
| AP_TG08_7 | 181400.00 | 434900.00 | 278.40 | 1860.00 | BDL | BDL | 324.00 | 949.00 | 142.70 | 748.00 | 261.90 | 29.10 | 325.00 | 57.10 | 341.00 | 66.60 | 169.10 | 21.38 | 121.30 | 15.24 |
| AP_TG08_8 | 181800.00 | 427000.00 | 283.10 | 2309.00 | BDL | BDL | 403.00 | 1159.00 | 172.60 | 899.00 | 319.00 | 35.50 | 388.00 | 69.50 | 418.00 | 81.30 | 207.60 | 26.20 | 156.00 | 18.90 |
| AP_TG08_9 | 180800.00 | 431000.00 | 288.80 | 2610.00 | 0.12 | BDL | 451.00 | 1317.00 | 197.00 | 996.00 | 359.00 | 39.00 | 437.00 | 79.30 | 481.00 | 91.50 | 239.00 | 31.80 | 184.00 | 22.90 |
| AP_TG08_10 | 180500.00 | 431000.00 | 281.40 | 2540.00 | 0.08 | BDL | 425.00 | 1242.00 | 190.00 | 966.00 | 343.00 | 36.20 | 416.00 | 75.00 | 456.00 | 89.50 | 229.00 | 30.60 | 181.00 | 22.50 |
| AP_TG08_11 | 181100.00 | 441000.00 | 279.20 | 2330.00 | 0.05 | BDL | 346.90 | 1099.00 | 171.10 | 932.00 | 359.10 | 36.90 | 449.00 | 77.40 | 464.00 | 88.50 | 221.30 | 27.76 | 156.40 | 18.20 |
| AP_TG08_12 | 176100.00 | 430000.00 | 267.60 | 2360.00 | 0.03 | BDL | 376.00 | 1117.00 | 172.60 | 895.00 | 330.00 | 33.20 | 402.00 | 71.90 | 439.00 | 84.20 | 213.00 | 27.90 | 161.00 | 20.30 |
| AP_TG08_13 | 178800.00 | 441000.00 | 266.50 | 2266.00 | 60.00 | BDL | 345.00 | 1015.00 | 154.40 | 818.00 | 309.00 | 30.80 | 389.00 | 67.20 | 411.00 | 79.60 | 198.30 | 26.30 | 152.20 | 18.60 |
| AP_TG08_14 | 182000.00 | 434000.00 | 279.50 | 2310.00 | 0.09 | BDL | 317.00 | 1049.00 | 170.60 | 905.00 | 354.00 | 38.50 | 452.00 | 78.60 | 470.00 | 90.70 | 221.00 | 28.10 | 156.30 | 18.80 |
| AP_TG08_15 | 181800.00 | 430100.00 | 245.50 | 757.00 | 0.07 | BDL | 1061.00 | 2550.00 | 319.00 | 1342.00 | 257.00 | 43.90 | 194.00 | 25.30 | 128.00 | 23.40 | 63.00 | 9.59 | 64.70 | 8.89 |
| AP_TG08_16 | 179100.00 | 429100.00 | 242.90 | 744.00 | BDL | BDL | 1027.00 | 2510.00 | 315.00 | 1300.00 | 255.00 | 43.30 | 190.00 | 24.50 | 127.00 | 23.40 | 61.50 | 9.20 | 63.50 | 8.67 |
| AP_TG08_17 | 176900.00 | 433000.00 | 240.70 | 650.00 | 0.05 | BDL | 876.00 | 2148.00 | 271.50 | 1161.00 | 217.00 | 36.30 | 168.10 | 21.20 | 112.20 | 19.75 | 52.00 | 7.68 | 52.90 | 7.17 |
| AP_TG08_18 | 182800.00 | 442700.00 | 250.10 | 748.00 | 0.01 | BDL | 904.00 | 2259.00 | 286.00 | 1221.00 | 242.00 | 38.20 | 186.00 | 23.90 | 123.80 | 22.70 | 60.10 | 8.77 | 59.30 | 7.87 |
| AP_TG08_19 | 180500.00 | 437000.00 | 255.50 | 1692.00 | 1.00 | BDL | 521.00 | 1491.00 | 216.30 | 1104.00 | 360.00 | 38.10 | 389.00 | 61.00 | 338.00 | 59.90 | 138.70 | 16.42 | 92.90 | 11.22 |
| AP_TG08_20 | 181000.00 | 431700.00 | 263.60 | 1623.00 | BDL | BDL | 547.00 | 1513.00 | 224.70 | 1113.00 | 362.70 | 37.08 | 385.60 | 60.80 | 330.10 | 58.30 | 135.40 | 15.70 | 85.80 | 10.23 |
| AP_TG08_21 | 181700.00 | 438000.00 | 298.00 | 1347.00 | 0.03 | BDL | 245.00 | 733.00 | 115.30 | 584.00 | 204.00 | 22.10 | 261.00 | 43.80 | 257.00 | 50.50 | 124.20 | 15.12 | 82.20 | 10.03 |
| AP_TG08_22 | 178500.00 | 436300.00 | 561.00 | 207.00 | BDL | BDL | 30.10 | 89.00 | 14.60 | 89.20 | 32.50 | 15.70 | 42.80 | 6.01 | 31.00 | 5.86 | 14.71 | 1.75 | 10.28 | 1.37 |
| AP_TG08_23 | 180300.00 | 432000.00 | 535.00 | 129.70 | 0.00 | BDL | 29.40 | 85.90 | 14.13 | 80.10 | 25.90 | 15.44 | 30.40 | 3.78 | 17.80 | 3.66 | 8.76 | 1.14 | 6.00 | 0.89 |
| AP_TG08_24 | 185300.00 | 442200.00 | 296.10 | 1206.00 | 0.03 | BDL | 103.50 | 330.80 | 53.80 | 311.00 | 122.90 | 12.47 | 165.90 | 30.05 | 188.70 | 41.48 | 114.10 | 14.54 | 85.80 | 10.40 |
| AP_TG08_25 | 182000.00 | 440300.00 | 301.80 | 1208.00 | BDL | BDL | 115.10 | 416.00 | 74.50 | 429.00 | 164.70 | 16.75 | 217.40 | 38.00 | 225.80 | 45.20 | 116.40 | 14.74 | 82.50 | 10.17 |
| AP_TG08_26 | 183400.00 | 437000.00 | 272.20 | 2330.00 | 0.04 | BDL | 364.80 | 1080.00 | 166.10 | 865.00 | 314.80 | 32.01 | 389.00 | 70.60 | 417.70 | 81.00 | 206.00 | 27.20 | 160.50 | 19.74 |
| AP_TG08_27 | 181700.00 | 434400.00 | 256.20 | 2347.00 | BDL | BDL | 319.00 | 953.00 | 149.70 | 798.00 | 315.00 | 34.20 | 402.00 | 72.10 | 428.00 | 81.90 | 206.70 | 26.90 | 153.90 | 18.80 |
| AP_TG08_28 | 180700.00 | 435800.00 | 264.60 | 2493.00 | BDL | BDL | 382.00 | 1117.00 | 170.70 | 872.00 | 343.80 | 35.10 | 429.00 | 76.40 | 461.40 | 87.10 | 221.80 | 28.96 | 174.00 | 21.17 |
| AP_TG08_29 | 182100.00 | 425900.00 | 285.50 | 2443.00 | BDL | BDL | 504.00 | 1430.00 | 214.00 | 1059.00 | 391.00 | 33.60 | 452.00 | 79.30 | 464.00 | 86.20 | 213.60 | 27.81 | 159.50 | 19.04 |
| AP_TG08_30 | 183100.00 | 444300.00 | 290.30 | 2534.00 | 0.04 | BDL | 516.90 | 1490.00 | 219.80 | 1107.00 | 392.20 | 35.10 | 470.00 | 81.50 | 479.00 | 89.10 | 222.80 | 28.55 | 166.80 | 20.29 |
| AP_TG08_31 | 182900.00 | 442000.00 | 282.80 | 2330.00 | 0.70 | BDL | 437.00 | 1273.00 | 189.90 | 954.00 | 332.00 | 34.50 | 406.00 | 71.40 | 426.40 | 81.70 | 210.90 | 27.14 | 163.30 | 20.36 |
| AP_TG08_32 | 185300.00 | 437000.00 | 272.40 | 2306.00 | 0.02 | BDL | 402.00 | 1164.00 | 175.40 | 901.00 | 319.10 | 32.70 | 396.00 | 69.20 | 415.00 | 79.20 | 202.60 | 27.32 | 158.80 | 19.91 |
| AP_TG08_33 | 183200.00 | 440000.00 | 275.60 | 2376.00 | 0.04 | BDL | 398.00 | 1165.00 | 174.80 | 887.00 | 323.00 | 32.10 | 398.00 | 71.20 | 422.00 | 81.00 | 208.40 | 27.87 | 162.10 | 19.91 |
| AP_TG08_34 | 182400.00 | 441000.00 | 278.90 | 2453.00 | 0.04 | BDL | 425.00 | 1218.00 | 184.70 | 925.00 | 337.30 | 33.30 | 411.50 | 73.00 | 433.40 | 84.20 | 218.30 | 28.78 | 170.50 | 21.63 |
| AP_TG08_35 | 183700.00 | 444000.00 | 278.20 | 2120.00 | 0.05 | BDL | 348.00 | 984.00 | 151.00 | 771.00 | 273.00 | 30.50 | 337.00 | 60.20 | 368.00 | 72.60 | 185.00 | 24.00 | 143.00 | 17.80 |
| AP_TG08_36 | 182900.00 | 439000.00 | 282.30 | 2350.00 | 0.02 | BDL | 415.00 | 1192.00 | 179.00 | 901.00 | 315.00 | 34.60 | 387.00 | 68.50 | 418.00 | 81.20 | 208.00 | 27.80 | 164.00 | 20.40 |
| AP_TG08_37 | 183300.00 | 424000.00 | 265.70 | 2021.00 | 0.13 | BDL | 416.30 | 1253.00 | 193.40 | 1012.00 | 354.50 | 31.14 | 413.70 | 68.20 | 392.30 | 71.50 | 174.10 | 22.59 | 133.60 | 16.47 |
| AP_TG08_38 | 183000.00 | 434000.00 | 258.30 | 2003.00 | BDL | BDL | 363.50 | 1137.00 | 179.20 | 961.00 | 348.00 | 28.40 | 406.00 | 67.60 | 387.00 | 71.10 | 174.50 | 22.05 | 127.50 | 16.00 |
| AP_TG08_39 | 182800.00 | 439100.00 | 272.20 | 2333.00 | 1.54 | 0.02 | 394.00 | 1147.00 | 174.20 | 869.00 | 318.20 | 32.19 | 385.50 | 68.40 | 413.00 | 80.60 | 205.70 | 27.43 | 160.30 | 20.20 |
| AP_TG08_40 | 183200.00 | 441000.00 | 276.90 | 2770.00 | 0.07 | BDL | 467.00 | 1374.00 | 205.80 | 1046.00 | 380.00 | 39.00 | 458.00 | 83.10 | 503.00 | 96.90 | 254.00 | 33.50 | 199.00 | 25.20 |
| AP_TG08_41 | 181600.00 | 436400.00 | 269.20 | 2573.00 | 27.10 | 0.03 | 443.00 | 1187.00 | 197.60 | 1009.00 | 370.00 | 37.60 | 446.00 | 79.60 | 474.00 | 90.50 | 232.20 | 30.34 | 176.60 | 22.16 |
| AP_TG08_42 | 184500.00 | 437000.00 | 269.20 | 2453.00 | 0.02 | BDL | 367.00 | 1114.00 | 172.80 | 906.00 | 343.70 | 34.20 | 419.50 | 75.50 | 450.90 | 86.40 | 218.10 | 28.44 | 168.50 | 20.75 |
| AP_TG08_43 | 182700.00 | 432400.00 | 277.60 | 2306.00 | 0.00 | BDL | 416.00 | 1194.00 | 176.80 | 923.00 | 312.00 | 34.20 | 373.00 | 67.40 | 409.00 | 80.10 | 207.50 | 28.00 | 164.30 | 20.63 |
| AP_TG08_44 | 182600.00 | 437000.00 | 263.00 | 2353.00 | 0.01 | BDL | 376.00 | 1098.00 | 166.10 | 857.00 | 313.00 | 33.60 | 393.00 | 70.20 | 425.00 | 82.00 | 212.30 | 27.80 | 164.10 | 21.14 |
| AP_TG08_45 | 187300.00 | 442700.00 | 261.00 | 2192.00 | 0.04 | BDL | 342.00 | 1010.00 | 153.40 | 801.00 | 292.00 | 31.70 | 368.00 | 65.40 | 391.00 | 76.00 | 194.40 | 25.23 | 149.20 | 18.40 |
| AP_TG08_46 | 184900.00 | 441200.00 | 275.00 | 2113.00 | 0.02 | BDL | 371.00 | 1090.00 | 163.50 | 864.00 | 310.00 | 28.90 | 380.00 | 66.90 | 391.00 | 74.20 | 185.60 | 23.50 | 141.60 | 17.20 |
| AP_TG08_47 | 188100.00 | 446000.00 | 262.20 | 1966.00 | 0.03 | BDL | 304.00 | 923.00 | 143.00 | 752.00 | 286.80 | 32.30 | 368.00 | 64.30 | 378.00 | 71.70 | 175.40 | 22.13 | 126.50 | 15.09 |
| AP_TG08_48 | 178000.00 | 432600.00 | 267.30 | 1666.00 | 0.05 | BDL | 417.00 | 1270.00 | 198.80 | 1037.00 | 341.60 | 36.40 | 367.40 | 57.80 | 320.40 | 57.90 | 139.70 | 17.79 | 102.00 | 12.98 |
| AP_TG08_49 | 180700.00 | 436800.00 | 264.50 | 1581.00 | 0.28 | BDL | 343.00 | 1099.00 | 174.70 | 939.00 | 317.70 | 33.80 | 340.20 | 54.60 | 302.70 | 55.40 | 134.50 | 17.35 | 101.10 | 12.61 |
| AP_TG08_50 | 181500.00 | 434400.00 | 256.00 | 2107.00 | 0.00 | BDL | 297.00 | 898.00 | 143.80 | 767.00 | 292.40 | 31.60 | 371.00 | 65.80 | 391.00 | 74.60 | 184.60 | 23.00 | 131.80 | 15.50 |
| AP_TG08_51 | 182300.00 | 442100.00 | 259.40 | 1825.00 | 0.07 | BDL | 253.00 | 763.00 | 119.30 | 656.00 | 250.80 | 27.40 | 331.00 | 57.30 | 331.90 | 63.00 | 152.60 | 19.10 | 104.50 | 12.60 |
| AP_TG08_52 | 181800.00 | 437000.00 | 273.20 | 2530.00 | 0.08 | BDL | 407.00 | 1199.00 | 181.80 | 947.00 | 340.00 | 33.90 | 421.00 | 73.90 | 447.00 | 86.20 | 224.00 | 29.60 | 177.00 | 22.30 |
| AP_TG08_53 | 187800.00 | 437000.00 | 267.10 | 2021.00 | BDL | BDL | 316.60 | 917.00 | 139.20 | 737.00 | 264.50 | 29.32 | 328.60 | 59.30 | 356.20 | 69.10 | 175.10 | 22.78 | 131.40 | 15.55 |
| AP_TG08_54 | 182400.00 | 436000.00 | 257.70 | 2120.00 | BDL | 0.00 | 307.40 | 906.00 | 140.40 | 745.00 | 277.00 | 30.50 | 339.00 | 61.80 | 377.00 | 73.60 | 185.00 | 24.20 | 136.90 | 16.46 |
| AP_TG08_55 | 180800.00 | 438000.00 | 259.80 | 1606.00 | BDL | BDL | 637.00 | 1710.00 | 253.00 | 1258.00 | 388.00 | 42.70 | 401.00 | 60.10 | 330.00 | 57.80 | 131.00 | 15.33 | 81.50 | 9.74 |
| AP_TG08_56 | 177900.00 | 434000.00 | 250.10 | 1446.00 | 140.00 | BDL | 591.00 | 1577.00 | 230.10 | 1166.00 | 348.20 | 36.40 | 357.70 | 54.49 | 298.00 | 52.70 | 117.70 | 13.94 | 72.00 | 8.37 |
| AP_TG08_57 | 176200.00 | 432800.00 | 273.90 | 2930.00 | 23.00 | 0.03 | 471.00 | 1403.00 | 212.90 | 1122.00 | 410.00 | 41.00 | 502.00 | 89.90 | 536.00 | 105.00 | 269.00 | 36.10 | 217.00 | 27.30 |
| AP_TG08_58 | 179000.00 | 434600.00 | 269.30 | 2880.00 | 1020.00 | BDL | 451.00 | 1333.00 | 209.70 | 1079.00 | 407.00 | 40.60 | 490.00 | 89.10 | 529.00 | 102.70 | 262.00 | 34.60 | 203.60 | 25.30 |
| AP_TG08_59 | 176500.00 | 436000.00 | 290.70 | 2020.00 | 0.10 | 0.05 | 259.60 | 893.00 | 149.40 | 814.00 | 294.80 | 31.20 | 369.00 | 65.70 | 400.00 | 77.00 | 199.20 | 24.22 | 138.10 | 16.34 |
| AP_TG08_60 | 149600.00 | 430000.00 | 268.10 | 2357.00 | 31.60 | BDL | 423.00 | 1075.00 | 184.60 | 936.00 | 338.40 | 35.20 | 411.00 | 71.90 | 424.60 | 80.80 | 207.40 | 27.52 | 159.20 | 20.39 |
| AP_TG08_61 | 178400.00 | 425900.00 | 272.40 | 1460.00 | 0.02 | BDL | 232.00 | 708.00 | 112.00 | 618.00 | 223.00 | 24.70 | 289.00 | 49.70 | 292.00 | 55.20 | 137.00 | 17.00 | 89.90 | 10.60 |
| AP_TG08_62 | 182900.00 | 441100.00 | 269.60 | 2072.00 | 420.00 | 0.03 | 311.00 | 917.00 | 143.20 | 756.00 | 286.00 | 29.30 | 364.00 | 62.70 | 370.00 | 70.00 | 179.00 | 22.80 | 134.70 | 16.44 |
| AP_TG08_63 | 180400.00 | 438000.00 | 276.40 | 2389.00 | 0.03 | BDL | 398.00 | 1173.00 | 180.60 | 942.00 | 338.00 | 33.50 | 417.00 | 72.90 | 435.00 | 82.30 | 209.40 | 27.45 | 157.00 | 20.31 |
| AP_TG08_64 | 179600.00 | 443700.00 | 284.70 | 3437.00 | 0.18 | BDL | 561.00 | 1652.00 | 248.10 | 1257.00 | 461.00 | 48.20 | 557.00 | 101.80 | 612.00 | 119.70 | 310.90 | 42.00 | 254.70 | 31.94 |
| AP_TG08_65 | 181300.00 | 439000.00 | 276.20 | 2177.00 | 0.01 | BDL | 373.00 | 1079.00 | 163.90 | 829.00 | 296.60 | 31.10 | 364.40 | 64.80 | 388.80 | 76.60 | 194.00 | 25.70 | 150.90 | 18.24 |
| AP_TG08_66 | 182600.00 | 443000.00 | 274.60 | 1853.00 | 0.02 | 0.00 | 317.60 | 935.00 | 145.50 | 754.00 | 275.20 | 30.00 | 337.00 | 58.90 | 352.40 | 66.40 | 168.60 | 21.23 | 119.60 | 14.06 |
| AP_TG08_67 | 177600.00 | 434400.00 | 272.70 | 1959.00 | BDL | BDL | 331.80 | 1000.00 | 155.00 | 808.00 | 292.00 | 30.90 | 362.00 | 63.60 | 374.00 | 72.60 | 178.40 | 22.89 | 129.60 | 15.98 |
| AP_TG08_68 | 175700.00 | 434500.00 | 304.70 | 889.00 | BDL | 0.01 | 75.30 | 283.00 | 50.80 | 309.00 | 124.60 | 13.49 | 174.20 | 30.00 | 176.80 | 35.30 | 83.50 | 9.87 | 49.40 | 5.65 |
| AP_TG08_69 | 178200.00 | 429800.00 | 261.80 | 3138.00 | 290.00 | BDL | 471.00 | 1399.00 | 215.50 | 1097.00 | 402.00 | 42.50 | 487.00 | 88.80 | 557.00 | 109.10 | 287.60 | 38.50 | 233.90 | 29.00 |
| AP_TG08_70 | 177400.00 | 441000.00 | 303.70 | 1470.00 | BDL | BDL | 609.00 | 1666.00 | 245.50 | 1212.00 | 371.40 | 33.80 | 380.00 | 56.40 | 306.00 | 52.90 | 123.30 | 13.79 | 71.80 | 7.97 |
| AP_TG08_71 | 167400.00 | 438300.00 | 275.50 | 1712.00 | 2.94 | BDL | 278.70 | 827.00 | 128.00 | 676.00 | 243.80 | 27.00 | 306.30 | 54.70 | 320.00 | 61.50 | 151.90 | 19.25 | 106.50 | 13.40 |
| AP_TG08_72 | 176200.00 | 436900.00 | 284.40 | 1930.00 | BDL | BDL | 345.00 | 1011.00 | 154.60 | 790.00 | 282.00 | 30.40 | 345.00 | 61.00 | 367.00 | 70.60 | 176.00 | 22.00 | 129.90 | 15.80 |
| AP_TG08_74 | 176700.00 | 439300.00 | 290.00 | 1755.00 | 1.23 | 0.06 | 271.50 | 806.00 | 129.10 | 674.00 | 248.80 | 27.00 | 319.10 | 55.40 | 327.30 | 62.30 | 156.10 | 20.14 | 108.40 | 13.10 |
| AP_TG08_75 | 177900.00 | 436000.00 | 265.00 | 3280.00 | 0.07 | BDL | 473.00 | 1420.00 | 218.00 | 1130.00 | 414.00 | 45.70 | 514.00 | 95.00 | 591.00 | 115.00 | 301.00 | 39.90 | 246.00 | 30.10 |
| AP_TG08_76 | 176500.00 | 437000.00 | 263.10 | 2950.00 | 0.15 | BDL | 463.00 | 1345.00 | 206.00 | 1042.00 | 379.00 | 39.80 | 466.00 | 85.20 | 520.00 | 101.10 | 267.00 | 35.90 | 215.00 | 26.60 |
| AP_TG08_77 | 177300.00 | 442000.00 | 259.90 | 2149.00 | BDL | BDL | 259.70 | 875.00 | 145.90 | 812.00 | 324.60 | 34.70 | 410.00 | 72.20 | 426.00 | 80.60 | 198.00 | 25.17 | 140.90 | 16.76 |
| AP_TG08_78 | 177100.00 | 440100.00 | 272.20 | 2120.00 | BDL | BDL | 338.00 | 983.00 | 149.90 | 770.00 | 279.90 | 30.70 | 350.00 | 61.00 | 372.00 | 72.40 | 184.40 | 23.99 | 138.20 | 17.59 |
| AP_TG08_79 | 176400.00 | 434700.00 | 276.70 | 2910.00 | 0.06 | BDL | 464.00 | 1363.00 | 206.00 | 1066.00 | 390.00 | 40.70 | 478.00 | 85.90 | 524.00 | 101.80 | 263.00 | 35.40 | 214.00 | 26.60 |
| AP_TG08_80 | 177900.00 | 438000.00 | 273.90 | 2315.00 | 0.03 | BDL | 388.00 | 1115.00 | 166.60 | 857.00 | 303.90 | 32.60 | 367.00 | 66.80 | 405.00 | 79.30 | 205.40 | 27.03 | 164.20 | 19.77 |
| AP_TG08_81 | 177200.00 | 435000.00 | 272.30 | 2450.00 | 0.06 | BDL | 419.00 | 1192.00 | 179.40 | 907.00 | 322.00 | 34.40 | 393.00 | 69.90 | 432.00 | 84.80 | 216.20 | 28.98 | 170.70 | 21.40 |
| AP_TG08_82 | 178600.00 | 442000.00 | 283.40 | 1761.00 | 0.01 | BDL | 332.60 | 983.00 | 152.90 | 760.00 | 275.80 | 28.77 | 336.10 | 57.40 | 337.80 | 64.70 | 161.80 | 19.87 | 111.50 | 13.62 |
| AP_TG08_83 | 179500.00 | 434300.00 | 270.00 | 1592.00 | 0.01 | BDL | 218.00 | 658.00 | 105.30 | 557.00 | 207.50 | 21.41 | 268.00 | 46.50 | 276.90 | 55.00 | 138.90 | 17.87 | 103.70 | 12.61 |
| AP_TG08_84 | 172500.00 | 432300.00 | 291.60 | 1118.00 | 0.05 | 0.02 | 190.30 | 592.00 | 94.80 | 527.00 | 188.60 | 19.49 | 241.10 | 38.46 | 225.60 | 42.50 | 101.50 | 12.11 | 63.90 | 7.33 |
| AP_TG08_85 | 173000.00 | 439000.00 | 268.50 | 2308.00 | 0.02 | BDL | 362.00 | 1060.00 | 163.00 | 843.00 | 304.00 | 33.70 | 381.00 | 69.00 | 421.00 | 82.10 | 208.80 | 27.00 | 154.40 | 19.70 |

| Spot | Sample PSB09 Zircon - REE elements (ppm) - Quad ICP-MS | | | | | | | | | | | | | |
|---|---|---|---|---|---|---|---|---|---|---|---|---|---|---|
| | La | Ce | Pr | Nd | Sm | Eu | Gd | Tb | Dy | Ho | Er | Yb | Y | Lu |
| PSB09_1 | 15.80 | 49.80 | 5.58 | 29.10 | 13.40 | 4.10 | 27.70 | 7.68 | 76.90 | 26.40 | 112.90 | 190.00 | 890.00 | 33.80 |
| PSB09_2 | 2.19 | 26.70 | 1.86 | 11.80 | 5.49 | 1.11 | 13.10 | 5.01 | 68.50 | 29.40 | 158.30 | 459.00 | 893.00 | 99.20 |
| PSB09_3 | 672.00 | 3690.00 | 488.00 | 2940.00 | 1460.00 | 743.00 | 1830.00 | 376.00 | 2920.00 | 691.00 | 2260.00 | 2840.00 | 23500.00 | 388.00 |
| PSB09_4 | 0.33 | 12.40 | 0.53 | 3.68 | 3.51 | 0.52 | 12.77 | 4.57 | 55.40 | 20.49 | 96.40 | 192.90 | 605.00 | 39.00 |
| PSB09_5 | 0.16 | 5.80 | 0.09 | 1.32 | 1.51 | 0.11 | 7.80 | 3.03 | 42.90 | 18.45 | 94.80 | 243.00 | 560.00 | 49.20 |
| PSB09_6 | 59.00 | 620.00 | 116.00 | 660.00 | 219.00 | 71.00 | 199.00 | 29.50 | 194.00 | 42.00 | 124.00 | 143.00 | 1430.00 | 24.80 |
| PSB09_7 | 4.47 | 16.50 | 1.86 | 10.40 | 7.20 | 2.08 | 26.60 | 8.73 | 102.00 | 38.50 | 171.00 | 321.00 | 1110.00 | 64.40 |
| PSB09_8 | 725.00 | 4610.00 | 577.00 | 3220.00 | 1730.00 | 790.00 | 2350.00 | 579.00 | 4720.00 | 1105.00 | 3550.00 | 3870.00 | 35300.00 | 512.00 |
| PSB09_9 | 0.12 | 21.10 | 0.57 | 7.13 | 8.42 | 2.87 | 27.30 | 5.82 | 47.90 | 13.96 | 50.70 | 80.20 | 402.00 | 15.87 |
| PSB09_10 | 60.00 | 580.00 | 89.00 | 610.00 | 420.00 | 152.00 | 510.00 | 106.00 | 770.00 | 171.00 | 520.00 | 570.00 | 5300.00 | 84.00 |
| PSB09_11 | 0.00 | 3.40 | 0.02 | 0.27 | 0.43 | 0.04 | 3.31 | 1.37 | 18.70 | 8.53 | 44.90 | 117.30 | 290.00 | 26.30 |
| PSB09_12 | 0.03 | 30.70 | 0.27 | 3.97 | 6.74 | 2.93 | 29.60 | 8.39 | 83.50 | 28.00 | 111.90 | 187.60 | 815.00 | 36.10 |
| PSB09_13 | 34.80 | 252.00 | 36.00 | 211.00 | 104.00 | 45.00 | 132.00 | 26.10 | 192.00 | 45.00 | 145.00 | 179.00 | 1640.00 | 28.70 |
| PSB09_14 | 1.48 | 43.70 | 1.41 | 12.00 | 10.87 | 3.95 | 28.80 | 7.05 | 65.80 | 20.20 | 76.90 | 122.30 | 604.00 | 23.45 |
| PSB09_15 | 11.00 | 45.50 | 5.57 | 36.60 | 28.10 | 6.54 | 71.60 | 18.71 | 184.60 | 56.40 | 216.30 | 327.10 | 1611.00 | 59.60 |
| PSB09_16 | 0.09 | 47.70 | 0.49 | 7.50 | 10.34 | 3.57 | 36.40 | 8.92 | 78.60 | 23.00 | 81.20 | 121.00 | 663.00 | 22.00 |
| PSB09_17 | 110.50 | 819.00 | 127.00 | 850.00 | 599.00 | 220.00 | 672.00 | 128.00 | 840.00 | 175.00 | 505.00 | 621.00 | 5670.00 | 97.60 |
| PSB09_18 | 154.00 | 1697.00 | 251.00 | 1541.00 | 1008.00 | 394.00 | 1283.00 | 289.00 | 2120.00 | 470.00 | 1382.00 | 1307.00 | 15540.00 | 173.90 |
| PSB09_19 | 72.00 | 297.00 | 37.00 | 192.00 | 112.00 | 38.50 | 155.00 | 31.00 | 228.00 | 55.10 | 167.00 | 206.00 | 1770.00 | 33.30 |
| PSB09_20 | 108.00 | 1290.00 | 207.00 | 1370.00 | 799.00 | 278.00 | 890.00 | 171.00 | 1190.00 | 256.00 | 726.00 | 714.00 | 8500.00 | 100.90 |
| PSB09_21 | 60.00 | 126.00 | 17.50 | 76.00 | 40.20 | 14.20 | 59.40 | 13.10 | 107.30 | 26.30 | 81.40 | 85.20 | 798.00 | 13.26 |
| PSB09_22 | 0.76 | 30.80 | 0.55 | 5.35 | 6.00 | 1.71 | 20.50 | 6.27 | 63.50 | 20.50 | 78.50 | 120.70 | 602.00 | 22.80 |
| PSB09_23 | 527.00 | 5190.00 | 631.00 | 3654.00 | 1877.00 | 761.00 | 2379.00 | 506.60 | 3593.00 | 786.00 | 2191.00 | 1982.00 | 28740.00 | 269.90 |
| PSB09_24 | 4.10 | 64.00 | BDL | 22.00 | 15.70 | 4.20 | 29.10 | 8.50 | 84.00 | 29.00 | 126.40 | 251.30 | 960.00 | 52.60 |
| PSB09_25 | 0.06 | 10.85 | 0.08 | 1.44 | 2.99 | 0.58 | 12.20 | 3.52 | 33.70 | 10.80 | 41.50 | 68.90 | 312.00 | 13.30 |
| PSB09_26 | 0.00 | 12.28 | 0.12 | 1.97 | 5.12 | 0.68 | 20.60 | 5.56 | 49.50 | 13.83 | 47.30 | 60.40 | 415.00 | 10.28 |
| PSB09_27 | 2.30 | 62.90 | 4.60 | 32.00 | 26.40 | 9.80 | 62.00 | 13.80 | 113.00 | 30.10 | 104.90 | 148.00 | 924.00 | 26.00 |
| PSB09_28 | 128.00 | 1720.00 | 210.00 | 1292.00 | 917.00 | 388.00 | 1312.00 | 340.00 | 2840.00 | 660.00 | 2020.00 | 2050.00 | 20200.00 | 256.00 |
| PSB09_30 | 28.00 | 240.00 | 38.00 | 270.00 | 156.00 | 52.00 | 156.00 | 29.10 | 212.00 | 54.00 | 182.00 | 310.00 | 2110.00 | 53.00 |
| PSB09_31 | 0.80 | 60.50 | 1.71 | 15.30 | 16.90 | 5.11 | 49.30 | 11.00 | 92.00 | 26.20 | 88.00 | 124.00 | 742.00 | 21.80 |
| PSB09_32 | 1.71 | 33.10 | 2.35 | 15.50 | 11.40 | 4.50 | 27.00 | 6.75 | 60.00 | 17.80 | 64.70 | 110.00 | 542.00 | 19.30 |
| PSB09_33 | 9.50 | 73.70 | 6.80 | 45.00 | 29.60 | 11.40 | 45.70 | 12.50 | 112.00 | 32.10 | 130.40 | 256.00 | 1010.00 | 51.60 |
| PSB09_34 | 184.00 | 1646.00 | 208.90 | 1321.00 | 978.00 | 359.00 | 1292.00 | 317.00 | 2460.00 | 536.00 | 1600.00 | 1654.00 | 16330.00 | 216.40 |
| PSB09_35 | 0.84 | 35.90 | 0.97 | 8.70 | 8.50 | 3.44 | 27.10 | 6.59 | 57.80 | 17.40 | 64.00 | 94.50 | 515.00 | 17.40 |
| PSB09_36 | 260.00 | 1030.00 | 147.00 | 825.00 | 512.00 | 181.00 | 619.00 | 128.60 | 911.00 | 191.00 | 553.00 | 559.00 | 6160.00 | 74.70 |
| PSB09_37 | 88.90 | 393.00 | 70.40 | 471.00 | 427.00 | 156.10 | 586.00 | 123.90 | 825.00 | 161.50 | 444.00 | 461.00 | 5100.00 | 69.10 |
| PSB09_38 | 35.00 | 111.00 | 10.20 | 52.00 | 19.70 | 4.61 | 36.60 | 7.78 | 64.20 | 17.40 | 65.40 | 103.90 | 529.00 | 18.90 |
| PSB09_39 | 143.40 | 1410.00 | 210.00 | 1437.00 | 1001.00 | 388.00 | 1203.00 | 241.80 | 1721.00 | 371.00 | 1104.00 | 1124.00 | 12160.00 | 145.30 |
| PSB09_40 | 160.30 | 1430.00 | 206.00 | 1270.00 | 945.00 | 354.00 | 1228.00 | 294.00 | 2220.00 | 498.00 | 1500.00 | 1580.00 | 15300.00 | 213.00 |
| PSB09_41 | 79.40 | 659.00 | 99.90 | 652.00 | 495.00 | 174.00 | 655.00 | 141.40 | 991.00 | 211.20 | 615.00 | 635.00 | 6710.00 | 88.90 |
| PSB09_42 | 37.90 | 496.00 | 74.00 | 498.00 | 353.00 | 131.00 | 448.00 | 97.00 | 690.00 | 151.00 | 444.00 | 450.00 | 5000.00 | 65.90 |
| PSB09_43 | 2.70 | 67.00 | 6.00 | 47.00 | 36.00 | 12.50 | 61.00 | 12.50 | 101.00 | 26.10 | 88.00 | 127.00 | 820.00 | 22.30 |
| PSB09_44 | 135.20 | 1302.00 | 201.20 | 1334.00 | 1024.00 | 330.00 | 1102.00 | 196.70 | 1226.00 | 235.00 | 651.00 | 755.00 | 7980.00 | 119.00 |
| PSB09_45 | 107.00 | 878.00 | 115.00 | 768.00 | 602.00 | 216.00 | 705.00 | 138.00 | 924.00 | 197.00 | 584.00 | 619.00 | 6320.00 | 89.00 |
| PSB09_46 | 31.90 | 163.00 | 20.00 | 134.00 | 92.70 | 31.90 | 138.60 | 31.30 | 224.00 | 54.10 | 168.40 | 218.00 | 1697.00 | 35.70 |
| PSB09_47 | 139.00 | 1250.00 | 196.00 | 1256.00 | 928.00 | 316.00 | 1137.00 | 245.00 | 1680.00 | 352.00 | 1000.00 | 989.00 | 11140.00 | 137.60 |
| PSB09_48 | 14.00 | 190.00 | 19.70 | 115.00 | 64.30 | 21.80 | 96.20 | 22.10 | 173.20 | 44.90 | 154.00 | 206.00 | 1383.00 | 36.10 |
| PSB09_49 | 46.20 | 534.00 | 78.00 | 481.00 | 299.00 | 123.00 | 359.00 | 74.00 | 543.00 | 121.00 | 360.00 | 363.00 | 4280.00 | 57.00 |
| PSB09_50 | 4.19 | 71.00 | 7.90 | 56.00 | 37.90 | 14.40 | 61.80 | 13.00 | 106.00 | 26.60 | 90.50 | 121.00 | 838.00 | 21.10 |
| PSB09_51 | 12.90 | 113.00 | 12.30 | 80.00 | 58.00 | 20.60 | 90.00 | 20.20 | 159.00 | 42.10 | 141.00 | 192.00 | 1260.00 | 32.00 |
| PSB09_52 | 44.60 | 362.00 | 55.30 | 316.00 | 141.00 | 53.00 | 156.00 | 30.30 | 210.00 | 52.50 | 179.00 | 281.00 | 1770.00 | 49.70 |
| PSB09_53 | 256.00 | 2830.00 | 377.00 | 2210.00 | 1194.00 | 469.00 | 1447.00 | 302.00 | 2260.00 | 514.00 | 1529.00 | 1435.00 | 17190.00 | 193.00 |
| PSB09_54 | 172.00 | 1050.00 | 164.00 | 931.00 | 417.00 | 154.40 | 440.00 | 78.90 | 503.00 | 108.50 | 316.00 | 412.00 | 3810.00 | 72.30 |
| PSB09_55 | 59.60 | 570.00 | 81.00 | 493.00 | 242.00 | 125.00 | 286.00 | 56.30 | 390.00 | 88.30 | 264.00 | 313.00 | 3030.00 | 49.80 |
| PSB09_56 | 0.77 | 32.30 | 0.73 | 8.90 | 10.40 | 3.47 | 33.00 | 7.69 | 63.10 | 18.77 | 65.90 | 100.20 | 529.00 | 18.63 |
| PSB09_57 | 112.00 | 1053.00 | 153.00 | 986.00 | 710.00 | 263.00 | 856.00 | 176.00 | 1240.00 | 271.00 | 780.00 | 758.00 | 9170.00 | 102.00 |

| Spot | Sample PS42A - Titanite REE elements (ppm) - Quad ICP-MS | | | | | | | | | | | | | |
|---|---|---|---|---|---|---|---|---|---|---|---|---|---|---|
| | La | Ce | Pr | Nd | Sm | Eu | Gd | Tb | Dy | Ho | Er | Yb | Y | Lu |
| PS42A_SPH_1 | 177.80 | 1069.00 | 265.50 | 1814.00 | 868.00 | 295.00 | 826.00 | 123.80 | 635.00 | 105.00 | 256.00 | 233.00 | 2990.00 | 28.30 |
| PS42A_SPH_2 | 449.00 | 2543.00 | 551.80 | 3200.00 | 1009.00 | 186.10 | 771.60 | 97.30 | 447.60 | 71.10 | 162.80 | 130.50 | 1967.00 | 16.73 |
| PS42A_SPH_3 | 296.00 | 1500.00 | 335.00 | 2190.00 | 886.00 | 228.70 | 760.00 | 101.00 | 479.00 | 74.70 | 165.00 | 127.00 | 1890.00 | 14.90 |
| PS42A_SPH_4 | 874.00 | 4130.00 | 742.00 | 4040.00 | 1220.00 | 196.00 | 950.00 | 126.00 | 591.00 | 93.00 | 211.00 | 151.00 | 2480.00 | 17.00 |
| PS42A_SPH_5 | 656.00 | 3140.00 | 569.00 | 3020.00 | 908.00 | 181.00 | 774.00 | 107.00 | 518.00 | 81.40 | 174.00 | 105.30 | 2070.00 | 10.32 |
| PS42A_SPH_6 | 690.00 | 3320.00 | 645.00 | 3660.00 | 1200.00 | 221.30 | 939.00 | 120.80 | 562.00 | 86.30 | 194.00 | 157.00 | 2290.00 | 18.20 |
| PS42A_SPH_7 | 550.00 | 2880.00 | 629.40 | 3826.00 | 1390.00 | 209.70 | 1172.00 | 161.80 | 791.00 | 127.70 | 304.00 | 260.00 | 3550.00 | 31.80 |
| PS42A_SPH_8 | 448.00 | 2639.00 | 621.00 | 3943.00 | 1534.00 | 215.40 | 1317.00 | 182.00 | 896.00 | 146.00 | 349.00 | 317.00 | 4070.00 | 39.20 |
| PS42A_SPH_9 | 666.00 | 2861.00 | 491.80 | 2467.00 | 693.00 | 125.60 | 533.00 | 68.80 | 325.20 | 52.20 | 119.40 | 86.90 | 1385.00 | 9.73 |
| PS42A_SPH_10 | 150.30 | 913.00 | 243.00 | 1750.00 | 901.00 | 221.20 | 838.00 | 116.90 | 564.00 | 88.60 | 200.00 | 158.10 | 2281.00 | 18.20 |
| PS42A_SPH_11 | 536.00 | 3040.00 | 664.00 | 3889.00 | 1226.00 | 204.70 | 944.00 | 121.20 | 571.00 | 91.00 | 212.60 | 184.00 | 2511.00 | 23.50 |
| PS42A_SPH_12 | 616.00 | 2858.00 | 537.00 | 2900.00 | 868.00 | 203.40 | 674.00 | 85.20 | 398.00 | 62.90 | 141.20 | 100.00 | 1675.00 | 11.23 |
| PS42A_SPH_13 | 493.00 | 2562.00 | 567.00 | 3518.00 | 1349.00 | 211.90 | 1159.00 | 160.10 | 768.00 | 121.00 | 270.10 | 195.10 | 3091.00 | 21.25 |
| PS42A_SPH_14 | 823.00 | 3120.00 | 466.00 | 2080.00 | 453.00 | 117.60 | 327.00 | 39.00 | 182.00 | 29.30 | 68.30 | 53.70 | 828.00 | 6.34 |
| PS42A_SPH_15 | 1153.00 | 5480.00 | 921.00 | 4680.00 | 1157.00 | 183.80 | 757.00 | 86.00 | 357.20 | 50.60 | 106.20 | 67.10 | 1260.00 | 7.40 |
| PS42A_SPH_16 | 1004.00 | 4040.00 | 591.00 | 2640.00 | 504.00 | 116.30 | 318.00 | 35.20 | 152.00 | 23.40 | 52.70 | 35.80 | 658.00 | 4.05 |
| PS42A_SPH_17 | 1205.00 | 5180.00 | 816.00 | 4041.00 | 1006.00 | 201.20 | 736.00 | 88.50 | 394.00 | 59.40 | 122.10 | 73.60 | 1555.00 | 8.12 |
| PS42A_SPH_18 | 1243.00 | 4700.00 | 643.60 | 2749.00 | 554.20 | 149.20 | 397.10 | 48.80 | 233.20 | 39.05 | 93.20 | 73.50 | 1147.00 | 8.16 |
| PS42A_SPH_19 | 1462.00 | 6051.00 | 963.00 | 4890.00 | 1208.00 | 270.00 | 877.00 | 104.90 | 459.00 | 67.10 | 137.00 | 74.40 | 1660.00 | 7.71 |
| PS42A_SPH_20 | 504.00 | 2610.00 | 588.00 | 3782.00 | 1593.00 | 242.60 | 1444.00 | 206.00 | 1031.00 | 163.00 | 371.00 | 284.00 | 4460.00 | 31.90 |
| PS42A_SPH_21 | 657.00 | 2941.00 | 520.40 | 2711.00 | 813.00 | 198.30 | 646.00 | 83.70 | 408.00 | 65.30 | 153.80 | 126.10 | 1786.00 | 15.04 |
| PS42A_SPH_22 | 818.00 | 4370.00 | 782.00 | 4121.00 | 1092.00 | 182.20 | 751.00 | 89.40 | 404.70 | 62.74 | 140.60 | 112.30 | 1650.00 | 13.85 |
| PS42A_SPH_23 | 161.30 | 962.00 | 233.50 | 1586.00 | 768.00 | 430.00 | 799.00 | 115.00 | 586.00 | 98.20 | 235.70 | 205.20 | 2910.00 | 25.04 |
| PS42A_SPH_24 | 1585.00 | 6490.00 | 1014.00 | 4890.00 | 1079.00 | 244.00 | 749.00 | 86.40 | 386.00 | 59.10 | 122.60 | 77.90 | 1440.00 | 7.97 |
| PS42A_SPH_25 | 982.00 | 3870.00 | 596.00 | 2920.00 | 832.00 | 163.80 | 642.00 | 78.10 | 353.00 | 53.80 | 115.20 | 80.70 | 1371.00 | 8.94 |
| PS42A_SPH_26 | 494.00 | 2683.00 | 594.00 | 3606.00 | 1229.00 | 221.50 | 962.00 | 123.10 | 577.00 | 91.10 | 206.30 | 172.00 | 2490.00 | 21.40 |
| PS42A_SPH_27 | 397.50 | 1915.00 | 393.20 | 2281.00 | 778.00 | 225.40 | 638.00 | 84.80 | 413.00 | 68.50 | 162.80 | 146.90 | 2003.00 | 18.49 |
| PS42A_SPH_28 | 187.90 | 881.00 | 162.40 | 828.00 | 215.50 | 289.80 | 169.20 | 20.03 | 99.80 | 16.98 | 42.80 | 44.30 | 594.00 | 6.72 |
| PS42A_SPH_29 | 73.60 | 439.00 | 103.80 | 649.00 | 229.00 | 196.30 | 182.00 | 22.30 | 104.90 | 17.40 | 42.50 | 36.10 | 535.00 | 5.20 |
| PS42A_SPH_30 | 1430.00 | 5990.00 | 956.00 | 4840.00 | 1092.00 | 242.30 | 695.00 | 76.40 | 336.00 | 49.30 | 101.90 | 59.00 | 1191.00 | 6.42 |
| PS42A_SPH_31 | 526.00 | 2420.00 | 475.00 | 2710.00 | 917.00 | 230.90 | 755.00 | 101.20 | 493.00 | 80.50 | 189.40 | 162.20 | 2257.00 | 19.91 |
| PS42A_SPH_32 | 302.00 | 1720.00 | 374.00 | 2150.00 | 711.00 | 184.10 | 570.00 | 73.50 | 337.00 | 52.40 | 111.70 | 79.60 | 1318.00 | 9.22 |
| PS42A_SPH_33 | 369.00 | 1630.00 | 300.00 | 1590.00 | 473.00 | 204.00 | 379.00 | 47.40 | 228.50 | 37.00 | 86.10 | 74.00 | 1076.00 | 9.01 |
| PS42A_SPH_34 | 48.84 | 314.90 | 82.70 | 581.00 | 261.00 | 154.80 | 234.00 | 30.90 | 147.00 | 23.60 | 55.10 | 47.20 | 673.00 | 6.25 |
| PS42A_SPH_35 | 440.00 | 2375.00 | 538.00 | 3370.00 | 1280.00 | 207.80 | 1088.00 | 148.00 | 718.00 | 112.30 | 251.00 | 190.00 | 2810.00 | 21.42 |
| PS42A_SPH_36 | 955.00 | 4730.00 | 898.00 | 5240.00 | 1757.00 | 329.10 | 1439.00 | 186.60 | 857.00 | 124.60 | 253.40 | 159.40 | 3024.00 | 17.20 |
| PS42A_SPH_37 | 1725.00 | 8070.00 | 1410.00 | 7700.00 | 2089.00 | 275.50 | 1328.00 | 142.20 | 558.00 | 73.10 | 131.10 | 65.20 | 1609.00 | 5.99 |
| PS42A_SPH_38 | 292.80 | 1606.00 | 352.60 | 2070.00 | 641.00 | 232.00 | 488.20 | 60.50 | 283.50 | 47.20 | 115.40 | 103.90 | 1463.00 | 13.92 |
| PS42A_SPH_39 | 1032.00 | 4060.00 | 588.00 | 2574.00 | 497.00 | 85.20 | 304.00 | 33.20 | 145.20 | 22.06 | 47.00 | 31.90 | 584.00 | 3.32 |
| PS42A_SPH_40 | 220.00 | 882.00 | 152.30 | 775.00 | 213.10 | 171.90 | 156.60 | 19.70 | 91.70 | 15.40 | 38.10 | 34.60 | 457.00 | 4.72 |
| PS42A_SPH_41 | 1279.00 | 4880.00 | 650.00 | 2707.00 | 463.00 | 131.20 | 301.20 | 35.28 | 172.60 | 31.76 | 84.70 | 83.50 | 1035.00 | 10.59 |
| PS42A_SPH_42 | 595.00 | 2840.00 | 591.00 | 3558.00 | 1412.00 | 212.00 | 1290.00 | 187.00 | 930.00 | 151.00 | 350.00 | 285.00 | 4090.00 | 31.50 |
| PS42A_SPH_43 | 621.00 | 3863.00 | 789.70 | 4508.00 | 1248.00 | 210.10 | 893.00 | 106.40 | 478.00 | 74.30 | 167.40 | 141.20 | 2002.00 | 18.01 |
| PS42A_SPH_44 | 320.00 | 1805.00 | 457.00 | 3215.00 | 1533.00 | 285.00 | 1375.00 | 197.00 | 976.00 | 153.00 | 344.00 | 288.00 | 4180.00 | 32.40 |
| PS42A_SPH_45 | 451.00 | 2479.00 | 550.00 | 3271.00 | 1094.00 | 210.60 | 873.00 | 111.40 | 527.00 | 84.80 | 192.20 | 154.20 | 2280.00 | 19.08 |
| PS42A_SPH_46 | 93.00 | 640.00 | 178.00 | 1250.00 | 547.00 | 159.10 | 467.00 | 63.60 | 306.00 | 49.20 | 113.60 | 92.20 | 1377.00 | 10.68 |
| PS42A_SPH_47 | 605.00 | 2926.00 | 604.00 | 3510.00 | 1190.00 | 201.20 | 953.00 | 122.80 | 583.00 | 89.70 | 199.00 | 151.00 | 2300.00 | 16.35 |
| PS42A_SPH_48 | 182.50 | 587.00 | 82.00 | 371.00 | 97.40 | 168.00 | 90.80 | 13.00 | 70.30 | 13.30 | 37.80 | 49.70 | 430.00 | 7.69 |
| PS42A_SPH_49 | 1244.00 | 5800.00 | 980.00 | 5110.00 | 1335.00 | 218.00 | 959.00 | 112.60 | 502.00 | 71.30 | 137.90 | 76.60 | 1740.00 | 7.24 |
| PS42A_SPH_50 | 189.10 | 1027.00 | 223.30 | 1334.00 | 440.00 | 289.00 | 314.00 | 38.80 | 177.90 | 29.33 | 71.30 | 65.90 | 889.00 | 9.03 |

# APÊNDICE C. Imagens (MEV) dos grãos de apatita, titanita e zircão analisados via LASS-ICP-MS

SAMPLE PS42A (MYLONITE)
Apatite U-Pb analyses
● 25 µm spot

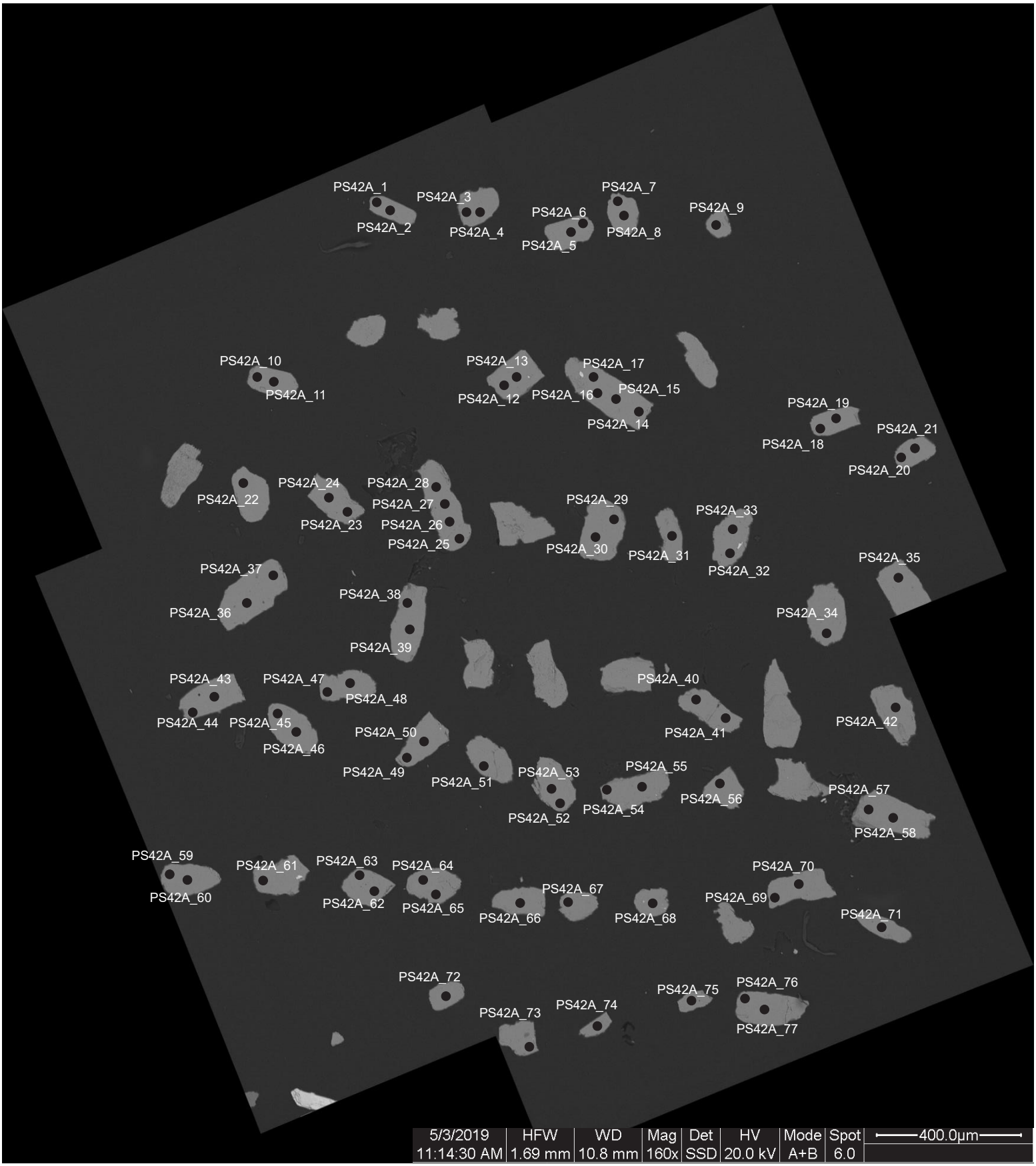

SAMPLE PSB09 (MYLONITE)
Apatite U-Pb analyses

- 25 um spot

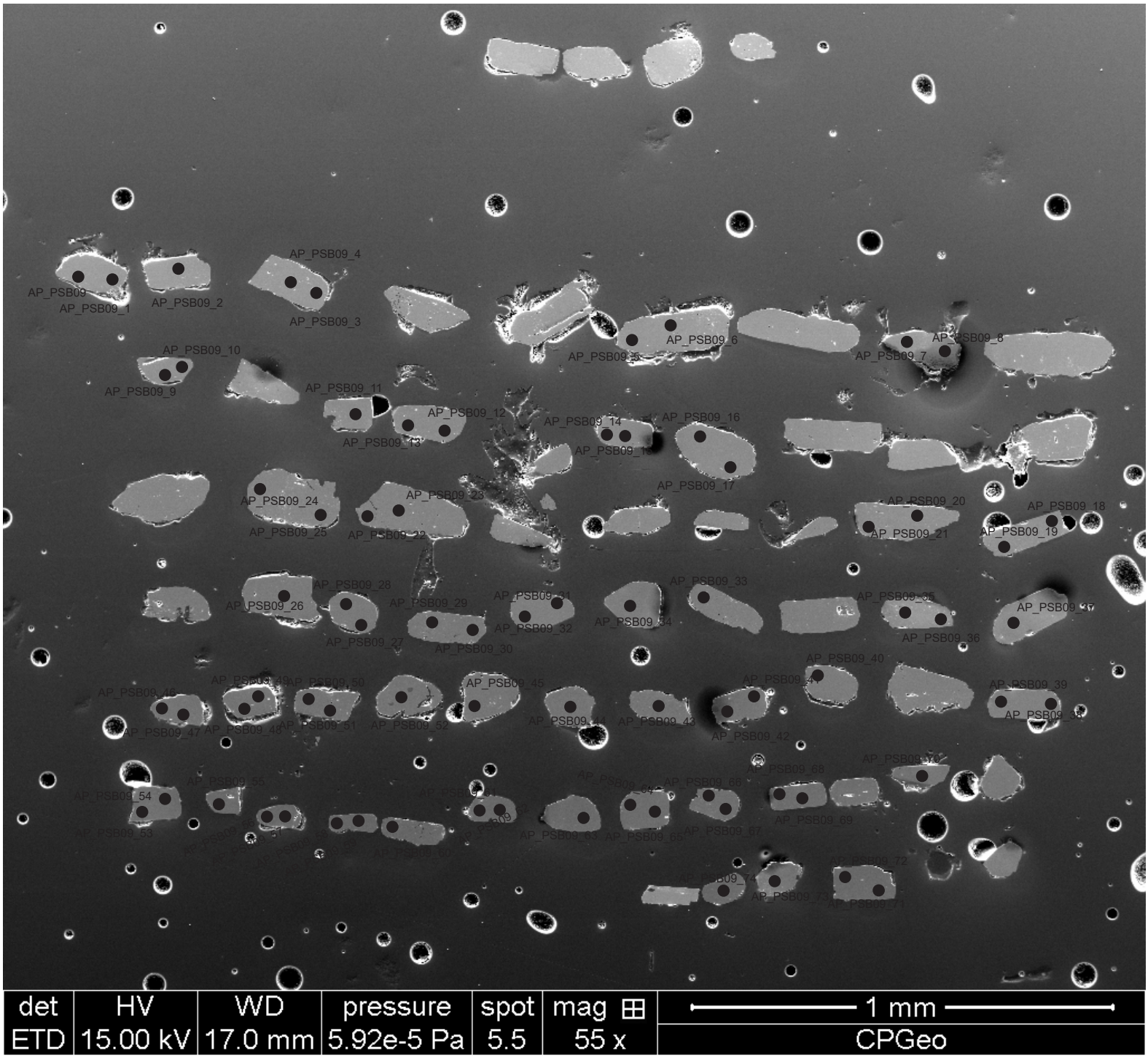

SAMPLE TG04 (GRANITE)
Apatite U-Pb analysis
● 25 µm - Apatite

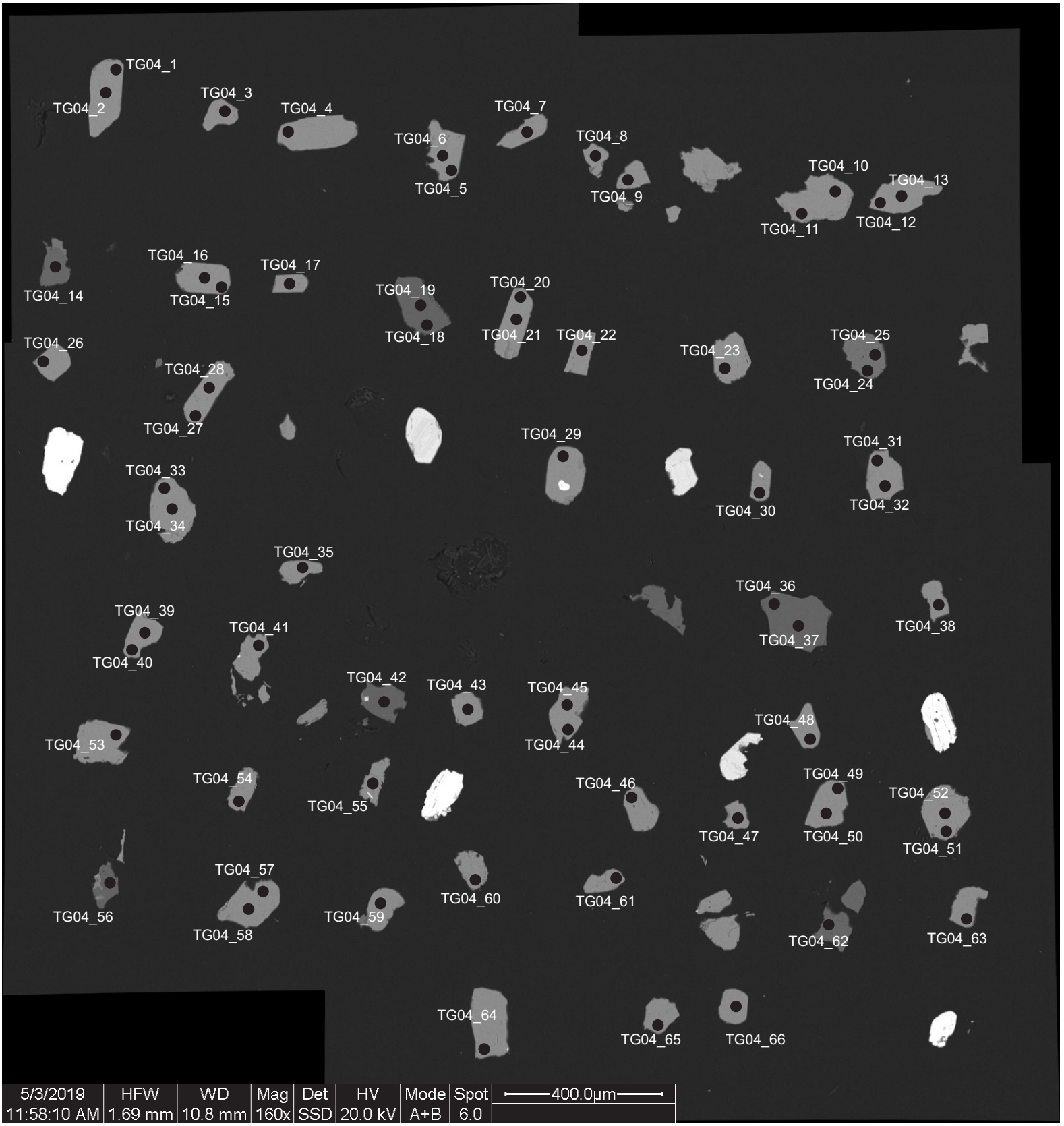

SAMPLE TG08 (GRANITE)
Apatite U-Pb analysis
● 25 µm spot

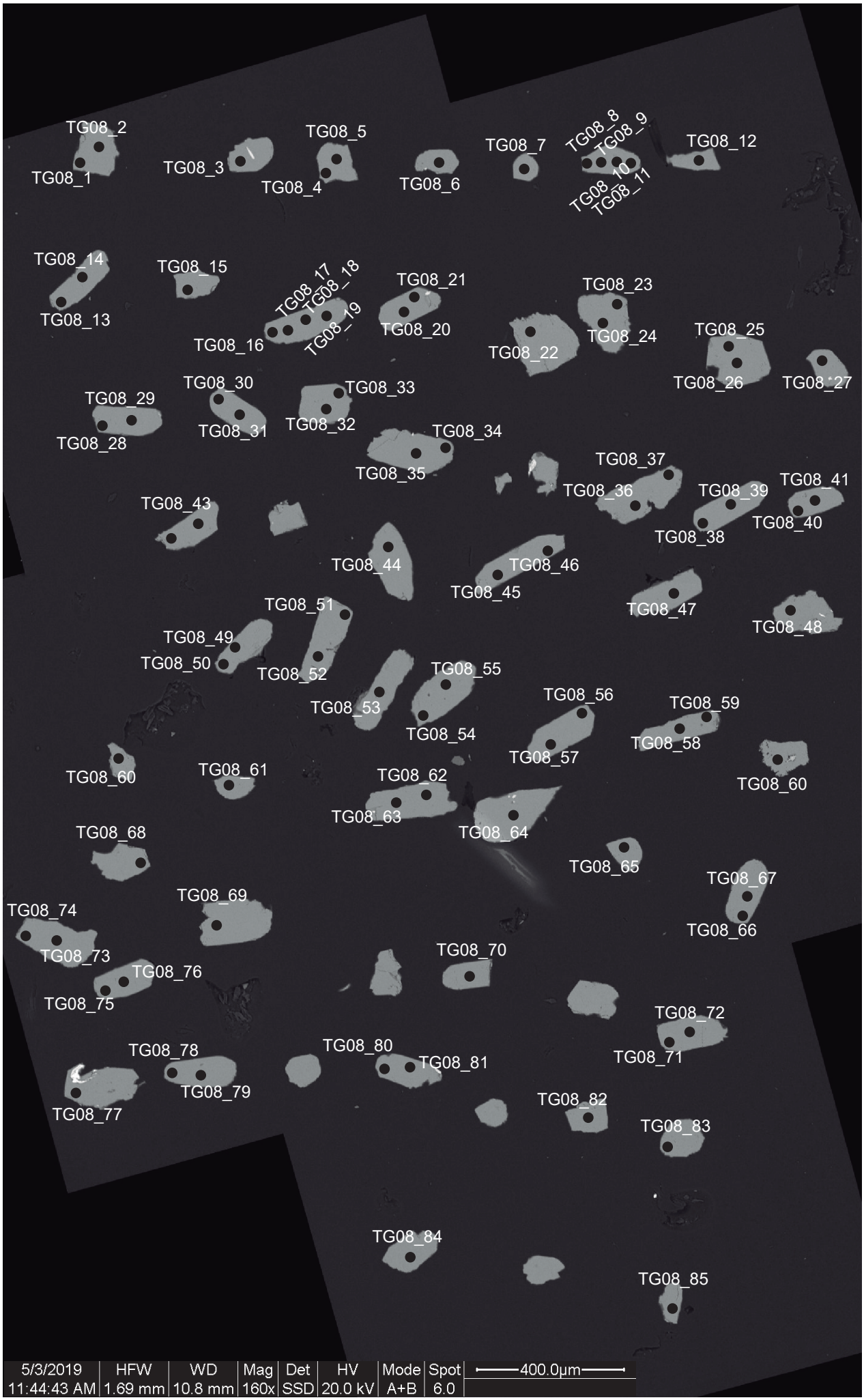

SAMPLE PS42A (MYLONITE) - 1/2
Titanite U-Pb analyses
○ 25 µm spot

SAMPLE PS42A (MYLONITE) - 2/2
Titanite U-Pb analyses
○ 25 µm spot

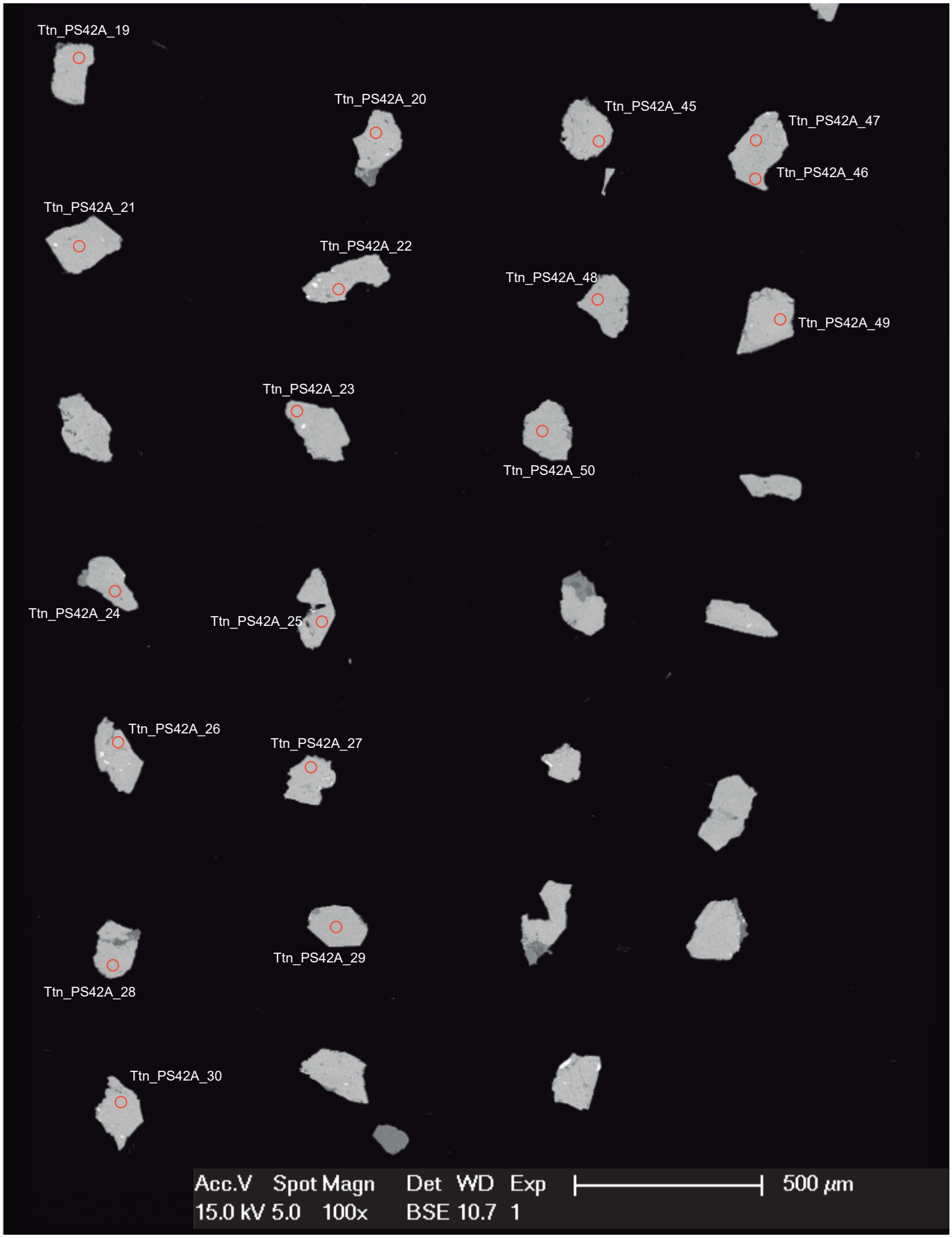

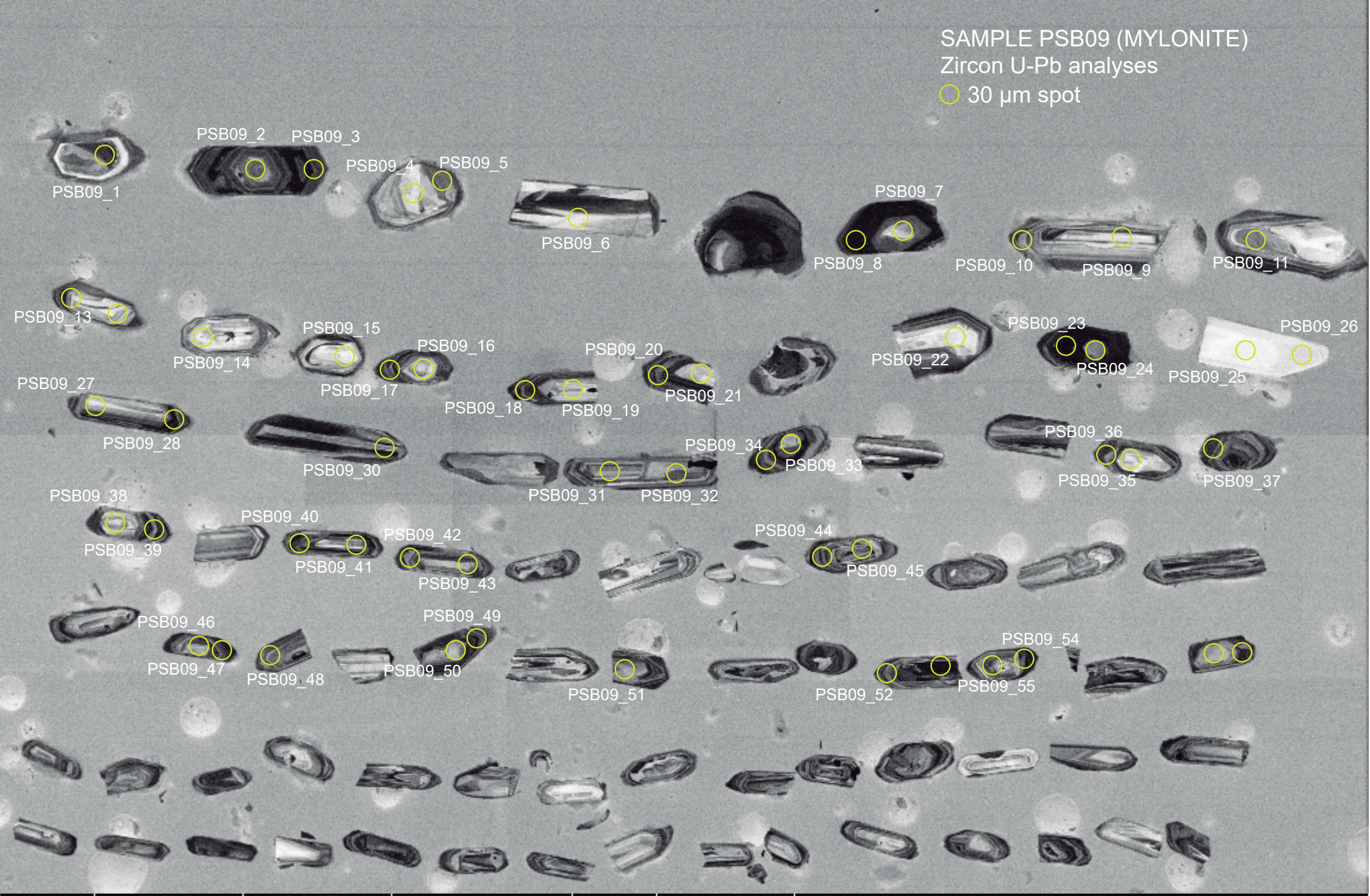
SAMPLE PSB09 (MYLONITE)
Zircon U-Pb analyses
30 µm spot
PSB09_1
PSB09_2
PSB09_3
PSB09_4
PSB09_5
PSB09_6
PSB09_7
PSB09_8
PSB09_9
PSB09_10
PSB09_11
PSB09_13
PSB09_14
PSB09_15
PSB09_16
PSB09_17
PSB09_18
PSB09_19
PSB09_20
PSB09_21
PSB09_22
PSB09_23
PSB09_24
PSB09_25
PSB09_26
PSB09_27
PSB09_28
PSB09_30
PSB09_31
PSB09_32
PSB09_33
PSB09_34
PSB09_35
PSB09_36
PSB09_37
PSB09_38
PSB09_39
PSB09_40
PSB09_41
PSB09_42
PSB09_43
PSB09_44
PSB09_45
PSB09_46
PSB09_47
PSB09_48
PSB09_49
PSB09_50
PSB09_51
PSB09_52
PSB09_54
PSB09_55
det
PMD
HV
15.00 kV
WD
17.0 mm
pressure
5.35e-5 Pa
spot
5.5
mag
65 x
500 µm
CPGeo